Considerations for Femtosecond Laser Electronic Excitation Tagging in High-Speed Flows

CHRISTOPHER JOHN PETERS

A DISSERTATION

PRESENTED TO THE FACULTY

OF PRINCETON UNIVERSITY

IN CANDIDACY FOR THE DEGREE

OF DOCTOR OF PHILOSOPHY

RECOMMENDED FOR ACCEPTANCE BY

THE DEPARTMENT OF

MECHANICAL AND AEROSPACE ENGINEERING

ADVISER: PROFESSOR RICHARD BRYANT MILES

September 2019

 $\ \, \ \, \ \,$ Copyright by Christopher John Peters, 2019. All rights reserved.

Abstract

Femtosecond laser electronic excitation tagging (FLEET) is an unseeded method for molecular tagging which offers valuable opportunities for measurement of high-speed (transonic, supersonic or hypersonic) flows. The unique nature of high-speed testing demands certain performance from FLEET such as satisfactory signal-to-noise ratio (SNR) at depressed static conditions (i.e., low temperatures, pressures and densities), wide dynamic range for velocity determination (especially single-shot), and measurements with acceptable accuracy and precision. This dissertation strives to evaluate FLEET in those regards and provide strategies to maximize the method's capabilities. A zero-dimensional kinetics model in nitrogen explains FLEET signal changes with pressure/density and/or temperature in terms of plasma-chemical reactions. Poorly known rate coefficients are tuned by comparing model output to measurements, with temporal agreement up to several hundred nanoseconds. Modeling reveals that initial signal peaks at reduced density because of slowed temporal evolution (and decay) of excited populations. Low temperatures enhance signal by enlarging cluster ion populations which contribute to excited species via electron-ion dissociative recombination. A purpose-built free jet facility provides experimental validation of the kinetics model and assesses FLEET velocimetry in low temperature and pressure/density conditions. Signal, lifetime, accuracy and precision results are obtained from unheated subsonic through Mach 4.0 operation of the facility, with best results noted. FLEET measurements of a sweeping jet (SWJ) actuator in compressible operation showcase its advantages in a highly unsteady jet containing subsonic through supersonic velocities. FLEET velocimetry is performed in the device's internal and external flow fields, with the latter compared to hot-wire anemometry. Internal measurements reveal the absence of shockwaves theorized to occur at high pressure ratios. Simultaneous qualitative measurements of compressible jet mixing are shown as a proof-of-concept. Overall, the work demonstrates that previous understanding of SWJ incompressible operation readily extends into the compressible realm. Practical aspects of performing FLEET velocimetry are detailed, along with strategies for improving measurement quality. Determination of a fundamental precision in nitrogen and air is attempted. Experiments show that increasing time delay and/or SNR improves velocimetry precision. A comparison of five camera systems indicates sensors with larger pixels capture higher SNR data and produce more precise results.

Acknowledgments

An extensive, but by no means exhaustive, compilation of acknowledgments.

First and foremost, I want to express my sincere gratitude to my Lord and Savior, Jesus Christ, for the many opportunities given to me in receiving this education and the endurance to finish the program.

Thank you to my mother, Karen Peters (née Peterman), who always encouraged me to pursue my passions to the fullest and attempt everything in life with my best effort. My sister and brother-in-law, Christine (née Peters) and Omar Ghaznawi, along with my aunt and uncle, Katherine (née Peterman) and Gary Emge, for their steadfast love and support. My late grandparents, John and Dorothy Peterman, who nurtured my interest in science and engineering at a very early age. I am thankful to my father, Kenneth Peters, for piquing my interest in aviation and space exploration with visits to the local air show and trips to the National Air and Space Museum.

My doctoral adviser, Richard Miles, for the opportunity to work in the Applied Physics Group and teaching me the importance of physical reasoning skills and the willingness to ask tough, but insightful questions.

Members of my doctoral committee, Luigi Martinelli and Marcus Hultmark, who furthered my understanding of fluid dynamics, both computational and experimental.

Readers of my dissertation, Mikhail Shneider and Julia Mikhailova, for diligent review of the manuscript and contributing to my understanding of plasma and laser physics.

I am deeply indebted to Tat Loon Chng, my dear friend, ever-helpful guru and trusted confidant, along with fellow students of the Applied Physics Group: David Feng, Matthew New-Tolley, Kristofer Meehan, Matthew Edwards, Nathan Calvert, Nicholas DeLuca, Yibin Zhang, Christopher Galea, Christopher Limbach, Sean McGuire and Maya Naphade.

Our laboratory staff who helped me with experiments and aided my understanding of experimental methods and practices: Nicolas Tkach, Arthur Dogariu, Andrey Starikovskiy and Benjamin Goldberg. Visiting researchers for their enlightening conversations and guidance: Kiyoshi Kinefuchi, Albina Tropina, Sean O'Byrne and Martiqua Post.

Michael Littman and Jonathan Prévost, for enhancing my understanding of electronics, instructing me in pedagogy and showing me the joys of teaching.

The late Sau-Hai "Harvey" Lam, for preparing me for the general examination with a solid foundation in theory and always making me certain to have an answer to the question, "Why is this important?"

Administrators Jill Ray and Jo Ann Kropilak-Love, who expertly facilitated my graduate studies and teaching activities in the department.

Members of my cohort in other research groups who provided invaluable support, technical advice and friendship: Sébastien Philippe, Joseph Tylka, Rahulram Sridhar, Patrick Vail, Yuyang Fan, Gregory Davies, Jesse Ault, Alta Fang, Christopher Wordingham and Mary Anne Peters-Limbach.

My NASA fellowship mentor, Paul Danehy, and other colleagues at NASA Langley Research Center such as Ross Burns, Brett Bathel, Jennifer Inman, Stephen Jones, Pacita Tiemsin and Gregory Jones, for fruitful collaborations, highly educational research experiences and cherished friendships.

Those from the greater Princeton community, Kelsey Ockert and Lili Cai, for their friendship, kindness and consideration.

The indelible support of childhood friends, Jordan Pernikoff and Andrew Costas, with whom I also share fond memories of playing the latest edition of *Microsoft Flight Simulator* and discussing our favorite quotes from *The Right Stuff*. Bryan Williams, for imparting some of his computer wisdom which undoubtedly aided the computational and programming efforts of this work.

Christopher Weaver and Matthew Plasek, whose conversations about science and plasma physics would inspire me and spark new wonder.

Martha Hasting of Washington University in Saint Louis, for instruction in mathematical principles used throughout this work. My undergraduate adviser, Michael Swartwout, for my first opportunity to engage in aerospace research.

Science Olympiad coaches, Martin Long and Roy White, who inspired me to love aerodynamics and ultimately pursue a career in aerospace engineering.

My family in Christ at the Lutheran Church of the Messiah in Princeton: Pastor Martin Erhardt, Paul Majsztrik and Laura Bennett, John Fischer II, Werner and Karen Hartl, Patricia Oelrich, Miranda Hempel, David Steinnagel, John and Esther Fischer, Anne Bolick, Peter and Renate Giller, Doris and Hank Gerwers, Jon and Patricia Hlafter, Nancy Amidon, Debra Baer, F. Steven and Beverly Bauman, Nathaniel "Nat" and Rachel Tabris, Skye Jerpbak, Ryan Spaude, Grant Schultheis, Hephzibah Penumaka and Kyle Sorkness.

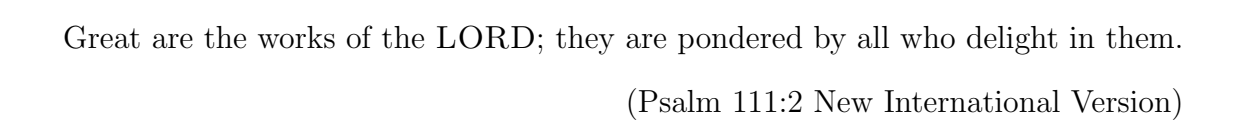
Princeton Graduate Christian Fellowship: The Reverend B. Keith Brewer, Alex Howe, Thomas Carlson, Erin Gray, Melissa Isaacs, Josephine Duh, Jonathan Ng, Jamie Tan, Jessica Lowe, Benjamin Reimold and Robert Kaita.

Lin Miao, for her loving-kindness and prayers during the preparation of the manuscript.

Student work generously supported by a NASA Space Technology Research Fellowship (NSTRF), the Air Force Office of Scientific Research and the Office of Naval Research (Code 32).

This dissertation carries T#3382 in the records of the Department of Mechanical and Aerospace Engineering.





Contents

	Abs	Abstract			
	Ack	nowledg	gments	V	
	List	of Tab	les	XV	
	List	of Figu	ires	XV.	
1	Intr	oduct	ion	1	
	1.1	Backg	ground Information for Method	1	
	1.2	Motiv	ation for Exploring High-Speed Flow Considerations	2	
	1.3	Releva	ant Major Past Works	5	
	1.4	Descri	iptive Outline of Core Chapters	F. 5	
		1.4.1	Use of Hyperlinks	7	
2	Kin	etics 1	Model in Nitrogen	8	
	2.1	Backg	ground and Motivation	8	
	2.2	Kineti	ics Model	S	
		2.2.1	Fluorescence, Recombination and Quenching	11	
		2.2.2	Electron-Neutral Collisions	13	
		2.2.3	Species, Charge and Energy Balance Considerations	15	
		2.2.4	Initial Conditions and Photoionization	20	
		2.2.5	Solution of Equations	24	
	2.3	Tunin	g of Rate Coefficients and FLEET Spectral Measurements	25	

		2.3.1	Random ('Monte Carlo') Parameter Search for Tuning Rate	
			Coefficients in Model	25
		2.3.2	Measurement of FLEET Spectrum	29
		2.3.3	Formulas and Assumptions for Relating Spectrometer, Photo-	
			multiplier and Model Results	32
		2.3.4	Bandpass Filters for Isolating VIS and UV Signal	34
		2.3.5	Photomultiplier (PMT) Experiment and Comparison to Model	35
	2.4	Model	ing Results, Discussion and Comparison to Experiment	40
		2.4.1	Species Populations and Contributing Reactions at Atmo-	
			spheric Conditions	40
		2.4.2	Ionization and Dissociation Fraction at Atmospheric Conditions	45
		2.4.3	Temperature Evolution and Contributing Processes at Atmo-	
			spheric Conditions	46
		2.4.4	Estimate for Maximum Gas Temperature Rise	48
		2.4.5	Initial Electronic Temperature Based on Above Atmospheric	
			Density Experimental Results	49
		2.4.6	Comparison to Below Atmospheric Density Experimental Results	51
	2.5	Summ	ary and Conclusions	51
3	Sign	nal, Lif	etime, Accuracy and Precision in Low Temperatures and	
	Pre	ssures		55
	3.1	Backg	round and Motivation	55
	3.2	Experi	mental Setup	56
		3.2.1	Variable Temperature and Pressure Flow Facility	56
		3.2.2	Intensified Camera	60
		3.2.3	Nominal Laser Parameters	62
	3.3	Image	Acquisition and Processing	63
	3.4	Signal	Measurement Results	68

		3.4.1	Signal Intensity	68
		3.4.2	Considerations for Comparison to Kinetics Model	71
		3.4.3	Initial Signal Trends and Comparison to Model	72
		3.4.4	Signal Lifetime (via Exponential Fits) and Comparison to Model	78
	3.5	Veloci	ty Measurement Results	83
		3.5.1	Overview of Velocimetry in Flow Facility	83
		3.5.2	Measurement Accuracy	85
		3.5.3	Measurement Precision	88
	3.6	Summ	ary and Conclusions	91
4	Арр	olicatio	on of Method to Sweeping Jet Actuator in Compressible	
	Ope	eration		96
	4.1	Backg	round and Motivation	96
		4.1.1	General Device Characteristics	98
		4.1.2	Motivation for Studying Compressible Operation	99
	4.2	Exper	imental Setup and Technique	99
		4.2.1	Configuration of Sweeping Jet Actuator	99
		4.2.2	Measurement Systems and Methods	101
	4.3	Result	s and Discussion	108
		4.3.1	External Flow Field - Schlieren, FLEET and HWA	108
		4.3.2	Internal Flow Field - FLEET	119
		4.3.3	Concentration in the External Flow Field - FLEET	123
		4.3.4	Comparison of FLEET Velocimetry and Hot-Wire Anemometry	126
	4.4	Summ	ary and Conclusions	127
5	Pra	ctical	Considerations for Precise Measurements 1	130
	5.1	Backg	round and Motivation	130
		5.1.1	Alternative Unseeded Velocimetry Methods	131

	5.2	Experi	imental Setup and Technique	133
		5.2.1	Femtosecond Laser System	133
		5.2.2	Free Jet Configurations	134
		5.2.3	High-Speed CMOS Camera - pco.dimax HD	136
		5.2.4	High-Speed CMOS Camera System Comparison	139
		5.2.5	Data Processing and Techniques to Improve Precision	141
	5.3	Result	s and Discussion	147
		5.3.1	Improvement in Precision due to Row-wise Binning and Inter-	
			frame Delay	147
		5.3.2	High-Speed CMOS Camera Comparison	153
	5.4	Summ	ary and Conclusions	163
6	Con	clusio	n	168
	6.1	Conclu	iding Thoughts	168
	6.2	Future	e Work	170
		6.2.1	Kinetics Model Improvements	170
		6.2.2	Simultaneous Measurements of Density, Mixing and Velocity in	
			Compressible Flow	172
		6.2.3	Velocity Measurements in Supersonic Shape Morphing Flow Fa-	
			cility	173
	6.3	Autho	r's Contribution to Presented Work	176
A	Acc	uracy	and Precision	177
В	Infl	uence (of Mass Diffusivity on Low Temperature and Pressure Sig	5-
	nal	Result	${f s}$	178
	B.1	Width	(Thickness) of Tagged Region	178
	B.2	Integra	ated Signal Intensity	180
	B.3	Initial	Integrated Signal Compared to Model	182

C Sweeping Jet Actuator FLEET Measurement Details			
	C.1	Single-Shot Velocity Measurements	184
	C.2	Analysis of Velocity Precision	185
	C.3	Data Point Density of Internal Velocity Measurements	187
D	Cha	aracterization of Low-speed Jet	189
Bi	bliog	graphy	190

List of Tables

2.1	Reactions in model	10
2.2	Atomic recombination rate coefficient	12
2.3	Fast gas heating	16
2.4	Tuned rate coefficients	26
2.5	Second positive features used in calibration	31
3.1	Facility nozzle nominal specifications	57
5.1	Comparison of CMOS camera systems	140
5.2	Comparison of raw images	154
C.1	Precision comparison of FLEET in air	186

List of Figures

2.1	Spread of simulation results versus experiment	28
2.2	FLEET spectrum in nitrogen at ambient conditions	31
2.3	Spectral transmission for visible and ultraviolet filters	35
2.4	FLEET in free jet.	36
2.5	Simulation versus experiment for photon rates and excited populations.	38
2.6	Simulation species results for 300 K and $101.3 \times 10^3 \mathrm{Pa.}$	41
2.7	Reactions contributing to N	42
2.8	Reactions contributing to $N_2(B)$	43
2.9	Reactions contributing to $N_2(C)$	44
2.10	Reactions contributing to $N_2(A)$	45
2.11	Simulation temperature results for 300 K and 101.3 \times 10 ³ Pa	47
2.12	Processes contributing to electronic temperature	48
2.13	Effect of changing initial gas density and/or electronic temperature. $$.	51
3.1	Flow facility nozzles	57
3.2	Schlieren of free jet	58
3.3	Measured flow facility test conditions	60
3.4	Timing diagram for intensified camera	61
3.5	Filter spectral transmission function.	62
3.6	Raw and processed data	65
3.7		65
J. 1	Gaussian fit results	UJ

3.8	Signal as a function of density, temperature and delay (0.1–5 $\mu s).$	70
3.9	Initial signal of simulation versus experiment	73
3.10	Species curves at reduced and atmospheric density	74
3.11	Species curves at reduced and atmospheric temperature	77
3.12	Typical two-term exponential fits of signal	79
3.13	Two-term exponential fit before and after data exclusion	80
3.14	Signal lifetime of simulation and experiment	80
3.15	Measured velocities for flow facility test conditions	83
3.16	Accuracy as a function of density, temperature and time interval	86
3.17	Normalized accuracy as a function of density, temperature and time	
	interval	87
3.18	Precision as a function of density, temperature and time interval. $$	89
3.19	Normalized precision as a function of density, temperature and time	
	interval	90
4.1	Diagram of sweeping jet oscillation cycle	98
4.2	SWJ frequency as a function of NPR	100
4.3	FLEET external measurements	102
4.4	FLEET internal measurements	104
4.5	Single-shot schlieren for NPR of 1.4	108
4.6	Phase-averaged schlieren for various NPRs	109
4.7	Standard deviation of high-speed schlieren for various NPRs	110
4.8	FLEET and HWA mean measurements	112
4.9	FLEET and HWA fluctuation measurements	113
4.10	Histograms of FLEET and HWA measurements	116
4.11	FLEET measurements of internal flow field	121
4.12	Centerline velocities from internal measurements	122
4.13	Profiles of relative oxygen mole fraction	124

5.1	Top-view of optical setup with higher-speed jet	133		
5.2	Diagram and picture of inverted low-speed jet	135		
5.3	Diagram and picture of vertical higher-speed jet			
5.4	Three-shot framing technique to eliminate CMOS ghosting			
5.5	Time response of sensitivity of PCO CMOS sensor	138		
5.6	Typical Gaussian fits and raw data	142		
5.7	Diagram of binning types	144		
5.8	Effect of row-wise binning for un-intensified camera	149		
5.9	Effect of row-wise binning for intensified camera	149		
5.10	Effect of inter-frame delay in air and nitrogen	151		
5.11	Combined effect of inter-frame delay and row-wise binning in air and			
	nitrogen	152		
5.12	Precision of CMOS camera systems in air (no binning)	154		
5.13	Precision of CMOS camera systems in nitrogen (no binning)	155		
5.14	SNR of CMOS camera systems in air (no binning)	157		
5.15	SNR of CMOS camera systems in nitrogen (no binning)	157		
5.16	Precision of CMOS camera systems in air (with binning)	159		
5.17	Precision of CMOS camera systems in nitrogen (with binning)	160		
5.18	SNR of CMOS camera systems in air (with binning)	161		
5.19	SNR of CMOS camera systems in nitrogen (with binning)	162		
6.1	Side-view of supersonic shape morphing facility	174		
6.2	Contour shape and pressure distribution for shape morphing facility	174		
A.1	Depiction of accuracy and precision	177		
B.1	Radial width of tagged region as a function of density, temperature			
	and delay $(0.1-5\mu s)$	179		

В.2	Integrated signal as a function of density, temperature and delay	
	(0.1–5 $\mu s)$	181
В.3	Initial integrated signal of experiment versus simulation	182
C.1	FLEET single-shot profiles in SWJ	184
C.2	FLEET precision in quiescent air	185
C.3	FLEET data point density inside SWJ	187
D.1	Schlieren characterization of inverted low-speed jet	189

Chapter 1

Introduction

1.1 Background Information for Method

Femtosecond laser electronic excitation tagging (FLEET) is an unseeded¹ molecular tagging method that enables nonintrusive measurements of velocity [1, 2] and temperature [3] in gases containing N_2 . FLEET is easy to implement (requiring only a single laser and single camera) and versatile, capable of studying a wide range of flows, including turbulent [4], cryogenic [5], high-speed [6], combusting [7, 8], as well highly unsteady flows with both subsonic and supersonic components [9].

A focused, femtosecond-duration laser pulse generates a weakly ionized plasma in pure nitrogen or air. The resulting plasma-chemical kinetics create substantial populations of atomic and electronically-excited molecular nitrogen, ultimately yielding short- and long-lived signals from the spontaneous emission. Fluorescence primarily comes from the first and second positive system² of nitrogen. The long-lived signal (associated with the first positive emission) can last tens of microseconds after the exciting laser pulse in air [1, 8] and more than sixty microseconds in pure nitrogen [11]

 $^{^1\}mathrm{FLEET}$ functions without solid/liquid particles or gaseous species not normally present in air.

²Given by $N_2(B^3\Pi_g) \longrightarrow N_2(A^3\Sigma_u^+) + h\nu$ and $N_2(C^3\Pi_u) \longrightarrow N_2(B^3\Pi_g) + h\nu$, respectively. See Lofthus et al. [10] for more details.

because of the relatively slow rate of atomic recombination which produces³ the responsible excited species. Tagged regions appear as luminescent spots or lines⁴ in the gas (depending on the tightness of laser beam focusing), whose position and intensity can be tracked by a time-delayed, fast-gated imaging system (e.g., intensified camera). Velocities are determined by measuring the displacement that occurs during the time delay. Temperature is determined by resolving the second positive spectrum of nitrogen and then analyzing its distribution of rotational energy (with the assumption of equilibrium between the translational and rotational modes) [3]. Furthermore, there is demonstrated potential for simultaneous measurement of density (using the femtosecond laser Rayleigh scattering, initial signal intensity⁵ or fits of signal decay rate⁵) [12] and mixture fraction (leveraging the initial signal's sensitivity to oxygen concentration⁶) [13].

1.2 Motivation for Exploring High-Speed Flow Considerations

FLEET offers a valuable opportunity for measurement of high-speed flows (transonic, supersonic or hypersonic), especially when the advantages of relative simplicity, no seeding requirement and desire to track the flow itself (by tagging actual molecules) outweigh the reduced density of instantaneous spatial information associated with spots, lines, crosses, etc.⁷ The characteristic nature of high-speed ground testing demands certain performance from FLEET such as satisfactory signal-to-noise (SNR) ratio at depressed static conditions (i.e., low temperatures, pressures and densities),

 $^{^3{\}rm Via~the~three-body~reaction},\, 2\,{\rm N}+{\rm N}_2 \longrightarrow {\rm N}_2({\rm B}^3\Pi_{\rm g}) + {\rm N}_2.$

⁴With additional optics, multiple or crossed lines are possible.

⁵Approach only applies at atmospheric or higher densities since the initial signals and lifetimes at sub-atmospheric densities exhibit non-monotonic behavior. See Chapter 3 of the present work.

⁶A rise in oxygen mole fraction ($\leq 21\%$) reduces initial signal in a monotonic, nonlinear fashion.

⁷Current limitations on pulse energy output of ultrafast laser systems prevent readily writing dense grids of lines.

wide dynamic range for velocity determination (especially in a single shot), and, of course, measurements with acceptable accuracy and precision. This dissertation strives to evaluate FLEET in those regards and provide strategies to maximize the method's capabilities. Moreover, this dissertation seeks to answer practical questions, such as what measurement performance can be expected of FLEET in high-speed environments and what conditions are optimal for (or detrimental to) obtaining signal. The dissertation also endeavors to answer fundamental questions, such as what kinetic mechanisms are responsible for the emitting species at different timescales and what is the reason for the apparent signal enhancement at certain conditions (e.g., cryogenic).

Note that the preceding paragraph describes the general motivation for this work and each chapter of this dissertation contains more specific motivations and background information (not repeated here).

1.3 Relevant Major Past Works

Since publication of FLEET [1] by the Applied Physics Group at Princeton University in 2011, researchers have worked to refine the method and advance its state of the art. In particular, several theses and dissertations have focused on (or substantially contributed to) development of FLEET. The seminal bachelor's thesis of Edwards [2] explored numerous aspects of FLEET including an early demonstration of velocimetry in transonic and supersonic vertical free jets (in the open air) and measurement of the signal's dependence on pressure (at constant temperature) in both air and pure nitrogen. Based on figures in the thesis documenting the effect of pulse energy (showing a notable spread in the data) and conversations with M. R. Edwards, the particular femtosecond laser system used in experiments outputted somewhat inconsistent pulse-to-pulse energy which potentially contributed uncertainty to the measured trends with pressure (since signal intensity also depends nonlinearly on

pulse energy). Hence, the trends with pressure/density are remeasured in the present work with a more stable ultrafast laser system. As part of DeLuca's [14] investigation into using FLEET in an optical air data system for hypersonic vehicles, he performed variable pressure experiments (at constant temperature) to characterize the effect on signal intensity in air and nitrogen. However, the experiments utilized a shorter lens focal length ($f_{\rm L}=15\,{\rm cm}$) and a higher pulse energy ($U_{\rm L}=5.22\,{\rm mJ}$) than typically employed in FLEET velocimetry (to minimize energy deposition and thus perturbation to the gas). Lowering the laser fluence (e.g., $f_{\rm L} \approx 25-30\,{\rm cm}$ with $U_{\rm L} \lesssim 1\,{\rm mJ}$) subsequently changes the observed qualitative trends (cf. Chapter 3 of the present work). Calvert [15] presented an extensive characterization of FLEET (including its performance in gas mixtures other than air), a variety of flow measurements (including a comparison to particle image velocimetry), multidimensional velocity measurements, advanced image processing, and several other aspects. Moreover, his doctoral dissertation contained velocimetry of high-speed flows, such as the free jet from a nozzle with a novel lenticular-to-circular cross section and the compressible boundary layers which form on straight and curved⁸ razor surfaces immersed in a supersonic free jet. Furthermore, he studied signal intensity as a function of variable pressure (in constant-temperature air and nitrogen), though at moderately elevated pulse energies ($U_{\rm L} \approx 2.5\,{\rm mJ}$ with $f_{\rm L} = 30\,{\rm cm}$) and relatively long time delays ($t \ge 2 \,\mu s$)—time delays long enough for the signal's direct dependence on thermodynamic variables (e.g., density) to begin to break down in nitrogen (cf. Chapter 3 of the present work). Zhang [16] examined the effect of adding certain gases to initially pure nitrogen (such as oxygen, which quenches the signal, or argon, which enhances it), optimization of incompressible turbulence measurements and various approaches to near-wall velocimetry in high-speed flows. Specifically, her work into argon-nitrogen mixtures drove development of a kinetics model, elements of which are

⁸Orienting the laser beam tangential to the curvature facilitates near-wall measurements by reducing the interference from reflections and scattering off the surface.

extended to sub-atmospheric temperature and pressure environments in Chapter 2 of the present work. Although Limbach's [17] doctoral dissertation did not primarily focus on FLEET, it contributed noteworthy visualizations and attempts to quantify the temperature and density perturbations⁹ resulting from the focused femtosecond pulse.

1.4 Descriptive Outline of Core Chapters

Chapter 2 introduces a zero-dimensional kinetics model of FLEET to elucidate why signal intensity changes with pressure (really, density) and/or temperature. The model considers only pure nitrogen to simplify the scheme and focus on the reactions responsible for generating the signal. Rate coefficients with poorly known values are tuned by comparing the model output to photomultiplier tube measurements of the first and second positive emission. The model agrees with experimental results up to several hundred nanoseconds. Sources of discrepancy are discussed. Photoionization is approximated using elements from femtosecond filamentation theory. Figures display important contributions from plasma-chemical reactions over different timescales.

Chapter 3 experimentally validates the preceding kinetics model (in terms of initial, i.e., $t \ll 1\,\mu s$, signal and, to a lesser extent, signal lifetime) and evaluates FLEET velocimetry in conditions relevant to high-speed flows using results from a variable temperature and pressure free jet facility (purpose-built to test FLEET and other laser-based diagnostics). In comparison to free jet experiments in ambient air, the flow facility offers a contaminant-free environment for accurate characterization of signal intensity and lifetime in pure gases (or gas mixtures). Only results in nitrogen are shown since these are most applicable to the kinetics model. Overall, four sets of

 $^{^9}$ A crude analysis of the 'energy cascade' suggests energy deposition into the system (i.e., gas heating) since each molecule of N_2 requires $15.58\,\mathrm{eV}$ for ionization (by the laser) and $9.76\,\mathrm{eV}$ for dissociation, but only emits roughly $2.1–3.5\,\mathrm{eV}$ via fluorescence (first & second positive) [10, 18, 19].

results are obtained from unheated subsonic through Mach 4.0 flows: signal intensity (at various delays), signal lifetime $(1/e \text{ and } 1/e^2)$, velocity accuracy and velocity precision. Furthermore, this chapter includes the most detailed description of the image processing algorithms found throughout the dissertation.

Chapter 4 applies FLEET to a sweeping jet actuator (flow control device) operating in the compressible regime. At high pressure ratios, the device emits an unsteady jet containing subsonic through supersonic velocities. This realistic and challenging problem showcases advantages of the method, especially compared to traditional single-probe hot-wire anemometry (HWA). FLEET velocity measurements are performed in the internal (device is optically transparent) and external flow fields, complemented by schlieren imaging. Internal measurements reveal the absence of shockwaves theorized to occur at high pressure ratios. External measurements are compared to HWA. Simultaneous qualitative measurements of compressible jet mixing (via FLEET initial signal intensity) are demonstrated as a proof-of-concept. Overall, the work advances the state of understanding of sweeping jet actuators, showing that previous concepts regarding their incompressible operation readily extend into the compressible realm.

Chapter 5 details practical aspects of performing FLEET velocimetry along with strategies for improving not only the precision, but the measurement in general. Although experimental results are obtained in low-speed (0.2–60 m s⁻¹) flows, many of the approaches/conclusions likewise apply to high-speed flows (and are subsequently used during experimental efforts elsewhere in the dissertation). The chapter characterizes the fundamental precision of FLEET velocimetry using fast-framing complementary metal-oxide semiconductor (CMOS) cameras. Five different camera configurations are compared in terms of velocity precision and SNR of image data. The fundamental precision is compared to absolute precisions obtained in other FLEET studies and by alternative unseeded velocimetry methods. The performance demon-

strated by fast-framing CMOS cameras in this chapter encouraged their near exclusive use throughout the dissertation for acquisition of image data.

1.4.1 Use of Hyperlinks

Please note the use of hyperlinked cross-references and bibliographic citations in the electronic version of this dissertation.

Chapter 2

Kinetics Model in Nitrogen

Note that much of this chapter (text, tables and figures) is adapted from Reference [20].

2.1 Background and Motivation

The focused, femtosecond-duration laser pulse generates a weakly ionized plasma in nitrogen, setting into motion numerous plasma and chemical reactions that span across multiple timescales. The kinetics establish and maintain sizable populations of atomic nitrogen and electronically-excited molecular nitrogen, ultimately producing (via spontaneous emission) a long-lived signal in the visible along with a short-lived signal in the ultraviolet.¹

We devise a zero-dimensional kinetics simulation of femtosecond laser electronic excitation tagging (FLEET) by modifying the scheme suggested by Shneider et al. [21] for argon-nitrogen plasmas generated by picosecond lasers and extending the efforts of Zhang et al. [22] to model the FLEET signal enhancement resulting from the addition of argon to pure nitrogen. This new scheme incorporates over fifty plasma

¹In reality, the spectral components of the 'ultraviolet' and 'visible' signal span the nearultraviolet to blue and yellow to near-infrared, respectively. For brevity, these bands will be referred to simply as ultraviolet and visible throughout the dissertation.

and chemical reactions to determine the temporal evolution of ten nitrogen-derived species: atoms, N, molecules, N_2 , electronically-excited molecules such as $N_2(A)$, $N_2(B)$, $N_2(C)$, cations such as N^+ , N_2^+ , N_3^+ , N_4^+ , and free electrons, e^- , along with three temperatures: translational, T_g , vibrational, T_v , and electronic, T_e . Development of the model requires tuning of several rate coefficients with large uncertainty (to values within the range of variation found in literature) and comparison to experimental measurements (for tuning and overall validation).

Using the model, we seek to characterize the chemical kinetics that contribute to the emitting species of FLEET in nitrogen at the low temperatures and pressures relevant for velocimetry in supersonic and hypersonic testing facilities. Previous unpublished work has indicated a possible signal enhancement at cryogenic temperatures. Furthermore, the model offers potential for investigating the kinetics of flight-accurate Reynolds number transonic testing environments which maintain low temperatures, but atmospheric and higher pressures.

2.2 Kinetics Model

Table 2.1 lists all the chemical and plasma reactions included in the model (simulation). Note that the electronically-excited states are abbreviated as follows: $N_2(C) = N_2(C^3\Pi_u)$, $N_2(B) = N_2(B^3\Pi_g)$, $N_2(A) = N_2(A^3\Sigma_u^+)$ and $N_2(a') = N_2(a'^1\Sigma_u^-)$. When no electronic state is specified, the species is assumed to be in the electronic ground state: $N_2 = N_2(X^1\Sigma_g^+)$, $N_2^+ = N_2^+(X^2\Sigma_g^+)$ or $N = N(^4S)$. Also note the use of Avogadro's number, $N_A = 6.022 \times 10^{23} \, \text{mol}^{-1}$.

Throughout the chapter, n will signify the number density of the species indicated by the subscript (e.g., n_{N_2} for molecular nitrogen) in units² of cm⁻³ while T will represent the temperature of the mode indicated by the subscript in units of K.

²For the sake of brevity, implied units, such as atoms, molecules, particles, etc. will be omitted here and elsewhere.

Table 2.1: Chemical and plasma processes included in model and their associated rate coefficients.

Number	Reaction	Rate Coefficient, $k =$	Units	Reference
Atomic Reco	ombination			
R1	$2 N + N_2 \longrightarrow N_2(B) + N_2$	$8.27 \times 10^{-34} \exp\left(\frac{500}{T_{\rm g}}\right)$	$\mathrm{cm}^6\mathrm{s}^{-1}$	[23-30]
Fluorescence		' (¹g)		
R2	$N_2(A) \longrightarrow N_2 + h\nu$	0.5	$ \begin{array}{r} $	[18, 31]
R3	$N_2(B) \longrightarrow N_2(A) + h\nu$	1.52×10^{5}	s ⁻¹	[19, 26]
R4 Energy Pool	$N_2(C) \longrightarrow N_2(B) + h\nu$	2.69×10^{7}	s	[10, 19]
R5 ^{abc}	$\frac{\text{NS}}{2 \text{ N}_2(\text{A})} \longrightarrow \text{N}_2(\text{B}) + \text{N}_2(v) + \epsilon_{\text{tr}}$	$2.9 \times 10^{-9} \sqrt{\frac{T_{\rm g}}{T_{\rm g}}}$	${ m cm^3~s^{-1}}$	[32–35]
R6 ^{bcd}	$2 \operatorname{N}_2(A) \longrightarrow \operatorname{N}_2(C) + \operatorname{N}_2(v)$ $2 \operatorname{N}_2(A) \longrightarrow \operatorname{N}_2(C) + \operatorname{N}_2(v)$	$2.9 \times 10^{-9} \sqrt{\frac{T_{\rm g}}{300}}$ $2.6 \times 10^{-10} \sqrt{\frac{T_{\rm g}}{300}}$	${ m cm}^3 { m s}^{-1}$	[31, 35]
	Recombination & Ionization	$2.0 \times 10 \qquad \bigvee \overline{300}$	CIII S	[31, 30]
$R7^{a}$	$e^- + N_4^+ \longrightarrow N_2(A) + N_2$	$2.5\% \times 2.4 \times 10^{-6} \sqrt{\frac{300}{T_e}}$	${ m cm^3~s^{-1}}$	[34, 36, 37]
$R8^{a}$	$e^- + N_4^+ \longrightarrow N_2(B) + N_2$	$87\% \times 2.4 \times 10^{-6} \sqrt{\frac{300}{T_0}}$	${ m cm^3~s^{-1}}$	[34, 36-38]
$R9^{a}$	$e^- + N_4^+ \longrightarrow N_2(C) + N_2$	$11\% \times 2.4 \times 10^{-6} \sqrt{\frac{300}{T_e}}$	${ m cm^3~s^{-1}}$	[34, 36, 37, 39]
R10	$2 e^- + N_4^+ \longrightarrow e^- + 2 N_2$	$7 \times 10^{-20} \left(\frac{300}{T_e} \right)^{4.5}$	${ m cm}^6{ m s}^{-1}$	[34]
R11	$e^- + N_3^+ \longrightarrow N + N_2$	$2.0 \times 10^{-7} \sqrt{\frac{\frac{1e}{300}}{T_e}}$	${ m cm^3~s^{-1}}$	[26, 37]
$R12^{b}$	$e^- + N_2^+ \longrightarrow 2 N + \epsilon_{tr}$	2.8×10^{-7} , $\sqrt{\frac{1_{\rm e}}{300}}$	${ m cm^3~s^{-1}}$	[26, 40]
R13	$e^- + N_2^+ \longrightarrow N_2 + h\nu$	$2.8 \times 10^{-7} \sqrt{\frac{300}{T_e}}$ $4 \times 10^{-12} \left(\frac{300}{100}\right)^{0.7}$	${ m cm^3~s^{-1}}$	[41]
R14	$e^- + N_2^+ + N_2 \longrightarrow 2 N_2$	$4 \times 10^{-12} \left(\frac{300}{T_{\rm e}}\right)^{0.7}$ $6 \times 10^{-27} \left(\frac{300}{T_{\rm e}}\right)^{1.5}$	${ m cm}^6{ m s}^{-1}$	
	$e^{-} + N_2^{-} + N_2 \longrightarrow 2 N_2$ $2 e^{-} + N_2^{+} \longrightarrow e^{-} + N_2$	$6 \times 10 \left(\frac{T_{\rm e}}{T_{\rm e}}\right)$	$cm^6 s^{-1}$	[26]
R15		$ \begin{array}{c} 1 \times 10^{-19} \left(\frac{300}{T_e} \right)^{4.5} \\ 1 \times 10^{-19} \left(\frac{300}{T_e} \right)^{4.5} \\ 5.05 \times 10^{-11} \frac{\sqrt{T_e} + 1.10 \times 10^{-5} T_e^{1.5}}{\left(1.82 \times 10^5 \right)} \end{array} $		[26]
R16	$e^- + N_2 \longrightarrow 2e^- + N_2^+$	exp (1.02 × 10)	$\mathrm{cm^3\ s^{-1}}$	[42, 43]
R17	$e^- + N^+ \longrightarrow N + h\nu$	$3.5 \times 10^{-12} \left(\frac{300}{T_e}\right)^{0.7}$	$\mathrm{cm^3\ s^{-1}}$	[41]
R18	$e^- + N^+ + N_2 \longrightarrow N + N_2$	$6 \times 10^{-27} \left(\frac{300}{T_{\rm e}}\right)^{1.5}$	$\mathrm{cm}^6~\mathrm{s}^{-1}$	[26]
R19	$2 e^- + N^+ \longrightarrow e^- + N$	$6 \times 10^{-27} \left(\frac{300}{T_e}\right)^{1.5} 1 \times 10^{-19} \left(\frac{300}{T_e}\right)^{4.5}$	${ m cm^6~s^{-1}}$	[26]
Quenching	1 (1)		2 1	
R20 R21	$N_3^+ + N_2(A) \longrightarrow N^+ + 2 N_2$ $N_2^+ + N_2(A) \longrightarrow N_3^+ + N$	$ \begin{array}{c} 6 \times 10^{-10} \\ 3 \times 10^{-10} \end{array} $	$\frac{\text{cm}^3 \text{ s}^{-1}}{\text{cm}^3 \text{ s}^{-1}}$	[44, 45]
R21 R22	$N_2^+ + N_2(A) \longrightarrow N_3^+ + N$ $N_2^+ + N_2(A) \longrightarrow N^+ + N + N_2$	4×10^{-10}	$cm^{3}s^{-1}$	[26, 44, 46] [21, 44, 46]
R23 ^a	$N_2(A) + N_2 \longrightarrow 2N_2$	2.0×10^{-17}	${ m cm}^3 { m s}^{-1}$	[24, 36, 41, 47–51]
$R24^{a}$	$N + N_2(A) \longrightarrow N + N_2$	$6.2 \times 10^{-11} \left(\frac{300}{T_{\rm g}}\right)^{2/3}$	${ m cm^3~s^{-1}}$	$[34,\ 36,\ 41,\ 47,\ 5254]$
$R25^{ab}$	$N_2(B) + N_2 \longrightarrow N_2(A) + N_2(v)$	1.2×10^{-11}	$\mathrm{cm^3\ s^{-1}}$	[26,33,35,36,46,5558]
$R26^{bd}$	$N_2(C) + N_2 \longrightarrow N_2(B) + N_2(v)$	$1.2 \times 10^{-11} \left(\frac{300}{T_{\rm g}}\right)^{0.33}$	${ m cm^3~s^{-1}}$	[35, 59]
Ion Conversi	ion_	(1g)		
R27	$N_4^+ + N_2 \longrightarrow N_2^+ + 2 N_2$	$2.1 \times 10^{-16} \exp\left(\frac{T_{\rm g}}{121}\right)$	${ m cm^3~s^{-1}}$	[36, 46, 60, 61]
R28	$N_4^+ + N \longrightarrow N^+ + 2 N_2$	1×10^{-11}	$cm^{3} s^{-1}$	[26, 46]
R29	$N_4^+ + N \longrightarrow N_3^+ + N_2$	1×10^{-9}	$cm^{3} s^{-1}$	[62]
R30	$N_3^+ + N \longrightarrow N_2^+ + N_2$ $N_3^+ + N_2 \longrightarrow N^+ + 2 N_2$	$6.6 \times 10^{-11} \\ 6 \times 10^{-10}$	$\frac{\text{cm}^{3} \text{s}^{-1}}{\text{cm}^{3} \text{s}^{-1}}$	[26, 46]
R31 R32	$\begin{array}{c} N_3 + N_2 \longrightarrow N + 2N_2 \\ N_2 + N_2 \longrightarrow N^+ + N + N_2 \end{array}$	1.2×10^{-11}	$^{\mathrm{cm}}_{\mathrm{cm}^3}\mathrm{s}^{-1}$	[44, 46] $[44, 46]$
R33	$N_2^+ + N_2 \longrightarrow N_3^+ + N$	5.5×10^{-12}	$^{\rm cm^3s^{-1}}$	[44, 46]
R34	$N_2^+ + N \longrightarrow N^+ + N_2$		${ m cm}^3{ m s}^{-1}$	[21, 46]
R35	$N_2^+ + 2N_2 \longrightarrow N_4^+ + N_2$	$7.2 \times 10^{-13} \exp\left(\frac{300}{T_{\rm g}}\right)$ $6.8 \times 10^{-29} \left(\frac{300}{T_{\rm g}}\right)^{1.64}$	${ m cm}^6{ m s}^{-1}$	[61]
R36	$N_2^+ + N + N_2 \longrightarrow N_3^+ + N_2$	$0.9 \times 10^{-29} \text{ arg} \left(\frac{400}{400} \right)$	${ m cm}^6~{ m s}^{-1}$	[26, 46]
R37	$N^{+} + N_{2} \longrightarrow N_{2}^{+} + N$ $N^{+} + N_{2} \longrightarrow N_{2}^{+} + N$	$0.9 \times 10^{-29} \exp\left(\frac{400}{T_{\rm g}}\right)$ 1×10^{-13}	${ m cm}^3 { m s}^{-1}$	[44]
R38	$N^+ + N_2 \longrightarrow N_3^+ + N_2$ $N^+ + 2N_2 \longrightarrow N_3^+ + N_2$	$\frac{1 \times 10}{200 \times 10^{-29} (300)^{2.0}}$	$cm^6 s^{-1}$	
R38		$2.0 \times 10^{-29} \left(\frac{300}{T_{\rm g}}\right)^{2.0}$ $1 \times 10^{-29} \left(\frac{300}{T_{\rm g}}\right)$		[63]
R39	$N^+ + N + N_2 \longrightarrow N_2^+ + N_2$	$1 \times 10^{-29} \left(\frac{300}{T_{\rm g}} \right)$	${ m cm^6~s^{-1}}$	[41]
	utral Collisions	1.0 × 1025		
R40 ^b	$e^- + N_2 \longrightarrow e^- + 2N + \epsilon_{tr}$	$rac{1.2 imes 10^{25}}{N_{ m A} T_{ m e}^{1.6}} \exp\left(-rac{113200}{T_{ m e}} ight) \ f(T_{ m e}), { m e.g.},$	$cm^{3} s^{-1}$	[35, 43, 64, 65]
R41	$e^- + N_2 \longrightarrow e^- + N_2$	$f(11600 \mathrm{K}) \approx 8.25 \times 10^{-8}$	$\mathrm{cm}^3\mathrm{s}^{-1}$	[66–69]
R42	$e^- + N_2 \longrightarrow e^- + N_2(v)$	$f(T_{\rm e}), {\rm e.g.}, f(11600{\rm K}) \approx 8.45 \times 10^{-9}$	${ m cm^3~s^{-1}}$	[67–69]
R43 ^e	$e^- + N_2(v) \longrightarrow e^- + N_2$	$f(T_{\rm e}, T_{\rm v}), \text{ e.g.},$ $f(11600\text{K}, 600\text{K}) \approx 2.69 \times 10^{-11}$	${ m cm^3~s^{-1}}$	[67-69]
		$f(11600\mathrm{K},600\mathrm{K}) \approx 2.69 \times 10^{-11}$		

^a Tuned value for rate coefficient. See Table 2.4.

^b Reaction contributes to fast gas heating. See Table 2.3.

^c Temperature dependence derived from assumption that $k \propto \overline{v} \propto \sqrt{T_g}$.

^d Relatively large spread of rate coefficients reported in literature. Listed coefficient taken from cited reference. See Table 2.4 for additional references.

^e Superelastic rate coefficient calculated from inverse cross sections. See text for details.

Table 2.1: (Continued)

Number	Reaction	Rate Coefficient, $k =$	Units	Reference
R44	$\mathrm{e^-} + \mathrm{N_2} \longrightarrow \mathrm{e^-} + \mathrm{N_2}(\mathrm{A}, v = 04)$	$f(T_{\rm e}), {\rm e.g.},$ $f(11600{\rm K}) \approx 1.59 \times 10^{-12}$	${ m cm^3~s^{-1}}$	[67–69]
$\mathrm{R45}^{\mathrm{e}}$	$e^- + N_2(A, v = 0-4) \longrightarrow e^- + N_2$	$f(T_{\rm e}), \text{ e.g.},$ $f(11600{\rm K}) \approx 2.67 \times 10^{-11}$	$\mathrm{cm^3\ s^{-1}}$	[67-69]
R46	$e^- + N_2 \longrightarrow e^- + N_2(A, v = 5-9)$	$f(T_{\rm e}), \text{ e.g.},$ $f(11600{\rm K}) \approx 5.63 \times 10^{-12}$	$\mathrm{cm}^3 \mathrm{\ s}^{-1}$	[67-69]
$ m R47^e$	$e^- + N_2(A, v = 5-9) \longrightarrow e^- + N_2$	$f(T_{\rm e})$, e.g., $f(11600{\rm K}) \approx 1.80 \times 10^{-10}$	$\mathrm{cm}^3 \mathrm{s}^{-1}$	[67-69]
R48	$e^- + N_2 \longrightarrow e^- + N_2(B)$	$f(T_{\rm e}), \text{ e.g.},$ $f(11600{\rm K}) \approx 2.35 \times 10^{-11}$	$\mathrm{cm}^3 \mathrm{\ s}^{-1}$	[67-69]
$R49^{e}$	$e^- + N_2(B) \longrightarrow e^- + N_2$	$f(T_{\rm e})$, e.g., $f(11600{\rm K}) \approx 9.85 \times 10^{-10}$	$\mathrm{cm^3\ s^{-1}}$	[67-69]
R50	$e^- + N_2 \longrightarrow e^- + N_2(A, v > 9)$	$f(T_{\rm e})$, e.g., $f(11600{\rm K}) \approx 4.06 \times 10^{-12}$	$\mathrm{cm}^3 \mathrm{s}^{-1}$	[67-69]
R51 ^e	$e^- + N_2(A, v > 9) \longrightarrow e^- + N_2$	$f(T_{\rm e})$, e.g., $f(11600{\rm K})\approx 2.15\times 10^{-10}$	$\mathrm{cm}^3 \mathrm{s}^{-1}$	[67–69]
R52	$e^- + N_2 \longrightarrow e^- + N_2(C)$	$f(T_{\rm e}), \text{ e.g.},$ $f(11600{\rm K}) \approx 6.18 \times 10^{-12}$	$\mathrm{cm^3\ s^{-1}}$	[67–69]
$R53^{e}$	$e^- + N_2(C) \longrightarrow e^- + N_2$	$f(T_{\rm e}), \text{ e.g.},$ $f(11600{\rm K}) \approx 4.06 \times 10^{-9}$	$\mathrm{cm}^3 \mathrm{\ s}^{-1}$	[67-69]
Vibrational	-Translational Relaxation			
R54	$N_2(v) + N_2 \longrightarrow 2 N_2$	$f(T_{\rm g}), {\rm e.g.}, f(300 {\rm K}) \approx 3.05 \times 10^{-21}$	$\mathrm{cm}^3~\mathrm{s}^{-1}$	[70, 71]

Tuned value for rate coefficient. See Table 2.4.

2.2.1Fluorescence, Recombination and Quenching

We computed the rate coefficients for R3 and R4 by summing the spontaneous emission coefficients [19] of the readily observed (i.e., prominent) B-state transitions (11, 7) and (11, 8), and C-state transitions (0, 0), (0, 1), (0, 2), (0, 3) and (0, 4), respectively [2]. Although the FLEET signal contains other similarly prominent transitions, for modeling simplicity, we assume the population responsible for the first or second positive signal originates in either $N_2(B, v = 11)$ or $N_2(C, v = 0)$, respectively. The computed rate coefficients agree with those found in literature.

Although Popov [25] assumes nitrogen atoms recombine via $2N + N_2 \longrightarrow$ $N_2(A, B) + N_2$ and Koyssi et al. [26] through $2N + N_2 \longrightarrow N_2(X, A) + N_2$, our model assumes the reaction R1 solely proceeds according to $2\,\mathrm{N} + \mathrm{N}_2 \longrightarrow \mathrm{N}_2(\mathrm{B}) + \mathrm{N}_2$ because of the closer similarity in energy level between dissociation and $N_2(B, v \approx 11)$ than $N_2(A)$ or $N_2(X)$. Furthermore, three-body atomic recombination into $N_2(B)$ + N_2 agrees with Becker et al. [29] and Henriques et al. [24]. Also, Clyne et al. [27]

b Reaction contributes to fast gas heating. See Table 2.3. Temperature dependence derived from assumption that $k \propto \overline{v} \propto \sqrt{T_{\rm g}}$.

d Relatively large spread of rate coefficients reported in literature. Listed coefficient taken from cited reference. See Table 2.4 for additional references.

e Superelastic rate coefficient calculated from inverse cross sections. See text for details

and Campbell et al. [28] experimentally confirm the value of the R1 rate coefficient from cryogenic to above room temperatures while Yamashita [30] confirms the value at room temperature. We sought agreement among multiple sources for the coefficient's value and temperature dependence because of the reaction's importance for the long life of the first positive signal observed in FLEET and the possible signal enhancement that occurs at cryogenic temperatures. Evident from Table 2.2, the rate coefficient increases manyfold at cryogenic temperatures. Coupled with greater gas density at these temperatures, there was reason to believe that the R1 rate increases dramatically, producing significant quantities of $N_2(B)$ and thus enhanced first positive signal relative to room temperature. However, follow-up work (described in Chapter 3) indicates that the signal enhancement in low temperatures and pressures at early time delays occurs because of increased N_4 ⁺ cluster ion formation and thus greater dissociative recombination (along with excited species coupling, discussed later), not atomic recombination which rises to prominence too late. See Section 3.4.3 for more details.

Table 2.2: Relative effect of low temperature on the atomic recombination rate coefficient.

$T_{\mathrm{g}} [\mathrm{K}]$	100	200	400
$k_{\rm R1}(T_{\rm g})/k_{\rm R1}(300{\rm K})$	28	2.3	0.66

Some references [23, 26] include electron-cluster ion dissociative recombination with ground-state products, $e^- + N_4^+ \longrightarrow 2 N_2$; however, we neglected this reaction because we believed the roughly 15 eV of energy liberated by recombination would produce at least one electronically-excited molecule, i.e., $e^- + N_4^+ \longrightarrow N_2(A, B, C) + N_2$. The exact fraction of A-, B- or C-state nitrogen produced is not well known, certainly less known than the overall rate coefficient for the recombination process. Therefore, the rate coefficients of the constituent reactions R7, R8 and R9 were tuned (see Table 2.4).

For the quenching of C-state nitrogen, R26, we assumed the immediate production of B-state nitrogen, $N_2(C) + N_2 \longrightarrow N_2(B) + N_2(v)$, an approach used by several groups [34, 35]. This reaction approximates the actual probable mechanism, $N_2(C) + N_2 \longrightarrow N_2(a') + N_2$ and then $N_2(a') + N_2 \longrightarrow N_2(B) + N_2$, given by others [26, 36]. Since the a'-state is not considered within our current model, and the rate coefficients for quenching of $N_2(C)$ are nearly identical, we employed the approximation in which quenching directly populates the B-state.

2.2.2 Electron-Neutral Collisions

EEDF defined in the usual manner.

Most of the rate coefficients for electron-neutral collisions were calculated with the aid of BOLSIG+ (version 03/2016) [67] using the cross sections [68, 69] for electron scattering by nitrogen that accompany a standard installation of the software. BOLSIG+ numerically solves the Boltzmann equation for electrons in a weakly ionized gas under a uniform electric field to obtain rate coefficients, $k(T_e)$, from basic scattering cross sections, $\sigma(\epsilon_e)$, where ϵ_e denotes electron kinetic energy (in units of eV). By solving the Boltzmann equation, the software natively accounts for potential non-Maxwellian behavior of the electron energy distribution function (EEDF), $^3F_0(\epsilon_e)$, such as that which arises from the relatively large interaction cross sections between electrons and the vibrational modes of N_2 . Note that the ideal gas, fluid model (i.e., continuum) approach must remain valid (or at least approximately valid) for these rate coefficients and reactions to accurately reproduce the plasma kinetics.

Rate coefficients for impact excitation, R42, R44, R46, R48, R50 and R52, at varying mean energies (i.e., varying $T_{\rm e}$) were directly outputted by BOLSIG+ and then cast into a lookup table to enable $k=f(T_{\rm e})$ during the simulation. Even though our model only utilizes a subset of the BOLSIG+ output since it only tracks N(v), $N_2(A)$, $N_2(B)$ and $N_2(C)$, all elastic and inelastic scattering processes from $\overline{^3}$ BOLSIG+'s EEDF is given by $F_0(\epsilon_{\rm e}) = F(\epsilon_{\rm e})/\sqrt{\epsilon_{\rm e}}$ (in units of eV^{-1.5}), where $F(\epsilon_{\rm e})$ is the

the standard dataset [68, 69] for nitrogen were included so that the resulting EEDF and rate coefficients were representative of a realistic nitrogen plasma. Note that the coefficient listed for R42 is a summation of all vibrational excitation rate coefficients,⁴ $k_{\rm R42} = \sum_{v=1}^{8} k_v$.

The rate coefficient for elastic collisions, R41, was computed via

$$k(T_{\rm e}) = \sqrt{2q_{\rm e}/m_{\rm e}} \int \sigma(\epsilon_{\rm e}) F_0(\epsilon_{\rm e}) \epsilon_{\rm e} d\epsilon_{\rm e},$$
 (2.1)

using the momentum transfer cross sections, $\sigma(\epsilon_{\rm e})$, for electron collisions with nitrogen from Itikawa [66] and the EEDF calculated by BOLSIG+. Note that $q_{\rm e}=1.6022\times 10^{-19}\,{\rm C}$ and $m_{\rm e}=9.1094\times 10^{-31}\,{\rm kg}$ are the elementary charge and electron mass, respectively. The momentum frequency directly outputted by BOLSIG+ was not used since it included the effect of inelastic collisions. Recall that electron mean kinetic energy is given by $\bar{\epsilon}_{\rm e}=\int F_0(\epsilon_{\rm e})\epsilon_{\rm e}^{1.5}{\rm d}\epsilon_{\rm e}=\frac{3}{2q_{\rm e}}k_{\rm B}T_{\rm e}$. For example, $T_{\rm e}=11\,600\,{\rm K}$ implies $\bar{\epsilon}_{\rm e}\approx 1.5\,{\rm eV}$, a representative value of energy included in Table 2.1.

Superelastic collisions ensure equilibration of electron kinetic energy with other modes at very long times in the decaying plasma, such as $T_{\rm e}(t) \to T_{\rm v}(t)$ instead of the nonphysical situation of $T_{\rm e}(t) < T_{\rm v}(t)$. Rate coefficients for R45, R47, R49, R51 and R53 were computed using Equation (2.1) and inverse scattering cross sections derived via the principle of detailed balance, i.e., $\sigma^{\rm inv}(\epsilon_{\rm e}) = \frac{g^1}{g^u} \frac{\epsilon_{\rm e} + U}{\epsilon_{\rm e}} \sigma(\epsilon_{\rm e} + U)$, where g^1 and g^u denote the multiplicity of the lower and upper states, respectively, while U symbolizes the threshold energy for the transition from the lower to upper state. Computations of the rate coefficient for R43 additionally required inclusion of the fraction of ground state nitrogen in excited vibrational level v > 0. Specifically, $k_{\rm R43} = \sum_{v=1}^8 k_v^{\rm inv} \frac{n_{\rm N2}(v)}{n_{\rm N2}}$ where $k_v^{\rm inv}$ is the superelastic rate coefficient for quenching of vibrational level v (computed in the manner previously described) and $\frac{n_{\rm N2}(v)}{n_{\rm N2}}$ is the

⁴The standard installation of BOLSIG+ has cross sections for v = 1–8 and includes both resonant and non-resonant contributions for v = 1.

fraction of ground state nitrogen in vibrational level v. For a harmonic oscillator obeying a Boltzmann distribution [72],

$$\frac{n_{\text{N}_2(v)}}{n_{\text{N}_2}} = \frac{\exp\left(-v\frac{h\nu_v}{k_{\text{B}}T_v}\right)}{\sum_{v=0}^{\infty} \exp\left(-v\frac{h\nu_v}{k_{\text{B}}T_v}\right)},\tag{2.2}$$

where $h\nu_{\rm v}=3374~{\rm K}\times k_{\rm B}$ is the quantum of vibrational energy [72] for nitrogen and $k_{\rm B}=1.3806\times 10^{-23}~{\rm J}~{\rm K}^{-1}$ is the Boltzmann constant. Note that energy balance considerations (Section 2.2.3) also require the threshold energy for vibrational excitation, U_v , prior to summation: $\sum_{v=1}^8 U_v k_v^{\rm inv} \frac{n_{\rm N_2(v)}}{n_{\rm N_2}}$.

2.2.3 Species, Charge and Energy Balance Considerations

Species Balance

The rates coefficients and chemical equations within Table 2.1 are employed in the usual manner to formulate the generation and consumption terms for the time rate of change of each of the ten tracked species: N, N₂, N₂(A), N₂(B), N₂(C), N⁺, N₂⁺, N₃⁺, N₄⁺ and e⁻. Tracking of the electronic ground-state vibrational population, $n_{N_2(v)}$ (with units of cm⁻³), is accomplished by assuming a harmonic oscillator and Boltzmann distribution for vibrational energy (previously discussed in Section 2.2.2 for vibrational superelastic collisions), and accounting for changes in the total vibrational energy content as defined by Equation (2.4). Use of balanced chemical equations in Table 2.1 automatically ensured conservation of nitrogen atoms.

Charge Balance

Use of balanced chemical equations in Table 2.1 when formulating the generation and consumption terms for the species rates of change automatically ensured conservation of electrical charge.

Fast Gas Heating

Popov [35, 40] and others discuss "fast gas heating," or rapid energy release into the translational and vibrational modes of the gas during the post-discharge due to relaxation of energy stored in electronic states (including predissociation) and ionization. Popov defined "fast gas heating" as that which occurs within much shorter timescales than vibrational-translation (VT) relaxation and vibrational-vibrational (VV) exchange.

Table 2.3: Fast gas heating of translational and vibrational modes.

Number	Heating Value [eV]	Reference
	2 []	
$R5^{a}$	$\epsilon_{\mathrm{tr}} = 3.5, \epsilon_{\mathrm{v}} = 1.5$	[35]
$R6^{a}$	$\epsilon_{\rm v} = 1.3$	[35]
R12	$\epsilon_{\mathrm{tr}} = 3.5$	[40]
$R25^{a}$	$\epsilon_{ m v}=1.2$	[35]
$ m R26^{a}$	$\epsilon_{ m v} = 3.7$ $\epsilon_{ m tr} = 1$	[35]
R40	$\epsilon_{ m tr}=1$	[35]

^a $\epsilon_{\rm v}$ estimated from the energy difference of the products and reactants based on the values of their electronic states listed in Ref. [69].

Table 2.3 lists the fast gas heating values for the translational, $\epsilon_{\rm tr}$, and vibrational, $\epsilon_{\rm v}$, modes. To account for fast gas heating and improve the energy balance in the model, we added terms to the governing equations for ${\rm d}T_{\rm g}/{\rm d}t$ and ${\rm d}T_{\rm v}/{\rm d}t$ and assumed all energy released in fast gas heating reactions immediately acts to raise the temperature. The respective volumetric heating contributions (in units of J cm⁻³ s⁻¹) are given by $Q_{\rm tr} = \sum_i \epsilon_{{\rm tr},i} q_{\rm e} r_i$ and $Q_{\rm v} = \sum_i \epsilon_{{\rm v},i} q_{\rm e} r_i$, where r_i is the rate of reaction i (in units of cm⁻³ s⁻¹).

Energy Balance and Temperature Calculations

For the energy balance within our model, we adapted previous approaches [21, 73] of mapping out the energy flow within a decaying plasma. Our energy considerations

were primarily intended for capturing the evolution of $T_{\rm e}(t)$ since it undergoes significant (over an order of magnitude) variation over short timescales (tens of nanoseconds) and the plasma reaction rates strongly depend upon it. The variation of $T_{\rm e}$ is far greater and swifter than either $T_{\rm g}$ or $T_{\rm v}$ and thus needs satisfactory representation in the model. Although we included many effects in the energy balance (discussed in the following sections), several considerations were neglected that are important for accurately characterizing $T_{\rm g}(t)$ and $T_{\rm v}(t)$ and the development of the FLEET plasma beyond several hundred nanoseconds after the initial laser pulse. In particular, we did not consider expansion work done by the gas or any fluid dynamic effects since these would require at least one spatial dimension in the model. Experiments [74] and simulations [75] show that rapid heating of the tagged region leads to the expulsion of shockwaves, and gas dynamic expansion that lowers the density (with respect to the surroundings) within the first microsecond and persists for tens of microseconds. Furthermore, we neglected vibrational anharmonicity and VV exchange since there was no source of continuous pumping of the upper vibrational levels, although inclusion of these effects could potentially enhance the VT relaxation rates (since the quanta of upper vibrational levels more closely match the translational energy of molecules). Elastic Coulomb (electron-ion) collisions were omitted since electrons were far more likely to elastically collide with N_2 whose number density dwarfed those of ions. Lastly, the energy released by numerous recombination, quenching and ion conversion reactions was not included in the balance because of uncertainty in the distribution of the energy among the translational and vibrational modes of the products of these reactions. Neglecting this heat release leads to a lossy energy balance. All in all, the energy balance was believed to be adequate for characterizing $T_{\rm e}(t)$ in a zero-dimensional model (which itself fundamentally limits fidelity) of a decaying plasma, but inadequate for realistically portraying $T_{\rm g}(t)$ and $T_{\rm v}(t)$ at later times (i.e., microsecond timescale). Thus, solutions to $T_{\rm g}(t)$ and $T_{\rm v}(t)$ are approximate.

The total translational, vibrational [72] and electronic energy (in units of $\rm J\,cm^{-3}$) are respectively given by

$$E_{\rm tr}(T_{\rm g}) = n_{\rm N_2} \frac{3}{2} k_{\rm B} T_{\rm g},$$
 (2.3)

$$E_{\rm v}(T_{\rm v}) = \frac{n_{\rm N_2} h \nu_{\rm v}}{\exp\left(\frac{h\nu_{\rm v}}{k_{\rm B}T_{\rm v}}\right) - 1},\tag{2.4}$$

$$E_{\rm e}(T_{\rm e}) = n_{\rm e} \frac{3}{2} k_{\rm B} T_{\rm e},$$
 (2.5)

with the vibrational zero-point energy, $\frac{1}{2}h\nu_{\rm v}$, neglected in Equation (2.4) since it does not appear explicitly in any resulting expression. The governing equations for $T_{\rm g}$, $T_{\rm v}$ and $T_{\rm e}$ are derived from these formulas, along with the assumption that ${\rm d}n_{\rm N_2}/{\rm d}t\approx 0$. Throughout the section, Q will stand for various heating rates in units of J cm⁻³ s⁻¹.

The rate of change for the gas' translational temperature (in units of $K s^{-1}$) is given by

$$Q_{\rm R41} = \frac{3}{2} k_{\rm B} n_{\rm e} \nu_{\rm elas} (T_{\rm e} - T_{\rm g}) \delta_{\rm N_2}, \tag{2.6}$$

$$Q_{R54} = \frac{E_{\rm v}(T_{\rm v}) - E_{\rm v}(T_{\rm g})}{\tau_{\rm VT}},$$
 (2.7)

$$C_{\rm tr} = \frac{3}{2} k_{\rm B} n_{\rm N_2},$$
 (2.8)

$$\frac{dT_{\rm g}}{dt} = (Q_{\rm R41} + Q_{\rm R54} + Q_{\rm tr})/C_{\rm tr},\tag{2.9}$$

where $\nu_{\rm elas} = k_{\rm R41} n_{\rm N_2}$ gives the elastic collision frequency (in s⁻¹), $\delta_{\rm N_2} = 2m_{\rm e}/m_{\rm N_2}$ gives the mass ratio coefficient of electrons to gas molecules and $\tau_{\rm VT} = (k_{\rm R54} n_{\rm N_2})^{-1}$ provides the time constant for VT relaxation (in s). $Q_{\rm R41}$ represents gas heating from elastic collisions with electrons. The heating rate from VT relaxation, $Q_{\rm R54}$, utilizes the functional form of vibrational energy defined by Equation (2.4). $C_{\rm tr}$ is simply a coefficient resulting from Equation (2.3) with units of J cm⁻³ K⁻¹.

The rate of change for the gas' vibrational temperature (in units of $K s^{-1}$) is given by the following

$$Q_{R42} = \sum_{v=1}^{8} U_v k_v n_{N_2} n_e, \qquad (2.10)$$

$$Q_{R43} = \sum_{v=1}^{8} U_v k_v^{\text{inv}} \frac{n_{N_2(v)}}{n_{N_2}} n_{N_2} n_e,$$
(2.11)

$$C_{\rm v} = n_{\rm N_2} \left(\frac{h\nu_{\rm v}}{T_{\rm v}}\right)^2 \frac{\exp\left(\frac{h\nu_{\rm v}}{k_{\rm B}T_{\rm v}}\right)}{k_{\rm B} \left(\exp\left(\frac{h\nu_{\rm v}}{k_{\rm B}T_{\rm v}}\right) - 1\right)^2},\tag{2.12}$$

$$\frac{dT_{\rm v}}{dt} = (Q_{\rm R42} + Q_{\rm v} - Q_{\rm R43} - Q_{\rm R54})/C_{\rm v}, \tag{2.13}$$

where Q_{R42} and Q_{R43} represent vibrational heating from impact excitation and superelastic collisions, respectively. Again, C_v is simply a coefficient with units of $J \text{ cm}^{-3} \text{ K}^{-1}$ that arises from differentiation [72] of Equation (2.4).

The rate of change for electronic temperature (in units of $K s^{-1}$) is given by the following set of equations

$$Q_{\text{supelas}} = r_{\text{R45}} U_{\text{N}_2(\text{A}, v = 0-4)} + r_{\text{R47}} U_{\text{N}_2(\text{A}, v = 5-9)}$$

$$+ r_{\text{R49}} U_{\text{N}_2(\text{B})} + r_{\text{R51}} U_{\text{N}_2(\text{A}, v > 9)}$$

$$+ r_{\text{R53}} U_{\text{N}_2(\text{C})},$$

$$(2.14)$$

$$Q_{\text{recomb}} = r_{\text{R}10} U_{\text{N}_2^+} + r_{\text{R}15} U_{\text{N}_2^+} + r_{\text{R}19} U_{\text{N}^+}, \tag{2.15}$$

$$Q_{\text{impact}} = r_{\text{R16}} U_{\text{N}_2^+} + r_{\text{R40}} U_{\text{diss}} + r_{\text{R44}} U_{\text{N}_2(\text{A}, v = 0-4)}$$

$$+ r_{\text{R46}} U_{\text{N}_2(\text{A}, v = 5-9)} + r_{\text{R48}} U_{\text{N}_2(\text{B})}$$

$$+ r_{\text{R50}} U_{\text{N}_2(\text{A}, v > 9)} + r_{\text{R52}} U_{\text{N}_2(\text{C})},$$

$$(2.16)$$

$$C_{\rm e} = \frac{3}{2}k_{\rm B}n_{\rm e},$$
 (2.17)

$$\frac{\mathrm{d}T_{\mathrm{e}}}{\mathrm{d}t} = (Q_{\mathrm{R43}} + Q_{\mathrm{supelas}} + Q_{\mathrm{recomb}} - Q_{\mathrm{R41}} - Q_{\mathrm{R42}} - Q_{\mathrm{impact}})/C_{\mathrm{e}} - \frac{\mathrm{d}n_{\mathrm{e}}}{\mathrm{d}t} \frac{T_{\mathrm{e}}}{n_{\mathrm{e}}},$$
(2.18)

where Q_{supelas} , Q_{recomb} and Q_{impact} denote the heating of electrons due to electronic superelastic collisions, recombination with ions,⁵ and impact with neutrals (excitation, dissociation and ionization), respectively. C_{e} is a coefficient with units of J cm⁻³ K⁻¹ that results from Equation (2.5) while r designates the reaction rate identified by the subscript in units of cm⁻³ s⁻¹. $U_{\text{N}_2(\text{A},v=0-4)}$, $U_{\text{N}_2(\text{A},v=5-9)}$, $U_{\text{N}_2(\text{B})}$, $U_{\text{N}_2(\text{A},v>9)}$ and $U_{\text{N}_2(\text{C})}$ represent the threshold energies for electronic excitation taken from the LXCat database [69]. U_{diss} symbolizes the dissociation energy of molecular nitrogen while U_{N^+} and $U_{\text{N}_2^+}$ signify the ionization energies of atomic and molecular nitrogen, respectively. All energies are in units of J. The last term on the right-hand side of Equation (2.18) arises from differentiation of Equation (2.5) and accounts for ϵ_{e} released or absorbed by electrons during recombination or ionization, respectively.

2.2.4 Initial Conditions and Photoionization

The model's initial conditions reflect the typical experimental parameters for FLEET velocimetry (which attempt to optimize accuracy and precision while minimizing perturbations to the gas).

Assumptions on Initial Species and Temperatures

User input supplies pre-pulse (t=0) values for pressure, p(0), and temperature, $T_{\rm g}(0)$. The ideal gas relation provides the pre-pulse number density of molecular nitrogen, $n_{\rm N_2}(0) = 1 \times 10^{-6} \frac{p(0)}{k_{\rm B} T_{\rm g}(0)}$ (e.g., $n_{\rm N_2}(0) \approx 2.4 \times 10^{19} \, {\rm cm}^{-3}$ at $101.3 \times 10^3 \, {\rm Pa}$, $300 \, {\rm K}$).

The photoionization model needs $n_{N_2}(0)$ to calculate $n_{N_2^+}(t_0)$ and $n_e(t_0)$ at the end of the laser pulse and start of the simulation ($t = t_0 = 70 \,\text{fs}$). We assume the presence of initially only N_2 , N_2^+ and e^- at that time. This assumption is predicated on the idea that the infrared laser light, an electromagnetic wave, more readily couples

 $^{^5\}mathrm{We}$ assumed that the much lighter electron third body absorbs all of the energy released during recombination and no energy goes into the translational or vibrational modes of the molecule(s). Furthermore, the dissociation energy of $\mathrm{N_2-N_2}^+$ in R10 was neglected.

to the molecules' electronic rather than vibrational modes and photoionization rather than photodissociation dominates. In reality, due to the extreme intensity of the focused, femtosecond-duration laser pulse, finite populations of other species may also be present including electronically-excited ions and molecules.

Since t_0 is much shorter than the timescales of thermalization, $T_g(t_0) = T_g(0)$. Assuming an unheated (room temperature) source of gas for the plenum and thermal equilibrium prior to the laser pulse,

$$T_{\rm v}(t_0) = \begin{cases} 300 \,\mathrm{K}, & T_{\rm g}(0) < 300 \,\mathrm{K} \\ T_{\rm g}(0), & T_{\rm g}(0) \ge 300 \,\mathrm{K} \end{cases}$$
(2.19)

since gas temperatures below 300 K are experimentally achieved by rapid expansion through a nozzle which freezes the vibrational modes.

Roughly approximating photoionization as an above-threshold, multiphoton process provides a simple way to estimate the initial electron temperature. For a multiphoton process, $N_{\rm ph}={\rm ceil}\left(\frac{U_{\rm N_2+}}{h\nu_{\rm L}}\right)$ gives the minimum number of photons required for ionization, where ${\rm ceil}(\cdot)$ is the ceiling function, $\nu_{\rm L}=\frac{\omega_{\rm L}}{2\pi}=\frac{c}{\lambda_{\rm L}}$ is the laser's central frequency, $h=6.626\times 10^{-34}\,{\rm J}\,{\rm s}$ is the Planck constant and $c=2.9979\times 10^8\,{\rm m\,s^{-1}}$ is the speed of light in vacuum. Therefore, a laser with a central wavelength of $\lambda_{\rm L}=800\times 10^{-9}\,{\rm m}$ requires $N_{\rm ph}=11$. If $N_{\rm ph,add}$ denotes the number of additional photons in excess of the ionization requirement, then the initial electronic temperature becomes

$$T_{\rm e}(t_0) = \frac{2}{3k_{\rm B}}(h\nu_{\rm L}(N_{\rm ph} + N_{\rm ph,add}) - U_{\rm N_2^+}).$$
 (2.20)

For $N_{\rm ph,add}=0$, $T_{\rm e}(t_0)\approx 11\,300\,{\rm K}$; however, $N_{\rm ph,add}=2$, $T_{\rm e}(t_0)\approx 35\,300\,{\rm K}$ seems to provide better agreement with experimental results, producing the correct signal trend with above-atmospheric density: $S\propto n_{\rm N_2}(0)$ (discussed more in Section 2.4.5).

Nominal Laser Parameters

We used a regeneratively-amplified Ti:sapphire laser (Spectra-Physics Solstice) during the experimental effort. Assuming a Gaussian pulse shape and intensity profile, with a pulse duration (FWHM) of $\Delta t_{\rm L}=t_0=70\times 10^{-15}\,{\rm s}$, a pulse energy of $U_{\rm L}=0.5\times 10^{-3}\,{\rm J}$, the same central wavelength of $\lambda_{\rm L}=800\times 10^{-9}\,{\rm m}$, a spectral bandwidth (FWHM) of $35\times 10^{-9}\,{\rm m}$, an incident beam diameter $(1/e^2)$ of $D_{\rm L}=7\times 10^{-3}\,{\rm m}$ and focused by a lens of focal length, $f_{\rm L}=0.3\,{\rm m}$, then geometric optics dictates a beam waist radius $(1/e^2)$ of $w_0=2\frac{\lambda_{\rm L}}{\pi}\frac{f_{\rm L}}{D_{\rm L}}\approx 22\times 10^{-6}\,{\rm m}$ and a Rayleigh range of $z_{\rm R}=\pi\frac{w_0^2}{\lambda_{\rm L}}\approx 1.9\times 10^{-3}\,{\rm m}$, which produces a peak power of $P_{\rm L}=2\sqrt{\frac{\ln(2)}{\pi}}\frac{U_{\rm L}}{\Delta t_{\rm L}}\approx 6.7\times 10^9\,{\rm W}$ and a peak intensity of $I_{\rm L}=2\frac{P_{\rm L}}{\pi w_0^2}\approx 9.0\times 10^{18}\,{\rm W}\,{\rm m}^{-2}$.

Photoionization Details

Calculation of the Keldysh parameter, $\gamma_{\rm K} = \omega_{\rm L} \frac{\sqrt{2m_{\rm e}U_{\rm N_2+}}}{q_{\rm e}E_{\rm L}} \approx 0.38 < 0.5$, indicates photoionization is dominated primarily by tunneling rather than multiphoton processes [76], where $E_{\rm L} = \sqrt{\frac{2I_{\rm L}}{c\epsilon_0}}$ is the laser's peak electric field strength and $\epsilon_0 = 8.8542 \times 10^{-12} \, {\rm F \, m^{-1}}$ is the permittivity of free space.

Talebpour et al. [77, 78] provide the photoionization rate as a function of intensity, $w_{\rm N_2^+}(I_{\rm L})$, for femtosecond lasers in N₂ with $\lambda_{\rm L}=800\,{\rm nm}$ and $8.2\times10^{16}\,{\rm W\,m^{-2}}\le I_{\rm L}\le 1.0\times10^{19}\,{\rm W\,m^{-2}}$, based on the experimentally validated theory of Perelomov, Popov and Terent'ev (PPT) for tunneling ionization. Interestingly, $w_{\rm N_2^+}(I_{\rm L})$ exhibits an approximate power law dependence on intensity [78], $w_{\rm N_2^+}\propto I_{\rm L}^{\alpha}$, with $\alpha\approx7.5$ for $I_{\rm L}<1\times10^{18}\,{\rm W\,m^{-2}}$, similar in mathematical form to multiphoton ionization, although with a smaller exponent [79].

With $w_{\rm N_2^+}(I_{\rm L})$ known, the ionization yield simply becomes [78, 79]

$$n_{\rm N_2^+}(t_0) = w_{\rm N_2^+}(I_{\rm L})n_{\rm N_2}(0)\Delta t_{\rm L},$$
 (2.21)

which linearly depends on initial gas density. Since the laser pulse is short compared to the time between collisions, collisional ionization processes (such as avalanche) can be disregarded. Conservation of charge and species implies

$$n_{\rm e}(t_0) = n_{\rm N_2}(t_0),$$
 (2.22)

$$n_{N_2}(t_0) = n_{N_2}(0) - n_{N_2}(t_0). (2.23)$$

Due to the high intensity of the focused femtosecond laser pulse, nonlinear effects arise that contribute to self-focusing (Kerr effect) and defocusing (plasma) of the beam, causing deviations from geometric optics and limiting the maximum achievable intensity (i.e., intensity clamping). Self-focusing is associated with an increase in refractive index given by [78–81] $\Delta \eta = \eta_2 I_{\rm L}$, with the Kerr nonlinear index taking the form $\eta_2(n_{\rm N_2}) = \eta_{2,\rm STP} \frac{n_{\rm N_2}}{n_{\rm STP}}$, where $\eta_{2,\rm STP} = 3.19 \times 10^{-23}\,{\rm m}^2\,{\rm W}^{-1}$ and $n_{\rm STP} \approx 2.4 \times 10^{19}\,{\rm cm}^{-3}$ respectively represent the index and density at atmospheric conditions (101.3 × 10³ Pa, 300 K). The density dependence was assumed to follow the observed linear pressure dependence [81, 82] and the value of $\eta_{2,\rm STP}$ for N₂ at 800 nm includes both the electronic and rotational (Raman) responses typical for a laser pulse of the duration used [83, 84]. Defocusing is associated with a decrease in refractive index due to the formation of a plasma and is given by [78–81] $\Delta \eta = -\frac{n_e}{2n_{\rm e,crit}}$, with n_e computed from Equations (2.21) and (2.22). The critical electron density (in cm⁻³) is $n_{\rm e,crit} = \frac{\epsilon_0 m_e}{1 \times 10^6 q_e^2} \omega_{\rm L}^2$, obtained by equating the laser's angular frequency with the electron plasma frequency, $\omega_{\rm L} = \omega_{\rm pe} = \sqrt{\frac{n_e q_e^2}{\epsilon_0 m_e}}$.

To roughly estimate the laser intensity and thus ionization at the focal point, we adapt the approach used in the study of femtosecond filamentation [78–81] in which Kerr self-focusing balances plasma defocusing and leads to the equality

$$\frac{\eta_{2,\text{STP}}}{n_{\text{STP}}} I_{\text{L}} = \frac{w_{\text{N}_2} + (I_{\text{L}}) \Delta t_{\text{L}}}{2n_{\text{e.crit}}},$$
 (2.24)

after neglecting diffraction and canceling out the linear dependence on gas density by both sides. Solving for laser intensity yields a constant, clamped value of $I_{\rm L} \approx 6.5 \times 10^{17} \, {\rm W \, m^{-2}}$ and from Equation (2.21) for room temperature and pressure, $n_{\rm e}(t_0) \approx 7.2 \times 10^{16} \, {\rm cm^{-3}}$, which agrees well with measurements in air [80] and greatly contrasts with the unrealistically high value, $n_{\rm e} \approx 2.2 \times 10^{22} \, {\rm cm^{-3}}$, obtained by assuming purely geometric focusing ($I_{\rm L} \approx 9.0 \times 10^{18} \, {\rm W \, m^{-2}}$). The independence of laser intensity on gas density⁶ in Equation (2.24) has been observed by others [81], although at low densities, self-focusing weakens with respect to geometric focusing and the balance should become one of geometric focusing and plasma defocusing. For modeling simplicity, the error incurred by using Equation (2.24) at low densities is assumed to be tolerable.

2.2.5 Solution of Equations

The rates of change for the ten species and three temperatures comprise a system of coupled, first-order, nonlinear, ordinary differential equations. We employed MAT-LAB's built-in ode15s function (a variable-step, variable-order, multi-step solver for stiff problems) to solve the system and evaluate the reaction rates, r(t), species number densities, n(t), and temperatures, T(t), at each time step. The visible (VIS) and ultraviolet (UV) signals, which correspond to the first and second positive systems of nitrogen, respectively, are given by

$$S_{VIS}(t) \propto r_{R3}(t) = k_{R3} n_{N_2(B)}(t),$$
 (2.25)

$$S_{\rm UV}(t) \propto r_{\rm R4}(t) = k_{\rm R4} n_{\rm N_2(C)}(t).$$
 (2.26)

⁶Pressure and density are assumed to be interchangeable in this context.

2.3 Tuning of Rate Coefficients and FLEET Spectral Measurements

Several reaction rate coefficients contain significant uncertainty in their value (i.e., a large spread is reported across literature, sometimes with orders of magnitude variation). Table 2.4 tabulates the seven tuned and two non-tuned rate coefficients with their reported ranges and associated references.⁷ These reactions strongly influence the rise time and peak value of $N_2(A)$, $N_2(B)$ and $N_2(C)$ at early times $(t \lesssim 0.01 \,\mu\text{s})$ and the lifetime at later times ($t \gtrsim 1 \,\mu s$). We sought to tune these coefficients (within the bounds set by previous reporting, Table 2.4) to best reproduce the $N_2(B)$ and N₂(C) populations (i.e., VIS and UV signal) observed in experiments at room temperature and atmospheric pressure. Although the model should ideally predict the populations over a wide range of conditions, for the purposes of coefficient tuning, the signal at 300 K and 101.3×10^3 Pa was chosen as the point of reference. The tuning effort required both computational and experimental elements. The computational aspect involved varying the model's rate coefficients, recording the output and then repeating the process for many different combinations of tuned values. The experimental effort entailed measuring the relative size and temporal behavior of $N_2(B)$ and N₂(C) in a nitrogen free jet. Both elements are discussed in detail in the following sections.

2.3.1 Random ('Monte Carlo') Parameter Search for Tuning Rate Coefficients in Model

In the spirit of the Monte Carlo method and multi-parameter optimization, the rate coefficients for reactions R5, R23, R24 and R25 were randomly varied over the ranges delineated in Table 2.4. The rate coefficients for dissociative recombination of cluster

⁷An extensive, though certainly non-exhaustive listing of references.

Table 2.4: Reactions with relatively high uncertainty in rate coefficients (in units of $cm^3 s^{-1}$).

Number	Min. / Max.	Ref.	Additional Ref.	
R5	$7.7 \pm 1.1 \times 10^{-11} \\ 1.1^{+2}_{-0.5} \times 10^{-9}$	[33] [32]	[34]	
$ m R6^a$	$2.1 \times 10^{-11} 2.6^{+2}_{-1.4} \times 10^{-10}$	[85] [31]	[34, 48, 86]	
$ m R7^{b}$	2.6×10^{-7} $4.6 \pm 0.9 \times 10^{-6}$	[34] [37]	[36]	
$ m R8^{b}$	2.6×10^{-7} $4.6 \pm 0.9 \times 10^{-6}$	[34] [37]	[36, 38]	
$ m R9^b$	$2.6 \pm 0.3 \times 10^{-6}$ $4.6 \pm 0.9 \times 10^{-6}$	[34, 39] [37]	[36]	
$R23^{c}$	3×10^{-19} 3×10^{-16}	[41, 50, 51] [24, 36]	[47–49]	
R24	$5 \times 10^{-12} \\ 6.5 \times 10^{-11}$	[41, 53] [52]	[34, 36, 47, 54]	
R25	$1.61 \pm 0.08 \times 10^{-12}$ 1×10^{-10}	[57] [36]	[26, 33, 46, 55, 56, 58]	
R26 ^a	1×10^{-11} $2.67 \pm 0.14 \times 10^{-11}$	[34] [59]	[58, 87]	

^a Non-tuned coefficient with a relatively large spread of values across literature.

^b Ikezoe et al. [37] and Gordiets et al. [36] did not explicitly specify the electronic state of the products.

^c The listed maximum of $k = 3 \times 10^{-16}$ was used by the kinetic schemes of Henriques et al. [24] and Gordiets et al. [36]. However, the original citation [48] described a much smaller coefficient, $k < 3 \times 10^{-18}$. Therefore, the upper limit considered during tuning was $k = 3.8 \pm 0.4 \times 10^{-17}$, taken from Levron et al. [49].

ions (R7, R8 and R9) were varied in a slightly different manner. A value for the base coefficient was randomly selected from the range 2.6×10^{-7} to 5.5×10^{-6} cm³ s⁻¹ (the entire extent of the range for this type of reaction). Once the base coefficient was selected, each of the three reactions was randomly assigned a fraction of the base coefficient's value. This approach assumed that previous efforts to characterize the rate coefficient were actually measurements of the overall reaction (i.e., base coefficient) and not its constituent processes. See the discussion in Section 2.2.1 for more details.

Once values for the seven tuned coefficients were assigned, the system was solved in the manner previously described and its solution (i.e., $n_{N_2(B)}(t)$ and $n_{N_2(C)}(t)$) was recorded. This process was repeated over 240 000 times (trials) in an attempt to adequately sample all of the possible combinations of rate coefficient values. The sampling size was considered satisfactory for the sake of an example of tuning by random parameter search. More precise and efficient tuning would require use of an optimization algorithm.

Figure 2.1 plots the normalized populations of B-state (red) and C-state (blue) nitrogen from 19 'Monte Carlo' trials (solid lines) to roughly illustrate the model's sensitivity to the tuned rate coefficients. Photomultiplier (PMT) experimental data (boxes) are superimposed for reference and discussed in detail in Section 2.3.5. In the figure, the results were normalized by the value of $n_{N_2(B)}$ at $t = 2.9 \times 10^{-3} \,\mu s$ (the starting time for the experimental data). The 19 trials were chosen according to their rank in a least-squares best fit to the experimental data based on matching the ratio of $n_{N_2(B)}$ to $n_{N_2(C)}$. The the 1st through 5th best fits are shown along with progressively poorer fits (i.e., 10th, 20th, 50th, 100th, 200th, ..., 200 000th) to provide some sense of the spread. Observe the large spread for $t \lesssim 3 \times 10^{-3} \,\mu s$ and $t \gtrsim 3 \,\mu s$ when the best fit metric fails due to a lack of experimental data. Also, note

a population inversion, $n_{\rm N_2(C)} > n_{\rm N_2(B)}$, in a few cases for $t \gtrsim 1 \times 10^{-3} \,\mu s$, which we considered unlikely to occur in this decaying plasma.

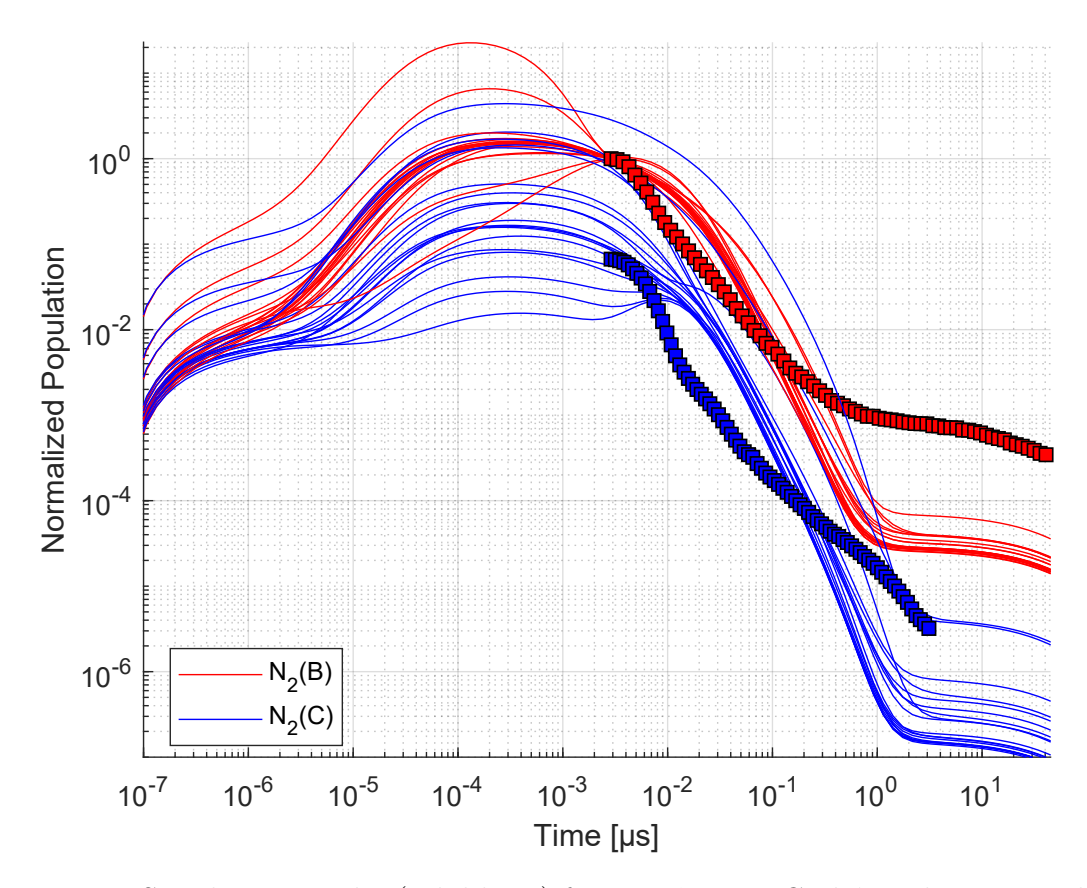


Figure 2.1: Simulation results (solid lines) from 19 'Monte Carlo' trials compared to PMT experimental data (boxes).

One takeaway from the spread shown in Figure 2.1 is that the rate coefficients for energy pooling and dissociative recombination, which are not precisely known, can be found by tuning this relatively simple kinetics model to fit the experimental data. With this approach, additional time-resolved data would need to be obtained, for example, at earlier time delays when the populations achieve their maximum value, to uniquely determine the coefficients. Furthermore, an optimization algorithm (such as an artificial neural network), instead of a random parameter search, would be employed to intelligently and efficiently tune the rate coefficients. Such efforts would increase the confidence in the values obtained for the tuned coefficients in Table 2.1

given the large range for the rate coefficients (Table 2.4) and the model's sensitivity to them (Figure 2.1).

The formula for the residuals used to compare the ratio of excited populations in the simulation (sim) and experiment (exp) was

$$\operatorname{res} = \frac{\log \left(n_{\text{N}_2(\text{B}), \text{sim}}(t) \right)}{\log \left(n_{\text{N}_2(\text{C}), \text{sim}}(t) \right)} - \frac{\log \left(n_{\text{N}_2(\text{B}), \text{exp}}(t) \right)}{\log \left(n_{\text{N}_2(\text{C}), \text{exp}}(t) \right)}, \tag{2.27}$$

with the number densities first normalized in the manner described for Figure 2.1 and then discretely sampled at logarithmic intervals of t. Use of logarithms ensured fairer weighting over the extensive span of time and variation in amplitude. Ranking of the trials was based on least squares of the residuals. The purpose of the metric was to find the simulation trial (i.e., set of tuned rate coefficients) that best replicated the experiment's temporal behavior and ratio of $N_2(B)$ to $N_2(C)$.

2.3.2 Measurement of FLEET Spectrum

In order to quantitatively compare the $N_2(B)$ and $N_2(C)$ populations, it was first necessary to measure the relative strength of the visible and ultraviolet emission of these excited states. This task was accomplished by spectroscopy of FLEET in nitrogen and several key assumptions and approximations. Once the relative strength had been established, the time varying behavior of the signals (populations) could then be quantified with a photomultiplier tube and bandpass filters.

We acquired the spectrum of FLEET in a quartz cell flowing pure nitrogen (≥ 99.998%) at approximately room temperature and atmospheric pressure using a half-meter focal length spectrometer (Princeton Instruments Acton SP-500i) calibrated for wavelength and a diffraction grating (Princeton Instruments, 600 gr mm⁻¹, 500 nm blaze wavelength). A scientific camera (Princeton Instruments PIXIS 512B CCD) recorded background-subtracted spectra using five-second integration times.

The femtosecond laser (Spectra-Physics Solstice) was operated at a repetition rate of 1000 Hz with the same nominal parameters as listed in Section 2.2.4 except for a slightly lower⁸ pulse energy of 0.3×10^{-3} J.

Unfortunately, the experiment lacked both a notch filter to block the laser light⁹ and a longpass filter to block the second-order modes of the diffraction grating. We subtracted the laser line from the FLEET spectrum by assuming a Gaussian line shape (with the spectral parameters given by Section 2.2.4) and choosing the amplitude of the Gaussian such that the signal in regions without known spectral features went exactly to zero (as would be expected if no laser contamination were present). Subtraction of the second-order modes within the first positive spectrum was not possible and though non-ideal, was assumed to be tolerable since the first negative features, not accounted for by the model, already contaminated the second positive spectrum and could likewise not be subtracted.

Manufacturer provided data on camera quantum efficiency, $QE_{\text{cam}}(\lambda)$, and grating efficiency, $\eta_{\text{gr}}(\lambda)$, enabled correction of the acquired FLEET spectrum for instrument sensitivity. Further correction of the UV portion of the spectrum was achieved by leveraging the second positive lines of $N_2(C, v = 0)$. See Table 2.5 and, additionally, Section 2.2.1. A continuous correction curve was formed from calibration points at the specified wavelengths, λ . The calibration points were adjusted so that the ratios of the integrated second positive features and spontaneous emission coefficients equaled one another, i.e., $\int S(\lambda) d\lambda / \int S_{(0,4)}(\lambda) d\lambda = k/k_{(0,4)}$. The (0,4) feature was chosen as the reference point because it was far enough into the visible spectrum to not need UV correction and strong enough to have satisfactory signal-to-noise ratio (SNR).

⁸The pulse energies are effectively equivalent from the point of view of the model.

⁹We could have alternated between the laser's first and second harmonic when generating FLEET to produce two separate spectra and then judiciously stitch together a composite spectrum without either laser line. However, we wished to avoid introducing additional experimental parameters into the measurement and therefore used solely 800 nm.

 $^{^{10}} Reaction$ given by ${N_2}^+(B^2\Sigma_u^+) \longrightarrow {N_2}^+(X^2\Sigma_g^+) + h\nu$

Table 2.5: Second positive features used to calibrate UV region.

$\overline{(v',v'')}$	(0, 0)	(0, 1)	(0, 2)	(0, 3)	(0, 4)	Unit	Ref.
λ	337.1	357.7	380.5	405.9	434.4	nm	[10]
$k/k_{(0,4)}$	46.2	30.9	12.3	3.81	1	s^{-1}	[19]

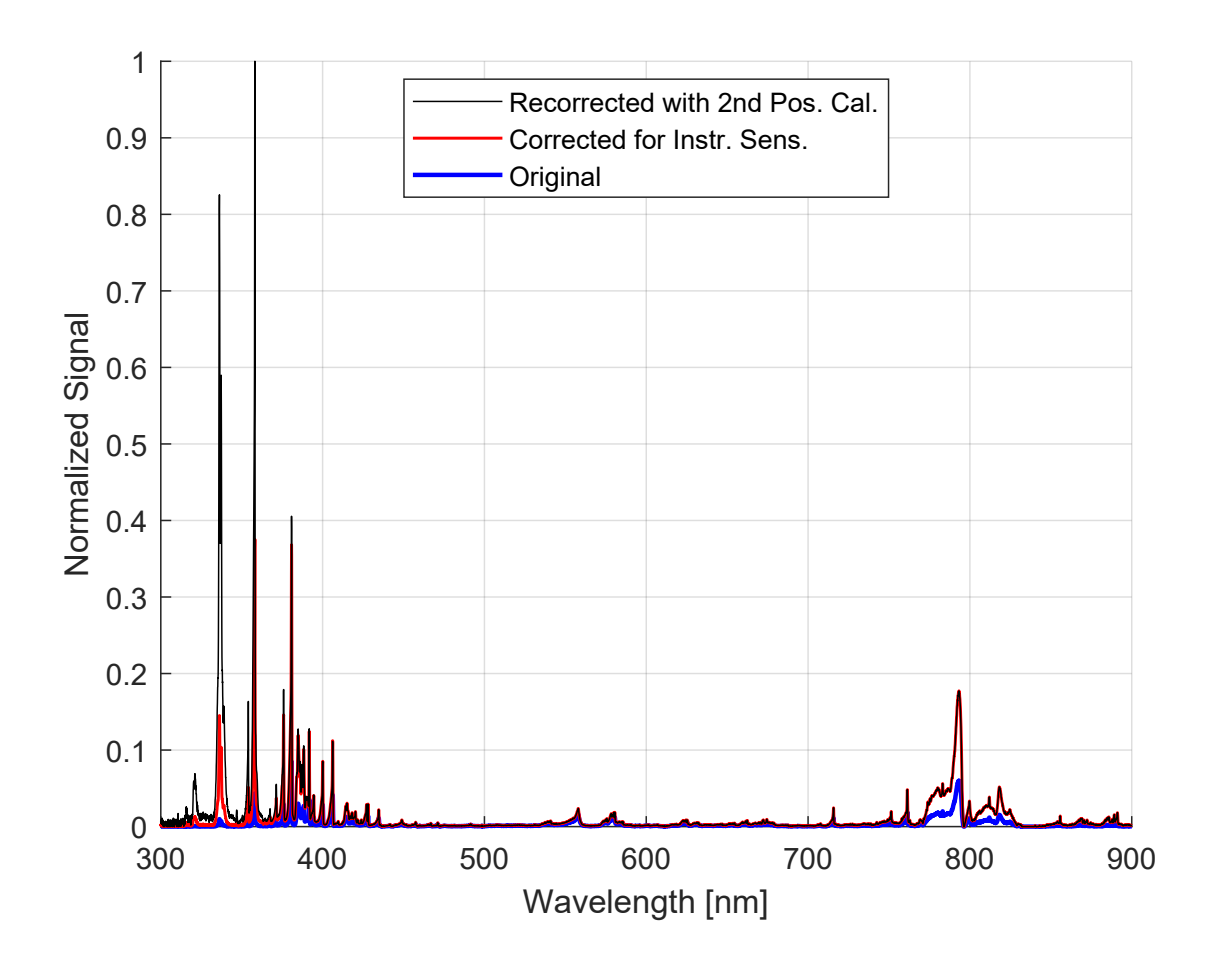


Figure 2.2: FLEET spectrum in nitrogen at ambient temperature and pressure with laser line shape subtracted.

Figure 2.2 plots the FLEET spectrum in nitrogen, superimposing the original acquisition from the spectrometer (blue), the spectrum corrected for instrument sensitivity (red), and the spectrum recorrected with the second positive calibration (black) which was actually used in calculations. The curves in the plot had the laser line shape subtracted out and were normalized by the peak signal of the recorrected spectrum. Observe that each correction progressively bolsters the strength of the UV signal with respect to the VIS signal.

2.3.3 Formulas and Assumptions for Relating Spectrometer, Photomultiplier and Model Results

If $r_{\rm ph}(\lambda,t)$ symbolizes the theoretical spectral rate of change of photon density in the tagged region (in units of cm⁻³ s⁻¹ nm⁻¹), then the signal on the spectrometer is related via

$$S_{\rm spec}(\lambda) \propto \int Q E_{\rm cam}(\lambda) \widetilde{\eta}_{\rm gr}(\lambda) r_{\rm ph}(\lambda, t) dt,$$
 (2.28)

with the second positive calibration absorbed into a modified grating efficiency $\tilde{\eta}_{gr}(\lambda)$ and the collection efficiency and unit conversion factors neglected.

Since the model only considers VIS and UV emission, the entire FLEET spectrum was consolidated into two bands: a VIS band given by $\Delta\lambda_{\rm VIS} = 498-895\,\rm nm$ and a UV band given by $\Delta\lambda_{\rm UV} = 332-493\,\rm nm$. Selection of these ranges was based on the prominent lines of the first and second positive systems listed in Lofthus et al. [10], identifiable features in the measured spectrum (Figure 2.2) and exclusion of the first negative features around 315 nm and 320 nm. For example, the signal in the VIS band would be given by $S_{\rm spec,VIS} = \int_{\Delta\lambda_{\rm VIS}} S_{\rm spec}(\lambda) {\rm d}\lambda$, or equivalently,

$$S_{\text{spec,VIS}} = \int S_{\text{spec}}(\lambda) T'_{\Delta\lambda_{\text{VIS}}}(\lambda) d\lambda,$$
 (2.29)

where $T'_{\Delta\lambda_{\text{VIS}}}(\lambda)$ is an ideal rectangular bandpass filter that passes 100 % within $\Delta\lambda_{\text{VIS}}$ and 0 % otherwise. Similarly, the VIS signal in the model is related to $r_{\text{ph}}(\lambda, t)$ by

$$r_{\rm R3}(t) = \int r_{\rm ph}(\lambda, t) T'_{\Delta\lambda_{\rm VIS}}(\lambda) d\lambda.$$
 (2.30)

Furthermore, the VIS signal collected by the PMT has the form

$$S_{\rm PMT,VIS}(t) \propto \int QE_{\rm PMT}(\lambda)T_{\rm VIS}(\lambda)r_{\rm ph}(\lambda,t)T'_{\Delta\lambda_{\rm VIS}}(\lambda)d\lambda,$$
 (2.31)

with the collection efficiency and unit conversion factors neglected and the PMT quantum efficiency, $QE_{\rm PMT}(\lambda)$, provided by the manufacturer. $T_{\rm VIS}(\lambda)$ represents the VIS bandpass filter function used in the PMT experiment (shown in Figure 2.3 and described in Section 2.3.4). With the appropriate substitutions, UV band quantities such as $S_{\rm spec,UV}$, $r_{\rm R4}(t)$ and $S_{\rm PMT,UV}(t)$ are calculated in the same manner.

Relating the time integrated FLEET spectrum, $S_{\rm spec}(\lambda)$, to a spectrally integrated photomultiplier signal such as $S_{\rm PMT,VIS}(t)$ requires an assumption that the spectral lines within the band, $\Delta \lambda_{\rm VIS}$, evolve monolithically in time. In other words, the relative strengths of the spectral lines within a band are invariant in time, although the strengths can vary uniformly by a time-dependent factor, say, $f_{\rm VIS}(t)$.

Noting t as the variable of integration, Equation (2.28) can be rewritten as $\frac{S_{\rm spec}(\lambda)}{QE_{\rm cam}(\lambda)\tilde{\eta}_{\rm gr}(\lambda)} \propto \int r_{\rm ph}(\lambda,t) dt$. We limit this new equation to a particular band by multiplying both sides by $T'_{\Delta\lambda_{\rm VIS}}(\lambda)$. Then, by invoking the assumption of monolithic evolution, the integral on the right-hand side can be taken over any arbitrary time interval and therefore eliminated, yielding

$$\frac{S_{\rm spec}(\lambda)T'_{\Delta\lambda_{\rm VIS}}}{QE_{\rm cam}(\lambda)\widetilde{\eta}_{\rm gr}(\lambda)}f_{\rm VIS}(t) \propto r_{\rm ph}(\lambda,t)T'_{\Delta\lambda_{\rm VIS}}(\lambda),\tag{2.32}$$

where the factor $f_{\text{VIS}}(t)$ accounts for the monolithic variation of the signal in $\Delta\lambda_{\text{VIS}}$ over time. This equation enables us to formulate a ratio between the signal observed by an instrument and the signal that would have been collected from the desired band of the FLEET spectrum (in Figure 2.2) had the instrument possessed ideal rectangular spectral sensitivity. In practice, the factor $f_{\text{VIS}}(t)$ cancels out along with any unit conversion factors. Also, with the appropriate substitutions, the above formulas readily apply to the UV band as well.

2.3.4 Bandpass Filters for Isolating VIS and UV Signal

For the experiment, we isolated the VIS and UV bands by layering multiple colored glass filters together. The VIS filter was composed of a longpass (Edmund Optics 66-088, 550 nm cut-on) and a shortpass (Edmund Optics 84-725, 650 nm cut-off). The goal was to maximize light collection from the relatively dim, but long-lived VIS signal. The UV filter was composed of two bandpasses (Thorlabs FGB37, 332-608 nm, and Lattice Electro Optics BG39-20, 350-587 nm) to suppress leakage around 650 nm, a shortpass (Edmund Optics 84-715, 400 nm cut-off) and a neutral density filter (Thorlabs ND10A, 1.0 OD) to attenuate the relatively bright, but short-lived UV signal. Manufacturer provided data enabled calculation of the filter transmission functions shown in Figure 2.3 and denoted respectively by $T_{\text{VIS}}(\lambda)$ and $T_{\text{UV}}(\lambda)$. Although the filters only transmit a subset of the total emission within $\Delta \lambda_{\text{VIS}}$ and $\Delta \lambda_{\text{UV}}$, they nevertheless attempt to capture the strongest lines observed [2, 88] within the bands.

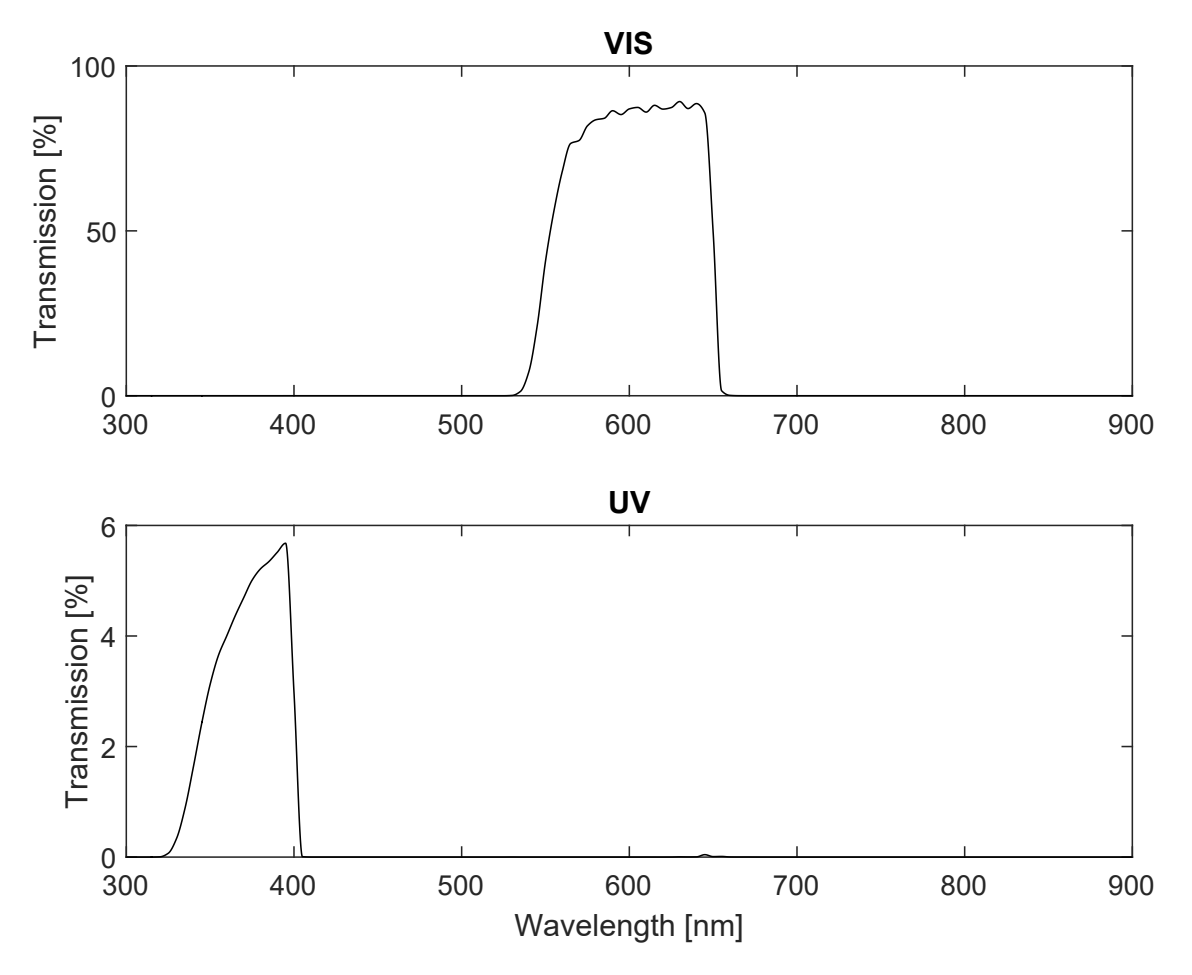


Figure 2.3: Spectral transmission functions for the visible and ultraviolet filters, denoted by $T_{\text{VIS}}(\lambda)$ and $T_{\text{UV}}(\lambda)$, respectively. Note the UV filter transmits significantly less light and slightly leaks around 645 nm.

2.3.5 Photomultiplier (PMT) Experiment and Comparison to Model

Using the nominal parameters listed in Section 2.2.4 and a repetition rate of 1000 Hz, the laser (Spectra-Physics Solstice) generated FLEET in a pure nitrogen ($\geq 99.998 \%$) free jet of large overall diameter ($29 \times 10^{-3} \,\mathrm{m}$) relative to the confocal parameter ($b = 2z_{\mathrm{R}} \approx 3.7 \times 10^{-3} \,\mathrm{m}$). Figure 2.4 depicts FLEET in the free jet as captured by a smartphone camera using an exposure of $\frac{1}{15}$ s. The nozzle configuration delivered the gas at approximately room temperature and atmospheric pressure. We estimated the volume of the tagged region as $vol_{\mathrm{tag}} = 1 \times 10^6 \pi w_0^2 b \approx 5.6 \times 10^{-6} \,\mathrm{cm}^3$.



Figure 2.4: FLEET in free jet from co-flow nozzle. Note long-lived visible emission. Innermost diameter is 16 mm while annular diameter is 19–29 mm. Both outlets flow N_2 at about 1 m s^{-1} . FLEET was radially centered during experiments.

The linearity of the PMT (Hamamatsu R636-10, 2 ns rise time) operating at 1025 VDC with the expected signal levels was confirmed by comparison to photodiode (Thorlabs DET10A, 1 ns rise time) measurements. Efforts to reduce stray light and laser scattering included painting relevant surfaces matte black, placing the PMT with its 2.1 mm diameter entrance aperture and collection optics in a light tube, and passing the beam through a half-wave plate to rotate its linear polarization vector. The entrance to the collection optics consisted of a lens of diameter $D_{\rm col} = 0.075 \, {\rm m}$ offset from the tagged region by its focal length, $L_{\rm col} = 0.12 \, {\rm m}$, which corresponded to a light cone collection efficiency of $\eta_{\rm col} = \frac{1}{2} - \frac{L_{\rm col}}{2\sqrt{L_{\rm col}^2 + D_{\rm col}^2/4}} \approx 2.3 \, \%$.

A digital oscilloscope (LeCroy WaveJet 334, 350 MHz bandwidth) acquired signals from the PMT via impedance-matched cables and terminations. Since the signal amplitude varied by orders of magnitude, low and high input ranges on the oscilloscope were used ($\pm 1\,\mathrm{V}$ and $\pm 10\,\mathrm{V}$). The resulting signals were then spliced together (after deconvolution in post-processing) to prevent saturation at early times when the signal was strong and improve the signal-to-noise ratio at later times when the

signal was weak. To compensate for noise, on-scope averaging of 256 waveforms was performed. Due to output limitations of the oscilloscope operating in this mode, variance went unmeasured, preventing calculation of error bars for the data. Even with on-scope averaging, the SNR decreased with time and noise became perceptible at about $t \approx 0.3\,\mu s$. Therefore, the signals were further refined by averaging a set of 10 on-scope averages (or 2560 single-shot measurements in total). All signal traces were background subtracted and deconvolved from an instrument response function based on laser scattering. The noise floor was clearly distinguishable and signal below this threshold was discarded, explaining the abrupt termination of the fast-decaying UV signal at $t = 3.2\,\mu s$ in the figures. The slow-decaying VIS signal, in contrast, never dropped below the noise floor and was retained completely (up to $t = 47\,\mu s$). Spurious signal reflections were omitted and a moving average filter of variable window size was applied to slightly smooth the data.

Relying on the assumptions of Section 2.3.3 and utilizing Equations (2.30)–(2.31) yield a relationship between the PMT voltage signal (as measured by the oscilloscope) and the rate of change of photon density in the simulation,

$$V_{\rm PMT,VIS}(t) = r_{\rm R3}(t) \frac{\int QE_{\rm PMT}(\lambda) T_{\rm VIS}(\lambda) r_{\rm ph}(\lambda, t) T'_{\Delta\lambda_{\rm VIS}}(\lambda) d\lambda}{\int r_{\rm ph}(\lambda, t) T'_{\Delta\lambda_{\rm VIS}}(\lambda) d\lambda}$$

$$\times vol_{\rm tag} \eta_{\rm col} \eta_{\rm aper} g_{\rm PMT} q_{\rm e} R_{\rm scope},$$
(2.33)

where $vol_{\rm tag}$ and $\eta_{\rm col}$ are defined previously, $g_{\rm PMT}=1\times 10^5$ is the approximate PMT gain at 1025 VDC and $R_{\rm scope}=50\,\Omega$ is the oscilloscope input impedance. A scaling factor of $\eta_{\rm aper}=2.5\,\%$ accounts for the clipping of incoming light by the PMT's aperture and other experimental uncertainties. Equation (2.32) enables substitution of the $\Delta\lambda_{\rm VIS}$ band of the measured FLEET spectrum (black line in Figure 2.2) for $r_{\rm ph}(\lambda,t)T'_{\Delta\lambda_{\rm VIS}}(\lambda)$ in the ratio. The resulting equation for the VIS band (and one similarly constructed for the UV band) can be solved for $r_{\rm R3}(t)$ (or $r_{\rm R4}(t)$) to convert

the experimental results with units of V into a rate of change of photon density with units of $cm^{-3} s^{-1}$.

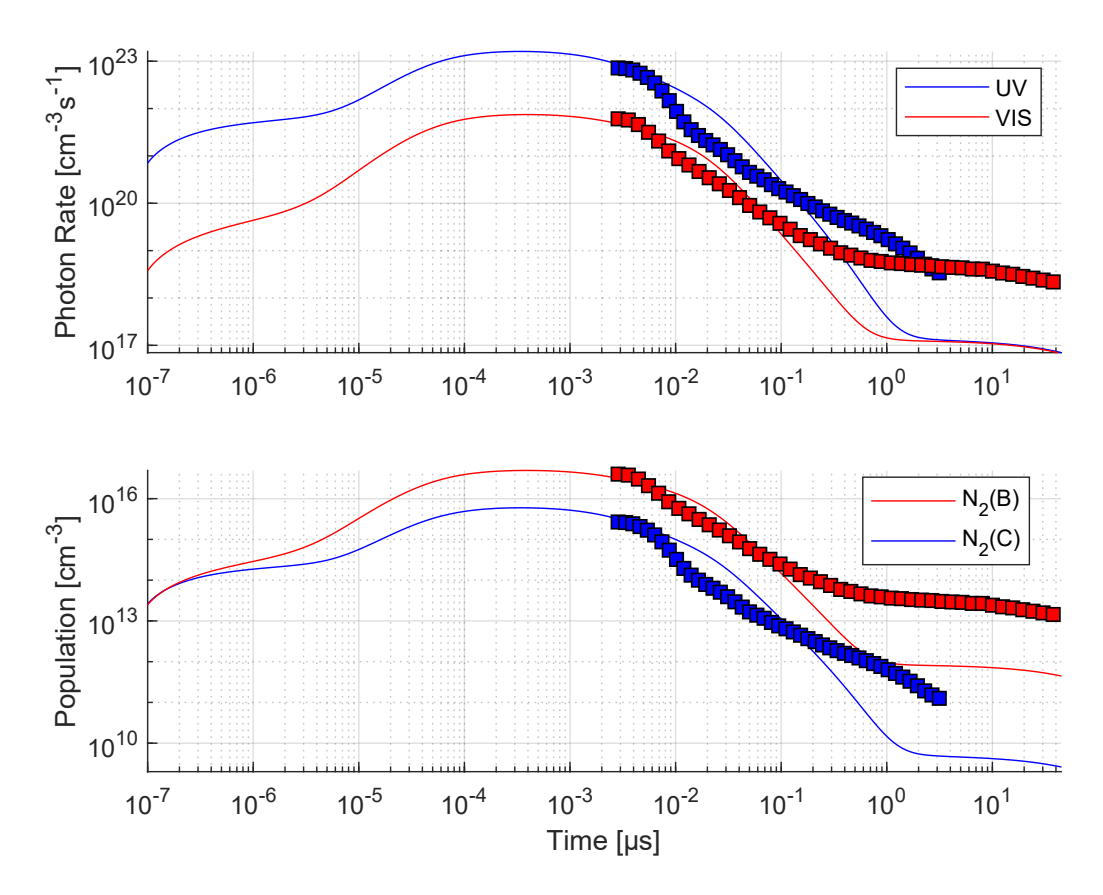


Figure 2.5: Photon density rate in the tagged region (upper) and excited-state populations (lower) for the simulation (solid lines) and PMT experiment (boxes) in nitrogen at $300 \,\mathrm{K}$ and $101.3 \times 10^3 \,\mathrm{Pa}$. Note that a normalized version of the lower subfigure is presented with other 'Monte Carlo' trials in Figure 2.1.

Figure 2.5 shows these converted experimental results (boxes) along with the best fit simulation (solid lines) from the 'Monte Carlo' trials. Recall that Equations (2.25) and (2.26) relate the rate of change of the photon density (upper subfigure) in the tagged region to its corresponding excited-state population (lower subfigure). Note that without the scaling factor $\eta_{\rm aper}$, the experimental curves would lie below the simulation results. Also, note that a normalized version of the lower subfigure appears in Figure 2.1 along with other 'Monte Carlo' trials. Importantly,

the red curves exhibit the general behavior of fast decay followed by slow decay, which has been observed in many time-resolved experiments [1, 2, 14, 15, 88].

Regarding similarities, the simulation and experiment curves show relatively good agreement in absolute magnitude¹¹ and ratio of blue to red at $t = 2.9 \times 10^{-3} \,\mu s$. Like the experimental red curves (although unobserved in the blue curves because of the early truncation), the simulation curves level off before beginning to decay again. For the photon rates, the blue and red curves of the simulation intersect each other like those of the experiment.

Regarding differences, the simulation lacks an inflection point that occurs around $t \approx 0.01\,\mu s$ in the experiment curves, although this inflection may be spurious, an artifact of PMT saturation and/or error in the deconvolution. The simulation curves generally decay faster, and, for the case of the red curve, longer than the experiment. The faster decay is probably explained by the model's neglect of gas dynamic expansion (which lowers the overall density) and spatial distribution of species. The model effectively concentrates all species into a zero-dimensional point with constant overall density, hastening the reaction rates compared to reality (or a model which includes these physics). The simulation appears to have a stronger coupling between the red and blue curves than the experiment. In the model, for $t \gtrsim 1 \times 10^{-3}\,\mu s$, the repopulation of N₂(B) and N₂(C) by energy pooling of N₂(A) drives this coupling, with some additional contributions to coupling from the decay of N₂(C) into N₂(B) by quenching and fluorescence. Furthermore, N₂(B) and N₂(C) ultimately decay into N₂(A), which feeds the energy pooling process and adds to the coupling.

¹¹The scaling factor required for agreement is reasonable considering the number of estimations and uncertainties required to back calculate the photon density rate in the tagged region.

2.4 Modeling Results, Discussion and Comparison to Experiment

2.4.1 Species Populations and Contributing Reactions at Atmospheric Conditions

Figure 2.6 plots the number densities of atoms (solid lines), electronically-excited molecules (dotted lines) and charged species (dashed lines) in time. The effectively constant concentration of molecular nitrogen $(n_{\rm N_2}(t) \approx 2.4 \times 10^{19} \, {\rm cm^{-3}})$ lies well above the displayed data. The N₂(B) and N₂(C) populations shown here are the same as depicted in Figure 2.5 (lower) and were repeated in this figure for reference. Except for N₂⁺ and e⁻ which began with finite population, all the species rapidly grew from zero population at $t = t_0 = 7 \times 10^{-8} \, \mu \text{s}$ to their values at $t = 1 \times 10^{-7} \, \mu \text{s}$. We should emphasize the speculative nature of results for $t \gtrsim 1 \, \mu \text{s}$ (and certainly for $t \gg 1 \, \mu \text{s}$) since important physics, such as fluid dynamics and spatial variation of species, are neglected. Omission of these physics fundamentally alters the rate computations within the model, causing the N₂(B) and N₂(C) populations to decay faster than observed experimentally (see Figure 2.5 and Section 2.3.5).

Observe the persistently large population of atomic nitrogen at this pressure and temperature. Figure 2.7 plots the production (solid lines) and consumption (dashed lines) reactions contributing to the N population, with the absolute rates (in units of cm⁻³ s⁻¹) in the upper subfigure and the relative contribution fraction (in units of %) in the lower subfigure. The contribution fraction is computed by dividing a given rate by the sum of the absolute value of each of the rates contributing to the production and consumption of the species at an instant in time. For clarity, only reactions with a contribution fraction of at least 10 % are shown; therefore, the curves do not necessarily sum to 100 %. According to the figure, impact dissociation (R40)

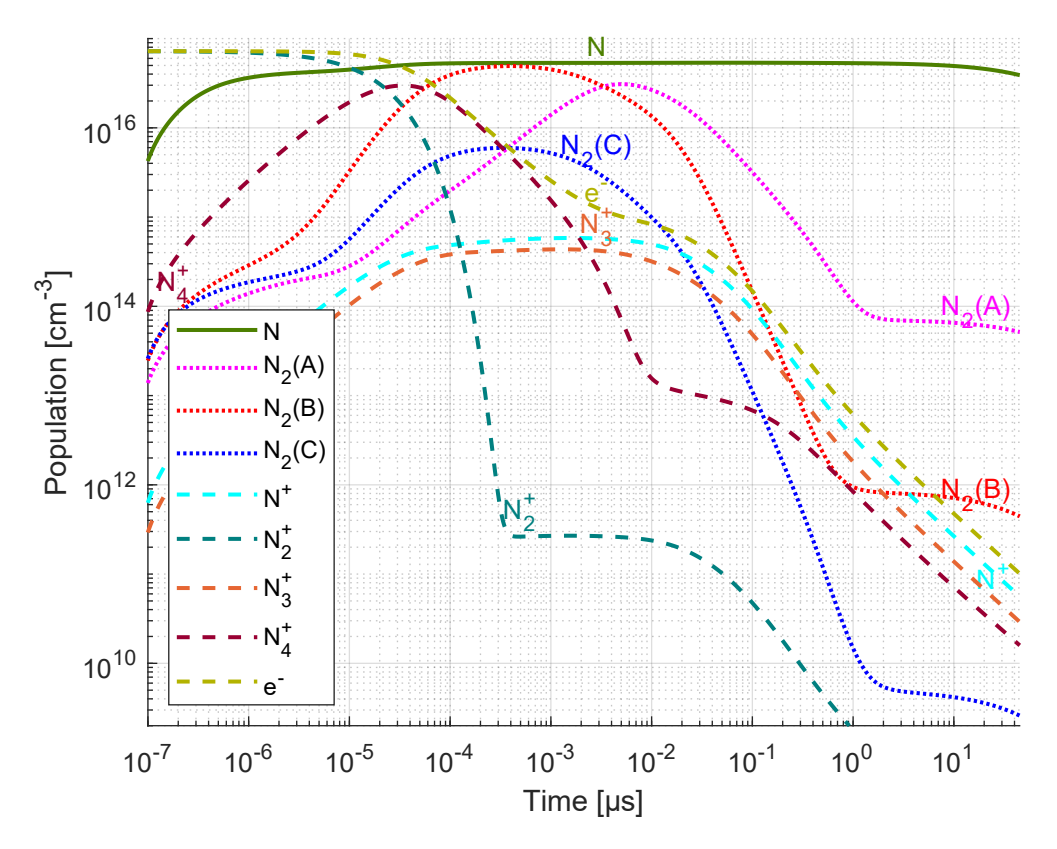


Figure 2.6: Number densities of atoms (solid line), excited molecules (dotted lines) and charged species (dashed lines) in the simulation for nitrogen at 300 K and 101.3×10^3 Pa. Note that $n_{\rm N_2}(t) \approx 2.4 \times 10^{19}$ cm⁻³.

and dissociative recombination (R12 and later, R11) contribute to the growth of N, whose population peaks around $t \approx 0.06\,\mu s$. Electron impact processes, such as R40, dominate at early timescales when $n_{\rm e}$ and $T_{\rm e}$ are greatest. The second peak of the R40 curve (Figure 2.7, lower) occurs because the rate of dissociative recombination of N₂⁺ plummeted as $n_{\rm N_2^+}$ plummeted, enabling R40 to reassert dominance over R12. Ion exchange reactions (R29 and R39) and three-body atomic recombination (R1) consume N. At later timescales ($t \gtrsim 0.2\,\mu s$), atomic recombination dominates, drawing from the large reservoir of N to bolster the N₂(B) population and indirectly, the N₂(A) (by quenching of B-state) and N₂(C) (by energy pooling of A-state) popula-

tions. The presence of R1, as opposed to its absence,¹² dramatically lengthens the lifetimes of these electronically-excited species for $t \gtrsim 1 \,\mu s$ in Figure 2.6.

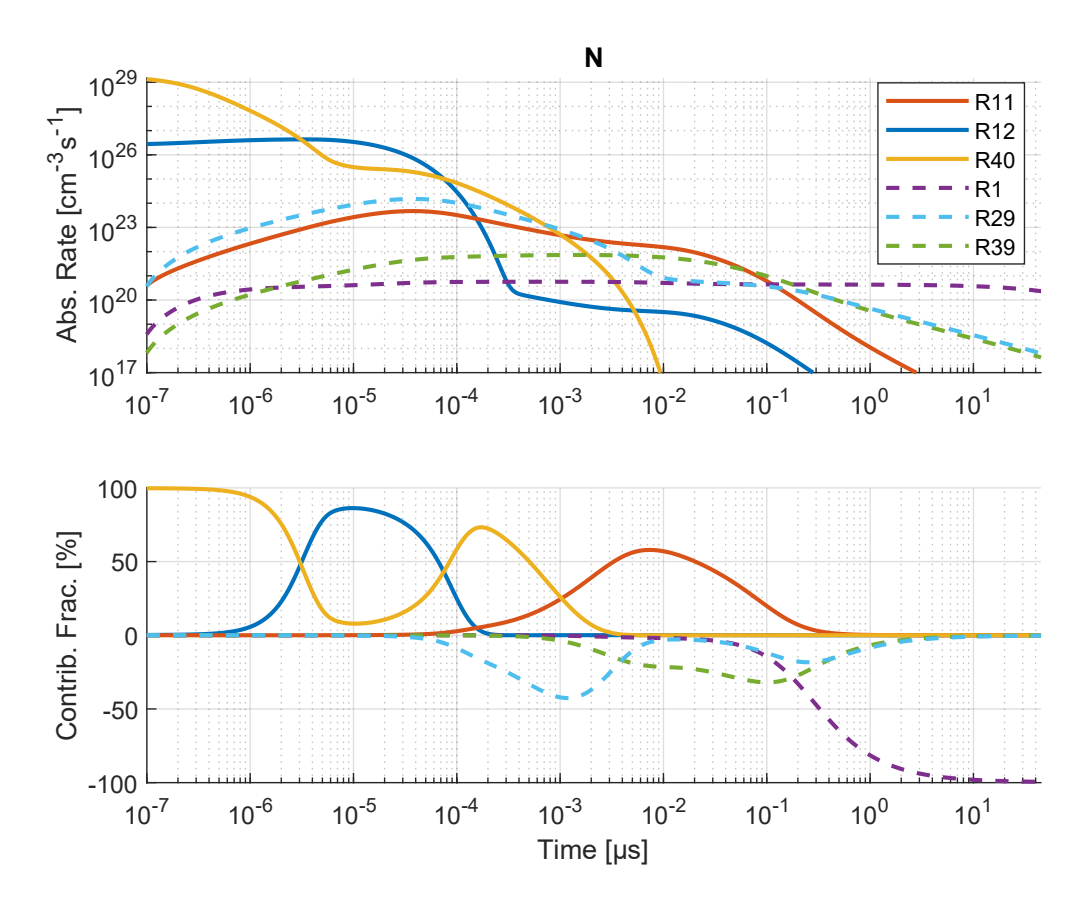


Figure 2.7: Reactions contributing to the production (solid lines) or consumption (dashed lines) of N. Upper subfigure shows absolute value of rates while lower subfigure depicts each rate's contribution fraction at a particular time. Only reaction rates with relative contributions of at least 10% are shown.

Figure 2.8 shows the reactions contributing to $N_2(B)$. Impact excitation (R48) dominates early on, followed by dissociative recombination of N_4^+ cluster ions (R8) and then $N_2(A)$ energy pooling (R5). Note these latter two reactions had tuned rate coefficients. R48 terminates abruptly at $t \approx 1 \times 10^{-5} \,\mu s$ because T_e fell outside the computed domain for $k = f(T_e)$, or in terms of kinetic energy, $\bar{\epsilon}_e \ll U_{N_2(B)}/q_e$. There was some contribution, $\leq 9.0 \,\%$, from the quenching of $N_2(C)$ (R26) when the population of $N_2(C)$ reached its maximum. At later timescales, atomic recombination

 $^{^{12}}$ When atomic recombination is disabled, the curves for N₂(A), N₂(B) and N₂(C) have no 'knee' around $t\approx 0.8-2\,\mu s$ and instead continue to rapidly decay.

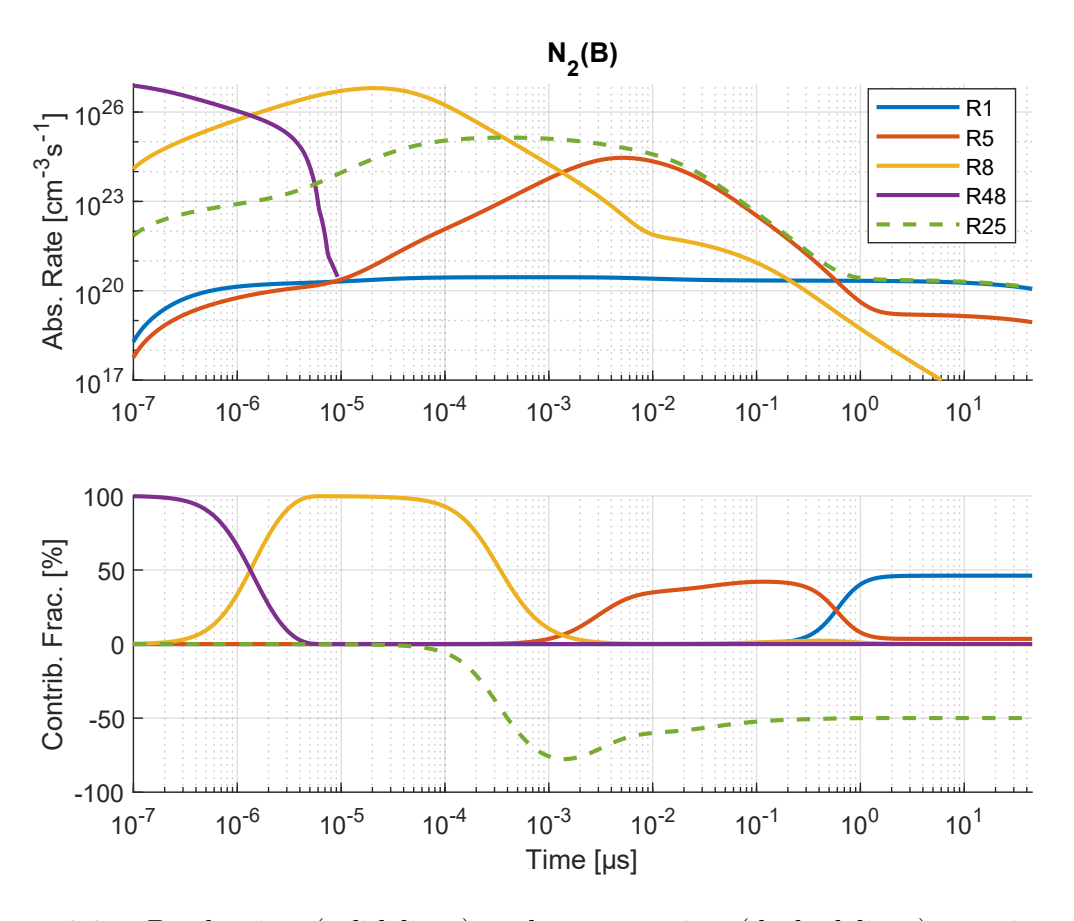


Figure 2.8: Production (solid lines) and consumption (dashed lines) reactions for $N_2(B)$. See caption in Figure 2.7 for details.

(R1) rose to prominence, contributing to the relatively long lifetime of $N_2(B)$ and the VIS signal. The quenching of $N_2(B)$ (R25), with its tuned rate coefficient, far exceeded the first positive fluorescence (R3) which had a maximum (absolute) fraction of about 0.04%.

Figure 2.9 showcases the reactions that contribute to $N_2(C)$. Similar to $N_2(B)$, impact excitation (R52) dominates at the start, followed by dissociative recombination of N_4^+ cluster ions (R9, a tuned reaction) and then $N_2(A)$ energy pooling (R6). R52 terminates abruptly around $t \approx 1 \times 10^{-5} \,\mu s$ for the same reasons as in Figure 2.8. Like for $N_2(B)$, quenching (R26) dominates the $N_2(C)$ loss rates, though the second positive fluorescence (R4) has a much larger maximum (absolute) fraction, about 7.5%, because of its higher spontaneous emission probability.

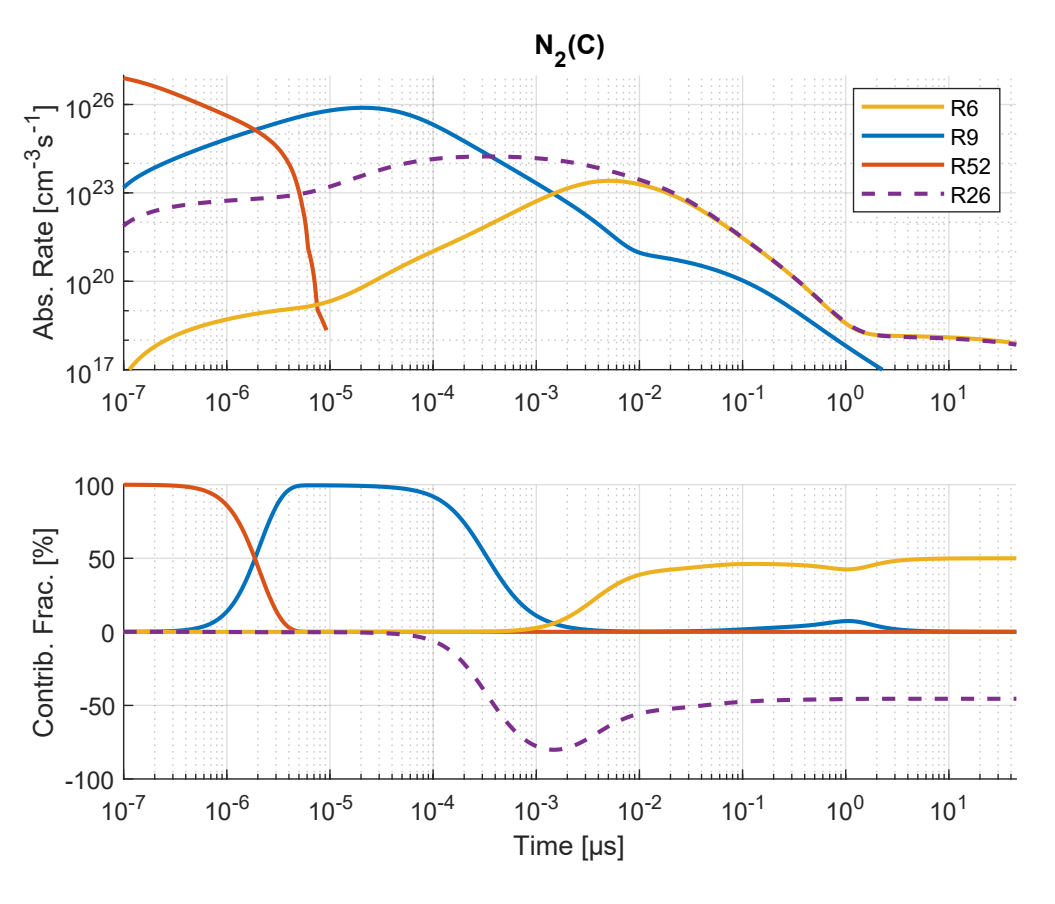


Figure 2.9: Production (solid lines) and consumption (dashed lines) reactions for $N_2(C)$. See caption in Figure 2.7 for details.

Figure 2.10 plots the reaction contributions for $N_2(A)$. The impact excitation reactions (R44, R46 and R50) dominate early timescales, with the magnitude of their contribution simply a reflection of the interaction cross sections for different A-state vibrational levels. As time progresses, dissociative recombination of N_4^+ cluster ions (R7) and then quenching of $N_2(B)$ (R25), both tuned reactions, dominate the generation of $N_2(A)$. Another set of tuned reactions, energy pooling into $N_2(B)$ (R5) and then quenching by atomic nitrogen (R24), drive the depletion of $N_2(A)$. Pooling of $N_2(A)$ into $N_2(C)$ (R6) is small, $\leq 4.8 \,\%$, while quenching of N(A) by N_2 (R23) is practically negligible, $< 0.1 \,\%$, for its tuned rate coefficient.

Finally, observe the coupling among the $N_2(A)$, $N_2(B)$ and $N_2(C)$ populations in Figure 2.6 due to the energy pooling and cascade reactions discussed in Section 2.3.5.

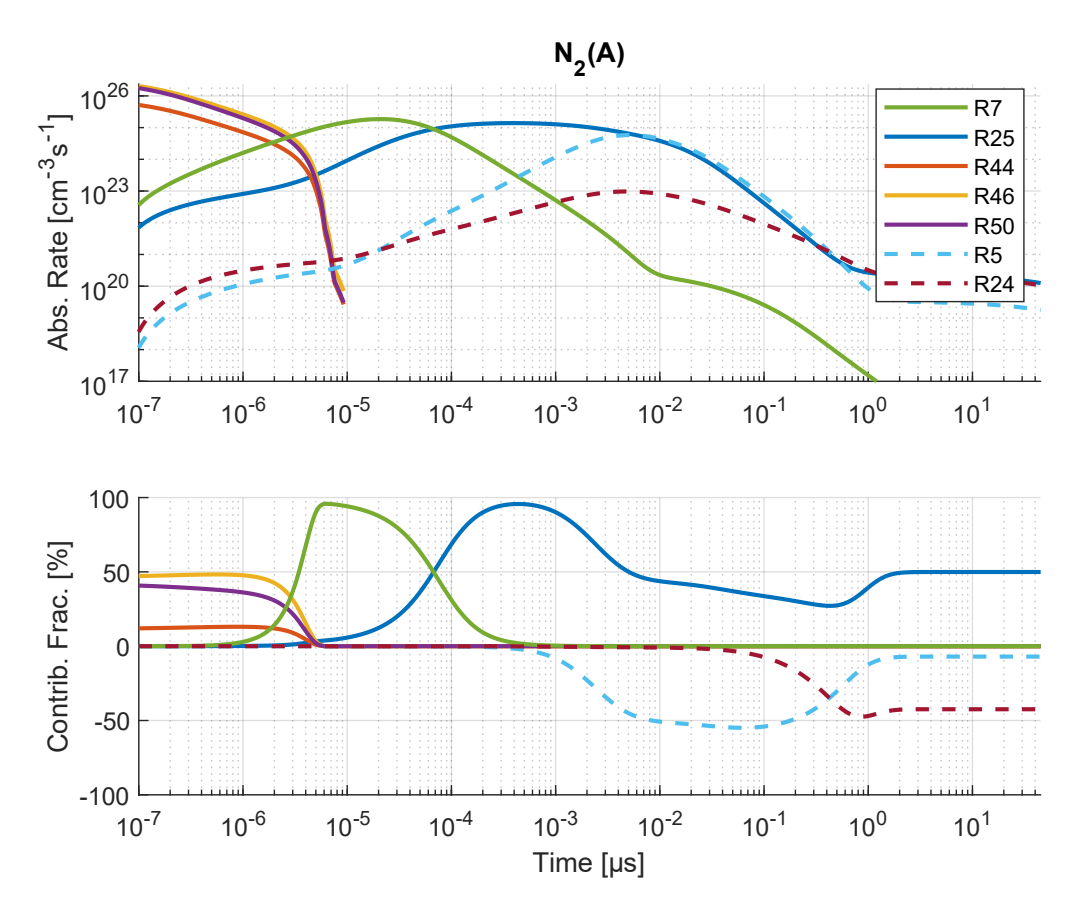


Figure 2.10: Production (solid lines) and consumption (dashed lines) reactions for $N_2(A)$. See caption in Figure 2.7 for details.

The presence of these energy pooling reactions, as opposed to their absence, ¹³ greatly enhances the lifetime of $N_2(C)$ for $t \gtrsim 1 \,\mu s$.

2.4.2 Ionization and Dissociation Fraction at Atmospheric Conditions

The initial ionization fraction was $\chi_{\rm e}(t_0) = \frac{n_{\rm e}(t_0)}{n_{\rm N_2}(0) + n_{\rm e}(t_0)} \approx 0.29\,\%$. The peak dissociation fraction was $\alpha_{\rm diss,max} = {\rm max}\left(\frac{n_{\rm N}(t)}{n_{\rm N}(t) + 2n_{\rm N_2}(t)}\right) \approx 0.11\,\%$ and occurred around $t \approx 0.05\,\mu{\rm s}$, although this fraction remained relatively constant ($\pm 2\,\%$ of its peak) between $t \gtrsim 1 \times 10^{-4}\,\mu{\rm s}$ and $t \lesssim 1\,\mu{\rm s}$. Furthermore, this fraction is substantially lower

 $^{^{13}}$ With energy pooling disabled, the N₂(A) and N₂(B) curves look approximately like their counterparts in Figure 2.6, but the N₂(C) curve loses its 'knee' around $t\approx 2\,\mu s$ and instead maintains its rapid descent to eventual zero population.

than $\alpha_{\rm diss,max}=38$ –46% measured by Limbach et al. [74] with Rayleigh scattering polarimetry. That experiment relied on a shorter focal length lens, $f_{\rm L}=0.175\,\rm m$, and a shorter duration laser pulse, $\Delta t_{\rm L}=50\times 10^{-15}\,\rm s$, which increased the geometric focusing intensity approximately 2.6–6.4 times. Multiplying the clamped intensity ($I_{\rm L}\approx 6.5\times 10^{17}\,\rm W\,m^{-2}$) by this factor of 2.6–6.4 and then substituting it into Equation (2.21) produces $\chi_{\rm e}(t_0)\approx 42$ –100%. This result perhaps explains the considerably larger dissociation fraction (via dissociative recombination of electrons and ions), but neglects plasma defocusing which would act to limit the laser intensity and prevent it from significantly exceeding its clamped value. Therefore, the reason for the discrepancy remains unresolved.

2.4.3 Temperature Evolution and Contributing Processes at Atmospheric Conditions

Figure 2.11 shows the translational $(T_{\rm g})$, vibrational $(T_{\rm v})$ and electronic $(T_{\rm e})$ temperatures in time for nitrogen at atmospheric conditions.

Fast gas heating (described in Section 2.2.3) provided the bulk of the energy imparted to the translational mode in the model. The absolute rate of translational fast gas heating ($Q_{\rm tr}$) monotonically decreased in time (as did heating by elastic collisions, R41) except between $4 \times 10^{-4} \, \mu s \lesssim t \lesssim 0.05 \, \mu s$. Over this interval, instead of decreasing, the rate of fast gas heating increased up to 15 fold, causing the inflection in the curve of $T_{\rm g}$ that began around $t \approx 3 \times 10^{-3} \, \mu s$.

Impact excitation of vibrational modes (R42) primarily drove the growth of $T_{\rm v}$ until around $t \approx 3 \times 10^{-4} \,\mu{\rm s}$ when vibrational fast gas heating $(Q_{\rm v})$ overtook it to become the dominant contributor. Similar to fast gas heating for translation, the absolute rate for vibration monotonically decreased in time (as did R42) except over the interval $3 \times 10^{-6} \,\mu{\rm s} \lesssim t \lesssim 0.03 \,\mu{\rm s}$ in which it experienced up to a 22 fold increase, producing the inflection in the curve of $T_{\rm v}$ that began around $t \approx 3 \times 10^{-4} \,\mu{\rm s}$.

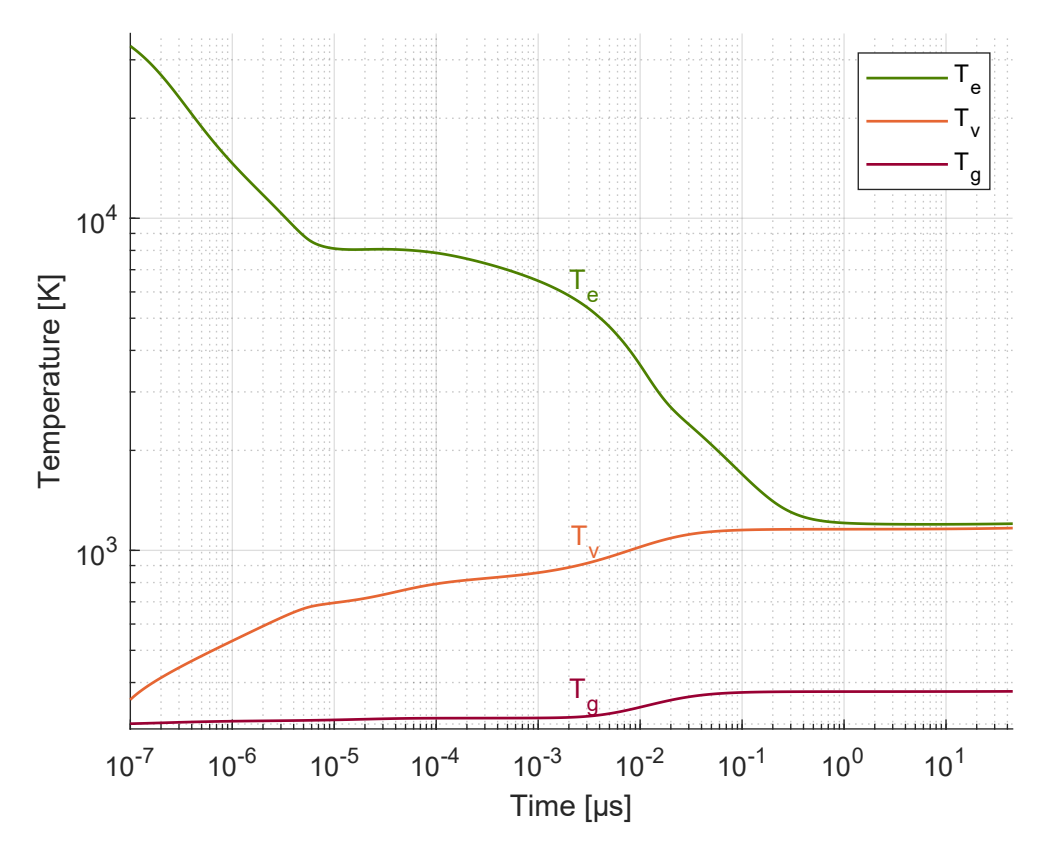


Figure 2.11: Translational (T_g) , vibrational (T_v) and electronic (T_e) temperature in the simulation for nitrogen at 300 K and 101.3 × 10³ Pa. Note $T_g(t_0) = T_v(t_0) = 300$ K (not shown).

Although fast gas heating dominated the rate contributions for both $T_{\rm g}$ and $T_{\rm v}$ at later times, the absolute value of the rate diminished over time by many orders of magnitude. The severely weakened rate could only effect a marginal increase in temperature, explaining the apparent plateau for $t \gtrsim 0.2\,\mu \rm s$.

 $T_{\rm e}$ monotonically decreases in time generally much faster than the other temperatures increase. In such a situation, characteristic of a decaying plasma, the electron kinetic energy losses equal or exceed gains. Figure 2.12 depicts this condition in a set of plots constructed similarly to those previously shown except with absolute rates in units of $K s^{-1}$. The figure shows impact dissociation (R40) leading the loss terms at early times, followed by impact excitation of vibrational modes (R42), and then, to a lesser extent, elastic collisions (R41). The (absolute) contribution fraction from

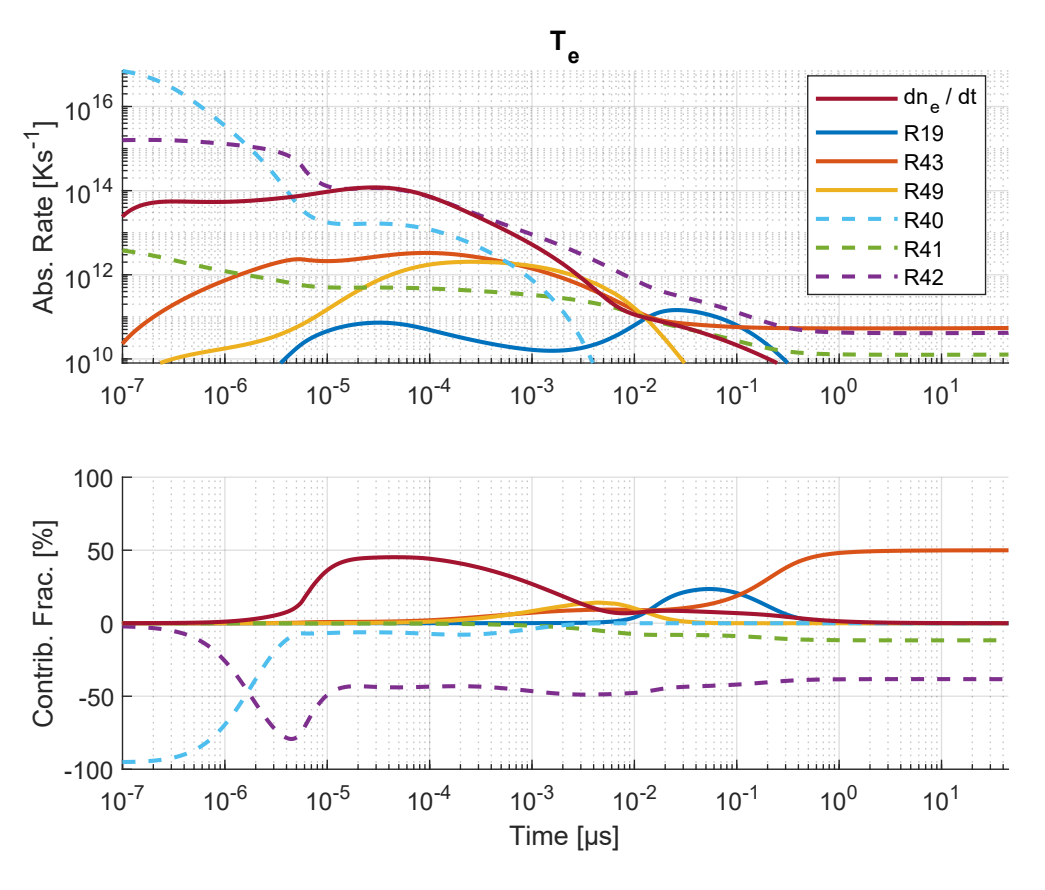


Figure 2.12: Processes contributing to the rise (solid lines) and fall (dashed lines) of $T_{\rm e}$ in time with their absolute rates (upper) and contribution fractions (lower). Only processes with a relative contribution of at least 10 % are presented.

R42 remains between about 38–49% after $t \gtrsim 1 \times 10^{-5} \,\mu\text{s}$. The kinetic energy released by electrons recombining with ions (denoted by dn_e/dt) acts to counter the loss terms. Furthermore, vibrational superelastic collisions (R43) balance the losses at later times, slowing the decay of $T_e(t)$ and causing it to track the value of $T_v(t)$. Three-body electron-ion recombination (R19), which releases U_{N^+} , and electronic superelastic collisions (R49) also slow the fall of T_e , but to a much lesser extent.

2.4.4 Estimate for Maximum Gas Temperature Rise

An estimate of the maximum rise in translational temperature from complete thermalization of the laser energy imparted during above-threshold ionization is given by

$$\Delta T_{\rm g} \approx \frac{n_{\rm e}(t_0) \left(\frac{3}{2} k_{\rm B} T_{\rm e}(t_0) + U_{\rm N_2}^{+}\right)}{n_{\rm N_2}(0) c_p} \approx 197 \,\rm K,$$
 (2.34)

with initial conditions from Section 2.2.4 and nitrogen's specific heat at constant pressure, $c_p = \frac{7}{2}k_{\rm B}~{\rm J\,K^{-1}}$. This value agrees with $\Delta T_{\rm g} \approx 120\text{--}230\,{\rm K}$ found by Edwards et al. [3] based on fitting a theoretical spectrum (with an elevated rotational temperature) to the observed spectrum of the second positive system. Such an agreement indicates that the model's values for $n_{\rm e}(t_0)$ and $T_{\rm e}(t_0)$ are likely within an order of magnitude of their experimental value. Note that each additional photon of the prototypical above-threshold process increases the temperature rise by roughly 15 K.

2.4.5 Initial Electronic Temperature Based on Above Atmospheric Density Experimental Results

Using an image intensifier lens-coupled to a camera, Burns et al. [5] observed a linear relationship¹⁴ between FLEET initial signal and gas density, $S(t_1) \propto n_{\rm N_2}(0)$, in nitrogen for $t_1 \approx 0.07$ –0.08 µs and $\frac{n_{\rm N_2}(0)}{n_{\rm STP}} \approx 1$ –5.5. For the model to produce a comparable trend over similar densities and time delays, an increased initial electronic temperature (i.e., $N_{\rm ph,add} > 0$) was required.

As $n_{\rm N_2}(0)$ is increased within the model, the species curves shift earlier in time (due to overall quickening of reactions) and higher in population (due to greater initial densities) relative to the depiction in Figure 2.6. Additionally, the 'knees' of $N_2(A)$, $N_2(B)$ and $N_2(C)$, which occur around $t \approx 0.8$ –2 μ s in Figure 2.6, shift earlier and higher as well. As $T_{\rm e}(t_0)$ is increased within the model, the initial growth of $N_2(A)$, $N_2(B)$ and $N_2(C)$ prior to $1 \times 10^{-7} \,\mu$ s is accelerated (due to expedited electron impact reactions) and the dissociation of nitrogen is more complete, yielding a greater 'steady-state' concentration of N. The elevated level of N encourages more

 $[\]overline{^{14}\mathrm{We~assume~the~relationship~holds}}$ for constant temperature (300 K) and variable pressure.

vigorous atomic recombination, shifting the 'knees' in the decay curves of $N_2(A)$, $N_2(B)$ and $N_2(C)$ to earlier times and larger populations. Recall the ability of atomic recombination to enhance not only the lifetime of the B-state, but also the A-state (via quenching of B-state) and the C-state (via energy pooling of A-state). Importantly, when combined with density changes, increasing the initial electronic temperature magnifies the curve shifts (and shifts of the 'knees') caused by increased density.

The time and population at which these 'knees' occur dictates the signal measured by the gated intensifier. Figure 2.13 attempts to illustrate this point. If the intensifier's integration period, $\Delta t_{\rm gate}$, occurs over the steeper part of the curve ahead of the 'knee,' any shifting of the curve earlier in time because of density increases will lead to a lower recorded signal (Figure 2.13, left) and thus an inverse trend. In contrast, when the integration period is taken over the flatter part of the curve after the 'knee,' whose value of population increases with density increases, a higher recorded signal results (Figure 2.13, right). In this way, a higher $T_{\rm e}(t_0)$ can shift the location of the 'knee' to a more favorable time with respect to the integration period (or delay, t_1), causing the recorded signal to increase with increasing density.

In the model, $T_{\rm e}(t_0)$ was set by incrementally increasing the value of $N_{\rm ph,add}$ in Equation (2.20) until the signal exhibited an approximately linear relationship with density over the range $\frac{n_{\rm N_2}(0)}{n_{\rm STP}} \approx 1\text{--}5.5$ for a delay $t_1 \approx 0.4\,\mu{\rm s}$ and an assumed gate width $\Delta t_{\rm gate} = 1\,\mu{\rm s}$. Although further increments to $N_{\rm ph,add}$ enabled the model to better replicate the linear dependence as time delays approached those in the experiment ($t_1 \approx 0.07\text{--}0.08\,\mu{\rm s}$), there was concern that the number of additional photons, and thus, the initial electronic temperature, was unrealistically high. Therefore, a compromise of $N_{\rm ph,add} = 2$ was used. Measurements of electron temperature (e.g., Thomson scattering) are needed to validate this choice for $N_{\rm ph,add}$.

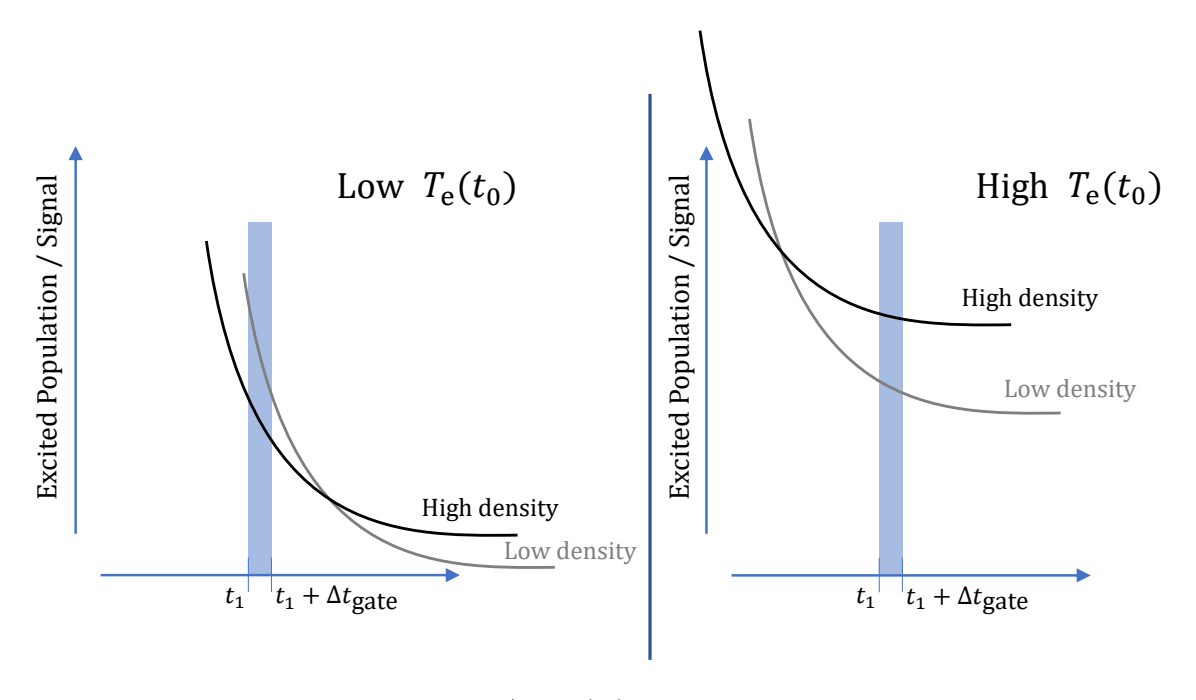


Figure 2.13: Increasing density and/or $T_{\rm e}(t_0)$ shifts the 'knee' of the curve in time and magnitude, affecting the recorded signal. For a given t_1 and $\Delta t_{\rm gate}$, at low $T_{\rm e}(t_0)$, the low density curve will record a greater signal (left), but at high $T_{\rm e}(t_0)$, the opposite prevails (right).

2.4.6 Comparison to Below Atmospheric Density Experimental Results

Consult Chapter 3 for a comparison of the model to experimental results for initial signal intensity (Section 3.4.3) and signal lifetime (Section 3.4.4) at sub-atmospheric densities (i.e., low pressures and temperatures).

2.5 Summary and Conclusions

We proposed a zero-dimensional kinetics model of FLEET in nitrogen with fast gas heating, tuned rate coefficients, electron scattering (elastic and inelastic) from BOL-SIG+ and photoionization based on filamentation. The model is summarily described by

fs laser
$$\to n_{\rm N_2^+} + n_{\rm e} + n_{\rm N_2} \to {\rm reactions} \to n_{\rm N_2(B)} + n_{\rm N_2(C)} + \cdots$$
 (2.35)

At the outset of the simulation, we consider only N_2^+ , e^- and N_2 , excluding other species such as atoms (from photodissociation), electronically-excited cations (such as those responsible for first negative emission) or multiply-ionized cations. The plasma and chemical reactions ultimately produce sizable populations of $N_2(B)$ and $N_2(C)$, giving rise to observable visible (to near infrared) and ultraviolet signal, respectively. According to time-resolved measurements using a bandpass-filtered photomultiplier tube (tempered by FLEET spectral measurements), the ultraviolet signal initially dominates until overtaken by the visible signal around $t \approx 2-3\,\mu s$. We developed equations to accurately relate the model (which consolidates the emission into two ideal bands) to the experimental measurements (made with a PMT and spectrometer).

At atmospheric conditions, the time-varying signals of the model compare favorably to those from the PMT in terms of absolute magnitude, ratio of VIS to UV and general behavior (fast and slow decay regimes). Regrettably, the model exhibits a noticeably faster decay rate, departing from the experimental results within the first several hundred nanoseconds. This departure limits the applicability of modeling results to the microsecond timescale. We attribute the disagreement to the neglect of fluid dynamics (e.g., gas expansion) and lack of spatial dimensions (e.g., no molecular or ambipolar diffusion) which concentrate all mass into a point and artificially accelerate the reaction rates. Moreover, the energy balance, intended for tracking the swift decay of electronic temperature, only approximately resolves the translational and vibrational temperature evolution. Accurate awareness of translational temperature becomes necessary when considering fluid dynamic effects driven by heating (at the later timescales).

The simplicity of the model and its response to changes in rate coefficients affords an opportunity to accurately determine (via tuning) poorly known rate coefficients such as dissociative electron-cluster ion recombination, A- and B-state quenching, and A-state energy pooling. We tune the model to fit the time-resolved PMT measurements at atmospheric conditions, but constrain our tuning to the rate coefficient ranges reported in literature. Given that our effort represents a first attempt at tuning, we emphasize the need for additional refinement and validation of the tuned values.

The electronically-excited states exhibit an interdependence or coupling in time within the model. This coupling arises from the decay cascade of $N_2(C)$ into $N_2(B)$ and then into $N_2(A)$, primarily from collisional quenching, but also from fluorescence (second positive) at the lowest gas densities. Energy pooling by $N_2(A)$ which repopulates $N_2(B)$ and $N_2(C)$ also contributes to the coupling. At long times, these excited species establish a quasi-equilibrium (evident in the figures by their slowed decay) because recombination of N into $N_2(B)$ counteracts the losses sustained by quenching of $N_2(A)$ into N_2 . The quasi-equilibrium persists as long as sufficient N population exists.

At atmospheric densities and above, increases to the initial electronic temperature shift the 'knees' in the curves (i.e., quasi-equilibrium) of the excited-state populations earlier in time and larger in magnitude. Higher $T_{\rm e}(t_0)$ yields more complete dissociation of N₂ which naturally accelerates the rate of atomic recombination. More vigorous atomic recombination, combined with the coupling of the excited-state populations, drives the shifts of the 'knees.'

The model outputs the contribution fraction of the consumption and generation reactions for each of the tracked species (showing figures for the species important to FLEET signal). At atmospheric conditions, electron-containing reactions dominate the earliest timescales (where impact processes lead recombination with ions), followed by quenching, energy pooling and finally, atomic recombination. Changes in initial gas density affect the contribution fractions. In general, decreasing gas density elongates the duration of early reactions and delays the start of later reactions.

Currently, the only comparisons to experiment are based on the first and second positive emissions; however, we desire additional experimental validation of the model. Microwave scattering [89] could measure the instantaneous number density of electrons at different initial conditions to validate the photoionization model (probing its gas density dependence) and the overall recombination rate of electrons. Laser Thomson scattering would enable measurement of the initial electronic temperature and its decay in time (to validate the model's electron energy balance). Accurate relative measurements (within about ten percent¹⁵) would prove more valuable than absolute measurements for characterizing the behavior of these electronic parameters with varying initial conditions (e.g., gas pressure) or time. Laser absorption (or laser-induced fluorescence) could monitor the population of metastable N₂(A) to justify its size and the rate coefficients of energy pooling (which contribute to the coupling of the excited molecules). In the nanosecond and later timescales, the Astate population decays from roughly $3 \times 10^{16} \, \mathrm{cm}^{-3}$ to $6 \times 10^{13} \, \mathrm{cm}^{-3}$. Since energy pooling is an important gain mechanism for the B-state and especially C-state population at these timescales, it would be beneficial to measure the absolute size of the A-state population to within several tens of percent¹⁵ (at least while it is above the detection threshold). We would like to test (or refine) the monolithic assumption for the spectral bands within the time-varying signal. Therefore, we require better spectrally- and time-resolved measurements, such as from a photomultiplier tube with a monochromator to isolate individual rovibrational features (instead of entire bands) and ensure proper extinction of unwanted wavelengths. 16 These measurements would initially be taken at atmospheric conditions and then extended to other pressures (and temperatures).

¹⁵Based on cursory sensitivity analysis at atmospheric conditions.

 $^{^{16}}$ Such an effort would take care to eliminate contamination from second-order diffraction and laser light.

Chapter 3

Signal, Lifetime, Accuracy and Precision in Low Temperatures and Pressures

Note that much of this chapter (text, tables and figures) is adapted from Reference [90].

3.1 Background and Motivation

The significant gas dynamic expansion employed to accelerate flows to supersonic and hypersonic speeds often results in low temperatures and pressures.¹ Additionally, the desire to simulate flight conditions at high altitudes ($\gtrsim 30\,\mathrm{km}$) drives supersonic and hypersonic wind tunnel testing to reduced pressures² and/or temperatures. Furthermore, some transonic ground testing facilities³ rely on cryogenic nitrogen to dra-

¹E.g., indraft wind tunnels at Princeton University (Applied Physics Group).

²E.g., Hypervelocity Wind Tunnel 9 at Arnold Engineering Development Complex.

³E.g., 0.3-Meter Transonic Cryogenic Tunnel and National Transonic Facility at NASA Langley Research Center.

matically increase the Reynolds number⁴ to flight-accurate values. Frequently, these high-speed wind tunnels operate with pure nitrogen since it is readily liquefied (necessary for cryogenic functionality), contains little to no water vapor (to prevent fog and ice formation), is nonreactive (to reduce oxidation of tunnel components in heated plenums), and well simulates air (constituting 78% of air by volume). Therefore, it is important to experimentally characterize femtosecond laser electronic excitation tagging (FLEET) velocimetry and validate the kinetics model in nitrogen at these lower temperature and/or pressure conditions. For the experimental characterization, we evaluate four metrics of performance, namely, signal intensity, signal lifetime, velocity accuracy and velocity precision. See Appendix A for an illustration of the difference between accuracy and precision. For validation of the kinetics model, we compare the initial signal (and lifetime) results of the simulation to those of the experiment at each of the tested conditions. Moreover, we leverage the kinetics model to explain some of the experimental observations in terms of plasma-chemical reactions and pathways.

3.2 Experimental Setup

3.2.1 Variable Temperature and Pressure Flow Facility

In a free jet facility custom-built⁵ for testing laser-based diagnostics at NASA Langley Research Center, FLEET was studied in pure nitrogen ($\geq 99.995\%$) over a range of temperature (72–298 K) and pressure (0.228–101 kPa) conditions. Gas cylinders supplied high-pressure (≤ 1 MPa) flow to an axisymmetric, converging-diverging nozzle to produce a pressure-matched free jet inside a hermetically sealed and continuously evacuated chamber instrumented for optical access. A mass flow controller (Alicat

⁴Recall that decreasing the temperature of a gas decreases its dynamic viscosity, increases its density and thus increases its Reynolds number for a given velocity and characteristic length.

⁵Designed and assembled by R. A. Burns, C. J. Peters and P. M. Danehy in 2017 and later characterized by Dedic et al. [91] using hybrid fs/ps coherent anti-Stokes Raman scattering.

Scientific MCRS-1000SLPM-D-5M) regulated the stagnation pressure to control the jet's static pressure. Manual adjustment of a gate valve leading to the vacuum pump established the back pressure inside the chamber for ideal expansion of the jet. A variety of interchangeable nozzles provided the nominal Mach number (subsonic, Mach 1.0, 1.8, 2.7 or 4.0) of the flow. For near-constant stagnation temperature, the nozzle's unique expansion contour set the jet's static temperature. Figure 3.1 shows four of the five nozzles prior to the addition of compression fittings which enabled rapid replacement and installation during Mach number changes. Tight manufacturing tolerances during selective laser sintering of the nozzles ensured acceptable surface roughness. Table 3.1 lists the nominal specifications of each nozzle. NASA's IMOCND computer program [92, 93], which solved the compressible potential flow equation using the method of characteristics, aided the design of the nozzle contours.



Mach 1.0 Mach 1.8 Mach 2.7 Mach 4.0

Figure 3.1: Upstream view of the converging-diverging nozzles prior to installation. See Table 3.1 for specifications. Subsonic nozzle (i.e., straight pipe) not shown.

Table 3.1: Facility nozzle nominal specifications.

NT 1	0.1.	M 1 1 0	M 1 1 0	M. 1.07	M 1 4 0
Nozzle	Subsonic	Mach 1.0	Mach 1.8	Mach 2.7	Mach 4.0
Throat Dia. [mm]	$None^{a}$	10.00	8.34	4.20	1.65
Exit Dia. [mm]	10.00	10.00	10.00	7.50	5.40

^a Subsonic nozzle fabricated from commercially available tubing with constant inside diameter.

For each test condition, schlieren imaging provided confirmation of the absence of shockwaves and collimation of the free jet, ensuring spatially uniform conditions. Figure 3.2 depicts the free jet operating in this ideal, pressure-matched condition (left) in contrast to the non-ideal, under-expanded condition (right). High-accuracy sensors tracked the stagnation pressure in the plenum, p_0 , (Omega Engineering PX409, 250 PSIA), static pressure in the chamber, p_b , (Setra Model 730, 1000 Torr) and pitot pressure of the jet (Omega Engineering PX409, 250 PSIA). A thermocouple (T-type probe) monitored the stagnation temperature in the plenum, T_0 . Camera triggering was recorded for indexing FLEET image sequences to flow facility measurements. Commercially available hardware running at a sampling rate of 100 Hz provided data acquisition and control (National Instruments Ethernet chassis cDAQ-9184 with modules NI-9214 for thermocouple input, NI-9220 for analog input and NI-9264 for analog output) while custom software written in MATLAB processed the acquired data (with live plotting and calculations to facilitate data collection) and set the mass flow rate.

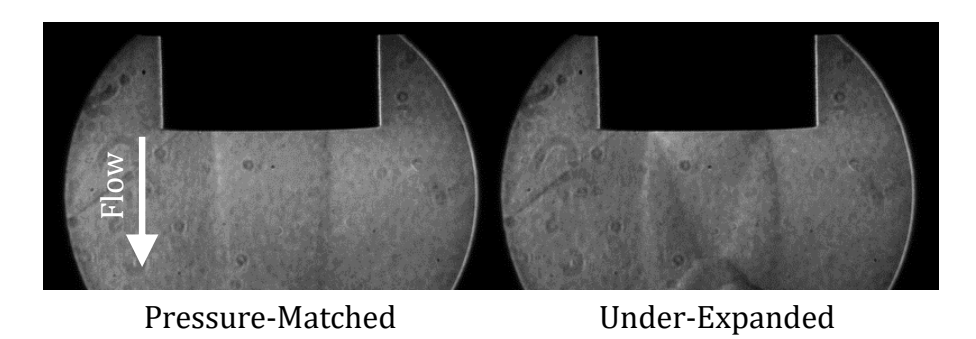


Figure 3.2: Typical schlieren images of the free jet comparing pressure-matched operation (left) used in experiments to under-expanded operation (right). Mach 1.0 test shown.

We computed the Mach number, M, of the free jet using the (compressible) isentropic flow relations [94] and the ratio of static pressure in the chamber to stagnation pressure in the plenum,

$$M = \sqrt{\frac{2}{\gamma - 1} \left(\left(\frac{p_{\rm b}}{p_0} \right)^{\frac{1}{\gamma} - 1} - 1 \right)},\tag{3.1}$$

where $\gamma = 1.4$ denotes the ratio of specific heats for nitrogen. Ideal expansion (confirmed by schlieren) implied that the static pressure inside of the free jet matched that of the chamber, $p = p_{\rm b}$. The resulting Mach numbers were verified using the normal shock relations⁶ and the ratio of pitot pressure to stagnation pressure in the plenum. Over the tested pressure range, the pressure sensor for the chamber had superior accuracy to that for the pitot probe; therefore, in calculations, we used the Mach number based on the ratio of chamber pressure to stagnation pressure. After determination of Mach number, the isentropic flow relations [94] and ideal gas law yielded the remaining static properties (temperature, T, and density, ρ) within the free jet,

$$T = T_0 \left(1 + \frac{\gamma - 1}{2} M^2 \right)^{-1}, \tag{3.2}$$

$$\rho = \frac{p}{R_{\rm N_2}T},\tag{3.3}$$

with the individual gas constant for nitrogen, $R_{\rm N_2} \approx 296.80\,\mathrm{J\,kg^{-1}\,K^{-1}}$. Note that T and ρ , or equivalently, T(0) and $\rho(0)$, corresponded to the initial conditions of the gas at the beginning of the femtosecond laser pulse (or outset of the kinetics simulation described in Chapter 2). The effective velocity of the free jet (used to evaluate the accuracy of FLEET) was then

$$v_{\rm DAQ} = M\sqrt{\gamma R_{\rm N_2} T}.$$
 (3.4)

Figure 3.3 shows the temperatures (circles, left) and densities (circles, right) measured by the flow facility data acquisition (DAQ) system. The nominal temperatures (dotted lines) were given by Equation (3.2) with M from the nominal, i.e., design, Mach number and $T_0 = 300 \,\mathrm{K}$. For each Mach (nozzle) setting, the pressures p_0

⁶We assumed that a normal shock reasonably characterized the bow shock of the pitot probe in supersonic flow and its associated stagnation pressure losses.

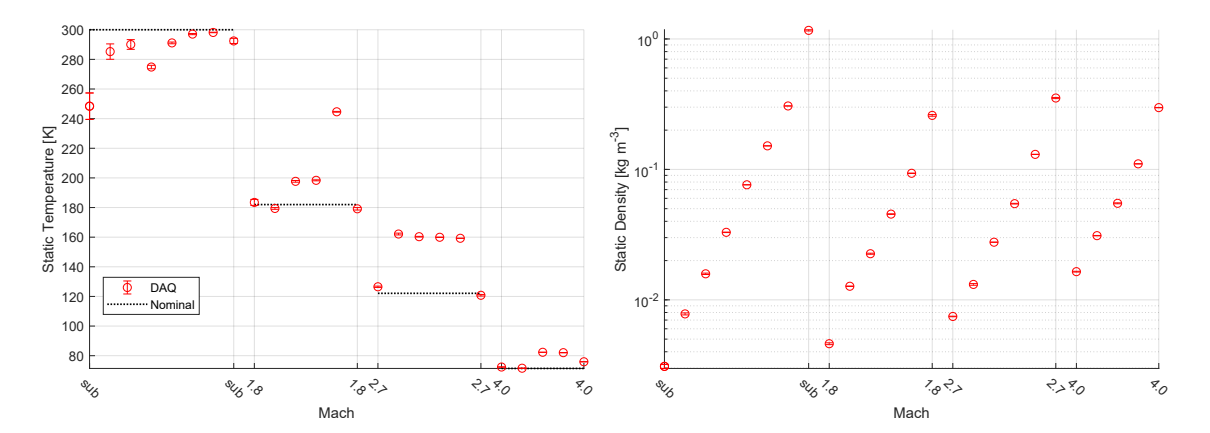


Figure 3.3: All 25 flow facility test conditions for different Mach and pressure settings. Markers and error bars denote mean and standard deviation, respectively, based on over 1300 measurements.

and p_b were incrementally increased to raise the density. Although Figure 3.3 (left) portrays seemingly large discrepancies between the DAQ (measured) and nominal (predicted) temperatures for Mach 1.8 and 2.7 (probably because of incorrect pressure ratio settings, p_b/p_0 , for the desired Mach number), the actual DAQ and FLEET velocity measurements show good agreement (see Figures 3.15 and 3.17 in the following sections).

3.2.2 Intensified Camera

A fast-framing camera (Photron FASTCAM Mini AX200 CMOS, 20 μ m pixels, 100 kHz rate) lens-coupled to a two-stage image intensifier (LaVision HighSpeed IRO S25) recorded the FLEET signal using a gate width of $\Delta t_{\rm gate} = 0.5 \,\mu$ s and time delays of 0.1, 0.2, 0.5, 1.0, 2.0, 5.0, 10.1, 20.1 and 30.1 μ s (respectively corresponding to t_1, t_2, \ldots, t_9 in Figure 3.4). For early delays, $t \leq 1 \,\mu$ s, the gate width was excessive relative to the decay rate (which is very rapid at early timescales), leading to longer lifetime estimates than would be obtained from the instantaneous signal curve (based

⁷The appropriate gate width is short enough to make the decay curve appear effectively flat within the gate window (i.e., any increase in gate duration linearly increases the integrated signal), but long enough to maintain adequate signal-to-noise ratio.

on subsequent photomultiplier tube measurements at atmospheric conditions). Maintaining a constant gate width was intended to ensure more consistent comparison across delays (acquired in separate burst series) and avoid introduction of an extra experimental parameter.

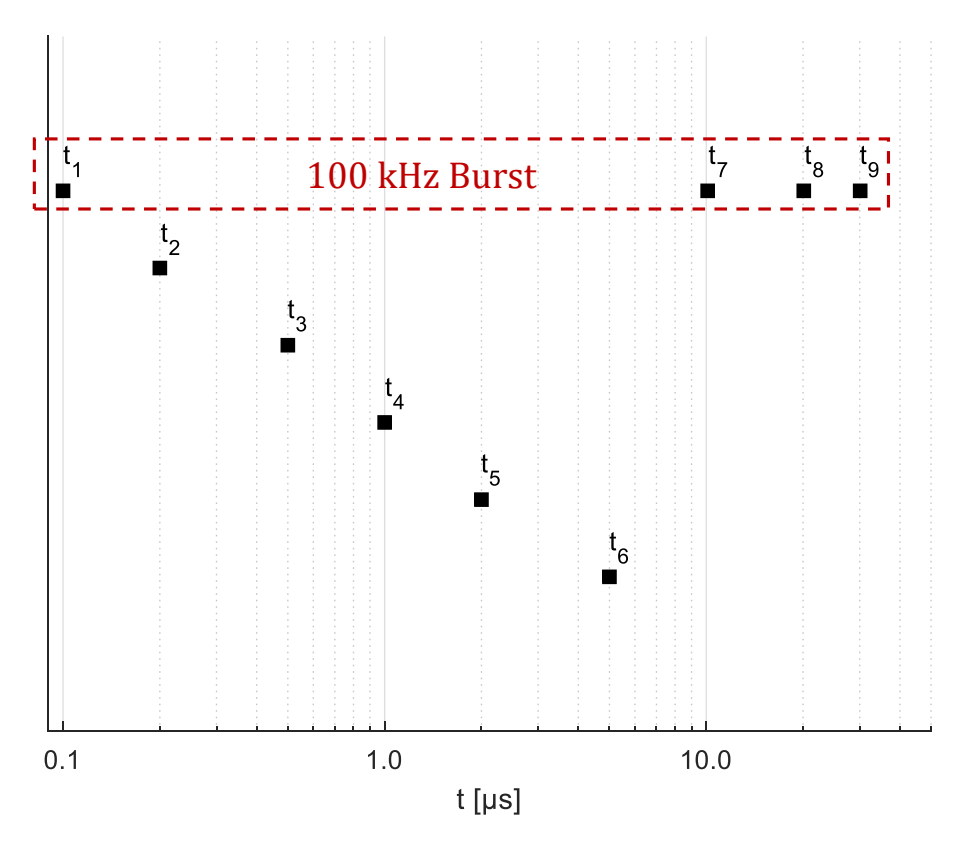


Figure 3.4: Timing diagram for intensified camera with delays of 0.1, 0.2, 0.5, 1.0, 2.0, 5.0, 10.1, 20.1 and 30.1 μ s after laser pulse. t_1 , t_7 , t_8 and t_9 come from same framing burst while t_2 through t_6 correspond to separate acquisitions.

A bandpass filter (Semrock custom, 385–771 nm) was placed in front of the intensifier's objective lens (Nikon Nikkor 135 mm f/2). Figure 3.5 shows the filter's transmission function, $T_{\rm BP}(\lambda)$, which passes both the visible (VIS), $\Delta\lambda_{\rm VIS}=498–895$ nm, and ultraviolet (UV), $\Delta\lambda_{\rm UV}=332–493$ nm, spectral bands⁸ of FLEET and thus mixes these two signal components. Based on the objective lens' diameter of $D_{\rm col}=67.5\times10^{-3}$ m and an offset distance from the tagged region of ap-

⁸Although the spectral components of the 'ultraviolet' and 'visible' signal respectively span the near-ultraviolet to blue and yellow to near-infrared, for brevity, they will be referred to simply as the ultraviolet and visible.

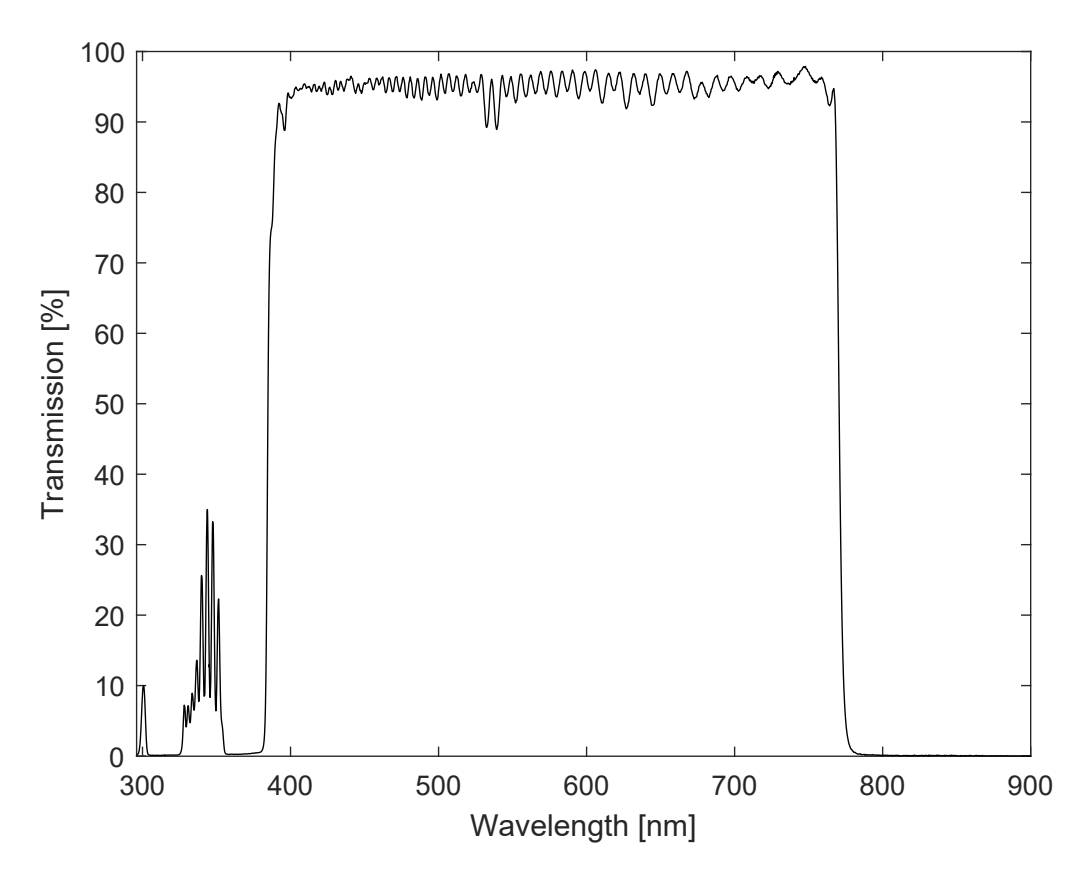


Figure 3.5: Measured spectral transmission function, $T_{\rm BP}(\lambda)$, of bandpass filter for image intensifier. Note passage of UV in addition to visible. Data from P. M. Danehy.

proximately $L_{\rm col} \approx 0.56$ m, we estimated a light cone collection efficiency of roughly $\eta_{\rm col} = \frac{1}{2} - \frac{L_{\rm col}}{2\sqrt{L_{\rm col}^2 + D_{\rm col}^2/4}} \approx 0.09\%$.

3.2.3 Nominal Laser Parameters

We operated the regeneratively-amplified Ti:sapphire laser (Spectra-Physics Solstice) at a repetition rate of 1000 Hz, a central wavelength of $\lambda_{\rm L}=800\times10^{-9}\,{\rm m}$ and a pulse energy of $U_{\rm L}\approx0.9\times10^{-3}\,{\rm J}$. For a beam with an assumed diameter $(1/e^2)$ of $D_{\rm L}=7\times10^{-3}\,{\rm m}$ focused by a lens of focal length $f_{\rm L}=0.25\,{\rm m}$, geometric optics dictated a beam waist radius $(1/e^2)$ of $w_0=2\frac{\lambda_{\rm L}}{\pi}\frac{f_{\rm L}}{D_{\rm L}}\approx18\times10^{-6}\,{\rm m}$ and a Rayleigh range of $z_{\rm R}=\pi\frac{w_0^2}{\lambda_{\rm L}}\approx1.3\times10^{-3}\,{\rm m}$. From the perspective of the kinetics model described in Chapter 2, these laser parameters were essentially equivalent to previous experiments

(Section 2.2.4) because photoionization remained within the tunneling regime (small Keldysh parameter, $\gamma_{\rm K} \approx 0.24 < 0.5$, see Section 2.2.4) and the assumption of intensity clamping fixed the laser intensity and thus electron yield. For this focal length, the approximate tagged volume equaled $vol_{\rm tag} = 1 \times 10^6 \pi w_0^2 b \approx 2.7 \times 10^{-6} \, {\rm cm}^3$, where the confocal parameter was $b = 2z_{\rm R}$. The laser beam was oriented radially through the center of the jet to write FLEET lines in the core flow just below nozzle exit in Figure 3.2 (left).

3.3 Image Acquisition and Processing

Over 6600 single-shot measurements were taken at each time delay for every temperature and pressure (density) combination. Each laser shot corresponded to a seven-frame burst of the imaging system. Three frames preceded the laser pulse, clearing the camera sensor of accumulation and ghosting artifacts [11], and providing a suitable background image for subtraction.⁹ Four data frames followed the laser pulse, capturing the FLEET signal at the desired delay and additional offsets. Since time delays t_1 through t_6 (i.e., $0.1-5.0\,\mu s$) corresponded to separate, independent acquisitions, signal analysis relied upon aggregate statistics rather than single-shot values. Note that latter delays t_7 through t_9 (i.e., $10.1-30.1\,\mu s$) actually came from the same framing burst as t_1 (see Figure 3.4 for details).

The resulting images were minimally dewarped¹⁰ based on a dot-card calibration. Figure 3.6 (left) shows a typical dewarped image from the highest signal-to-noise ratio (SNR) data set at $72 \, \text{K}$, $1.6 \times 10^{-2} \, \text{kg m}^{-3}$ and $0.1 \, \mu \text{s}$ delay. The x-axis and y-axis corresponded to the laser beam and advection directions, respectively, with the flow from left to right. Note a scale of $78.0 \times 10^{-6} \, \text{m px}^{-1}$ and that the radial width along the y-axis of the tagged region at this delay is tens of times larger than the exciting

⁹The camera's built-in shading (black level) correction made additional background subtraction unnecessary.

¹⁰Using an algorithm developed by R. A. Burns.

laser's beam waist radius ($w_0 \approx 18 \times 10^{-6}$ m, calculated previously in Section 3.2.3). The rapid diffusion of atomic nitrogen and perhaps even the gas dynamic expansion associated with energy deposition [75] are thought to explain this widening of the tagged region. Appendix B discusses the effect of mass diffusivity and how width (based on Gaussian fits) changes in response to static conditions.

The tagged region (line) in each image was initially identified by finding all pixels (red circles in Figure 3.6, right) that contained signal two standard deviations¹¹ above the mean signal of the image. Based on the assumption of a relatively contiguous tagged region, the identified pixels were then required to lie within a certain neighborhood, specifically within three¹² median absolute deviations (MADs) from the median pixel coordinates, to eliminate inclusion of spurious data. These thresholds were empirically selected to ensure reliable identification of the line within each image. The intensity-weighted centroid (blue asterisk in Figure 3.6, right) of the tagged region was calculated from this set of signal-containing pixels. Next, the longest contiguous length of pixels along the FLEET line (x-axis) was fit with a series of transverse Gaussian profiles [11]. At each location, x, along this length, the center (indicated by green pluses in Figure 3.6, right), width and peak signal of the profile were determined according to a Gaussian least-squares fit. Figure 3.7 shows two fits from this data set at $x = 59 \,\mathrm{px}$ (left) and $x = 70 \,\mathrm{px}$ (right), with the corresponding Gaussian regions of interest (ROIs) demarcated by cyan circles in Figure 3.6 (right). The algorithm included tolerance for saturated pixels, replacing them with interpolated values from the Gaussian fit of unsaturated data (Figure 3.7, right), although the resulting width and peak signal may lack uniqueness in instances of extreme saturation. Only the

¹¹Throughout the chapter, 'standard deviation' will refer to the sample standard deviation, i.e., normalization by (n-1), where n is the number of samples.

¹²The MAD threshold was actually two, with an additional factor of 1.4826 linked to the assumed underlying normal distribution [95]. $2 \times 1.4826 \approx 3.0$. For brevity, this factor of 1.4826 will be absorbed into the MAD threshold here and elsewhere.

highest signal cases, such as the test condition shown, exhibited saturation. Therefore, the peak signal statistics in those cases may have been artificially depressed.

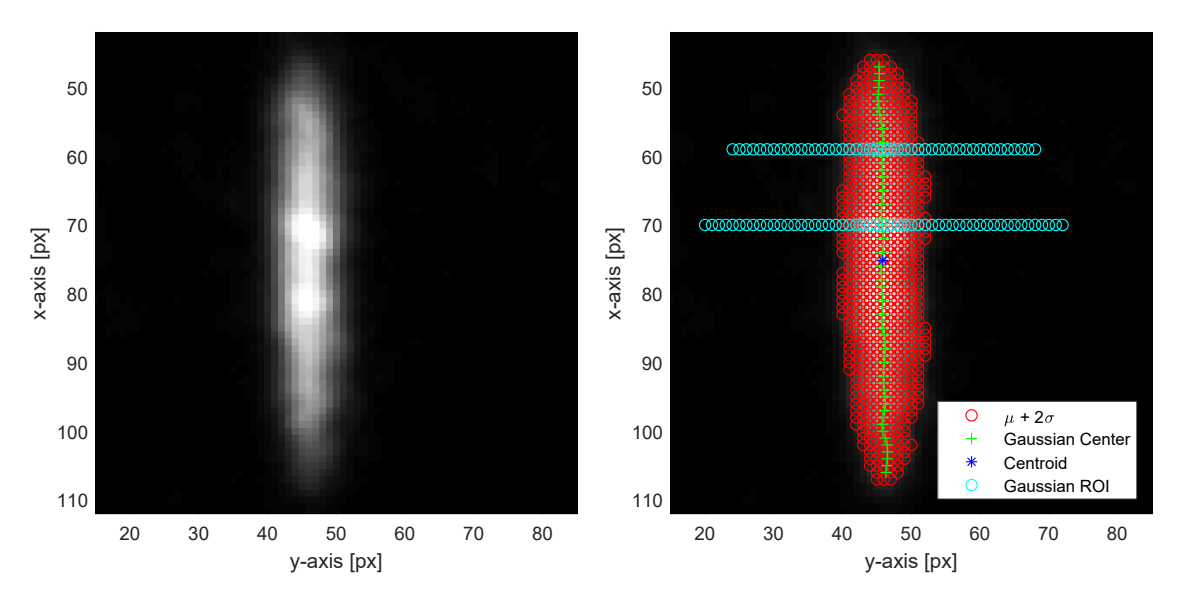


Figure 3.6: Single-shot data after dewarping (left) and processing (right) for 72 K and $1.6 \times 10^{-2} \,\mathrm{kg}\,\mathrm{m}^{-3}$ (highest SNR case) at a delay of $0.1 \,\mu\mathrm{s}$. Flow is left to right.

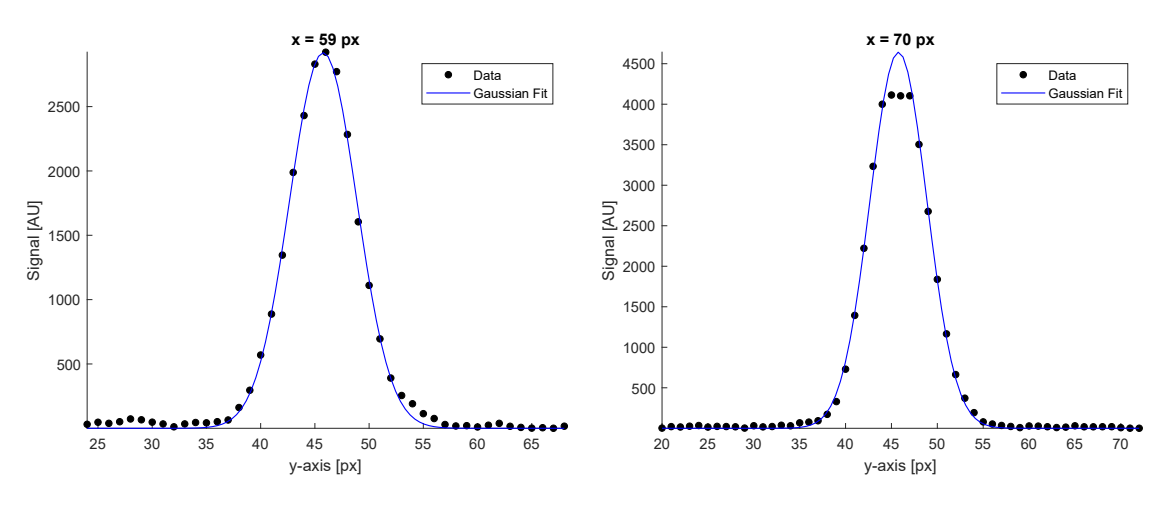


Figure 3.7: Typical Gaussian fits from high SNR case shown in Figure 3.6 with examples of unsaturated (left) and saturated (right) data. Flow is left to right.

Data pruning methods filtered the results for outliers, poor fits or otherwise unacceptable data (e.g., low SNR) using aggregate statistics at a particular delay and testing condition. On a whole-image basis, we classified images as outliers when a metric of their tagged region (e.g., red circles in Figure 3.6, right) exceeded 5.9 MADs

from the median of the metric over the entire image series (roughly 6600 single-shot images). The five considered metrics of the tagged region were its size (number of pixels), centroid (y-position) and lumped signal statistics (sum, mean and standard deviation). Once identified, these suspect images (and any Gaussian fits associated with them) were purged from further data processing. Next, we filtered the results on an individual-fit basis, classifying fits as outliers when their Gaussian peak signal exceeded 7.4 MADs from the median, Gaussian center or width exceeded 5.9 MADs from the median or coefficient of determination, R^2 , dropped below 0.95. Outlying fits were excluded from further data processing. All of the Gaussian fits in all of the images were lumped together to compute the median statistics. The filter thresholds were empirically chosen to eliminate egregious outliers that could unduly influence the mean while keeping valid data that possessed large variance. These filter thresholds were kept constant across delays and testing conditions to ensure consistent processing of the data.

For a given time delay at a testing condition, we calculated the mean and standard deviation of the tagged region metrics across the image series and the Gaussian fit parameters at each location, x, across the image series. To reduce the dimensionality of the data for an image series, we condensed the Gaussian fit results into a single, representative set of parameters. We combined (i.e., aggregated) the statistics at five central points within the free jet using

$$n = \sum_{x} n_x, \tag{3.5}$$

$$\mu = \sum_{x} \frac{n_x \mu_x}{n},\tag{3.6}$$

$$\sigma = \sqrt{\sum_{x} \frac{(n_x - 1)\sigma_x^2 + n_x(\mu_x - \mu)^2}{n - 1}}.$$
 (3.7)

In the above, n_x , μ_x and σ_x respectively represent the number of samples, mean and standard deviation of some quantity for the data subset at each point, x, while variables without a subscript denote the combined statistics for the data aggregate. We reasoned that the jet center would contain the undisturbed core flow and thus have uniform properties that adequately represented a particular testing condition. The selection of the central points was based on the mean Gaussian peak signal (as a function of x), which achieved a maximum near the radial center, clearly indicating of the core. Results were included in the overall analysis when at least three of the five points exceeded a minimum specified number of single-shot measurements ($n_x > 140$), otherwise they were excluded. The Gaussian fitting procedure was more discriminating and selective than the tagged region identification and therefore provided a more robust measure of FLEET quantities (e.g., peak signal, line center), especially at low SNR. The number of satisfactory single-shot measurements generally started around 6600 at $t_1 = 0.1 \,\mu s$ and gradually dwindled with increasing delay up to $2 \,\mu s$. Beyond 2 μs, or for certain jet conditions with short lifetimes, the decrease was more dramatic and fitting Gaussian profiles to the line or even simply distinguishing the signal from noise in the image became problematic. Thus, the number of successful Gaussian fits served as an effective indicator of SNR.

FLEET velocity measurements were based on the translation of the line (i.e., change in y-position) between two time delays, $t_i < t_j$, as determined by either the tagged region centroid or Gaussian line center. For a time interval $\Delta t = t_j - t_i$, with equal gate widths at delays t_i and t_j and corresponding position measurements y_i and y_j , the velocity in the positive y-direction was $v = \frac{y_j - y_i}{\Delta t}$. The mean and variance of velocity were then

$$\overline{v} = \frac{\overline{y}_j - \overline{y}_i}{\Delta t},\tag{3.8}$$

$$\operatorname{Var}(v) = \frac{\operatorname{Var}(y_j) + \operatorname{Var}(y_i) - 2\operatorname{Cov}(y_j, y_i)}{(\Delta t)^2}.$$
 (3.9)

Since position measurements y_i and y_j came from separate bursts, we assumed they were uncorrelated and had negligible covariance. Thus, the precision (standard deviation) of velocity simplified to

$$\sigma(v) = \frac{\sqrt{\operatorname{Var}(y_j) + \operatorname{Var}(y_i)}}{\Delta t}.$$
(3.10)

Major sources of variance included position determination (which became less precise as signal-to-noise ratio decreased) and inherent unsteadiness (fluctuations) within the flow. Note that the latter source of variance persists even for time delays and gate widths much shorter than the characteristic timescale of the flow.

Lastly, Equations (3.8) to (3.10) technically only applied to data sets of equal length, but by assuming converged statistics (i.e., sufficiently large sample sizes), we used these equations to estimate the effective mean velocity and precision.

3.4 Signal Measurement Results

3.4.1 Signal Intensity

Figure 3.8 plots FLEET signal as a function of density, temperature and time delay based on the peak value of the Gaussian fit (boxes) and the mean value of the tagged region (triangles). The markers and error bars denote the mean and standard deviation, respectively, taken over single-shot measurements¹³ for a particular condition and delay (as described in the previous section). The tagged region results very nearly replicated the Gaussian results, albeit severalfold lower in absolute magnitude since they accounted for the entire tagged region, not just the highest intensity pixels near the center. Therefore, for plotting clarity, the tagged region results

 $^{^{13}}$ The number of Gaussian measurements varied wildly, ranging from $n \approx 5 \times 6600 = 33\,000$ at early delays to $n \approx 750$ for a few points at $5\,\mu s$. On the other hand, the number of tagged region measurements generally remained around $n \approx 6600$.

were not shown beyond the initial time delay. Some results ($\rho \approx 0.03$ –0.05 kg m⁻³ and $\rho \approx 0.07$ –0.2 kg m⁻³) were excluded for $t_6 = 5 \,\mu s$ because they failed to meet the single-pixel criterion for number of Gaussian fits ($n_x < 140$) due to low SNR. In contrast, for a few conditions, a substantial extension of signal lifetime enabled measurements out to $10.1 \,\mu s$ ($0.35 \,\mathrm{kg} \,\mathrm{m}^{-3}$, $121 \,\mathrm{K}$) and out to $30.1 \,\mu s$ ($0.31 \,\mathrm{kg} \,\mathrm{m}^{-3}$, $298 \,\mathrm{K}$ and $1.16 \,\mathrm{kg} \,\mathrm{m}^{-3}$, $292 \,\mathrm{K}$). The last condition represents the atmospheric reference case. Previous results [11] have similarly demonstrated long-lived signal in pure nitrogen at atmospheric conditions.

Although we can plot FLEET signal as a function of pressure or temperature, plotting with density along the abscissa best collapses the data to reveal its true dependence on density. Burns et al. [5] observed a similar collapse for initial signal and lifetime at above atmospheric densities (albeit with different trends at these higher pressure conditions). Furthermore, like Burns et al., ¹⁴ we observed a breakdown in the density dependence for long time delays. The breakdown began around $\rho \approx 0.3 \,\mathrm{kg}\,\mathrm{m}^{-3}$ and progressed into the lower densities as time delay increased. The importance of early time delays has been noted in FLEET concentration measurements. The signal monotonically depended upon oxygen concentration (up to 21%) only at short time delays¹⁵ ($t \lesssim 1\,\mu\mathrm{s}$). In particular, contrast the nitrogen-oxygen mixture results of Halls et al. [13] at short delays with those of Zhang [16] at long delays. Therefore, unique determination of thermodynamic properties or mixture fractions via FLEET signal intensity necessitates measurement at early time delays.

According to Figure 3.8, signal intensity achieved its optimal value at reduced density. The optimal point shifted toward lower densities as time delay increased. Other experiments in nitrogen [2, 15] have similarly shown the maximum signal at

¹⁴Burns et al. acquired measurements at $t_1 = 0.07$ –0.08 μs and every 5 μs thereafter, but saw no clear trend with respect to thermodynamic variables beyond the initial time delay.

¹⁵And commensurately short gate widths.

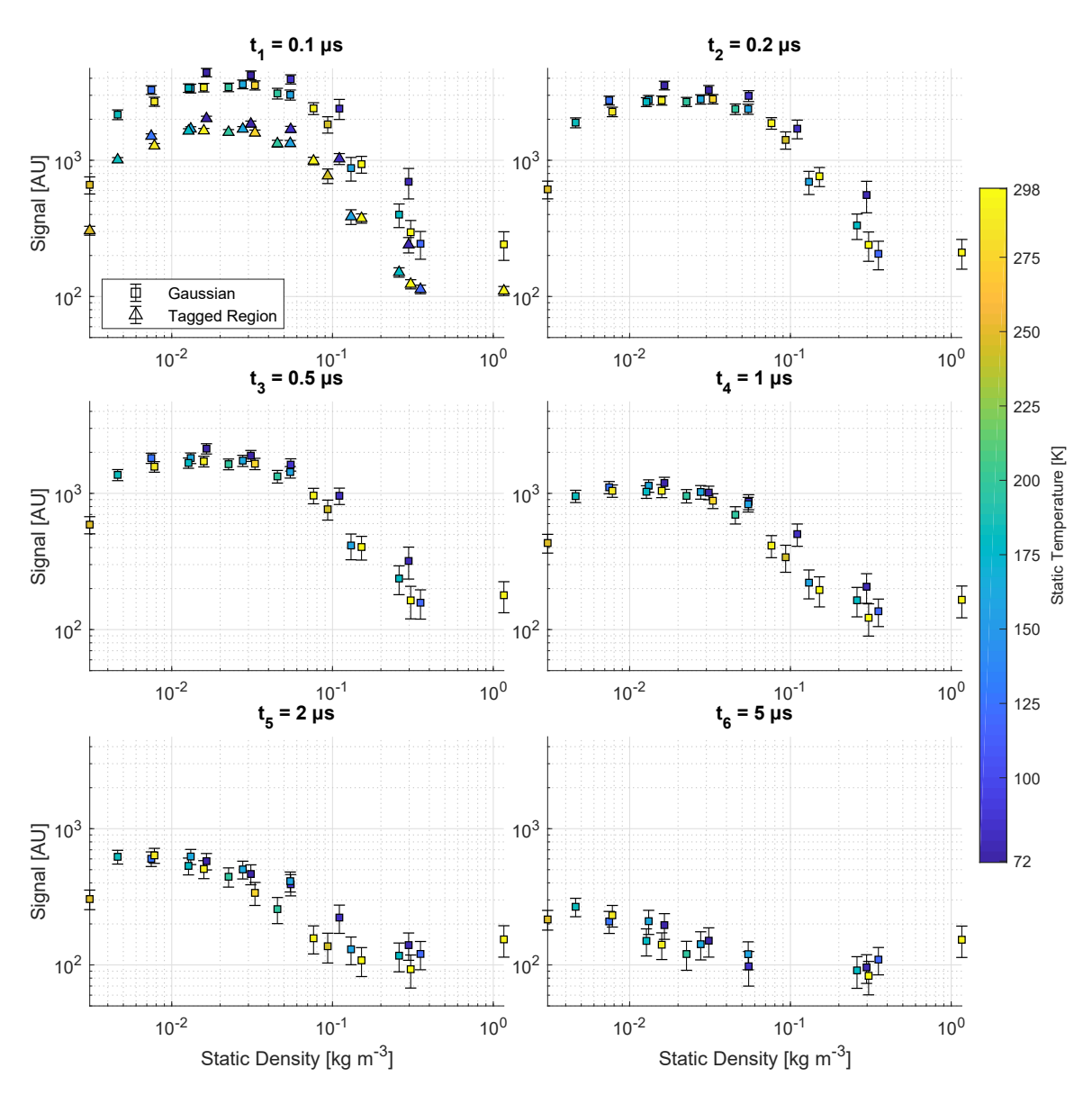


Figure 3.8: Gaussian peak signal (boxes) as a function of density, temperature and time delay ($\Delta t_{\rm gate} = 0.5 \,\mu s$). Mean signal of the tagged region (triangles) exhibited nearly identical behavior and, for clarity, is only shown for 0.1 μs . Markers and error bars denote mean and standard deviation, respectively.

short delays ($t \lesssim 2 \,\mu s$) occurring at reduced pressure (density) and exceeding the value at atmospheric conditions.

In addition to illustrating the primary dependence on density, the figure conveys the secondary dependence on temperature. However, gas temperature plays a weaker role in governing signal strength—only the coldest temperatures significantly alter the signal from the apparent curve.

Possible explanations for the above signal trends are discussed in Section 3.4.3 by comparing the experimental results to our kinetics model.

3.4.2 Considerations for Comparison to Kinetics Model

This section makes extensive use of the kinetics model developed in Chapter 2 and the theory in Sections 2.3.3 and 2.3.5 which relates it to the experimental results. See the chapter and sections for more details. Also, note that the reaction numbers come from Table 2.1.

In an approach similar to the one used to construct Equation (2.33), we relate the signal captured by the intensified camera (at some time delay t_i) to the rate of change of photon densities within the simulation,

$$S_{\text{int}}(t_{i}) = \left(\int_{t_{i}}^{t_{i}+\Delta t_{\text{gate}}} r_{\text{R3}}(t) \frac{\int QE_{\text{int}}(\lambda)T_{\text{BP}}(\lambda)r_{\text{ph}}(\lambda,t)T'_{\Delta\lambda_{\text{VIS}}}(\lambda)d\lambda}{\int r_{\text{ph}}(\lambda,t)T'_{\Delta\lambda_{\text{VIS}}}(\lambda)d\lambda} dt + \int_{t_{i}}^{t_{i}+\Delta t_{\text{gate}}} r_{\text{R4}}(t) \frac{\int QE_{\text{int}}(\lambda)T_{\text{BP}}(\lambda)r_{\text{ph}}(\lambda,t)T'_{\Delta\lambda_{\text{UV}}}(\lambda)d\lambda}{\int r_{\text{ph}}(\lambda,t)T'_{\Delta\lambda_{\text{UV}}}(\lambda)d\lambda} dt \right) \times vol_{\text{tag}}\eta_{\text{col}}g_{\text{int}},$$
(3.11)

where $QE_{\rm int}(\lambda)$ is the intensifier's quantum efficiency given by manufacturer. The tagged volume, $vol_{\rm tag}$, and estimated collection efficiency, $\eta_{\rm col}$, were previously calculated for the optical configuration. When using the intensifier with a similar camera

(CMOS sensor with 20 μ m pixels) and an identical gain setting of 60 %, the manufacturer provides the approximate conversion factor of $g_{\rm int} \approx 35.6 \, {\rm AU}$.

Similar to the derivation for Equation (2.33), Equation (2.32) enables substitution of the $\Delta \lambda_{\text{VIS}}$ band of the measured FLEET spectrum (black line in Figure 2.2) for $r_{\text{ph}}(\lambda, t) T'_{\Delta \lambda_{\text{VIS}}}(\lambda)$ while the UV counterpart to Equation (2.32) enables substitution of the $\Delta \lambda_{\text{UV}}$ band of the spectrum for $r_{\text{ph}}(\lambda, t) T'_{\Delta \lambda_{\text{UV}}}(\lambda)$.

However, unlike the derivation for Equation (2.33), the resulting equation cannot be solved for photon density rate because of the mixing of the VIS and UV contributions. Therefore, $r_{R3}(t)$ and $r_{R4}(t)$ must come from the model and the resulting equation provides a means to compare the model to the experiment in terms of recorded signal (i.e., convert the modeling results to the same arbitrary units, or AU, as the experiment).

3.4.3 Initial Signal Trends and Comparison to Model

Figure 3.9 plots the converted modeling (triangles) and experimental (boxes, repeated from Figure 3.8 for convenience) results for initial signal, $S(t_1)$, with $t_1 = 0.1 \,\mu s$ and $\Delta t_{\rm gate} = 0.5 \,\mu s$. The experimental markers and error bars correspond to mean and standard deviation, respectively, based on approximately 6600 single-shot images. Note that the experimental data at $3.1 \times 10^{-3} \,\mathrm{kg} \,\mathrm{m}^{-3}$, 248 K (box with thicker border) were replaced by results from a two-term exponential fit thought to be more representative of the actual signal at $0.1 \,\mu s$. See Section 3.4.4 and Figure 3.13 for details.

Figure 3.9 shows that the initial signal of the simulation, like the experiment, strongly depends upon density and achieves an optimal value at reduced density, though the optimal point differs between the two curves $(0.11 \,\mathrm{kg}\,\mathrm{m}^{-3})$ and $1.6 \times 10^{-2} \,\mathrm{kg}\,\mathrm{m}^{-3}$, respectively). Compare the species curves of the near-optimal signal case (left) at reduced density, $0.15 \,\mathrm{kg}\,\mathrm{m}^{-3}$, but similar temperature, to the

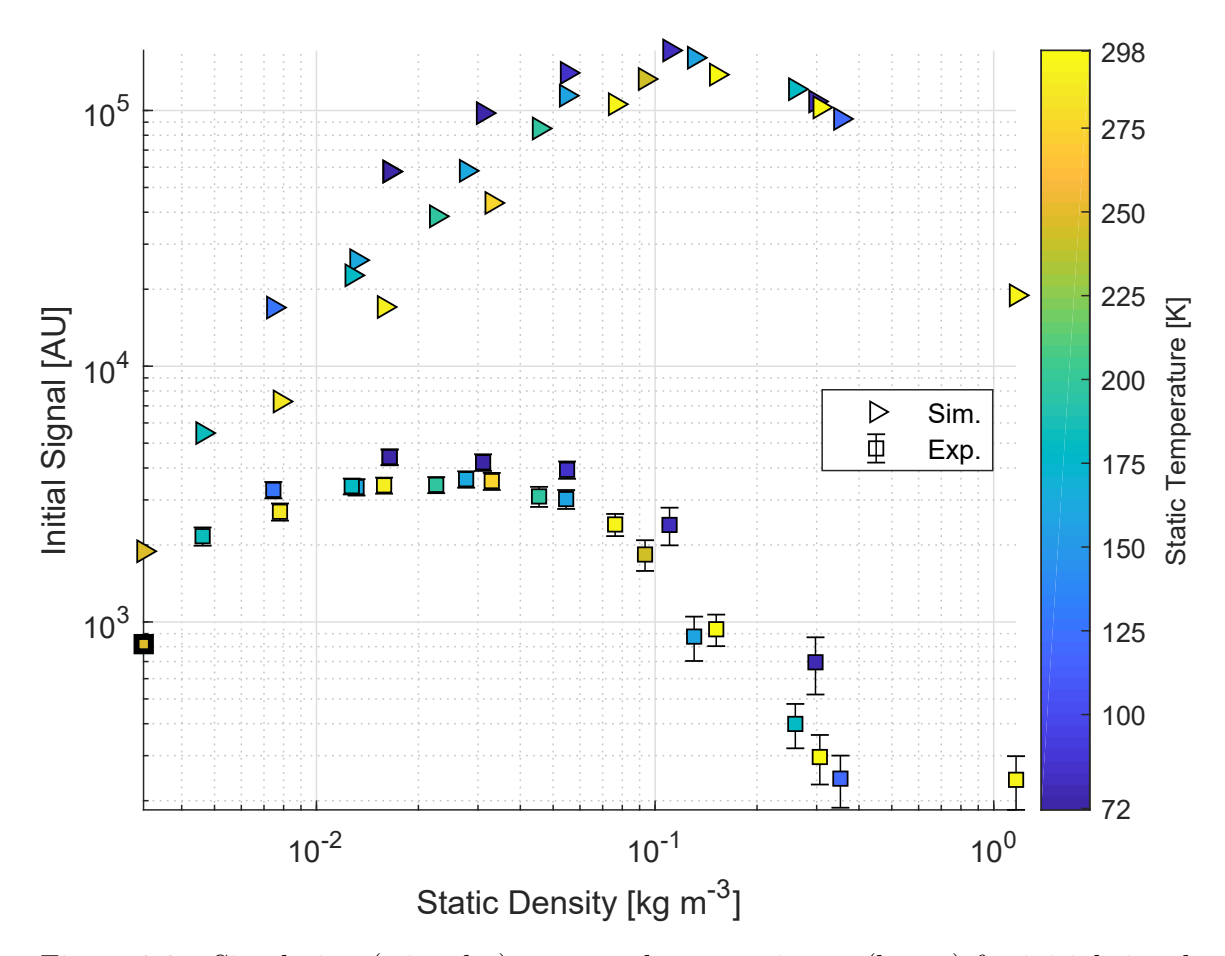


Figure 3.9: Simulation (triangles) compared to experiment (boxes) for initial signal as a function of density and temperature. Simulation accounts for total signal of tagged region whereas experiment considers only peak signal in center. Error bars correspond to one standard deviation. Experimental data at $3.1 \times 10^{-3} \,\mathrm{kg}\,\mathrm{m}^{-3}$ (box with thicker border) replaced by two-term exponential fit.

atmospheric case (right) in Figure 3.10, especially for $N_2(B)$ and $N_2(C)$ around $t=0.1\,\mu s$. The populations of these emitting species are higher at $0.1\,\mu s$ in the reduced density case. Thus, the optimization of signal arises not from increased dissociation fraction (see next paragraph), but from retardation of the temporal evolution of the electronically-excited species (due to overall slowing of reactions) which postpones their climax and slows their rate of decay before the opening of the intensifier gate at $t=0.1\,\mu s$. Although decreasing the density shifts the population curves later in time, it also depresses their magnitude (due to smaller initial conditions) so that further rarefaction actually reduces the recorded signal. Therefore, for

a particular time delay and gate width, there is an optimal value of gas density that maximizes the signal. Recall Section 2.4.5 also discusses population curves shifting in time and magnitude because of density changes.

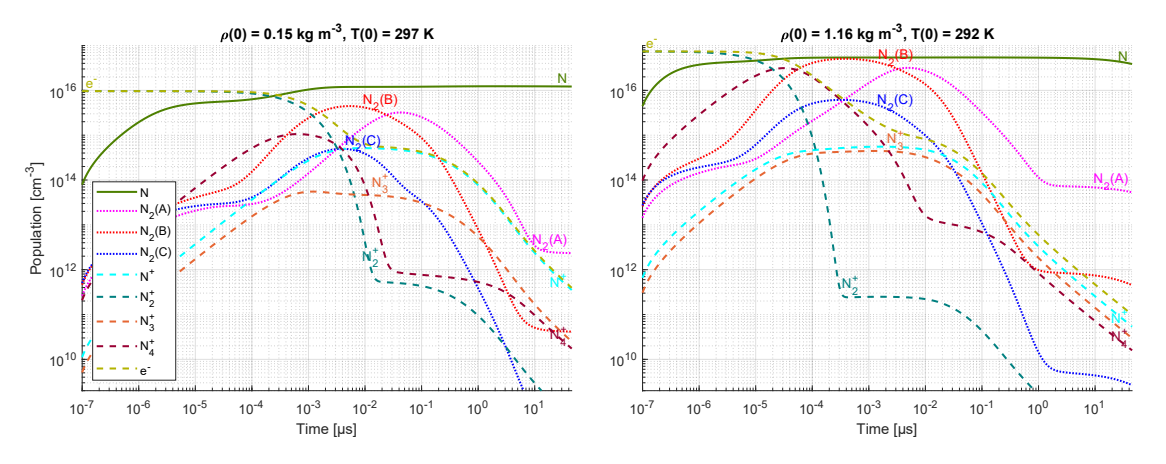


Figure 3.10: Simulation results at reduced (left) and atmospheric (right) gas density for atoms (solid line), excited molecules (dotted lines) and charged species (dashed lines). The effectively constant N_2 population is not shown. Note greater $N_2(B)$ and $N_2(C)$ population at $t = 0.1 \,\mu s$ for reduced density (left).

Peak dissociation fraction, $\alpha_{\rm diss,max} = \max\left(\frac{n_{\rm N}(t)}{n_{\rm N}(t)+2n_{\rm N_2}(t)}\right)$, where $n_{\rm N}(t)$ and $n_{\rm N_2}(t)$ respectively denote the number density of atoms and molecules, generally increases with decreasing static gas density as evident from Figure 3.10 with $\alpha_{\rm diss,max} \approx 0.19\,\%$ (left) versus $\alpha_{\rm diss,max} \approx 0.11\,\%$ (right). The rise in $\alpha_{\rm diss,max}$ occurs because of suppression and postponement of the loss pathways for N such as three-body atomic recombination (R1) and certain ion conversion reactions (R29 and R39). Additionally, low gas density elongates the timescales of action for impact dissociation (R40) and dissociative recombination (R11 and R12) at early times, while at later times, it prolongs ion conversion such as R32¹⁶ and R37, and for the warm cases, three-body electron-ion recombination (R19). Although this situation leads to a larger fraction of atomic nitrogen, it does little to boost the initial signal at low static densities because, for the same reasons, atomic recombination proceeds too slowly to affect

¹⁶The effect on reaction R32 is especially pronounced for the warm cases.

 $N_2(B)$ at the early delays (0.1–0.5 us). Furthermore, higher initial gas temperature slightly magnifies the rise in dissociation fraction associated with rarefaction.

Regarding the relative contributions of reactions for N, $N_2(A)$, $N_2(B)$ and $N_2(C)$, decreasing gas density generally elongates the timescales of early reactions (especially lengthening the duration of those involving e^-) and delays the start of later reactions. For N, the later, second peak of the impact dissociation (R40) curve in Figure 2.7 (lower) subsides. For $N_2(B)$, three-body atomic recombination (R1) becomes less important and fluorescence into B-state (R4) gains some importance at the lowest densities. For $N_2(C)$, energy pooling (R6) and quenching (R26) become relatively less important while fluorescence (R4) grows in importance.

Evident from Figure 3.9, the simulation and experiment share a relatively weak dependence on gas temperature (compared to gas density), with the temperature dependence being weaker for the experiment. Although colder temperatures consistently produce a stronger signal in the simulation, especially below $0.15\,\mathrm{kg}\,\mathrm{m}^{-3}$, only the coldest temperatures appear to do so in the experiment. The optimal (maximum) signals of the simulation and experiment at coldest temperature are merely 30% higher than the corresponding signals at similar density, but warmest temperature. For the experiment, saturation of the intensified camera system may have played a role in curtailing the enhancement at low temperatures. The three coldest experimental data between $\rho = 0.016-0.055 \,\mathrm{kg} \,\mathrm{m}^{-3}$, and to a much lesser extent, the two warmer data around $\rho \approx 0.03\,\mathrm{kg\,m^{-3}}$, experienced peak signal saturation. Although we attempted to compensate by interpolating the value of saturated pixels with a Gaussian fit, deleterious effects probably remained (e.g., error in interpolated peak value, nonlinearity of neighboring, but 'unsaturated' pixels), perhaps partly explaining why the other two coldest experimental data ($\rho > 0.1 \,\mathrm{kg}\,\mathrm{m}^{-3}$) exhibited greater enhancement. Since the simulation indicates similarly weak enhancement around the optimal point of the curve, we cannot attribute the effect entirely to saturation without additional measurements. The greatest low temperature signal enhancement took place at $1.6 \times 10^{-2} \,\mathrm{kg} \,\mathrm{m}^{-3}$ for the simulation (a factor of improvement of 3.4 times) and $0.3 \,\mathrm{kg}\,\mathrm{m}^{-3}$ for the experiment (a similar factor of 2.3 times). According to the modeling results shown in Figure 3.11, low temperatures favor the formation of cluster ions, boosting the size of the N_4^+ population. A larger N_4^+ population accelerates electron-cluster ion dissociative recombination and produces more electronically-excited species (primarily $N_2(B)$ via R8, but also $N_2(A)$ via R7 and N₂(C) via R9). Furthermore, greater B-state population begets greater A- and C-state populations because of the aforementioned 17 coupling mechanisms of energy pooling, quenching and even fluorescence (which becomes relatively important at low density). Ultimately, the levels of N₂(A), N₂(B) and N₂(C) are all elevated compared to the warm case, leading to consistently larger recorded signal for delays up to $t \le 1\,\mu\mathrm{s}$ in the simulation and $t \lesssim 5\,\mu\mathrm{s}$ in the experiment. For this range of conditions, three-body atomic recombination (R1) does not play a vital role in the low temperature enhancement. Retarded by the low densities, R1 rises to prominence far too late $(t > 10 \,\mu\text{s})$ to influence the signal at $0.1 \,\mu\text{s}$. Therefore, the magnitude of enhancement suggested by Table 2.2 because of $k_{\rm R1}(T) \propto \exp{(500/T)}$ is irrelevant.

In Figure 3.9, the optimal (0.11 kg m⁻³ and 82 K) and atmospheric reference signals of the simulation exceed the corresponding (i.e., same density and temperature) results of the experiment by 72 and 78 times, respectively. This seemingly great discrepancy in magnitude¹⁸ is partially explained by the fact that the simulation effectively sums the entire signal in the tagged region whereas the experiment only considers the average of the peak signal in the center. In particular, using the apparent thickness of a single pixel $(78 \times 10^{-6} \,\mathrm{m})$ instead of the confocal parameter $(2.6 \times 10^{-3} \,\mathrm{m})$ reduces vol_{tag} and thus the simulation results by roughly 33 times.

 $^{^{17}\}mathrm{See}$ Chapter 2 for more details.

¹⁸The simulation and experimental results are plotted in the same units without normalization or additional scaling coefficients.

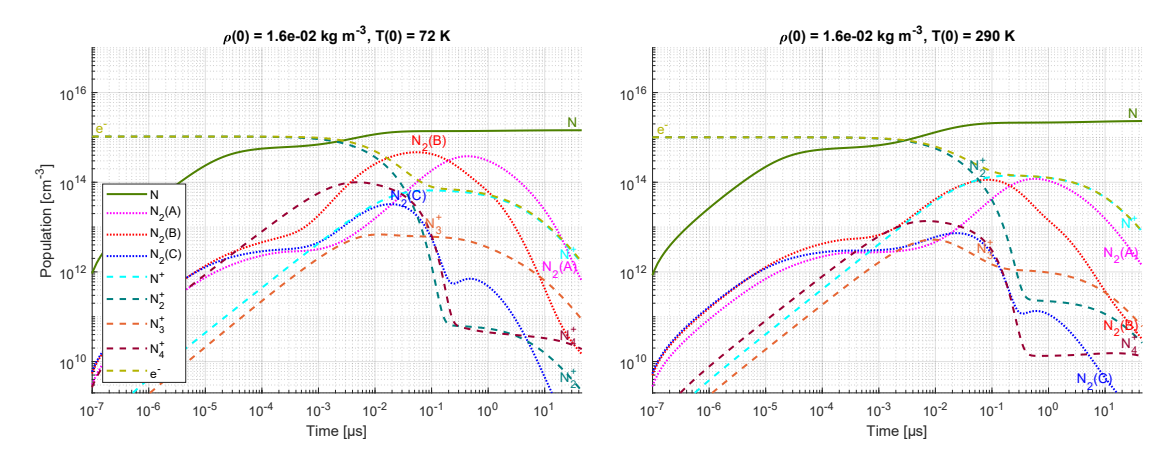


Figure 3.11: Simulation results at reduced (left) and atmospheric (right) gas temperature. Note greater maximum for N_4^+ and larger excited-state populations at $t = 0.1 \,\mu s$ for reduced temperature (left). See caption in Figure 3.10 for more details.

Furthermore, there is uncertainty in converting the model's photon density rates into the signal recorded by the intensified camera, namely in vol_{tag} (which probably changes with conditions), η_{col} (which is estimated) and g_{int} (which is also estimated). Moreover, recall that the experimental data in Figure 3.9 represent peak Gaussian signal. Alternatively, integrating the Gaussian fits along their intensity profiles (and then averaging the results near the center of tagging) produces data with comparable trends, but higher absolute magnitudes (see Figure B.3 in Appendix B). The higher magnitudes reduce the factor of disagreement between the simulation and experiment by five- to sevenfold. Integration also accounts for diffusion of the tagged line (i.e., variation of its width with gas density—see Appendix B). A more complete model (discussed as possible future work in Section 6.2 of Chapter 6) would include at least one spatial dimensional along with the physics responsible for widening the tagged line such as mass diffusivity and bulk fluid motion.

The ratio of optimal signal at reduced density to signal at atmospheric conditions is similar for the simulation (ratio of 9) and experiment (ratio of 18). Unfortunately, the range between the minimum and maximum signal for the simulation disagrees with that of the experiment, exhibiting a total variation of almost two orders of

magnitude. A breakdown in the validity of the modeling assumptions may explain this departure from the experimental signal trend at the lowest densities. We relied on a continuum approach to the plasma kinetics (necessary when using rate coefficients from BOLSIG+ and elsewhere). However, at the lowest density, the electron mean free path¹⁹ substantially exceeds the beam waist (i.e., radius of the tagged region), $\lambda_{\text{MFP,e}} \approx 140 \times 10^{-6} \,\mathrm{m} \gg w_0 \approx 18 \times 10^{-6} \,\mathrm{m}$, and a continuum does not accurately represent the rarefied condition. Furthermore, we approximated photoionization as independent of gas density based on the balance between self-focusing and plasma defocusing in Equation (2.24). However, at very low density, self-focusing weakens relative to geometric focusing and the balance should include the effect of geometric focusing instead of neglecting it. Inclusion of this new term would prevent gas density from simply canceling out, implying a dependence on it.

3.4.4 Signal Lifetime (via Exponential Fits) and Comparison to Model

Following an approach similar to previous efforts [1, 5], we calculated the lifetimes of the signal based on the 1/e and $1/e^2$ fall time from $t_1 = 0.1 \,\mu\text{s}$ of a two-term exponential fit of: the Gaussian peak data from Figure 3.8 for the experiment; the corresponding results of Equation (3.11) for the simulation. Using a fit instead of interpolation of experimental data improves noise tolerance [5] and enables determination of lifetimes which exceed the data window. To maintain consistency during comparison, we utilize this fitting approach for the simulation data as well. The two-term exponential, $S(t) = a_1 \exp(t/\tau_1) + a_2 \exp(t/\tau_2)$, with fitting parameters a_1 , τ_1 , a_2 and τ_2 , accounts for the fast and slow decay regimes that characterizes FLEET sig-

¹⁹Using $\lambda_{\rm MFP,e} = \sqrt{\frac{8k_{\rm B}T_{\rm e}}{\pi m_{\rm e}}}/\nu_{\rm elas}$, where $m_{\rm e}$, $T_{\rm e}$ and $\nu_{\rm elas}$ signify the mass, temperature and elastic collision frequency of the electrons, respectively, with the latter two quantities computed by the model. $k_{\rm B}$ symbolizes the Boltzmann constant.

nal measurements [1]. Figure 3.12 shows typical fits at two conditions with dissimilar lifetimes.

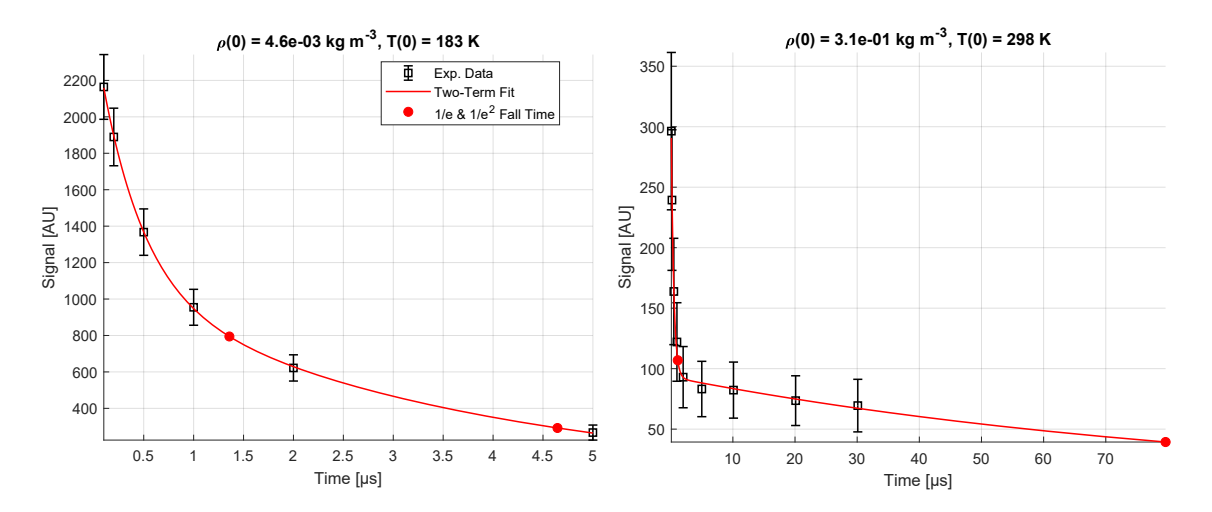


Figure 3.12: Typical two-term exponential fits (lines) and Gaussian experimental data (boxes) for conditions with vastly different lifetimes (red filled circles). Markers and error bars correspond to mean and standard deviation, respectively.

For the fitting procedure, we included all data shown in Figure 3.8 along with the extended delays of the long-lived signal at $0.35 \,\mathrm{kg} \,\mathrm{m}^{-3}$, $121 \,\mathrm{K} \,(10.1 \,\mu\mathrm{s})$, $0.31 \,\mathrm{kg} \,\mathrm{m}^{-3}$, $298 \,\mathrm{K} \,(10.1 - 30.1 \,\mu\mathrm{s})$ and $1.16 \,\mathrm{kg} \,\mathrm{m}^{-3}$, $292 \,\mathrm{K} \,(10.1 - 30.1 \,\mu\mathrm{s})$. However, we excluded the first two delays $(0.1 - 0.2 \,\mu\mathrm{s})$ at $3.1 \times 10^{-3} \,\mathrm{kg} \,\mathrm{m}^{-3}$, $248 \,\mathrm{K}$. At that operating condition, the most rarefied demonstrated by the facility, density fluctuations in the jet of roughly $5 - 10 \,\%$ caused the signal of the first two delays to deviate from the expected decay regime, yielding a nonsensical fit (Figure 3.13, left). Excluding these delays provided a more realistic fit (Figure 3.13, right) and enabled extrapolation of the likely value for the initial signal (box with thicker border in Figure 3.9). Nevertheless, the relatively significant density fluctuations suggest we should repeat that test condition using more stable (if possible) facility settings.

Figure 3.14 displays the 1/e (lower) and $1/e^2$ (upper) signal lifetimes for the converted modeling (triangles) and experimental (boxes) results. Since the experimental measurements were based on fitting of mean values (captured in non-sequential acquisitions), no error bars were computed.

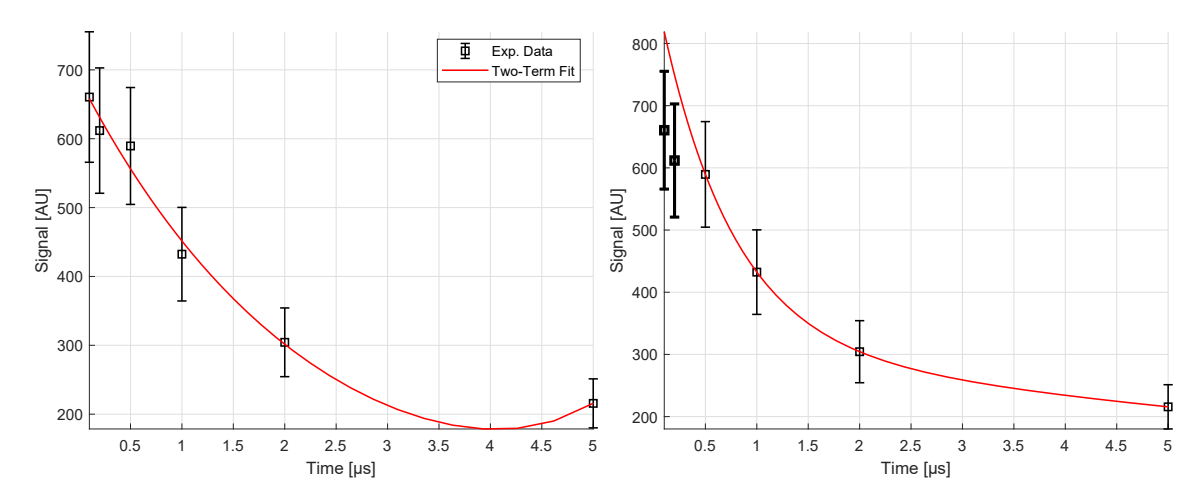


Figure 3.13: Two-term exponential fits for $3.1 \times 10^{-3} \,\mathrm{kg} \,\mathrm{m}^{-3}$ and 248 K before (left) and after (right) exclusion of suspect data at $0.1 - 0.2 \,\mu\mathrm{s}$ (thicker markers).

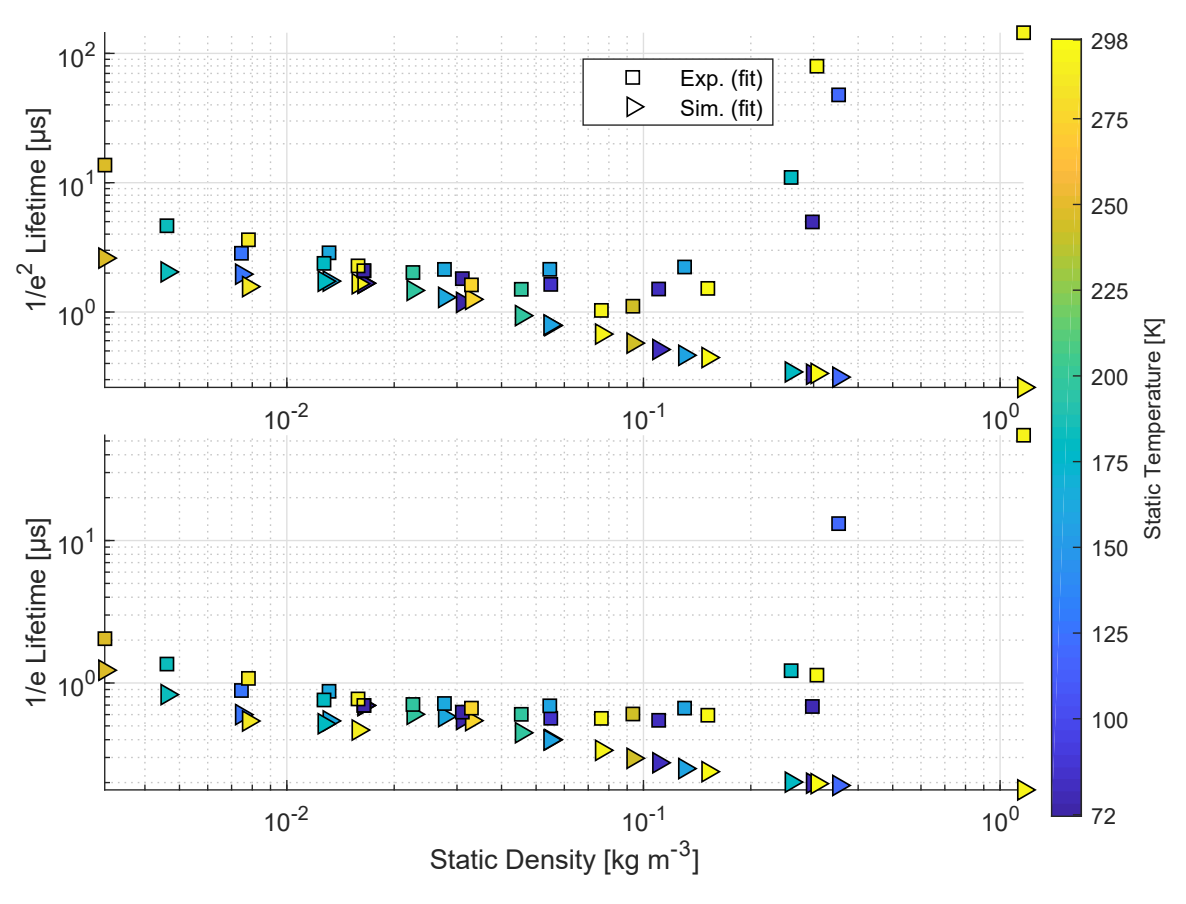


Figure 3.14: Simulation (triangles) compared to experiment (boxes) for 1/e (lower) and $1/e^2$ (upper) lifetimes of FLEET signal as a function of density and temperature.

As discussed in Section 3.2.2, the experimental lifetimes reported here are longer than photomultiplier tube (i.e., instantaneous) measurements due to an excessive gate width. Nevertheless, these experimental lifetimes do accurately reflect what would be expected from an intensifier with similar spectral sensitivity and settings (e.g., gain, gate, delay), agreeing with the values at atmospheric density measured by Burns et al. [5].

Comparing the simulation and experimental results, the simulation exhibits shorter lifetimes whose value and similitude to the experimental value decrease with increasing gas density (in the limit of large gas density). As explained in Section 2.3.5, the model's shorter lifetimes probably arise from its zero-dimensional nature. The model effectively concentrates all mass into a point of constant initial density, which accelerates reaction rates relative to an experiment that has spatially distributed species and experiences gas dynamic expansion.²⁰ Moreover, increasing the initial gas density in the simulation acts to hasten the reaction rates, further decreasing the signal lifetime. However, between roughly 5×10^{-3} to $0.02 \,\mathrm{kg}\,\mathrm{m}^{-3}$, the simulation lifetimes follow a noticeably flatter trend and even show a slight dependence on temperature (longer lifetimes being associated with colder temperatures). Within this density range, the species responsible for the UV signal component, $N_2(C)$, experiences non-monotonic decay, actually growing slightly around 0.2–0.4 µs as shown in Figure 3.11. This population growth notably contributes to the signal lifetime and occurs because energy pooling (R6) exceeds fluorescence (R4), the primary loss mechanism at low densities. At densities beneath this range, the population of $N_2(C)$ is too small relative to $N_2(B)$ for the non-monotonic behavior of $N_2(C)$ to significantly influence the total signal. At densities above this range, quenching (R26) becomes

 $^{^{20}}$ Bulk fluid motion (driven by heating) certainly contributes to signal intensity evolution. Assuming propagation at roughly sonic velocity, $173-352\,\mathrm{m\,s^{-1}}$ for $72-298\,\mathrm{K}$, after $1-2\,\mu\mathrm{s}$, gas expansion affects most, if not all, of the tagged radius, about $300-800\,\mu\mathrm{m}$ according to Appendix B. However, based on the initial laser beam waist of $18\,\mu\mathrm{m}$ (Section 3.2.3), this influence occurs within $0.1\,\mu\mathrm{s}$.

an important loss mechanism, which along with fluorescence, counteracts population gain processes to ensure monotonic decay for $N_2(C)$ as shown in Figure 3.10.

Like the simulation, the experimental lifetimes primarily depend on gas density. However, unlike the simulation, the experimental lifetimes follow a U-shaped trend, with a minimum around 0.07–0.1 kg m⁻³ (see Figure 3.14). Also, the experiment is, in general, more strongly affected by temperature, although the exact dependence is unclear. Furthermore, the low density results (of the present study) contrast with those for above atmospheric densities since the lifetimes in the latter case exhibit an inverse relationship to density [5].

Casual comparison of the simulation results (triangles) in Figures 3.9 and 3.14 might lead one to conclude an inverse relationship between initial signal intensity and lifetime, but closer inspection reveals the two curves actually depend upon density, not one another. For instance, points along the initial signal curve with multiple temperatures generally have 1/e lifetimes directly proportional to initial signal (especially for $\rho \leq 0.02\,\mathrm{kg\,m^{-3}}$), contradicting the apparent inverse trend with initial signal. Furthermore, the lifetimes fail to track the initial signal curve beyond the density of maximum initial signal ($\rho \approx 0.11\,\mathrm{kg\,m^{-3}}$), instead continuing to decrease in value. Had the lifetimes been truly inversely proportional to initial signal, they would have increased beyond this point.

Performing the same comparison for the experimental data (boxes), the lifetimes demonstrate a moderate dependence on initial signal intensity. In general, the longest lifetimes correspond to the weakest initial signals; however, the minimum lifetimes occur at densities higher than that of the maximum initial signal by roughly a factor of 4.6–6.7 (specifically, $\rho \approx 0.076$ –0.11 kg m⁻³ versus $\rho \approx 0.016$ kg m⁻³).

Lastly, we should state that the preceding analysis of simulation lifetimes utilized data from time delays beyond those for which the simulation notably deviated from the time-resolved experimental measurements at atmospheric conditions (i.e., around

several hundred nanoseconds in Figure 2.5). Although the simulation lifetime results are included for qualitative reference, caution is advised when drawing any conclusions from them.

3.5 Velocity Measurement Results

3.5.1 Overview of Velocimetry in Flow Facility

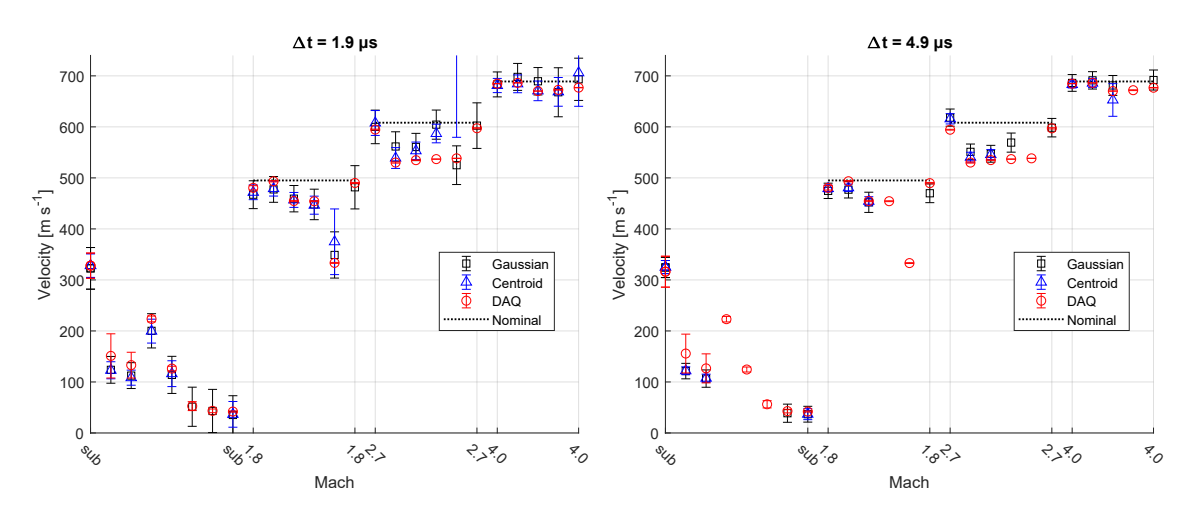


Figure 3.15: Measured velocities for all 25 flow facility test conditions (various Mach and pressure settings). Two values of Δt shown. Markers and error bars denote mean and standard deviation, respectively.

Figure 3.15 compares the measured velocities as a function of Mach (nozzle) and pressure setting for time intervals $\Delta t = 1.9 \,\mu\text{s}$ (left) and $\Delta t = 4.9 \,\mu\text{s}$ (right). These settings represent all 25 conditions tested in the flow facility (see Figure 3.3 for the temperatures and densities). Plotted velocities include those based on FLEET Gaussian line centers (black boxes), FLEET tagged region centroids (blue triangles), DAQ measurements (red circles) using Equations (3.1) to (3.4), and nominal (i.e., design) supersonic velocities (dotted lines) for $T_0 = 300 \,\text{K}$. The markers and error bars denote mean and standard deviation, respectively. Note that the DAQ velocities show no perceptible change between these two plots (taken several seconds apart). Ramping

up p_0 and p_b (plotted left to right within each nozzle range) causes the variation of velocity for a given nozzle setting. Accuracy and precision of FLEET velocimetry generally improve with increasing time interval Δt . For $\Delta t = 4.9\,\mu s$ (right), some DAQ measurements lack corresponding FLEET measurements because they fail the single-pixel criterion ($n_x < 140$ for three of the five central points) due to a drop-off in SNR. Moreover, the centroid velocities generally exhibit greater error and imprecision than the Gaussian velocities, with a number of results outside the plotted range.²¹ The increased error and imprecision result from comparatively greater intolerance to low SNR. At long time delays for a swiftly decaying signal (certain conditions), the centroid-based measurements do not strictly isolate the FLEET line in the images and instead include large swaths of spurious noise, throwing off determination of the centroid. In contrast, Gaussian fitting is more discriminating, consistently identifying pixels associated with the actual FLEET line rather than noise. For this reason, our signal analysis primarily relies on the more robust Gaussian-based measurements.

Also, note that some of the Mach 2.7 and all of the Mach 4.0 velocities are fast enough to allow the FLEET line to translate outside the camera's field of view for $\Delta t = 30 \,\mu s$.

Lastly, since the data for time delays t_1 through t_6 (i.e., 0.1–5 μ s) come from separate framing bursts, the FLEET velocity measurements are susceptible to additional sources of error and imprecision, namely, laser timing jitter (likely a small contribution), beam steering and facility vibrations. As discussed in Chapter 5, it is preferable to acquire image data sequentially (i.e., track a tagged line as it advects downstream) to eliminate these sources of error, but camera frame rate limitations prevented this approach.

²¹When only a Gaussian result is displayed, the corresponding centroid result is literally off the chart.

3.5.2 Measurement Accuracy

We define measurement accuracy as the absolute value of the difference between the DAQ, 22 $\overline{v}_{\rm DAQ}$, and Gaussian, \overline{v} , mean velocities, described in the preceding sections. Figure 3.16 plots this result as a function of density, temperature and time interval while Figure 3.17 shows the same result after normalization by the respective DAQ mean velocity (which remains effectively constant across time delays and intervals). As mentioned before, only several conditions, namely those with the longest lifetimes, allow for results out to 10.1 μ s and beyond. Therefore, for reference, we include measurements at $\Delta t = 30 \,\mu$ s, which typify the sparse results from $\Delta t = 10$ –30 μ s.

The accuracy figures show no clear trends with density or temperature. At the shortest time intervals, $\Delta t = 0.1$ –0.4 μ s, the colder temperatures portray worse accuracy in absolute terms (Figure 3.16), although in normalized terms (Figure 3.17), the inaccuracy becomes relatively less obvious. At longer time intervals, the colder temperatures actually demonstrate among the best accuracy results (especially in normalized terms). In general, the accuracy of the colder temperatures benefits the most from increasing the time interval.

The data for $\rho = 0.15 \,\mathrm{kg} \,\mathrm{m}^{-3}$, $T = 297 \,\mathrm{K}$ and $\Delta t = 0.1 \,\mathrm{\mu s}$ (outside the plotting domain of Figure 3.17) possess an anomalously large error of 110 %. The large error did not simply result from normalization by small velocities since subsonic measurements of similar magnitude (at $0.31 \,\mathrm{kg} \,\mathrm{m}^{-3}$, $298 \,\mathrm{K}$ and $1.16 \,\mathrm{kg} \,\mathrm{m}^{-3}$, $292 \,\mathrm{K}$) record errors of only 18–31 %. Meticulous review of DAQ and FLEET data reveal nothing noteworthy and indicate relatively steady flow conditions. Assuming a timing mistake and changing the delay from $t_2 = 0.2 \,\mathrm{\mu s}$ to $t_2 = 0.3 \,\mathrm{\mu s}$ significantly decreases the error to 5 % (with a precision around 400 %), but drastically deteriorates the two-term expo-

 $[\]overline{^{22}}$ We assume uniform velocity in the streamwise direction such that \overline{v}_{DAQ} applies to all positions and time delays as the tagged region advects downstream.

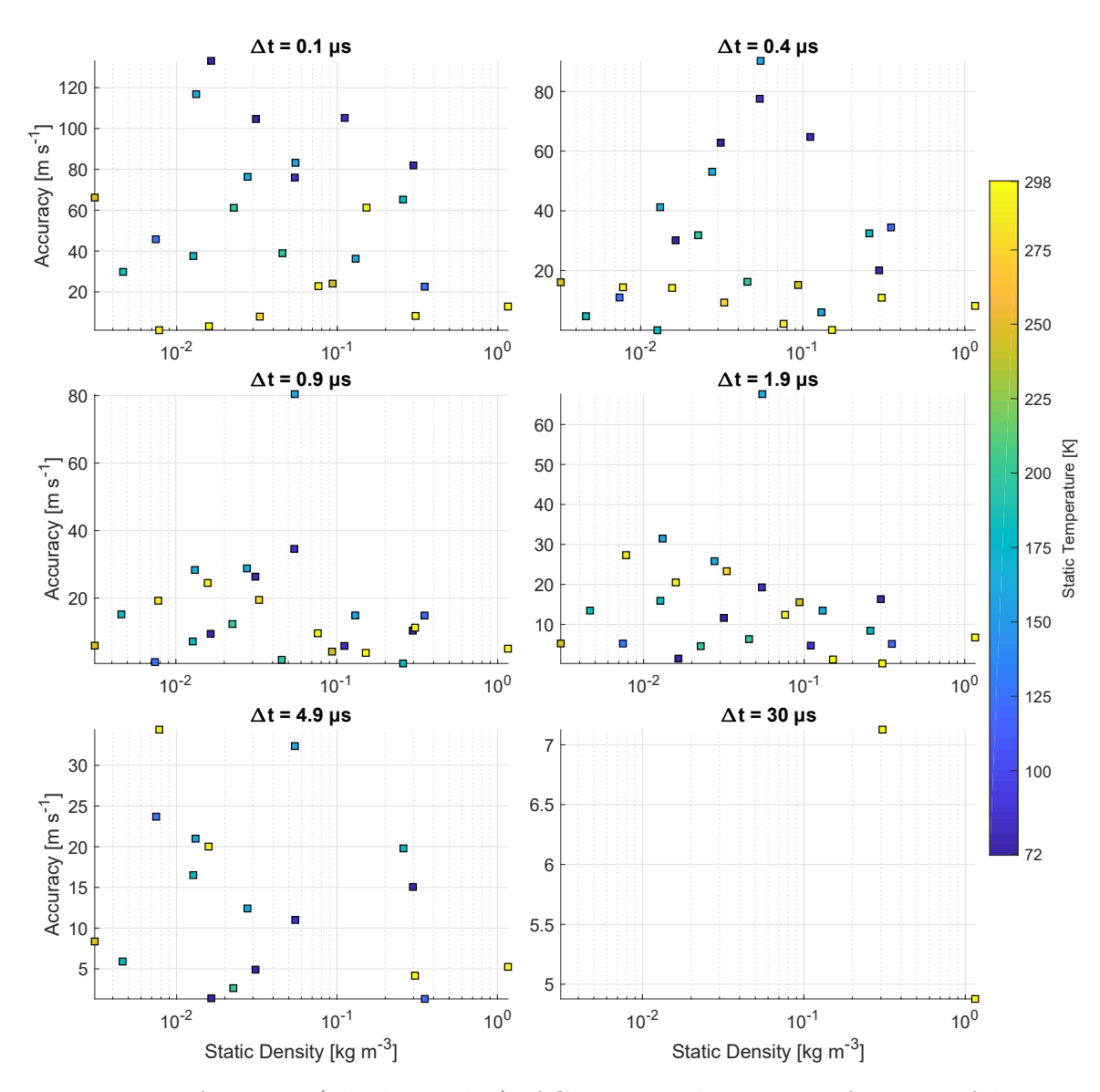


Figure 3.16: Accuracy (absolute value) of Gaussian velocities as a function of density, temperature and time interval. Note progressive shrinking of ordinate scale with increasing time interval.

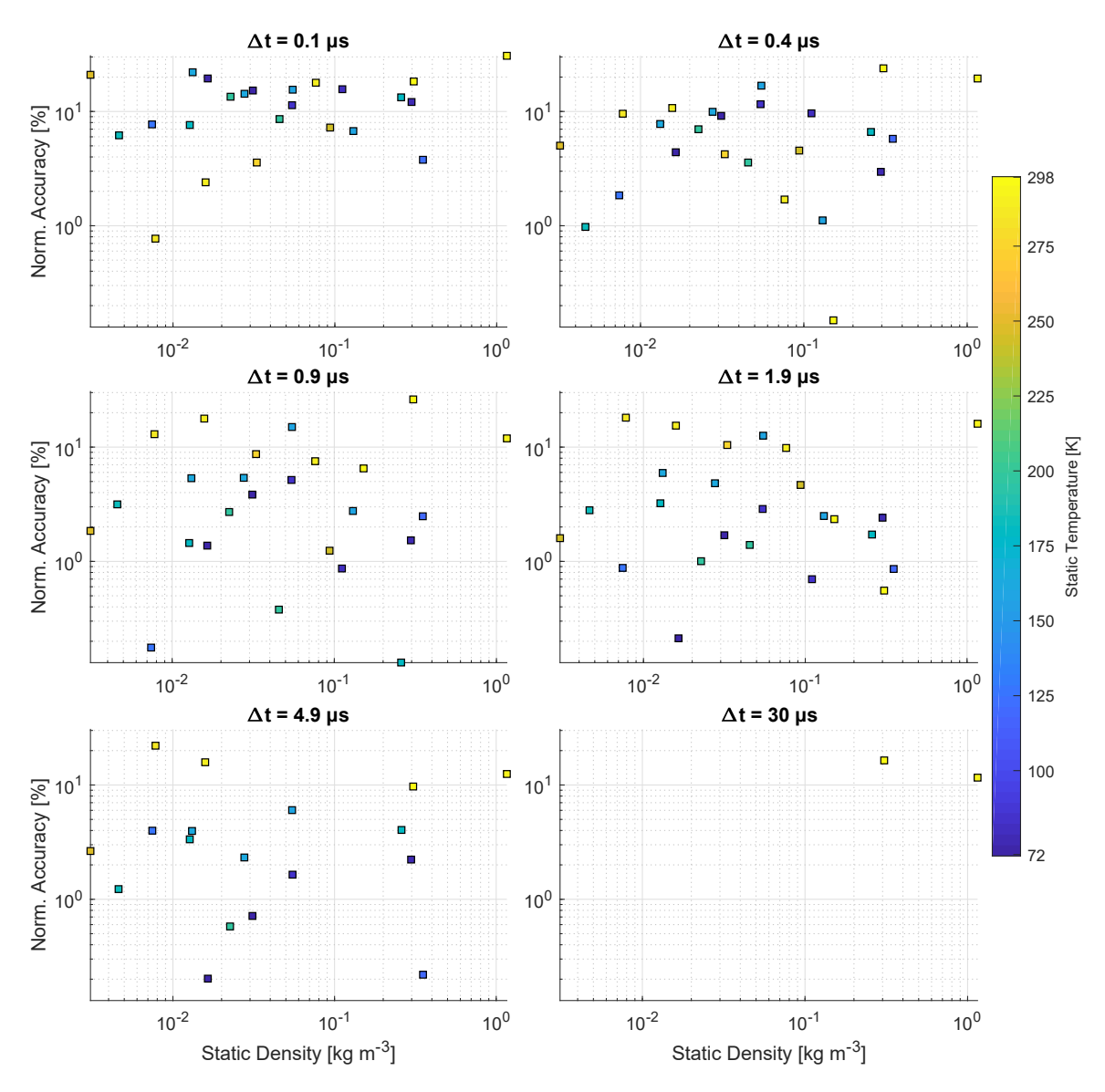


Figure 3.17: Normalization of previously shown accuracy data by respective mean DAQ velocities.

nential fit for the signal decay. Therefore, the reason for the anomalously large error at this condition remains unknown.

According to this very discrete data set, the best absolute accuracy is $< 0.01 \, \mathrm{m \, s^{-1}}$ for $0.013 \, \mathrm{kg \, m^{-3}}$ and $179 \, \mathrm{K}$ at $\Delta t = 0.4 \, \mathrm{\mu s}$ while the best normalized accuracy is $0.13 \, \%$ for $0.26 \, \mathrm{kg \, m^{-3}}$ and $179 \, \mathrm{K}$ at $\Delta t = 0.9 \, \mathrm{\mu s}$.

3.5.3 Measurement Precision

We define measurement precision as the standard deviation of Gaussian velocities, $\sigma(v)$, described in the preceding sections. Figure 3.18 plots this result as a function of density, temperature and time interval while Figure 3.19 shows the same result after normalization by the respective DAQ mean velocity. Like the accuracy plots, we include reference measurements at $\Delta t = 30 \,\mu s$ to characterize the sparse results for extended delays. Although the position measurements for these extended delays come from the same framing burst as the initial delay, calculations show the covariance to be negligible compared to the variance.

Unlike accuracy, precision clearly depends on density and temperature. This dependence becomes especially evident in the normalized results of Figure 3.19, which eliminate the confounding (distracting) effect of velocity magnitude, $\sigma(v) \propto |v|$, that varies widely across nozzle settings. The figure shows that precision is optimized around roughly $\rho \approx 0.016$ –0.055 kg m⁻³ and perhaps again at the lowest densities. Reduction of gas temperature further improves the value of precision in a progressive fashion. Comparing these plots to the corresponding signal strength of the first and relevant delay²³ in Figure 3.8 reveals a seemingly more fundamental relationship to signal strength, although colder temperatures consistently produce better precision even for similar values of signal (and density). Limited review of the raw images for the cold and warm data of similar signal intensity and density uncover no notewor-

 $^{^{23}}$ Each velocity measurement requires two positions and therefore involves two signal strengths. For example, $\Delta t = 1.9 \,\mu s$ involves $t_1 = 0.1 \,\mu s$ and $t_5 = 2 \,\mu s$ from Figure 3.8.

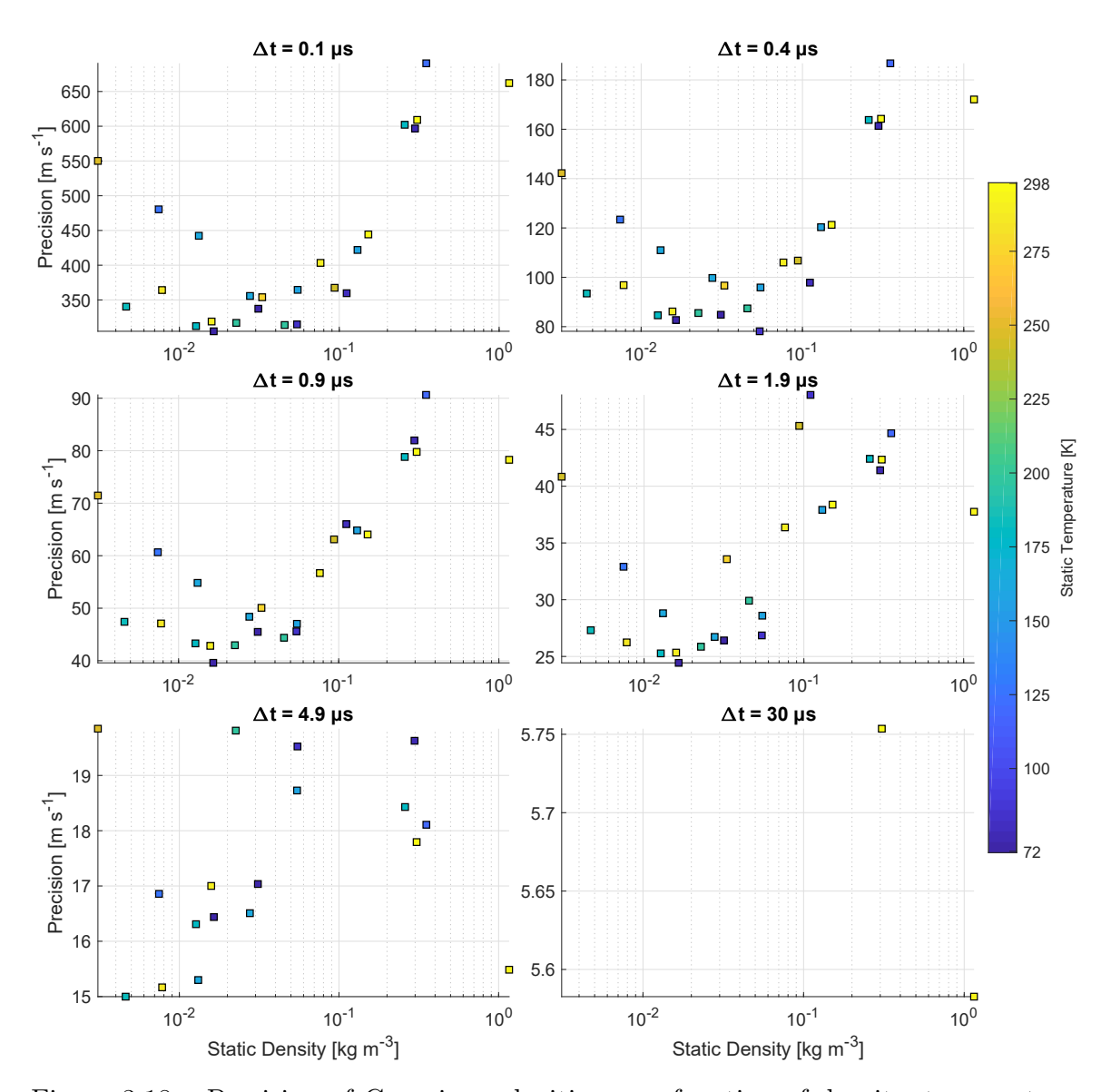


Figure 3.18: Precision of Gaussian velocities as a function of density, temperature and time interval. Note progressive shrinking of ordinate scale with increasing time interval.

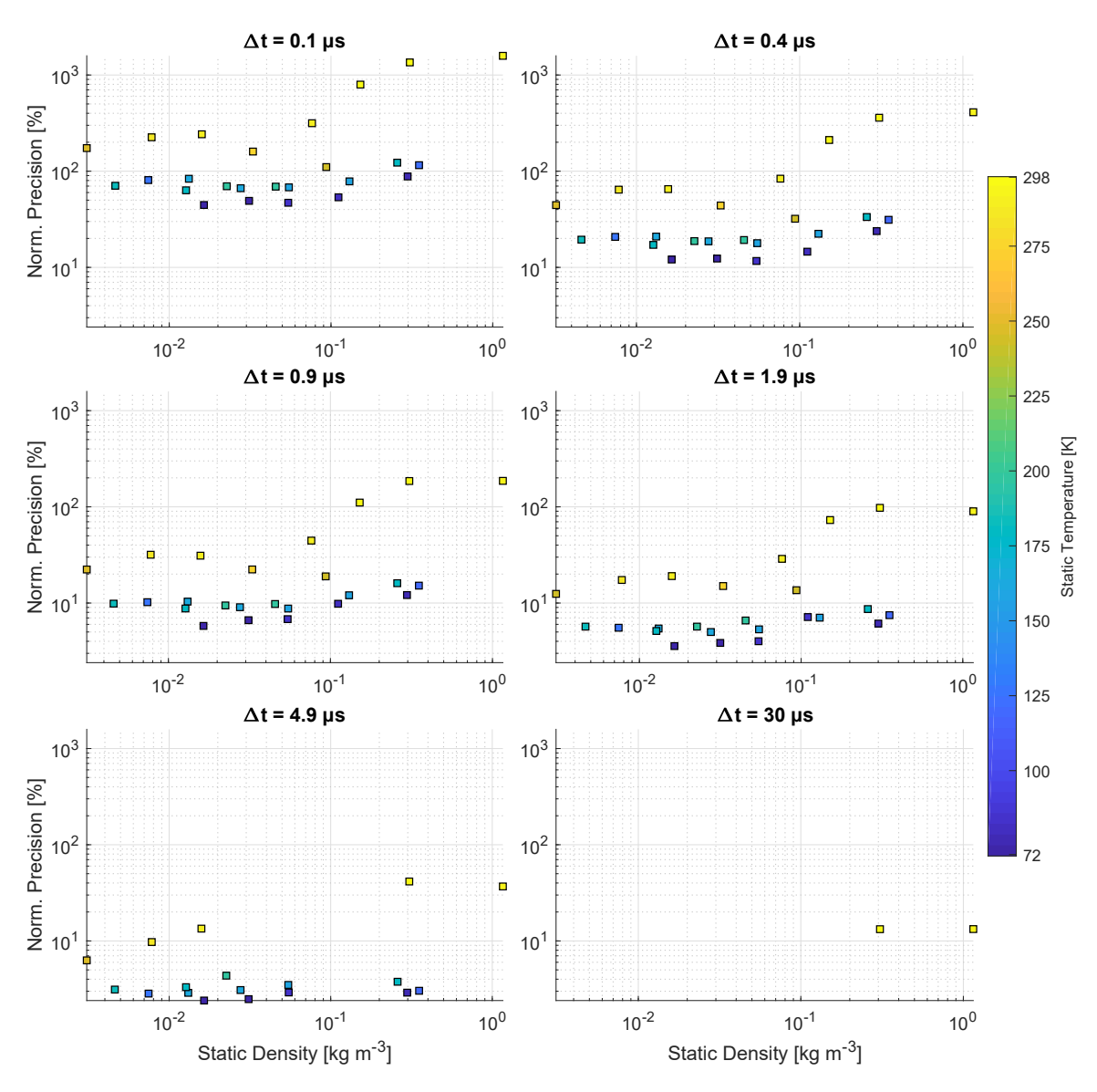


Figure 3.19: Normalization of previously shown precision data by respective mean DAQ velocity.

thy differences. Given that each temperature range employs a different contoured nozzle, with the warmest temperatures using a straight pipe, the loss of precision with temperature may be fluid dynamic in nature. Previous work [11] at constant, atmospheric conditions simply showed an inverse relationship between precision and signal (really, signal-to-noise ratio) since identification of the FLEET line improves with SNR.

In agreement with previous analyses,²⁴ i.e., $\sigma(v) \propto 1/\Delta t$, and experimental results [11], these plots illustrate an inverse relationship to time interval, with continual enhancement to precision for lengthening time intervals. In theory, the enhancement continues until the signal-to-noise ratio decays enough to counteract the advantage brought on by longer time intervals²⁵ (not shown).

According to this limited data set, the best absolute precision, apart from the extended time intervals, is $15\,\mathrm{m\,s^{-1}}$ for $4.6\times10^{-3}\,\mathrm{kg\,m^{-3}}$ and $183\,\mathrm{K}$ at $\Delta t = 4.9\,\mathrm{\mu s}$ while the best normalized precision is $2.4\,\%$ for $0.016\,\mathrm{kg\,m^{-3}}$ and $72\,\mathrm{K}$ at $\Delta t = 4.9\,\mathrm{\mu s}$. The absolute precisions, although on the high side, are comparable to other FLEET velocity measurements discussed in Section 5.4 of Chapter 5. However, the normalized precisions compare somewhat unfavorably to the $0.3\,\%$ and $0.5\,\%$ respectively reported for Mach $0.5\,$ [5] and Mach 14 [96] flows of nitrogen.

3.6 Summary and Conclusions

In a flow facility purpose-built for testing laser-based diagnostics prior to deployment in full-scale wind tunnels, we investigated the performance of FLEET at a variety of temperature (72–298 K) and pressure (0.228–101 kPa) conditions in pure nitrogen. Using an intensified camera system and bandpass filter (which passed VIS and some UV light), we acquired data over a range of discrete time delays ($t_i = 0.1$ –30.1 µs)

 $^{^{24}}$ See Equation (5.6) in Chapter 5.

 $^{^{25}}$ We assume the time interval always remains much smaller than the characteristic timescale of the flow when making instantaneous velocity measurements.

with a constant gate width ($\Delta t_{\text{gate}} = 0.5 \,\mu\text{s}$). We sought to analyze signal intensity and velocimetry trends with changing static conditions of the free jet (25 conditions in all).

This effort required systematic processing of a large number of raw images, well over 6 930 000 in total.²⁶ First, we identified and sorted data images. Then, for each data image, we found the tagged region (basically a vertically-oriented luminescent line) and fit a series of transverse Gaussian profiles to the intensity distribution at each transverse slice of the line. Data pruning algorithms based on the number of MADs from the median [95] of a given metric filtered out poor fits, outlying results and/or otherwise unacceptable data (e.g., low SNR). These algorithms were applied uniformly across the data sets to ensure consistency during comparisons and in an intentionally less restrictive fashion so as to avoid artificially altering the mean or reducing the variance of the results. For analysis of signal and velocimetry trends, we relied on the mean of the aggregated Gaussian fits at the center of the tagged region (i.e., center of the free jet).

Signal intensity plots showed a primary dependence on gas density and a secondary dependence on gas temperature. The dependence on density began to break down around $\rho \approx 0.3 \,\mathrm{kg}\,\mathrm{m}^{-3}$ and progressed into the lower densities with increasing time delay. Others [5] have observed a lack of correlation between signal intensity and thermodynamic variables at long time delays ($t \gg 1\,\mathrm{\mu s}$). This finding emphasizes the importance of using early time delays ($t \approx 0.1\,\mathrm{\mu s}$) when leveraging FLEET signal intensity to measure thermodynamic variables or species concentration [13]. The optimal (maximum) signal intensities were at sub-atmospheric densities ($\rho \approx 1.6 \times 10^{-2}\,\mathrm{kg}\,\mathrm{m}^{-3}$) and moved toward lower densities as time delay increased. The coldest temperatures produced the highest signal intensities, lying above the apparent curve, though the effect seemed to diminish at later delays. Furthermore, the

 $^{^{26}25}$ conditions $\times\,6$ delays $\times\,7$ frames $\times\,6600$ shots = $6\,930\,000$ images.

highest signal intensities ($t_1 = 0.1 \,\mu s$) suffered from mild saturation effects, so the actual values may be higher than reported and the low temperature enhancement may be stronger. Future experiments would utilize neutral density filters²⁷ to prevent saturation while maintaining constant intensifier gain and gate width settings. Neutral density filters would also enable use of higher intensifier gain and thus shorter gate widths²⁸ to better resolve the swift signal decay that occurs at early time delays.

Extending the equations derived in Chapter 2, we related the kinetics model (which summed the total signal of the entire tagged region) to the experimental measurements made by the intensified camera (which considered the peak Gaussian signal in the center of the tagged region). The modeling and experimental results were compared for initial (peak) signal at $t_1 = 0.1 \,\mu s$ and $\Delta t_{\rm gate} = 0.5 \,\mu s$. The model demonstrated a qualitatively similar trend with gas density, achieving an optimal signal at reduced density that exceeded the atmospheric value. Such an optimization holds promise for supersonic and hypersonic measurements that require satisfactory signal at short time delays and gate widths. The optimization arose from shifting the excited species populations in time (delaying their maximum and slowing their decay) such that the intensifier gate captured a higher signal. Since the absolute magnitudes of the population curves decreased with decreasing density, there existed an optimal density for a given time delay and gate width.

Reducing the initial gas temperature slightly enhanced the initial signal for both the simulation and experiment. The increase ranged from 30% to a factor of roughly 2–3. The simulation showed generally greater dependence on temperature. Modeling results indicated that dissociative recombination of N_4^+ cluster ions into excited molecules and the coupling among these excited species provided the enhancement (as opposed to atomic recombination, which occurred too late with respect to the time

²⁷I.e., attenuating filters that are spectrally flat over the bands of interest.

²⁸Alternatively, the gate width could be dynamically minimized such that any increase in gate duration linearly increases the integrated signal. See Footnote 7.

delay). Peak dissociation fraction did generally increase with decreasing density due to suppression or postponement of loss pathways and prolongation of gain processes.

At the lowest densities, the model departed from the experiment, experiencing a far greater roll-off of initial signal with decreasing density. We attribute this departure to a breakdown in the validity of key modeling assumptions.

Two-term exponential fits of signal as a function of delay facilitated calculation of 1/e and $1/e^2$ lifetimes. This fitting approach improved noise tolerance and enabled extrapolation of signal intensities (to replace faulty data) and lifetimes (that exceeded the maximum time delay). Given a faster framing camera ($\gtrsim 1 \,\mathrm{MHz}$), we would have acquired all time delays within the same framing burst to enable single-shot fitting and thus reporting of variance for lifetime.

Although the model departed from PMT measurements after several hundred nanoseconds, we included simulation lifetime results for qualitative reference. The model's zero-dimensional nature likely explained its departure and drastically shorter lifetimes for $\rho \gtrsim 0.1\,\mathrm{kg\,m^{-3}}$. The experiment and simulation primarily depended on gas density, with the experiment following an approximately U-shaped trend (minimum around $\rho \approx 0.07$ –0.1 kg m⁻³). This U-shaped trend differed from the behavior at above atmospheric densities in which lifetime simply related inversely to density [5]. The experiment had an unclear, secondary (in general) dependence on temperature. Furthermore, the experimental lifetimes demonstrated only a moderate inverse dependence on initial signal intensity.

The longest experimental lifetimes occurred for $\rho \gtrsim 0.31 \,\mathrm{kg} \,\mathrm{m}^{-3}$, with the greatest among these (55 µs for 1/e; 145 µs for $1/e^2$) observed at atmospheric density.

We evaluated FLEET (Gaussian fit) velocimetry at various static conditions in flows ranging from subsonic to supersonic (or roughly 42–690 m s⁻¹) as shown in Figure 3.15. Measurement accuracy was based on the absolute-valued difference of the mean velocities of FLEET and the DAQ system whereas measurement precision was

based on the standard deviation of FLEET velocities. Additionally, we normalized these results by their corresponding mean DAQ velocities (producing values in units of %) since error and precision were assumed proportional to velocity magnitude.

Accuracy showed no obvious trends with density or temperature other than the coldest temperatures benefiting the most from lengthening time interval (Δt). The best absolute accuracy demonstrated was $< 0.01\,\mathrm{m\,s^{-1}}$ for $0.013\,\mathrm{kg\,m^{-3}}$ and $179\,\mathrm{K}$ at $\Delta t = 0.4\,\mathrm{\mu s}$ while the best normalized accuracy was $0.13\,\%$ for $0.26\,\mathrm{kg\,m^{-3}}$ and $179\,\mathrm{K}$ at $\Delta t = 0.9\,\mathrm{\mu s}$.

In contrast to accuracy, precision clearly depended upon density and temperature as illustrated by the normalized results. Precision was optimized around roughly $\rho \approx 0.016$ –0.055 kg m⁻³ (and perhaps again at the lowest densities). Reducing gas temperature improved the precision in a progressive fashion. Comparison to the signal plots revealed a seemingly more fundamental dependence on signal strength, although colder temperatures consistently produced better precision²⁹ even for similar values of signal and density. Also, the results showed the expected inverse relationship to time interval, with continual enhancement to precision for lengthening time intervals. Previous work [11] at constant, atmospheric conditions has shown precision to be directly proportional to signal intensity (really, SNR) and inversely proportional to time interval. Apart from the extended time intervals ($\Delta t = 10$ –30 µs), the best absolute precision demonstrated was 15 m s⁻¹ for 4.6 × 10⁻³ kg m⁻³ and 183 K at $\Delta t = 4.9 \,\mu s$ while the best normalized precision was 2.4% for 0.016 kg m⁻³ and 72 K at $\Delta t = 4.9 \,\mu s$.

²⁹Perhaps simply because different temperatures were produced by different jets (from different nozzles) with slightly different flow characteristics.

Chapter 4

Application of Method to Sweeping Jet Actuator in Compressible Operation

Note that much of this chapter (text, tables and figures) is adapted from Reference [9].

4.1 Background and Motivation

A sweeping jet (SWJ) actuator is an active flow control device without moving parts that discharges a continuously blowing, spatially oscillating, planar jet when supplied with pressurized gas [97, 98]. At the time of this work (mid to late 2015), direct quantitative measurements of supersonic (highly compressible) sweeping jets were limited, and no internal velocity measurements of a supersonic sweeping jet had been reported [97]. Such measurements were particularly difficult in the device's internal flow path because probes obstructed the flow and optical methods like particle image velocimetry (PIV) and Rayleigh scattering suffered from interference from laser light scattering off of windows and walls or seed particles adhering to surfaces (for PIV). Numerical simulations [99] and high-speed schlieren imaging [100] of supersonic

sweeping jets had been performed, but internal velocity measurements were restricted to subsonic (incompressible) sweeping jets [98, 101, 102].

Femtosecond laser electronic excitation tagging (FLEET) enables nonintrusive measurements of the internal and external flow of the SWJ actuator irrespective of its operating regime. The versatility of FLEET makes it well suited for studying the highly unsteady, subsonic/supersonic flow emanating from a sweeping jet actuator. Since the primary FLEET signal is non-resonant with the initial excitation, and the data acquisition is delayed from the laser pulse, FLEET circumvents any optical interference from spurious scattered light that challenges scattering-based techniques. There is also possibility of providing simultaneous concentration measurements in order to gauge the quality of mixing [13]. Mixing is potentially important for mitigating the deleterious effects of shockwave boundary layer interactions (e.g., flow separation) that occur at off-design Mach numbers.

In this chapter, we seek to study the internal and external flow field of a sweeping jet actuator operating in the compressible flow regime using FLEET. The goals are:

1) to examine the external flow field characteristics (e.g., sweep angle and velocity) and internal flow features (e.g., choking and presence of shockwaves) as they pertain to possible flow control applications, and 2) to demonstrate FLEET as a velocimetry technique suitable for measuring highly unsteady, oscillatory flows having a wide dynamic range of velocities. To this end, FLEET will be qualitatively compared to single hot-wire anemometry (HWA) in the external flow field. High-speed and phase-averaged schlieren will provide whole-field visualization and phase information about the jet. Furthermore, the possibility of simultaneously measuring concentration (to estimate the jet's mixing with the quiescent air) will be explored. All in all, this chapter showcases the capabilities of FLEET in the context of a unique and challenging application.

4.1.1 General Device Characteristics

The behavior and operation of sweeping jet actuators has been extensively studied [97, 98]. The sweep frequency and velocity of the jet depend on the ratio of the plenum (i.e., device inlet) pressure to the ambient pressure, defined here as nozzle pressure ratio or (NPR).¹ The sweep frequency also depends on the size and geometry of the device.

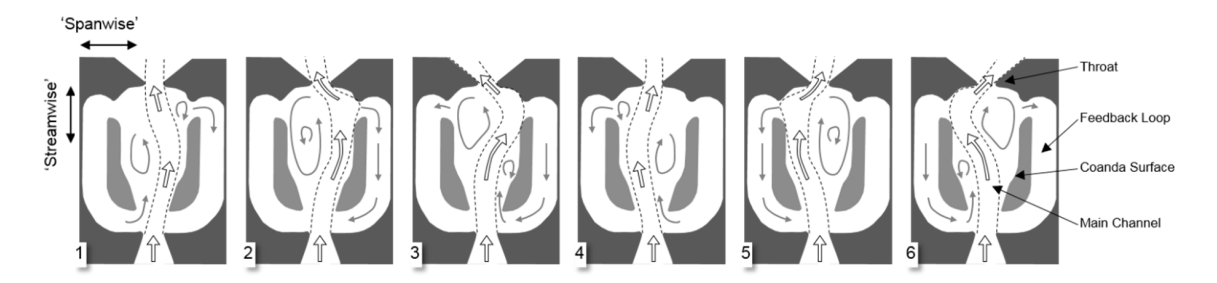


Figure 4.1: Diagram of sweeping jet actuator at six phases of its oscillation cycle. Diagram is modeled after diagrams in Ref. [103–105], but improved based upon findings from this work. Phases 1–6 correspond approximately to 0.2τ , 0.3τ , 0.5τ , 0.7τ , 0.8τ , and 1.0τ , respectively, where τ is SWJ's period. Diagram courtesy of B. F. Bathel.

Figure 4.1 shows an illustration of the device and its internal fluid dynamics at different phases of its oscillation cycle (after initial startup) as observed in the present study. The sweep mechanism can be briefly described as follows: 1–2) flow entering the main chamber entrains the surrounding air which generates a low pressure region and causes the jet to move towards and attach to one of the walls (Coandă effect); some of the flow enters the feedback loop closest to the jet, 3) flow from this feedback loop begins to strengthen the recirculation bubble (initially formed by flow separation) in between the wall and attached jet, 4) fed by the feedback loop, the recirculation bubble grows in size and eventually pushes the jet to other wall to which it attaches (Coandă effect), 5–6) the feedback process begins for the other wall and its completion marks one oscillation cycle [101]. The growth of the recirculation bubble governs the sweeping motion of the jet [106]. We will show that this description of the sweep

¹ "Pressure" is absolute pressure above vacuum.

mechanism based on incompressible results also applies to a SWJ actuator operating in the compressible regime.

4.1.2 Motivation for Studying Compressible Operation

There is considerable interest in sweeping jet actuators as an energy-efficient means of flow control since they have been shown to be as effective as steady blowing [101] while requiring less airflow [103, 107]. In one successful flow control application, SWJs were able to increase the maximum allowable deflection angle for a jetliner's rudder by delaying the onset of flow separation. This application allowed a smaller rudder (with less parasitic drag and weight) to produce the same amount of side force as a larger rudder [107]. The Boeing ecoDemonstrator 757 employs a linear array of SWJs on its vertical stabilizer for this purpose [108]. Researchers at NASA Langley Research Center desire to use SWJs to control the shock location and wake filling on a transonic wing during cruise. Steady blowing configurations showed drag improvements for offdesign cruise Mach numbers for a state-of-the-art wing [109]. These improvements are related to moving the outboard shock aft of the baseline location by as much as 5% without increasing the shock strength. The added momentum also reduces the wake deficit. Both of these phenomena imply a reduced drag. This result motivates the current study of sweeping jets operating at cruise Mach numbers greater than 0.8 (i.e., in the compressible regime) [110].

4.2 Experimental Setup and Technique

4.2.1 Configuration of Sweeping Jet Actuator

A transparent sweeping jet actuator amenable to optical measurements was constructed with an internal geometry (see Figure 4.1) similar to those being proposed for transonic flow control. The throat was approximately square with a width around

3.2 mm. The flow field was assumed to be predominantly planar since the out-of-plane depth was narrow relative to the streamwise length. External measurements of the spanwise velocity profile were made by FLEET and HWA in the plane of the jet at downstream distances of 2.5, 12.7, 25.4 and 50.8 mm from the exit. At each distance, the SWJ was operated with compressed air at pressure ratios of 1.4, 1.8, 2.0, 2.5 and 3.0. Extensive testing with other SWJ actuators revealed that these distances and NPRs were sufficient to characterize the operating behavior of the device. For the internal measurements, pure nitrogen was used instead of air at the same pressure ratios. The concentration measurements were performed with nitrogen at the downstream distances listed above for NPRs of 1.4, 1.8, 2.0 and 2.5, but the supply pressure limited the maximum achievable pressure ratio to about 2.8, as noted on the plots. Each NPR was associated with a dominant fundamental acoustic frequency as measured by a microphone (G.R.A.S. 40PP CCP Free-field QC Microphone) acquiring at a rate of 51.2 kHz. Figure 4.2 shows these data with the maximum observed frequency just below 1 kHz.

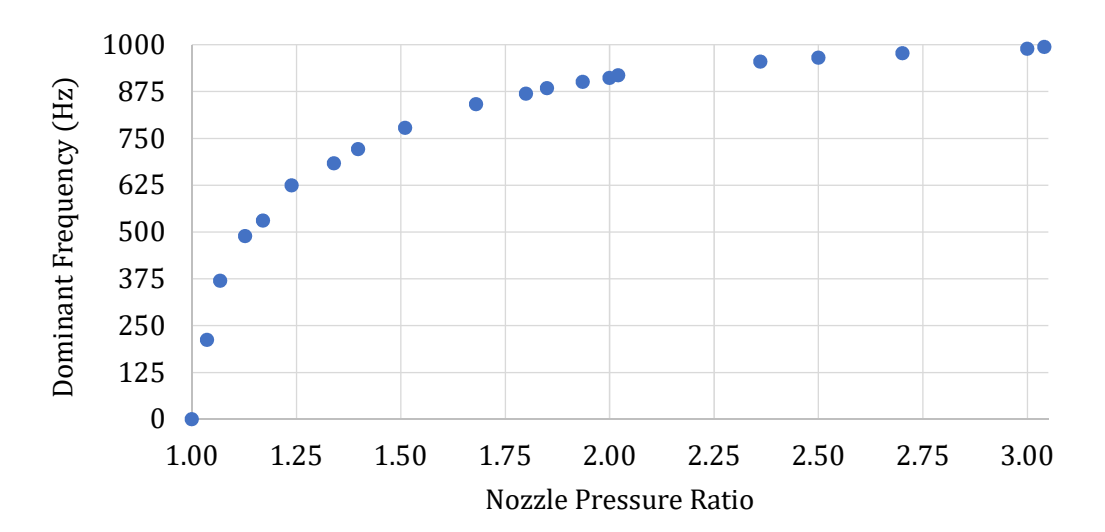


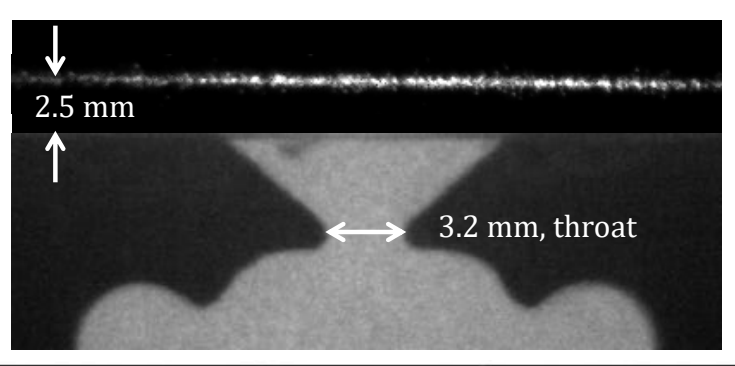
Figure 4.2: Dominant fundamental acoustic frequency as function of nozzle pressure ratio.

4.2.2 Measurement Systems and Methods

FLEET Velocimetry and Concentration Measurement

A regeneratively-amplified Ti:sapphire laser system (Spectra-Physics Solstice one-box ultrafast amplifier) generated the FLEET emission in both air and pure nitrogen. The system produced femtosecond-duration ($\approx 70 \, \text{fs}$) laser pulses centered around 800 nm at a repetition rate of 1 kHz. An ultrafast variable beam attenuator (Newport VA-800) enabled the laser pulse energy to be reduced from its maximum of 3.5 mJ. A power meter (Coherent 210) facilitated measurement of the beam energy after passage through the optical setup. Focusing and steering of the beam were accomplished with ultrafast anti-reflective lenses and ultrafast mirrors, respectively. For the external measurements, a beam with a pulse energy of 2.0 mJ (2.8 mJ for the concentration measurements) was focused by a 1-meter focal length (FL) lens. Figure 4.3 illustrates the orientation of the FLEET reference line and typical single-shot delayed lines for the external measurements. The delayed lines show the location of the jet and provide some sense of its orientation. The 1-meter FL lens enabled the writing of a FLEET line roughly 40 mm long across the jet. We intended for the long line to alleviate the need to pan the field of view to capture the entire spanwise profile and avoid perturbing the flow via energy deposition; however, writing a long line lowered the laser fluence, the FLEET signal intensity, and ultimately, adversely affected the measurement precision. This effect is discussed in more detail in Appendix C. The reduced signal intensity is evident along the edges of FLEET line in the single-shot delayed images of Figure 4.3. For the internal measurements, a pulse energy of 0.5 mJ was used along with a shorter focal length of 125 mm in order to generate a spot rather than a line.

The imaging system consisted of a two-stage intensifier (LaVision HighSpeed IRO) lens-coupled to a high-speed complementary metal-oxide semiconductor (CMOS)



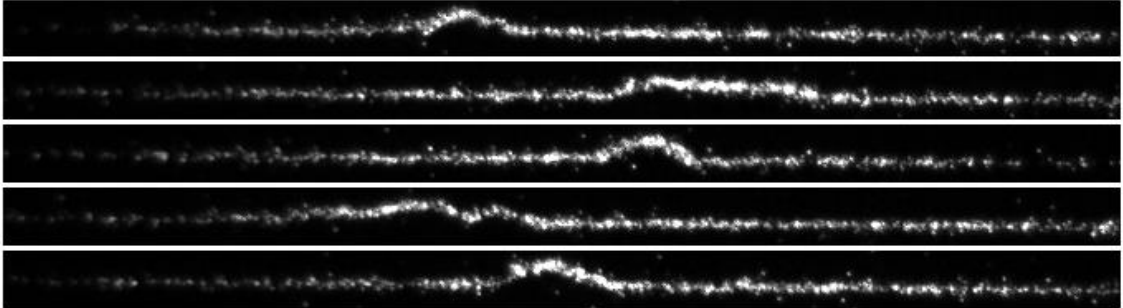


Figure 4.3: FLEET external measurements. (top) Initial spanwise reference line above actuator and (bottom) typical single-shot delayed lines for $2.5 \,\mathrm{mm}$ above exit when operating at NPR = 1.4. The single-shot images are $44.2 \,\mathrm{mm}$ wide.

camera (Photron FASTCAM Mini AX200). The camera had a full-frame (1024 by 1024 pixel) repetition rate of 6.4 kHz. The objective lens on the intensifier was an F-mount 105-millimeter FL (Nikon NIKKOR) with an aperture range of f/2 to f/16. Except for the concentration measurements, the intensifier gain was adjusted at the beginning of each run for maximum signal-to-noise (SNR) ratio. The maximum usable gain setting was that which avoided saturating the camera and avoided introducing an excessive amount of intensifier-induced spurious noise. Intensifier gate widths of 1 μ s (0.5 μ s for the concentration measurements) were used for the external and internal measurements.

The camera was unable to frame rapidly without some high spatial frequency ghosting artifacts appearing in delayed frames. So, the reference (starting) line of tagged molecules and the delayed (displaced) line were measured separately. The reference line was obtained by shutting the actuator off and then acquiring a series of images. These images were processed and the results were averaged together to

produce a reference line for calculating the displacement of the delayed line. Such a method is susceptible to errors introduced by facility vibrations or laser beam misalignment. Displacement calculations were based on the line center as determined by an in-house Gaussian fitting routine written in MATLAB. The routine calculated the displacement within each column of pixels in order to achieve spanwise velocity profiles. The resolution, at best, was roughly $65 \,\mu\text{m}\,\text{px}^{-1}$ ($15\,\text{px}\,\text{mm}^{-1}$) and was carefully measured with a dot-card target (i.e., a two-dimensional array of black dots on a white background) of known spacing. The time delays,² denoted by Δt , were adjusted for each run such that the displacement was at least several line thicknesses downstream while the signal-to-noise ratio remained acceptable. The initial intensity and lifetime of the FLEET signal were proportional to the laser fluence.

Concentration measurements (to gauge mixing) were accomplished by exploiting FLEET's signal dependence on the mole fraction of oxygen in the gas. The FLEET signal is strongest in pure nitrogen and decreases as the amount of oxygen in the gas increases since oxygen acts as a quenching agent. When imaged at short time delays, the FLEET signal varies monotonically with the concentration of oxygen [13]. Therefore, for the concentration experiments, we operated the sweeping jet with pure nitrogen. Since the SWJ emits into quiescent air, the pure nitrogen jet mixes with ambient air and the concentration of oxygen increases in proportion to the amount of mixing that occurs. Thus, the signal is highest in the unmixed regions and decreases as the mixing increases down to the point for which the oxygen concentration matches that of air. Signal intensity measurements were based on the amplitude as determined by the Gaussian fitting procedure. An initial calibration measurement was made in quiescent air in order to account for spanwise variation in the signal intensity as a result of variations in laser beam fluence. After normalization by the calibration in air, the FLEET signal intensity was assumed to depend linearly on oxygen mole

²I.e., time intervals used to calculate velocities.

fraction. Although this assumption adds uncertainty to the measurement since the relationship is actually nonlinear, this simplification was done primarily because a proper calibration curve for the signal as a function of oxygen concentration was not available for our particular setup [13]. Simultaneous concentration and velocity measurements were made by recording two data frames with each laser pulse. The first frame began 75 ns after the laser pulse and captured the reference location of the line and signal intensity used for the concentration measurement. The second frame began at the appropriate delay to capture the displaced line. Although simultaneous velocity and concentration measurements were acquired, rapid framing of the camera (and minimizing the time between subsequent exposures) led to high-spatial-frequency ghosting artifacts that impaired precise line center determination in the second frame.

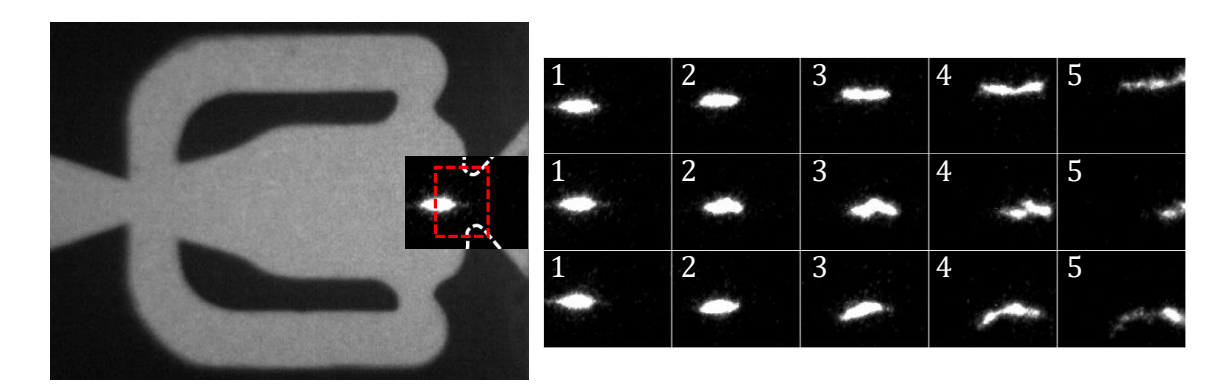


Figure 4.4: Field of view for FLEET internal measurements and typical images from bursts (frames 1-5 of 15). Flow is left to right. Pure nitrogen at NPR = 2.0. The time delay between frames was $5\,\mu s$. Image data acquired by R. A. Burns.

Internal velocity and trajectory measurements were performed by steering the laser beam into the actuator through the throat to generate a FLEET spot about 2 mm upstream of the throat as depicted in Figure 4.4 and operating with compressed nitrogen instead of air for longer FLEET signal lifetimes. Note that R. A. Burns acquired the image data used in this study. The spot advected downstream, across the field of view such that its position and thus velocity could be measured in each subsequent frame. The time delay between frames was fixed at 5 µs since the imaging

system was operated at 200 kHz in 15-frame bursts. An algorithm³ based on twodimensional cross-correlation determined the displacement of the tagged region in each frame after the initial frame. Due to the strain and breakup of the tagged region, especially during passage through the throat (see Figure 4.4), only a fraction of the 15 frames were usable. The red box approximately demarcates the domain for which internal results are reported. Note that the advection of the spot deviates from a purely streamwise motion since the jet is sweeping back and forth within the main channel as shown in Figure 4.1.

Over 2600 15-frame bursts were collected for each pressure ratio, generating an ensemble of velocity-position pairs for each pressure setting. The velocities were then grouped together according to proximity to points on a uniform grid. The grid size varied between 0.3–0.5 mm and was selected to be larger than the minimum diameter of the FLEET spot and to ensure convergence of the sum of squares of mean velocity magnitude. Grouping velocities into grid points enabled statistics such as mean and mean-subtracted RMS to be performed on the basis of position. For a plot of the grid's data point density, see Figure C.3 in Appendix C.

Hot-Wire Anemometry

Hot-wire measurements were made using a constant-temperature, single hot-wire anemometry system (Dantec 55M) with a 50 µm diameter by 2.5 mm long thin-film probe (TSI 1503). The probe was operated at an overheat ratio of 1.8 and was mounted to a three-axis traverse system for varying the spanwise and downstream position. Spanwise distance was incremented finely (0.6 mm) near the center of the jet where the velocity gradients were greatest and coarsely (1.3 mm) at the edges. Locations of spanwise measurement are noted by the individual markers on the plots. Data samples were acquired at a rate of 102.4 kHz.

³Developed by R. A. Burns.

Only external HWA measurements were performed because physical constraints prevented the insertion of hot-wire probes into the device. There was also a limit on how close the probes could be to the exit of the device where the flow is supersonic since the unsteady wind loading would damage the probes. The closest distance that did not lead to damage was 2.5 mm downstream. Also, it should be noted that HWA measurements were reported in terms of mass flux since the flow was highly compressible and the hot-wire probe is primarily sensitive to mass flux, ρu , rather than velocity, u, alone [111]. Note that ρ denotes density. Although this leads to HWA having different dimensions than FLEET, it is still possible to make qualitative comparisons between the spatial profiles of the two measurements. Hot-wire mass flux data were obtained at the same locations and operating conditions as the external FLEET measurements.

Schlieren Imaging

B. F. Bathel led the schlieren effort and his results (Figures 4.1 and 4.5–4.7) from Peters et al. [9] are included in this chapter because they provide whole-field visualization and well complement the point- and line-based measurements made by FLEET and HWA.

Density variations within the internal and external flow of the sweeping jet actuator were visualized with a two-lens schlieren system. Illumination was provided by a green LED (Luminus Devices CBT-120-G) driven by a fast laser diode driver (PicoLAS LDP-V 240-100 V3) that supplied 240-ampere pulses to the LED in a configuration similar to that described by Willert et al. [112]. A one-to-one imaging lens system was mounted in front of the LED to image its active area through an iris with a 1.25-millimeter aperture. This light was then collimated and subsequently refocused through two 400-millimeter FL, 75-millimeter diameter achromatic field lenses. A vertical knife-edge mounted to a three-axis translation stage was used to

filter the image of the sweeping jet actuator at the focus of the second achromatic lens. The resulting schlieren image was then captured through a 55-millimeter FL, f/2.8 objective lens mounted to a high-speed CMOS camera (PCO Dimax HD).

Two methods of schlieren flow visualization were employed: phase imaging and high-speed imaging. Phase imaging was accomplished by acquiring the acoustic output of the sweeping jet actuator with a microphone (G.R.A.S 40PP) powered by a constant-current power supply (G.R.A.S. 12AL CCP Module). The microphone was mounted to the right (relative to the orientation of Figures 4.5 to 4.7) of the actuator such that the top of the microphone was flush with the exit plane of the jet. The signal from the microphone was recorded with an oscilloscope (Tektronix DPO7104C). A trigger signal from the oscilloscope was used to identify the peak amplitude of the acoustic signal, which typically occurred when the jet was at the maximum extent of its sweep toward the microphone side. This trigger signal was then sent to a pulse generator (Berkeley Nucleonics Corporation 577 Digital Delay/Pulse Generator) that provided subsequent digital trigger signals to the LED unit and camera. Image sequences were acquired at sequential phases of the full sweep of the jet in increments of 50 µs. Images within any sequence that were noticeably out-of-phase with the remaining images in the sequence were removed prior to generating the 250shot phase-averaged images. For the high-speed imaging, a 10 kHz digital triggering signal from the pulse generator was sent to the LED unit and camera. For both visualization methods, a 1 µs camera exposure captured the 0.5 µs LED illumination pulse. For all of the schlieren images presented, a time-averaged background image (without flow) was subtracted from the original image sequences.

4.3 Results and Discussion

4.3.1 External Flow Field - Schlieren, FLEET and HWA

Figures 4.5 through 4.7 contain schlieren images and provide context to the quantitative FLEET and HWA results, showing the motion of the jet and the extent of its sweep. In particular, Figure 4.5 provides single-shot and 250-shot phase-averaged images of the sweeping jet (operating with air at NPR = 1.4) at approximately 0.2τ , 0.3τ , 0.5τ , 0.7τ , 0.8τ , and 1.0τ , where τ is the SWJ's period. The diagram in Figure 4.1 was based on these schlieren results. Note that simultaneous acquisition of schlieren with FLEET or HWA would have greatly complicated the experimental setup and therefore was not performed.

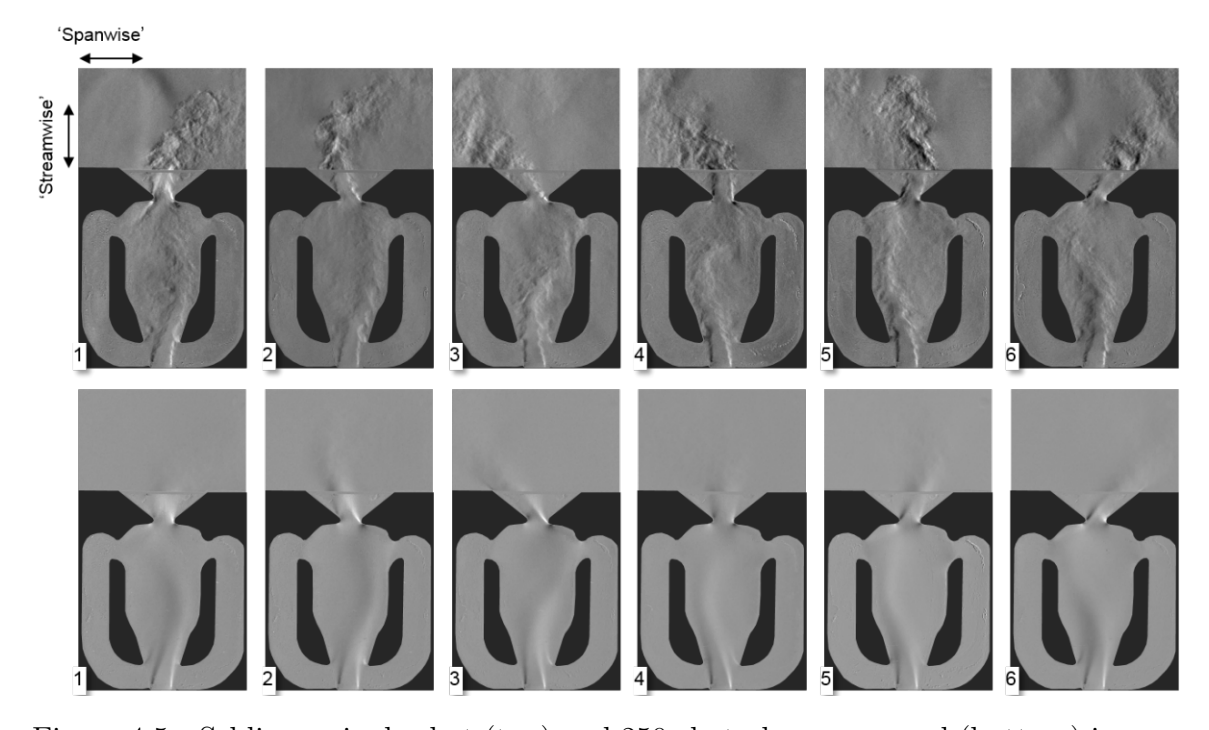


Figure 4.5: Schlieren single-shot (top) and 250-shot phase-averaged (bottom) images of sweeping jet actuator at six phases of its oscillation cycle. Operation with air at NPR = 1.4. Phases 1–6 correspond approximately to 0.2τ , 0.3τ , 0.5τ , 0.7τ , 0.8τ , and 1.0τ , respectively, where τ is SWJ's period. Image courtesy of B. F. Bathel.

Figure 4.6 compares the six phases of the jet's oscillation for each of the pressure ratios tested. The images were compiled by phase averaging 250 single shots.

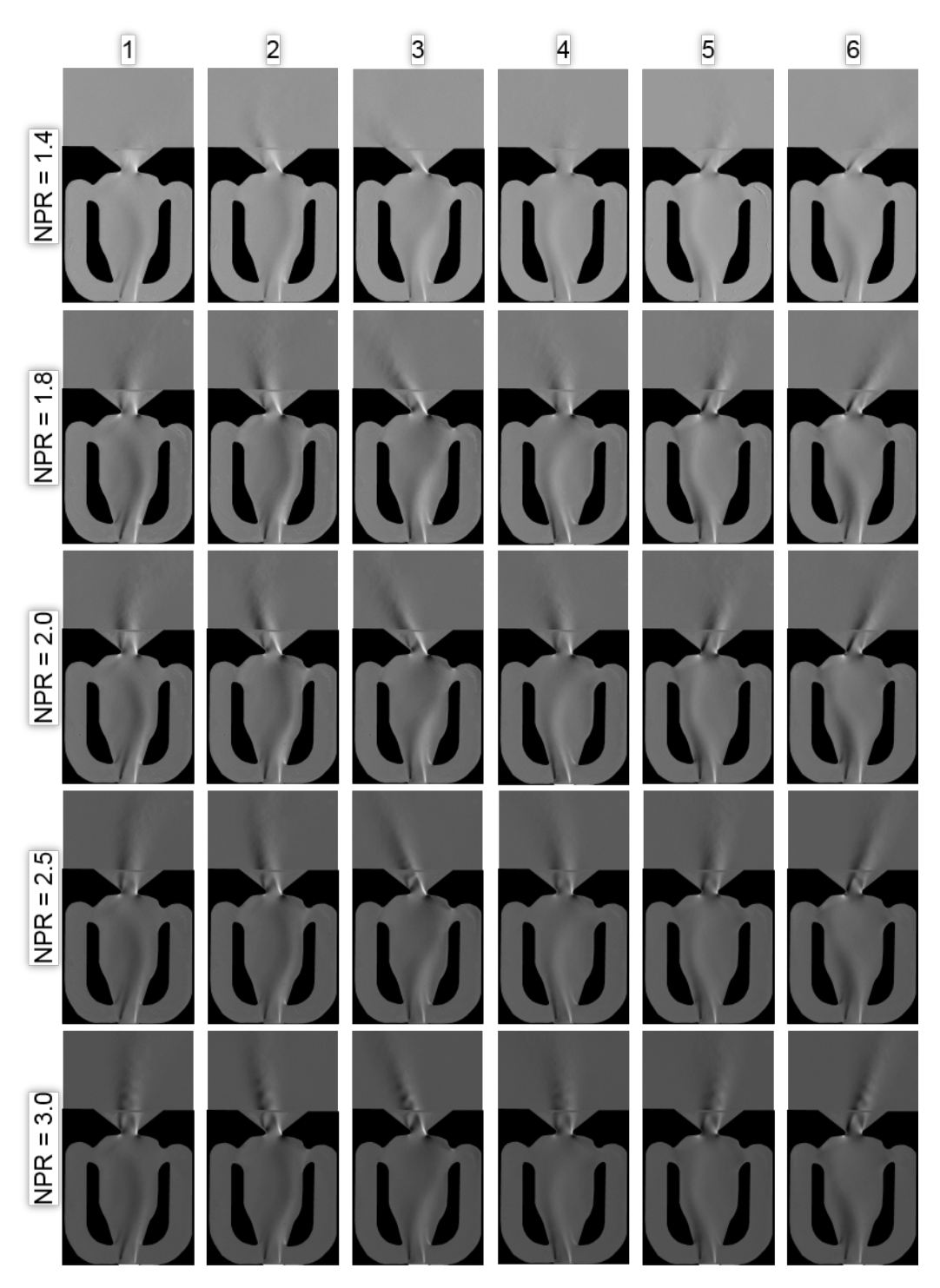


Figure 4.6: 250-shot phase-averaged images for various NPRs. Columns 1–6 correspond to same phases shown in Figures 4.1 and 4.5. Image courtesy of B. F. Bathel.

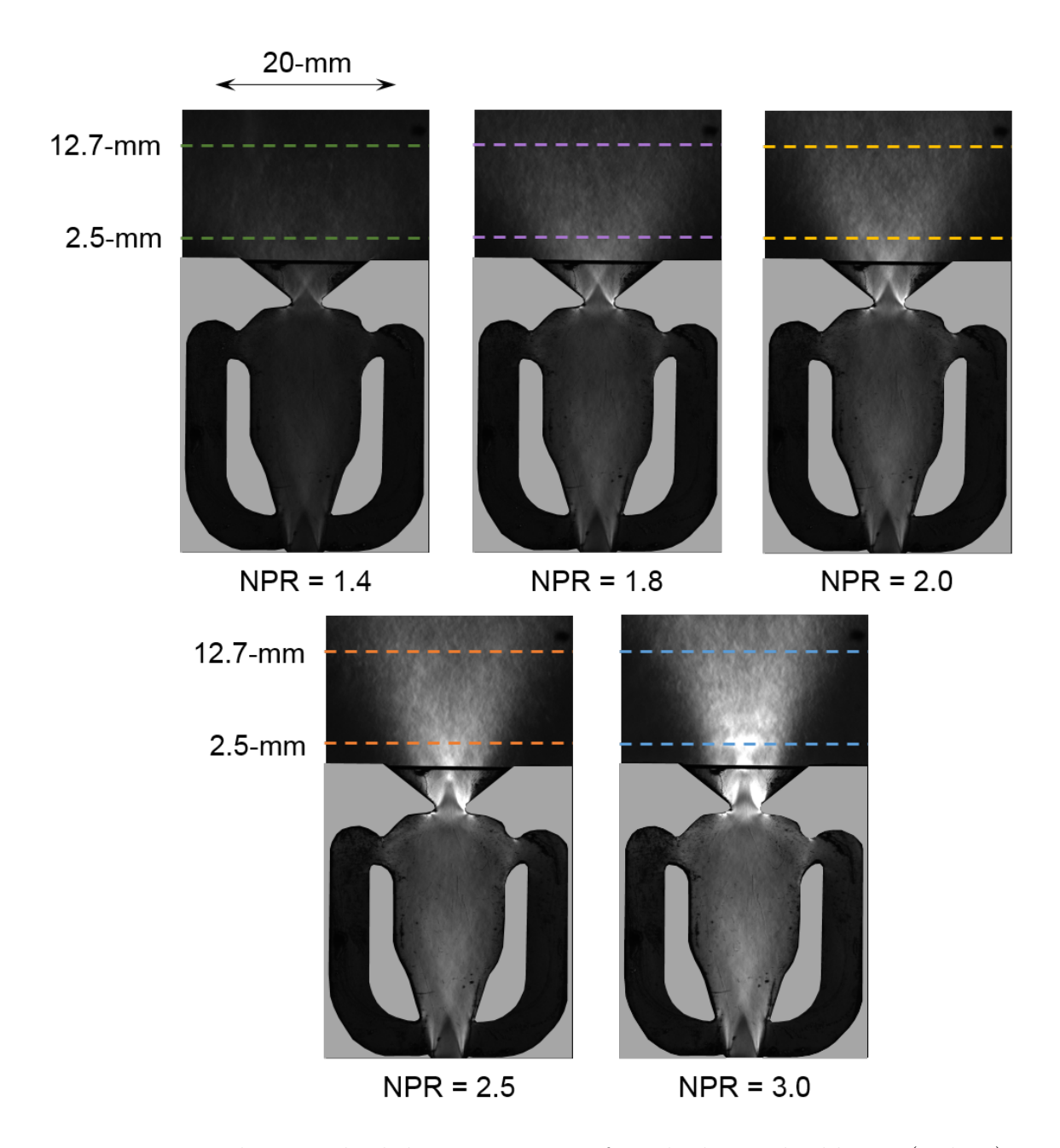


Figure 4.7: 250-shot standard deviation images from high-speed schlieren ($10\,\mathrm{kHz}$), revealing the extent of the sweep for various NPRs. Dashed lines represent the approximate locations of the external measurements. Image courtesy of B. F. Bathel.

Although the intensity of the gradients and prominence of existing flow features increases (and the external sweep angle of the jet decreases) with increasing pressure ratio, no new qualitative features arise within the internal flow field—the structure of the internal flow largely remains unchanged as the pressure ratio changes. Thus, the diagram in Figure 4.1 applies to not only an NPR of 1.4, but to all the NPRs tested, even those corresponding to compressible flow. Note, in Figure 4.6, the presence of shock diamonds in the jet exiting the device for pressure ratios of 2.5 and 3.0. These diamonds increase in intensity as the pressure ratio increases and are most visible when the jet is at the maximum extent of its sweep (i.e., columns 3 and 6). Additionally, the features visible downstream of the inlet to the main channel and in the vicinity of the throat in Figures 4.5 to 4.7, which help to define the jet, are not oblique shockwaves, but rather the shear layer of the jet. This is made clear by Figure 4.5 in which the location of the shear layer in the single shots corresponds to the location of these features in the phase-averaged images. Also, note that these shear layer features are present at subsonic pressure ratios (i.e., NPRs less than 2.0) further supporting the assertion that these are not shock structures. The only observed shockwaves were in the external jet as a result of under- or over-expansion.

Figure 4.7 shows standard deviation images of the sweeping jet operating at different NPRs (which indicate, at each pixel location, the standard deviation of the schlieren intensity based on 250 single shots acquired at 10 kHz). The dashed colored lines indicate the location of the first two external measurements relative to the nozzle exit. Figure 4.7 prominently showcases the aforementioned shear layer features, whose intensity increases as the pressure ratio increases. Also, the extent of the jet's external sweep is shown in these images, narrowing as the pressure ratio increases. Furthermore, no new flow features appear as the pressure ratio is increased, further emphasizing that the qualitative structure of the internal flow is independent of pressure ratio.

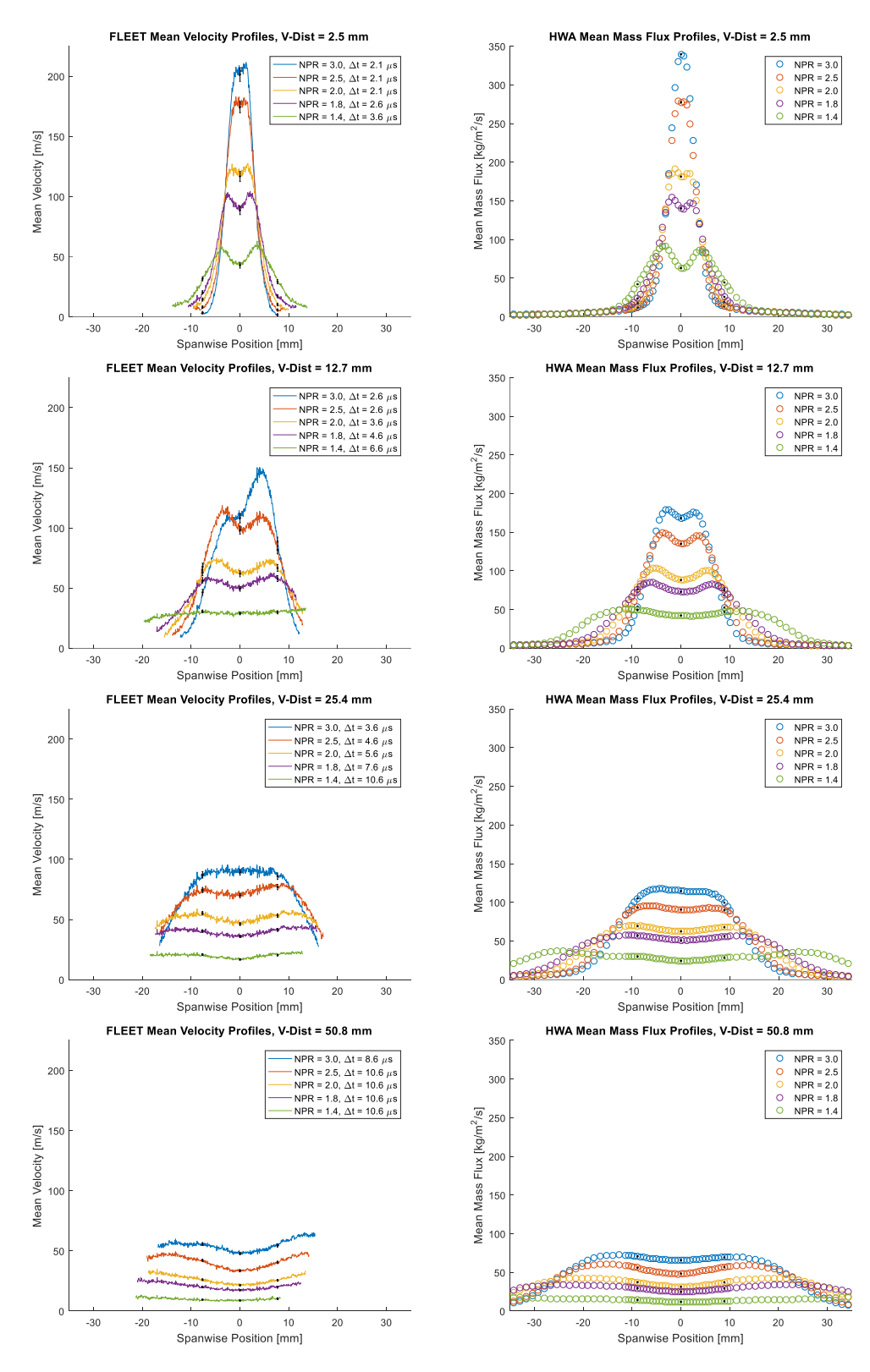


Figure 4.8: FLEET mean velocity versus HWA mean mass flux for a variety of pressure ratios and downstream distances. Black error bars correspond to 95 % confidence bounds. The time delays, Δt , for FLEET velocimetry are listed on the plots.

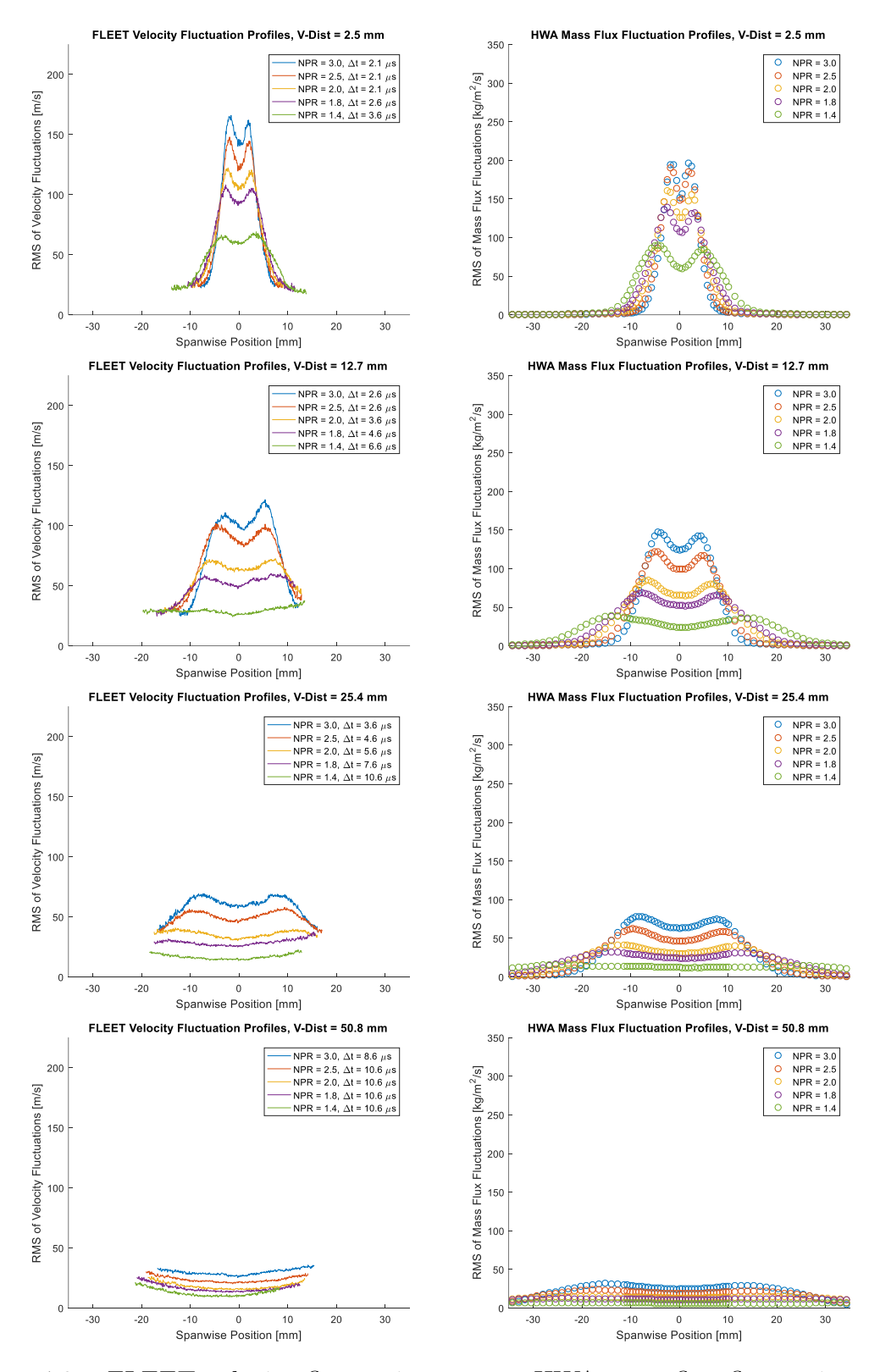


Figure 4.9: FLEET velocity fluctuations versus HWA mass flux fluctuations for a variety of pressure ratios and downstream distances.

Figures 4.8 and 4.9 contain the mean and fluctuation profiles, respectively, of the external flow field as measured by FLEET and HWA for different downstream distances and pressure ratios (for sample single-shot profiles, see Figure C.1 in Appendix C). The fluctuation profiles were obtained by computing the root mean square (RMS) of the mean-subtracted velocity fluctuations.⁴ The FLEET data were based on over 2400 single-shot measurements while hot-wire data were based on over 400 000 samples for each spanwise location. Note that excessively noisy FLEET data obtained at the ends of the probed region were excluded from the plots, explaining why the profiles do not span the entire abscissa. Data with excessive noise were identified by a loss of precision in the velocity fluctuation profiles—the measured value of fluctuations would 'diverge' from the values in the center of the jet, increasing two-to fivefold depending on the pressure ratio. Data after the point of divergence were excluded from both the fluctuating and mean profiles. The loss of precision was attributed primarily to the relatively low laser fluence and is discussed in more detail in Section C.2 of Appendix C.

Several general trends of sweeping jet actuators can be identified in the mean profiles of Figure 4.8. One such trend is that as the pressure ratio increases, the velocity increases, as expected, but the sweep angle decreases. This reduction in sweep angle with increasing pressure ratio, which is qualitatively depicted in Figure 4.7, has been observed in other studies and is undesirable because the size of the region of influence of the sweeping jet is diminished [107]. Another trend is that as the jet travels downstream, it loses velocity and broadens (consistent with PIV data) [101, 103]. These trends are expected for sweeping jets and even steady, axisymmetric jets, since the jet flow decelerates and spreads out as it transfers momentum to the quiescent surroundings. A documented feature of sweeping jets is that the rates of spreading and velocity decay are faster than a comparable steady, axisymmetric,

⁴Although equivalent to the standard deviation of velocity, we borrow this terminology from turbulent jet flows.

turbulent jet [101, 103]. Based on the HWA results, our sweeping jet exhibited a spreading rate of $\mathrm{d}y_{\frac{1}{2}}/\mathrm{d}x \approx 0.5$ –1.2, substantially larger than the spreading rate of $\mathrm{d}y_{\frac{1}{2}}/\mathrm{d}x \approx 0.1$ for steady turbulent jets [113]. Here and elsewhere, x and y stand for the streamwise and spanwise position coordinate, respectively. The spreading rate for the SWJ increased as pressure ratio decreased. Note that jet half-width, $y_{\frac{1}{2}}$, was defined as the average spanwise position for which the mass flux decreased to one-half of its maximum value within the spanwise profile.

It should also be noted that although the mean velocities are less than the local speed of sound ($\approx 320 \,\mathrm{m\,s^{-1}}$ for an isentropic expansion from the source with a total temperature of $T_0 = 308 \,\mathrm{K}$), the jet contains a significant number of instantaneous velocities that are supersonic. This is evident in the FLEET velocity histograms of Figure 4.10 for NPRs of 2.5 and 3.0 at 2.5 mm downstream, the single-shot velocities of Figure C.1 (in Appendix C) for an NPR of 3.0 and by the presence of shock diamonds in the phase-averaged images of Figure 4.6.

Visually comparing FLEET to HWA, the spanwise profiles are, in general, qualitatively similar. One difference is that the width of the jet was slightly broader for FLEET than HWA. This might be explained by 1) the measurement locations being at different downstream distances during the two sets of testing since the tests were performed in different laboratories and 2) the finite time delay of the FLEET measurements allowing for spanwise velocity components to effectively broaden the jet between the first and second exposures. Both effects were estimated to be of similar order. Another difference is that the FLEET data measured an asymmetrical jet profile in certain cases, particularly for 12.7 mm downstream at NPRs of 2.5 and 3.0. The jet may have been slightly disturbed during the data acquisition period (which occurs over 2.4 s), causing the profile to be skewed. It is also possible that jet and laser were partially phase-locked since they were operating at similar frequencies (near 1 kHz). However, the phase-locking would not have been complete since the jet

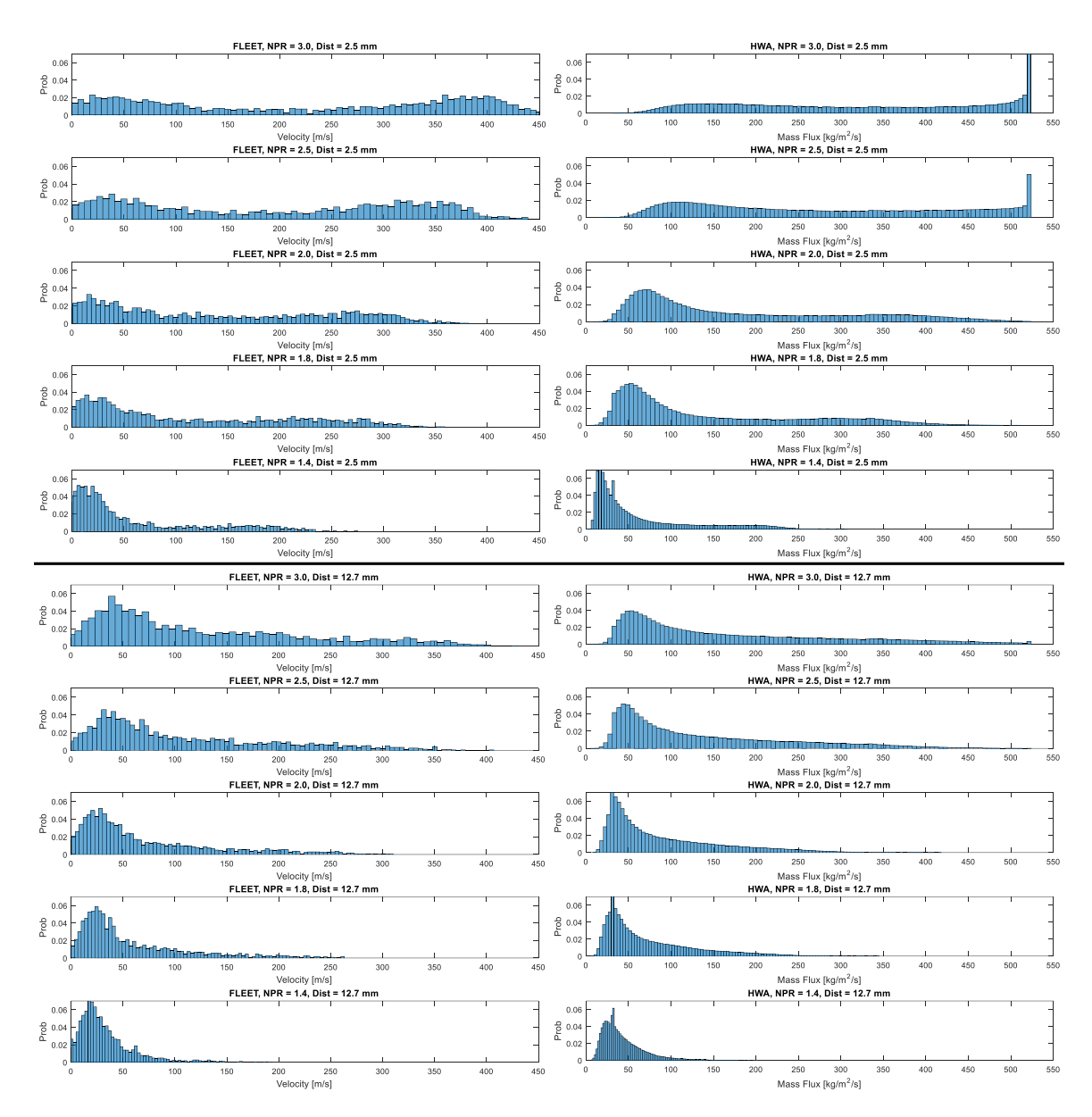


Figure 4.10: Histograms of centerline FLEET velocities versus HWA mass fluxes for a variety of pressure ratios and downstream distances. For sake of brevity, data at 25.4 and $50.8\,\mathrm{mm}$ were omitted.

has prominent overtones at frequencies other than its fundamental. There are also noticeable asymmetries in the data at 25.4 and 50.8 mm. This may have been the result of the translation stage, which enabled the downstream distance to be varied, not translating perfectly in the streamwise direction and causing the jet flow to be slanted.

It should also be mentioned that the HWA testing was not without its sources of uncertainty. During testing, the stagnation temperature of the flow drifted as much as $5 \, \mathrm{K}$ in some cases and was not accounted for in the calibration. Also, for the higher-speed data, some of the mass fluxes substantially exceeded the instrument's calibration range and were coerced to the highest value on the calibration curve (which itself was an extrapolation from the highest measured calibration point). This is evident by the peak around $520 \, \mathrm{kg} \, \mathrm{m}^{-2} \, \mathrm{s}^{-1}$ in the HWA mass flux histograms for $2.5 \, \mathrm{mm}$ downstream and NPRs of $2.5 \, \mathrm{and} \, 3.0$ (Figure 4.10).

The fluctuation quantities in Figure 4.9 are similar in magnitude to their counterpart mean quantities in Figure 4.8. The ratio of fluctuation to mean quantities is significantly larger than that of a comparable steady, axisymmetric, turbulent jet. This feature of SWJ actuators has been previously observed and is caused primarily by the sweeping motion of the jet (i.e., for a given location, the jet is present for certain instances and absent for others, leading to significant fluctuations with respect to time) [103].

Like the mean profiles, the fluctuation profiles are, in general, qualitatively similar for both FLEET and HWA. Again, the FLEET fluctuation profiles possess an asymmetry that is not present in the hot-wire data, probably for the same reasons mentioned above. Perhaps the most striking difference is that the FLEET fluctuation profiles exhibit an offset: in the low velocity, 'quiescent' regions, the profiles decay to a finite value (e.g., $\approx 25\,\mathrm{m\,s^{-1}}$ for 2.5 mm downstream) rather than zero. This offset

is attributed to the precision of the FLEET measurement which varies inversely with time delay [11] (see Appendix C for measurements of the precision).

Figure 4.10 shows the histograms of the FLEET and HWA measurements at the center spanwise location of the sweeping jet for 2.5 and 12.7 mm downstream for the five tested NPRs. The histograms at 25.4 and 50.8 mm were omitted for the sake of brevity. The general trend is that the spread of data narrows and amasses toward the lower values as downstream distance increases or pressure ratio decreases. This trend holds for 25.4 and 50.8 mm. The right-most peaks around 520 kg m⁻² s⁻¹ for 2.5 mm downstream at NPRs of 2.5 and 3.0 are a result of the hot-wire probe measuring fluxes above its calibration range. The highest calibration point was 470 kg m⁻² s⁻¹ and a third-order polynomial permitted extrapolation to 520 kg m⁻² s⁻¹. As mentioned previously, values exceeding the upper bound of extrapolation were coerced to 520 kg m⁻² s⁻¹. Conspicuous peaks for NPRs of 2.5 and 3.0 at 2.5 mm, along with evidence of supersonic velocities (from FLEET), indicate that the hot-wire calibration should have been extended to higher mass fluxes.

Regarding the FLEET data, there was substantial supersonic flow ($\gtrsim 320\,\mathrm{m\,s^{-1}}$) for NPRs of 2.5 and 3.0 at 2.5 mm, but this supersonic contribution diminished quickly once the pressure ratio was lowered or the downstream distance was increased. There were some supersonic velocities at 12.7 mm, but most of the velocities were subsonic with a large grouping below $100\,\mathrm{m\,s^{-1}}$.

Overall, the FLEET and HWA histograms were similar to one another and both flow quantities tended to decrease as distance increased or pressure ratio decreased. Nevertheless, there are several specific differences worth noting. First, the FLEET results appear nosier since they were computed from significantly fewer measurements than HWA (2400 versus 400 000). Second, there are relatively few results below $50 \,\mathrm{kg}\,\mathrm{m}^{-2}\,\mathrm{s}^{-1}$ for the hot-wire (i.e., an offset) whereas FLEET has measurements of zero velocity. This offset is most noticeable at 2.5 mm for NPRs of 2.5 and 3.0 and can

be attributed to several factors. One factor, which plays only a small part, is that the hot-wire suffers from reduced sensitivity to low mass fluxes. Another factor, which plays a larger part, is that the FLEET measurements (at 1 kHz) were inadvertently phase-locked to the jet (oscillating at nearly 1 kHz for these NPRs), leading to over sampling of the phases associated with lower velocity. The higher sampling rate of HWA (102.4 kHz) is more immune to phase-locking errors. One possible solution would have been to lower the FLEET data acquisition rate from its maximum of 1 kHz to, say, 10 Hz to achieve a more uniform sampling of the phases. A third and similarly important factor is that the hot-wire probe primarily senses net mass fluxes perpendicular to the axis of the wire whereas FLEET (in the present setup) only senses velocities in the streamwise direction. Therefore, when the jet is directed away from the centerline and at an angle relative to the streamwise direction, it has large spanwise velocity components (relative to the streamwise components) and the hot-wire would tend to measure higher mass fluxes (i.e., 'velocities') than FLEET which is insensitive to the spanwise components.

In general, FLEET is a direct measurement of velocity (resolving both magnitude and direction) for subsonic through supersonic flows whereas HWA has a limited ability to measure velocity magnitude outside a very specific range of flow regimes.

4.3.2 Internal Flow Field - FLEET

Figure 4.11 shows the mean streamlines, mean velocities and RMS of velocity fluctuations for an initial spot location of $(x, y) = (-6.2 \,\mathrm{mm}, 0.2 \,\mathrm{mm})$ at the five pressure ratios. Note that these data are presented with the SWJ oriented as shown in Figure 4.4, where the red box approximately demarcates the domain of reported measurements. Data for $x > -3.3 \,\mathrm{mm}$ were not reported because strain and breakup of the tagged region rendered the measurements unusable. It should also be noted that these plots are not true Eulerian velocity maps (as is commonly outputted by

computational fluid dynamics) since they were created by tracking the advection of a single tagged region a number of times. The measurement is analogous to injecting dye into a liquid flow at a point to visualize the flow field, but more quantitative. Also note that these results could be compared to a computer simulation with Lagrangian particle tracking and filtering for only those particles that pass through the initial spot location.

Inspecting Figure 4.11, the mean streamlines show that the flow is predominantly along the streamwise direction with some turning upstream of the throat (which is located at $x = -4.0 \,\mathrm{mm}$). The turning indicates that some of the flow is entering the feedback loops.

The mean velocity plot shows a positive velocity gradient in the streamwise direction and depressed velocities off of the centerline axis. The gradient is expected since this region of the actuator acts as a converging nozzle. Significant acceleration downstream of the throat for NPRs of 2.0 and above confirms the presence of choked flow (i.e., sonic at throat) since the flow continues to accelerate as it travels through the diverging diffuser.

The largest velocity fluctuations are localized to the region downstream of the throat (most conspicuously for NPRs of 2.5 and 3.0). These velocity fluctuations are roughly 40–60% of the values found in the external flow for the corresponding NPRs at 2.5 mm downstream (cf. Figure 4.9). This has several possible explanations: 1) the favorable pressure gradient in this region acts to suppress velocity fluctuations, 2) the measured velocities are spatially filtered such that the streakline must pass through the initial spot location, therefore, not all velocities (and velocity fluctuations) are included in this map, 3) there are no shocks in this region (unlike the external jet which has shock diamonds at NPRs of 2.5 and above) which tend to amplify turbulent fluctuations [114] and 4) the precision of the internal measurement is likely better than

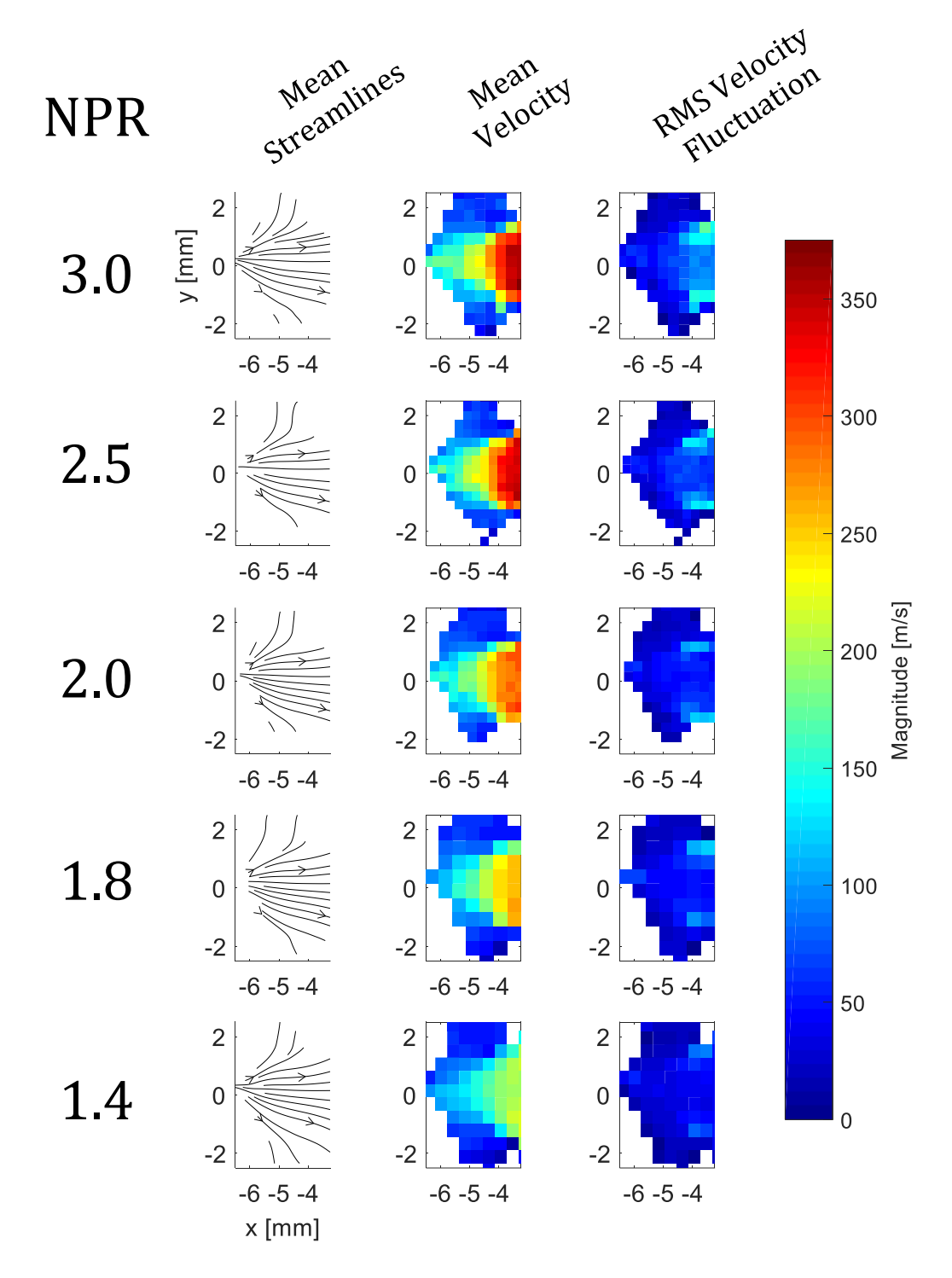


Figure 4.11: FLEET measurements of internal flow field. Throat and centerline were at positions of $x = -4.0 \,\text{mm}$ and $y = -0.2 \,\text{mm}$, respectively. The spot's origin was around $(x,y) = (-6.2 \,\text{mm}, 0.2 \,\text{mm})$.

the external measurement due to the improved SNR associated with the relatively high laser fluence and use of pure nitrogen.

Note that the gradients of mean velocity and velocity fluctuation both increase as NPR increases, with the mean velocity gradient having the more prominent increase.

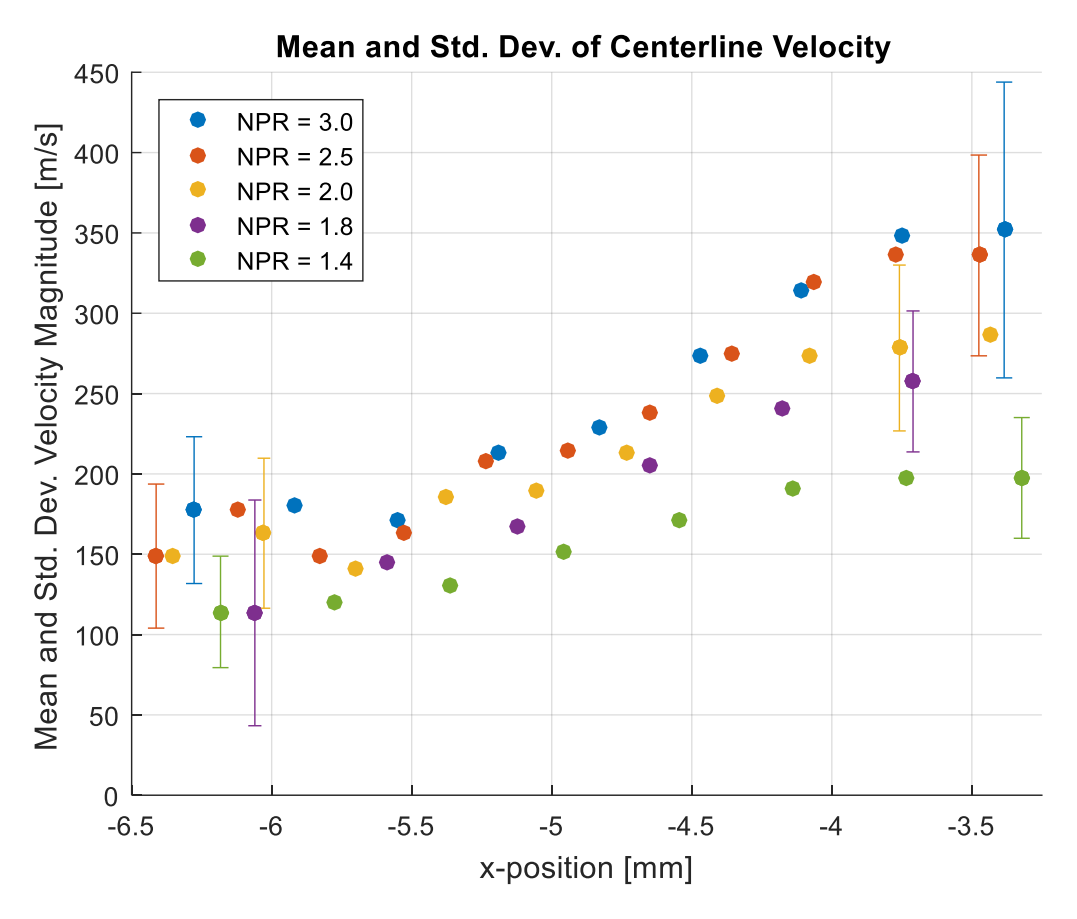


Figure 4.12: Mean centerline velocities from internal measurements. Error bars denote one standard deviation.

Figure 4.12 plots the mean velocity along the centerline axis to illustrate the dependence of acceleration on the nozzle pressure ratio. The error bars denote one standard deviation of velocity and indicate the magnitude of the fluctuations. Based on the plot, there was no evidence of a strong normal shockwave⁵ inside the actuator since a precipitous velocity decrease was absent. A strong shock was also noticeably absent from the schlieren images. Furthermore, the plot illustrates presence of

⁵There was initially some speculation that a shock might be present and causing the observed narrowing of the sweep angle with increasing pressure ratio.

supersonic flow for NPRs of 2.0 and above since the sum of the mean and standard deviation exceeds the local speed of sound ($\approx 310\,\mathrm{m\,s^{-1}}$ for an isentropic expansion from $T_0 \approx 294\,\mathrm{K}$), corroborating previous statements about NPRs of at least 2.0 exhibiting choked flow. In particular, NPRs of 2.5 and 3.0 experience 'mostly continuous' choking while an NPR of 2.0 experiences 'intermittent' choking. This is supported by the external velocity histograms in Figure 4.10 which display noteworthy supersonic contributions for NPRs of 2.0 and above. A pressure ratio of 1.8, just below the necessary isentropic value of 1.89, seems to be on the cusp of choking, but not yet choking; any apparent supersonic velocities in its histogram are likely an artifact of measurement imprecision rather than intermittent choking.

4.3.3 Concentration in the External Flow Field - FLEET

Figure 4.13 shows the mean profiles (based on 1200 single-shot images) of relative oxygen mole fraction as estimated from changes in FLEET signal intensity obtained 75 ns after the laser pulse. A relative mole fraction of zero corresponds to pure nitrogen whereas a mole fraction of one corresponds to air. Mixing is gauged by noting the jet's relative mole fraction evolution from zero to values approaching one. The profiles are grouped by pressure ratio with each curve denoting a different distance downstream of the exit. There were no discernible changes in signal intensity beyond 25.4 mm for pressure ratios of 1.4 and 1.8; therefore, data at 50.8 mm were not reported.

Note that these results have not been corrected for the signal variation that occurs due to the compressibility of the gas; experiments have shown that FLEET signal intensity depends linearly on gas density⁶ [5, 12]. Therefore, these plots are primarily proof-of-concept, qualitative estimates of mole fraction that showcase an added benefit of FLEET-based measurements. Nevertheless, there are potential ways

⁶See Section 3.4.1 in Chapter 3.

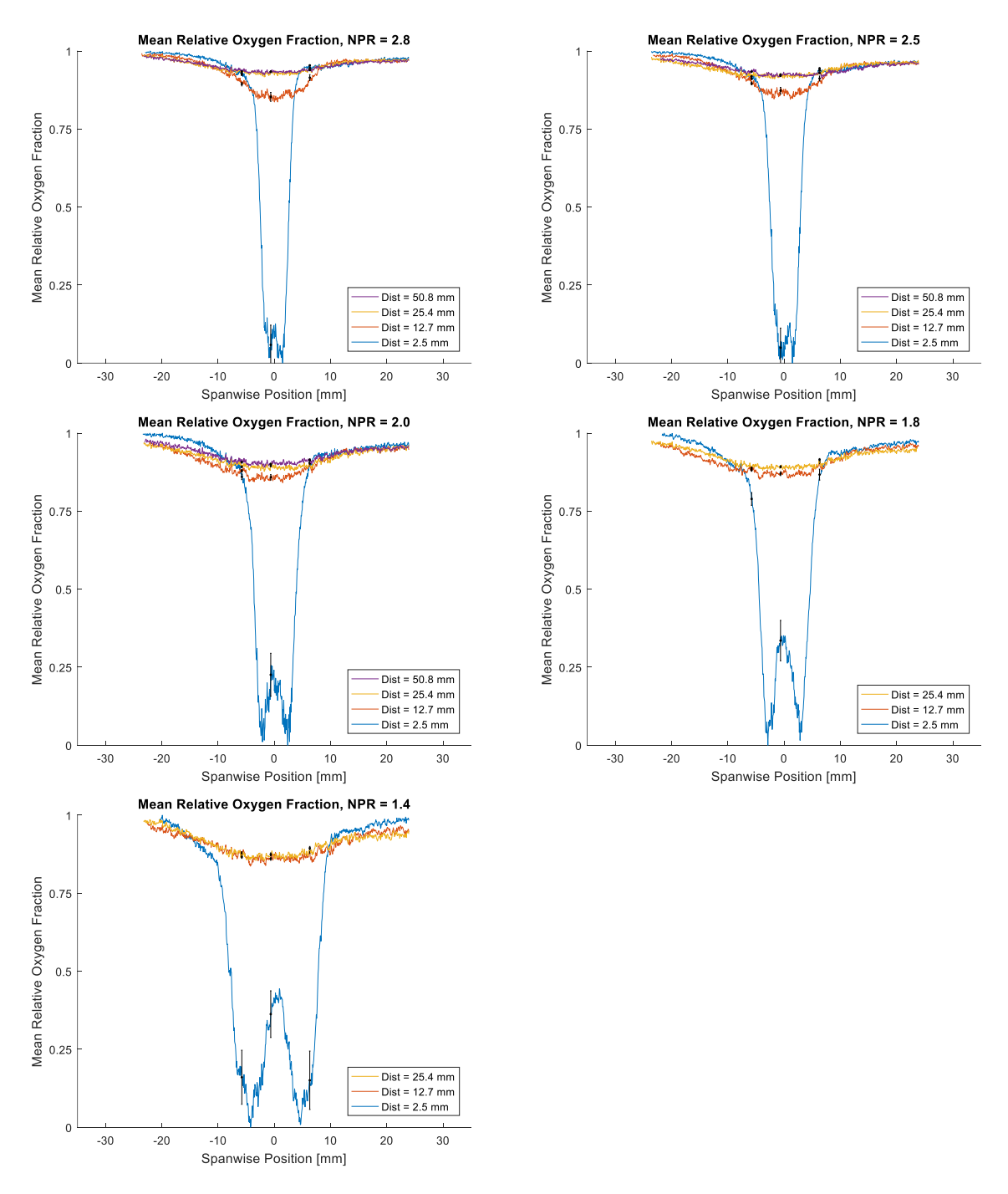


Figure 4.13: Profiles of relative oxygen mole fraction based on FLEET signal intensity for different pressure ratios and downstream distances. Black error bars denote $95\,\%$ confidence bounds.

of decoupling the influence of density on the concentration measurements. One such way is to take measurements of the SWJ running air instead of nitrogen as a type of calibration. The resulting mean profiles would contain only the effects of density and spatial variation of laser fluence since the concentration of oxygen would be fixed. Then, concentration measurements with the SWJ running compressed nitrogen could be taken. Dividing the nitrogen (data) curves by the air (calibration) curves should isolate concentration's effect on signal intensity and therefore yield an accurate mean measurement of oxygen concentration. A second option is to measure the Rayleigh scattering from the femtosecond laser pulse since Rayleigh scattering is proportional to gas density. This would have the advantage of allowing for single-shot density measurements in addition to time-averaged ones.

Neglecting the effect of variable density, these plots convey that the jet becomes well mixed (i.e., oxygen mole fraction increases to within a few percent of the ambient value) within 12.7 mm or roughly four throat widths downstream of the exit and fully mixed (i.e., oxygen mole fraction asymptotes to within a few tenths of a percent of the background level of oxygen in the vicinity of the SWJ outlet) within 25.4 mm or roughly eight throat widths. These changes in signal intensity would be difficult to attribute primarily to density since it did not change by a factor of 7 to 14 (which was the observed change in signal intensity). The dip in the center of the curves for pressure ratios of 2.0 and above is probably the combined result of density variation and the reduced mixing associated with lower velocity fluctuations (cf. dips in velocity fluctuations in Figure 4.9).

The lack of overlap for the wings of some of the curves was caused by the baseline calibration in air being taken without the jet running and with slightly different camera settings (unavoidable because of experimental difficulties). The inconsistencies in the wings should be given marginal weighting since, at the very least, density was not decoupled and a proper baseline calibration was not obtained. The overall trend of

rapid mixing should be accepted as reasonably valid since there were no other known sources which could account for the factor of 7 to 14 change in signal.

Although velocity measurements were made simultaneously with the concentration measurements, they are not reported herein. The simultaneous velocity measurements, made when operating the camera/intensifier in a frame-straddling mode, were excessively noisy because of difficultly in precisely discriminating the displaced line from an un-displaced ghosting artifact. The ghosting problem occurred when framing the camera at 40 kHz; if the falling edge of the first intensifier gate was very close to the end of the first camera exposure (necessary for achieving short time delays), up to 40 % of the signal would bleed into the next frame.

4.3.4 Comparison of FLEET Velocimetry and Hot-Wire Anemometry

Since both FLEET and HWA were utilized in this experimental investigation, it is worth discussing how FLEET velocimetry compares to more traditional, single hotwire anemometry.

- Strengths of FLEET relative to HWA:
 - Instantaneous line (or point) measurements of FLEET with every data capture; single-shot spatial cross-correlations and velocity profiles (via line measurements)
 - Faster data acquisition since no traversing is needed to obtain spatial profiles
 - Larger dynamic range of measurement (subsonic to supersonic, discriminate negative velocities)
 - Nonintrusive, tolerant of tight spatial constraints since laser-based: able
 to make measurements inside the actuator

Simpler calibration since only ruler/dot-card is needed in contrast to calibration wind tunnel

• Weaknesses of FLEET relative to HWA:

- More computationally intensive image processing rather than polynomial lookup
- Optical access required since laser-based
- Optics in path of laser beam must be compatible with femtosecond duration laser pulses
- Significantly more expensive acquisition system (laser, camera and intensifier)

The relatively poor precisions measured during post-SWJ testing were not listed as a weakness since they were not inherent to the technique, but rather the result of the particular experimental setup (which employed low laser fluences). Use of higher laser fluences can yield precisions in air of better than a few meters per second [11, 115].

4.4 Summary and Conclusions

FLEET velocimetry was successfully demonstrated in a highly unsteady, oscillatory flow containing subsonic, transonic, and supersonic velocities. Measurements were made in the external flow field with FLEET and single hot-wire anemometry (for qualitative comparison). Measurements of the internal flow field inside the actuator were made with FLEET alone. High-speed and phase-averaged schlieren provided visualization of both external and internal flows.

The external FLEET velocity profiles were, in general, qualitatively similar to the mass flux profiles measured by HWA; however, two potential drawbacks were noted. 1) The FLEET measurements (acquiring at $1\,\mathrm{kHz}$) may have been partially phase-locked with the sweeping jet (dominant frequency around $1\,\mathrm{kHz}$), possibly explaining the reason for asymmetric jet profiles which were not observed in the HWA results. 2) FLEET suffered from noticeably worse precision ($\lesssim 25\,\mathrm{m\,s^{-1}}$) than HWA, attributable to the relatively low laser fluences utilized in the experiment. The low laser fluence was a consequence of writing a long line to simplify data acquisition and minimize perturbation of the flow via energy deposition. Unfortunately, this low laser fluence ultimately resulted in degraded measurement precision. Previous experiments have reported precisions of a few meters per second in air and less than one meter per second in nitrogen when operating at higher laser fluences; therefore, the low precision was a result of the chosen experimental setup, not a fundamental limitation of the technique. In general, FLEET demonstrated better overall dynamic range and improved sensitivity to low velocities, in addition to explicitly measuring velocity in the compressible flow regime.

The expected trends in the external profile of the sweeping jet were observed such as an increasing jet velocity (desirable) and decreasing sweep angle (undesirable) with increasing pressure ratio. Furthermore, the jet had significant spreading and velocity decay rates as expected.

FLEET provided measurements of the internal flow field which were inaccessible to probe-based methods and would have been difficult to perform with certain other nonintrusive methods. The velocity and fluctuation gradients within the device were mapped out and indicated a choked condition (i.e., sonic flow at the throat) for pressure ratios greater than or equal to 2.0. Also, there was no evidence of a shockwave (sudden decrease in velocity) inside the device during operation.

Qualitative mixing measurements were demonstrated as a proof-of-concept. This is a potential added-benefit of FLEET velocimetry. The measurements were based on the signal intensity variation of FLEET with oxygen concentration and were pri-

marily qualitative since there was no correction for the density change resulting from compressibility. A method was described to correct for the density variation in future work. The mixing measurements conveyed that the jet became well mixed within 12.7 mm downstream (or roughly four throat widths downstream) and fully mixed within 25.4 mm (or roughly eight throat widths).

The high-speed and especially the phase-averaged schlieren images demonstrated that the general character of the internal flow is largely independent of pressure ratio—no new flow structures arise (other than changes to the magnitude of gradients or features). The structure of the external flow evolves with pressure ratio in the sense that the sweep angle decreases and shock diamonds appear.

Chapter 5

Practical Considerations for

Precise Measurements

Note that much of this chapter (text, tables and figures) is adapted from Reference [11].

5.1 Background and Motivation

In this chapter, we determine the fundamental precision¹ of femtosecond laser electronic excitation tagging (FLEET) velocimetry using high-speed (i.e., fast-framing) complementary metal-oxide semiconductor (CMOS) cameras, compare the performance of several different types of high-speed CMOS camera systems for acquiring FLEET velocimetry data and explore various strategies for enhancing FLEET measurement precision.

Based on the suitability demonstrated here for making satisfactory FLEET measurements, we utilized high-speed CMOS cameras almost exclusively when acquiring image data for the dissertation. Moreover, the performance comparison (Section 5.3.2) directly influenced the camera choice (Photron FASTCAM Mini AX200,

 $^{^1\}mathrm{See}$ Appendix A for the conceptual difference between accuracy and precision.

 $20\,\mu\text{m}$ pixels) for testing at transonic cryogenic conditions by Burns et al. [5]. Although this work was performed in relatively low speed (roughly $0.2\text{--}60\,\text{m}\,\text{s}^{-1}$) free jets of air and nitrogen, many of the experimental approaches likewise apply to measurements at much higher speeds (such as those presented in Chapters 3 and 4). In particular, the strategies from this chapter which were employed elsewhere to improve measurement quality include:

- Elongation of time delay (i.e., time interval) between successive exposures to enhance precision²
- Multiple-frame bursts to eliminate artifacts (ghosting and accumulation) and provide relevant backgrounds
- Double shutter operation (i.e., separate, sequential data frames) to simplify processing and reduce susceptibility to building vibrations or beam steering
- Gaussian fitting of intensity profiles for precise and robust³ determination of advective displacement
- Avoidance of repeated interrogation of stagnant regions at high rates which lowers signal intensity and thus precision

5.1.1 Alternative Unseeded Velocimetry Methods

In addition to FLEET, other laser-based diagnostic methods exist for performing velocimetry in unseeded⁴ air. A comparison of FLEET to these methods in terms of absolute precision is found within the conclusion (Section 5.4) of this chapter.

 $^{^2}$ This enhancement is clearly observed in Section 3.5.3 of Chapter 3 and Section C.2 of Appendix C.

³Section 3.5.1 of Chapter 3 showcases the advantages of Gaussian fits over intensity-weighted centroids for determination of displacement.

 $^{^4}$ Air containing only naturally occurring concentrations of constituent species, such as N_2 , O_2 , Ar, H_2O , etc.

For example, Raman excitation plus laser-induced electronic fluorescence (RE-LIEF) employs stimulated Raman excitation and laser-induced electronic fluorescence to track molecular oxygen [116, 117]. Air photolysis and recombination tracking (APART) relies on an ultraviolet laser to dissociate oxygen and nitrogen to form nitric oxide, which is then tracked by laser-induced fluorescence [118]. In ozone tagging velocimetry (OTV), an ultraviolet laser photo-chemically generates ozone which is then photodissociated into vibrationally excited oxygen to enable tracking by laserinduced fluorescence [119]. Filtered Rayleigh scattering (FRS) employs a narrow linewidth laser and a notch frequency filter to capture scattered light which has been Doppler shifted by the flow velocity, providing images of the velocity field, although results are usually time-averaged [120]. Another variation of Rayleigh scattering, called interferometric Rayleigh scattering (IRS) uses an etalon to disperse the scattered light from one or a few points in the flow to determine the velocity [121]. Laser induced thermal acoustics (LITA) uses crossed laser beams to generate an electrostriction grating that scatters a third beam resulting in a Doppler shift to measure flow velocity in unseeded air flows [122].

Although these methods enable velocimetry of unseeded air, they all involve more complicated diagnostic setups than FLEET. RELIEF requires three lasers (two⁵ to vibrationally tag oxygen molecules and one to interrogate them) along with an intensified camera. APART and OTV require two lasers (one to create the species of interest from air and another to interrogate the species) and an intensified camera. LITA requires two lasers, one for forming the grating and one to probe the grating and requires that all three beams must cross at a point in the flow. Although FRS and IRS use only one laser and one camera, they also require spectrally dispersive elements: a notch frequency filter (such as a molecular iodine or atomic mercury absorption cell) in the case of FRS and an interferometer in the case of IRS in order to

 $^{^{5}\}mathrm{A}$ Raman shift cell can be used to produce the second laser beam.

obtain velocity information about the flow. By comparison, FLEET uses a single laser and single camera, with an optional thin optical filter to block spurious laser light. Furthermore, FLEET shows promise for improved measurement precision compared to FRS and IRS.

5.2 Experimental Setup and Technique

5.2.1 Femtosecond Laser System

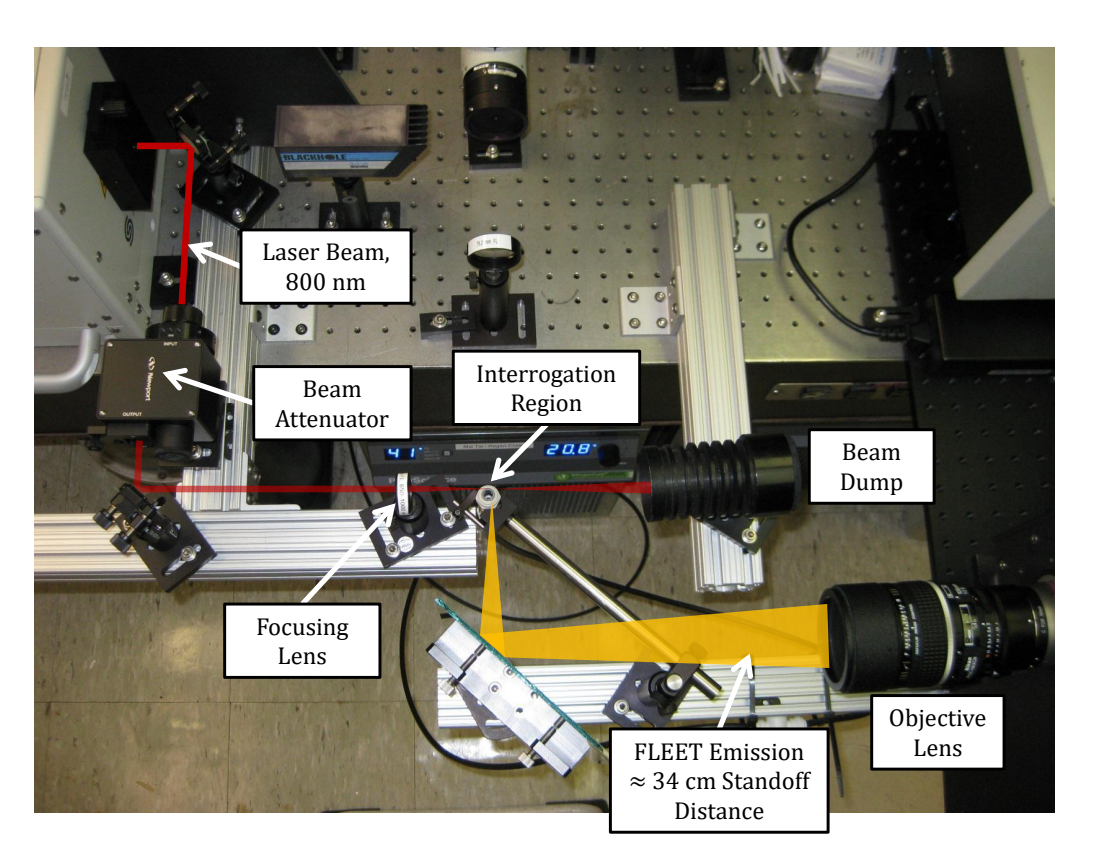


Figure 5.1: Top-view of optical setup as configured for vertical higher-speed jet.

A regeneratively-amplified Ti:sapphire laser system (Spectra-Physics Solstice one-box ultrafast amplifier) generated the FLEET emission in both nitrogen and air. The system produced 70 fs duration laser pulses centered at 800 nm with up to 3.5 mJ of energy per pulse and at a repetition rate up to 1 kHz. An ultrafast variable beam

attenuator (Newport VA-800) enabled the laser pulse energy to be varied. The majority of experiments in this study were conducted with pulse energies of 3.0 mJ. A power meter facilitated measurement of the beam energy after passage through the attenuator. Focusing and steering of the beam were accomplished with ultrafast anti-reflective lenses and ultrafast mirrors, respectively. A 50 cm focal length (FL) lens was used to obtain data, except as otherwise specified. Figure 5.1 shows a top-view of the optical setup with the 6.3 cm FL lens installed. For longer focal lengths, the lens was moved closer to the attenuator to prevent the beam focus from moving with respect to the interrogation region above the tube fitting.

5.2.2 Free Jet Configurations

Two flow configurations were used for the FLEET velocimetry study: an inverted low-speed free jet (bulk⁶ Reynolds numbers of 470–4600 and bulk velocities of 0.2– $2.2\,\mathrm{m\,s^{-1}}$) designed to provide a steady flow containing minimal velocity fluctuations and a vertical higher-speed free jet (bulk Reynolds numbers of 470– $24\,000$ and bulk velocities of 1.2– $58\,\mathrm{m\,s^{-1}}$) capable of producing turbulent flow with fluctuations and eddies.

Figures 5.2 and 5.3 show diagrams and pictures of the low and higher-speed free jet, respectively. The low-speed jet was a converging nozzle with a 32 mm diameter exit and a honeycomb flow straightener in its 71 mm diameter inlet. This nozzle was chosen to produce a core flow with a uniform velocity. Gas was injected into the upper corner of a sealed Styrofoam cooler and flowed out of the cooler through the nozzle as depicted in Figure 5.2 (left). FLEET velocity measurements were taken 2 cm downstream of the exit. See Figure D.1 in Appendix D for schlieren images of this region of the free jet. The insulated cooler permitted variable temperature operation, but measurements obtained using that feature are not reported here. The

 $^{^6\}mathrm{Exit}$ diameter is the characteristic length used to calculate bulk Reynolds number and bulk velocity.

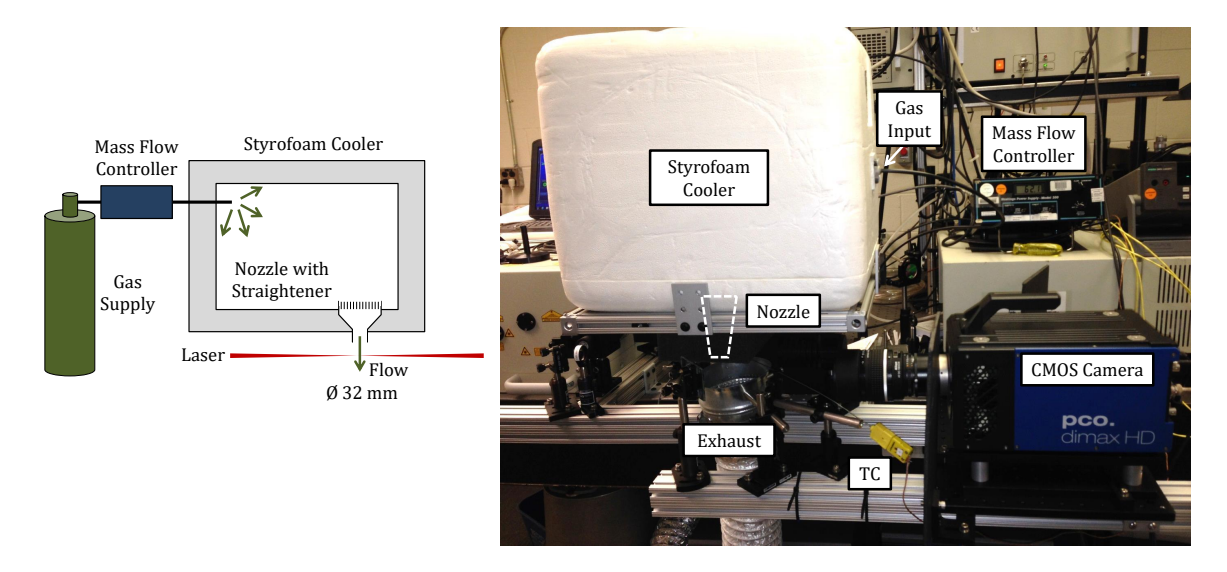


Figure 5.2: (Left) Diagram of setup for inverted low-speed jet (up to about $2 \,\mathrm{m\,s^{-1}}$). (Right) Side-view of experiment. White dashed outline roughly locates position of nozzle. Setup provides low fluctuation flow with variable temperature capability (not utilized in present study).

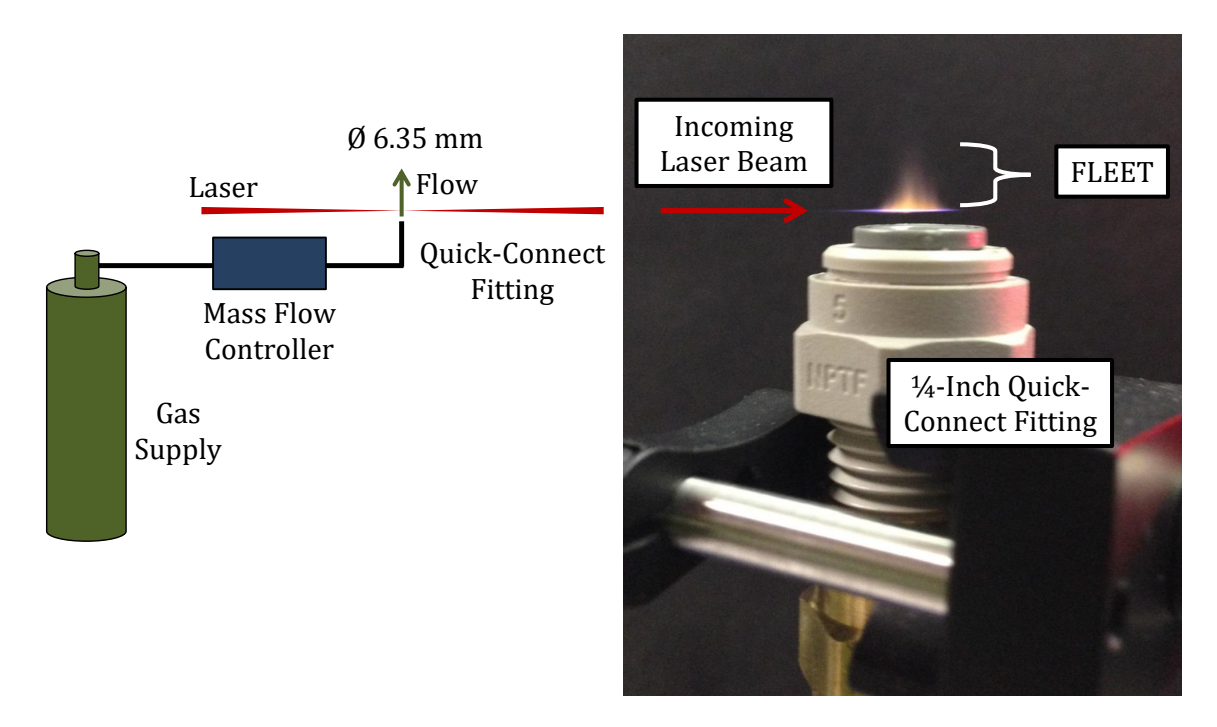


Figure 5.3: (Left) Diagram of setup for vertical higher-speed jet (up to about $60\,\mathrm{m\,s^{-1}}$). (Right) Side-view of experiment showing long-lived FLEET emission in pure nitrogen as obtained by smartphone camera (averaged over many laser pulses) and clearly visible to naked eye.

higher-speed jet utilized a quick-connect tube fitting with an internal diameter of 6.35 mm (Figure 5.3). This smaller diameter outlet allowed for higher bulk velocities than the low-speed jet (while using the same mass flow rates) and therefore allowed turbulent flow conditions to be more readily achieved. In both setups, a 100 standard liter per minute mass flow controller measured and regulated the gas flow rate in order to allow calculation of bulk velocity. Originally the bulk velocity was to be used as the reference velocity for determining the accuracy of FLEET, but it was soon discovered that this velocity was not fully representative of the region being probed and therefore was unsuitable. An alternative reference velocity measurement, such as hot-wire anemometry or particle image velocimetry (PIV), was not used in this study, but would be considered in future work.

5.2.3 High-Speed CMOS Camera - pco.dimax HD

The primary imaging system was an un-intensified pco.dimax HD high-speed CMOS camera with a Gigabit Ethernet data interface. The camera has a full-frame (1920 by 1080 pixel) repetition rate of 2.1 kHz and is capable of double shutter operation at half that rate in which a second exposure is taken about 5 µs after the end of the first exposure. Double shutter operation permits velocity measurement without using a previously measured initial location of the laser pulse. Rather, the reference (starting) position of the tagged molecules and the delayed (displaced) position are both captured for each laser pulse (i.e., two exposures are taken for every laser pulse). This approach is robust in large facilities where vibrations or beam steering can cause the position (or apparent position) of the laser beam to move on a shot-to-shot basis or can cause long-term misalignments which could lead to errors. Note that all of the FLEET velocimetry measurements in this study used two exposures (a reference and a delayed image) to compute the velocity of the tagged region. The objective lens used for this and the other cameras was an F-mount 105-millimeter FL (Nikon NIKKOR)

with an aperture range of f/2 to f/16. In an effort to replicate the standoff (i.e., the distance between the camera objective lens and the interrogation region) expected when performing FLEET measurements in a wind tunnel, a standoff of approximately 34 cm was maintained and held constant for the experiment. Macro rings were needed for proper focusing of the objective lens.

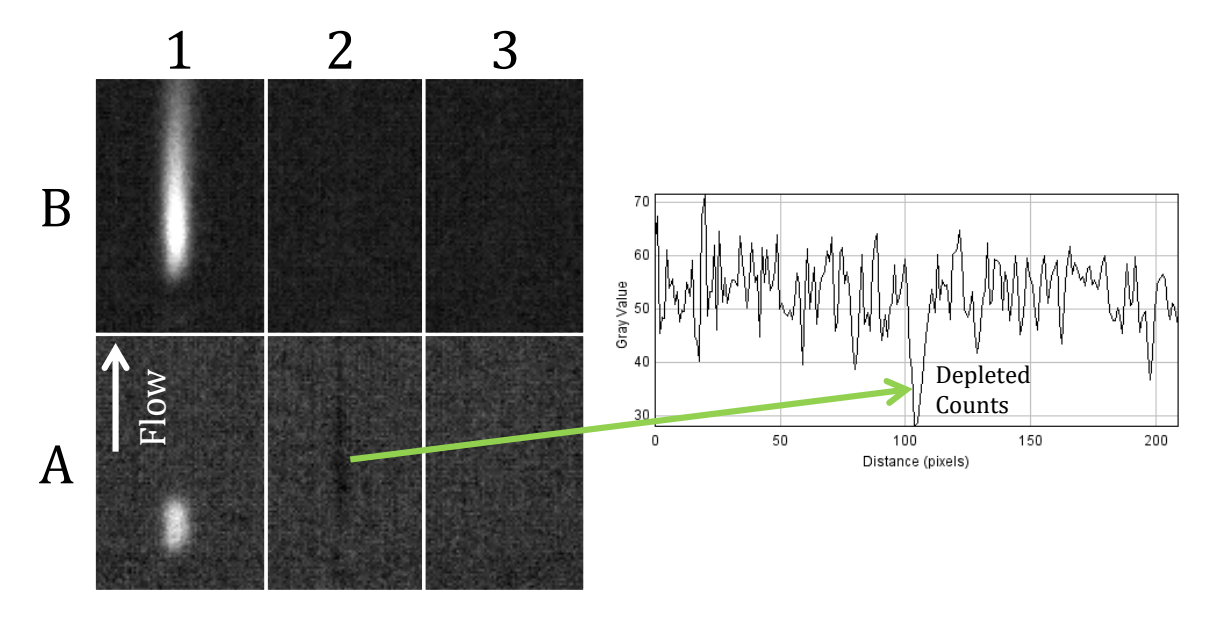


Figure 5.4: (Left) Example of three-shot framing technique used to eliminate the CMOS ghosting effect and produce a background image. Image pairs (1, 2 and 3) correspond to 1, 334 and 667 μs after laser pulse. Frames A and B correspond to first and second gates of double shutter mode (with respective durations of 2 and 83 μs). Laser beam (0.75 mJ energy, 6.3 cm focusing) passes right to left and nitrogen flows bottom to top. (Right) CMOS camera exhibits 'negative ghosting' in which relatively high intensity event (1B) causes depleted region in following frame (2A).

The pco.dimax HD camera (hereafter referred to as the "PCO camera") was characterized in detail. It was discovered that the CMOS sensor suffered from a 'negative ghosting' phenomenon in which a region of the sensor that recorded a relatively high intensity event exhibited depleted signal counts in the following exposure. This might have been an artifact of operating the camera in the lower end of its dynamic range. A method used to mitigate this problem was to capture a background image containing the negative ghosting and then discard that image. Exposures subsequent to this discarded image would not contain the negative ghost. Additionally, it was observed

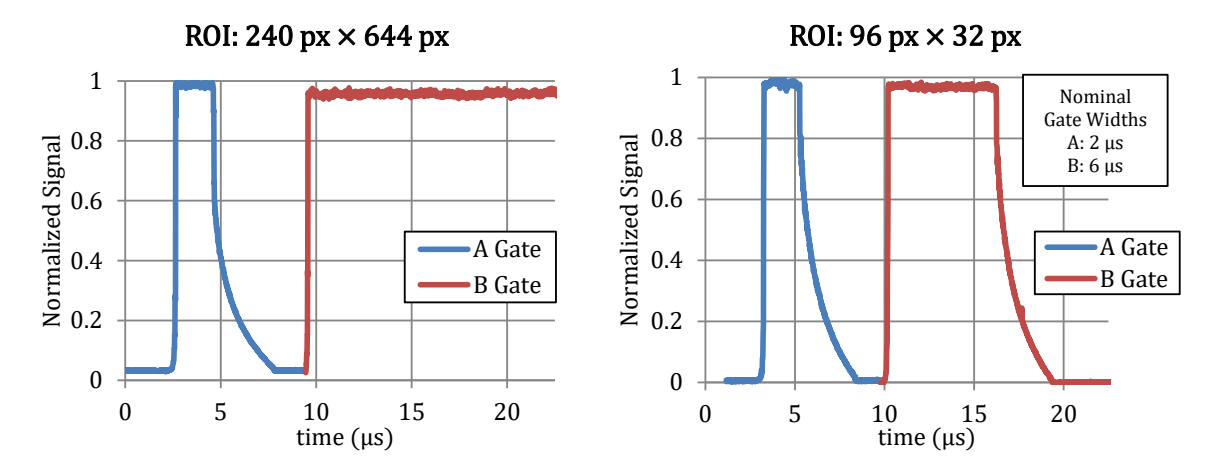


Figure 5.5: Time response of sensitivity of PCO CMOS sensor in double shutter operation for large (left) and small (right) region of interest. Decreasing ROI shortens length of second gate (gate B). The curves are normalized by peak sensitivity.

that the mean background intensity varied temporally on the order of minutes. To effectively correct for background counts, the background images would need to be acquired simultaneously with the data. Both of these issues were addressed by taking three image pairs for each laser pulse (i.e., running the laser at 1 kHz and the camera at 3 kHz at a reduced image size). The first exposure pair would contain the FLEET data, the second pair would clear the sensor of ghosting artifacts and the third pair would provide a background suitable for use in background subtraction. Figure 5.4 shows the three-shot framing technique and an example of negative ghosting.

Although the PCO camera allowed for direct control of the first exposure duration, the duration of the second exposure could not be directly set in the software. Nevertheless, it was desirable to find a way to shorten the second gate from hundreds of microseconds to several microseconds. We empirically determined that the duration of the second gate in double shutter operation is roughly proportional to the size of the region of interest (ROI). Therefore, the second gate could be shortened by shrinking the ROI. This principle is illustrated in Figure 5.5 which shows the temporal evolution of the camera gates for a large and small ROI. The temporal evolution was determined by capturing the Rayleigh scattering of the femtosecond

laser pulse in air and marching the triggering of the gates in time with respect to the pulse. Time steps of $10\,\mathrm{ns}$ were used for the marching. A ROI of 96 by 32 pixels was selected in order to produce a $6\,\mu\mathrm{s}$ long second gate which proved satisfactory for FLEET velocity measurements. Note that Figure 5.5 shows a gradual decay in sensitivity at the end of each exposure instead of an ideal 'top hat' time response.

5.2.4 High-Speed CMOS Camera System Comparison

Five different intensified and un-intensified high-speed CMOS camera configurations were evaluated for performing FLEET velocimetry. The systems and their settings are tabulated in Table 5.1. A target gate width of 2 μs and inter-frame⁷ delay of 6 μs were chosen when possible to provide a fair comparison between systems. A longer inter-frame delay was used in three instances in an attempt to improve the precision of the velocity measurement. For all the systems, the first exposure was taken 1 µs after the laser pulse. In addition to the PCO camera previously discussed, a Photron FASTCAM SA-X2 capable of full-framing (1024 by 1024 pixels) at 12.5 kHz and a LaVision Imager scientific CMOS (sCMOS) capable of full-framing (2560 by 2160 pixels) at 0.1 kHz, were tested. The Photron and LaVision used Gigabit Ethernet and Camera Link data interfaces, respectively. The Photron possessed the fastest native framing rate and the LaVision, with its sCMOS sensor, offered the lowest readout noise. Both the PCO and LaVision were capable of double shutter operation, with fixed inter-frame delays of $5 \mu s$ and $0.125 \mu s$, respectively. An un-intensified LaVision was not tested because the camera's native inter-frame delay was too short for the flow velocities being considered. The Photron had built-in background subtraction. The bit depth was 12 bits for the Photron and PCO cameras and 16 bits for the LaVision.

⁷Duration of imaging insensitivity which starts at the end of the first exposure (gate) and ends at the start of the second exposure (gate). It is the primary component of the time interval used to calculate velocity of the tagged line.

Table 5.1: Five high-speed CMOS camera systems from comparison study. CMOS sensor pixel sizes in parentheses. Intensifier is LaVision HighSpeed IRO (described in text).

 $\underline{\text{pco.dimax HD}}$ (11 μ m)

1st Gate: $2 \mu s$; 2nd Gate: $6.1 \mu s$

Inter-frame Delay: 5 µs

pco.dimax HD with Intensifier $(11 \,\mu\text{m})$

1st & 2nd Gates: $2 \mu s$

Inter-frame Delay: $6 \,\mu s \,\&\, 21.6 \,\mu s$

Photron FASTCAM SA-X2 (20 µm)

1st & 2nd Gates: $\approx 2\,\mu s$

Inter-frame Delay: $\approx 6.4 \,\mu s \,\& \approx 23.0 \,\mu s$

Photron FASTCAM SA-X2 with Intensifier (20 μm)

1st & 2nd Gates: $2 \mu s$

Inter-frame Delay: $6.3 \,\mu s \,\&\, 23.0 \,\mu s$

LaVision Imager sCMOS with Intensifier (6.5 μm)

1st & 2nd Gates: $2 \mu s$ Inter-frame Delay: $6 \mu s$











A two-stage LaVision HighSpeed IRO intensifier was used in conjunction with the cameras to permit viewing of FLEET in air as well as nitrogen. This particular intensifier was chosen because its first stage photocathode (S25) has high sensitivity in the red to near-infrared region where the long-lived FLEET emission is strong and the phosphor screen (P46) has a fast decay time allowing for high repetition rates. The second stage also used the fast P46 phosphor, but had a different photocathode (S20) in order to more efficiently amplify the output of first stage phosphorescence. The PCO and Photron cameras were also tested without the intensifier, but only in pure nitrogen since the signal in air was too weak to be observed. Oxygen has a quenching effect on the FLEET signal and causes it to be much weaker (and shorter

lived) in air than in pure nitrogen. Therefore, we determined that observation of FLEET in air requires intensification, at least for the camera and lens configurations tested in the present study. The intensifier gain was adjusted for each camera system and gas until the FLEET signal appeared (qualitatively) to have an optimum or at least acceptable signal-to-noise ratio. The maximum usable gain setting was that which avoided saturating the camera and avoided introducing an excessive amount of intensifier-induced spurious noise.

5.2.5 Data Processing and Techniques to Improve Precision

Data Processing

In order to measure the displacement of the FLEET line due to advection, the line center of the tagged gas must be accurately determined in two locations (reference and displaced) within the camera's field of view. Since the spatial profile of the laser intensity is approximately Gaussian, the spatial profile of the signal intensity of the tagged region, S(x), also resembles a Gaussian. Therefore, an in-house Gaussian fitting routine written in MATLAB was utilized to find the line center, x_0 , line thickness, σ_0 , and peak intensity, S_0 , of the FLEET signal according to the functional form

$$S(x) = S_0 \exp\left(\frac{-(x - x_0)^2}{2\sigma_0^2}\right).$$
 (5.1)

Figure 5.6 depicts typical Gaussian curve fits for signal intensity data (left) and the raw image pair containing the original data (right). The difference between the line centers in the two exposures constitutes the displacement due to advection. The data shown in Figure 5.6 were obtained from a FLEET experiment in the pure nitrogen higher-speed jet with an estimated bulk velocity⁸ of $35 \,\mathrm{m\,s^{-1}}$. Advection was in the

 $^{^8} The$ estimated bulk velocity compares well to the FLEET calculated mean and standard deviation of $(29.5\pm7.8)\,\rm m\,s^{-1}$ based on 333 single shots.

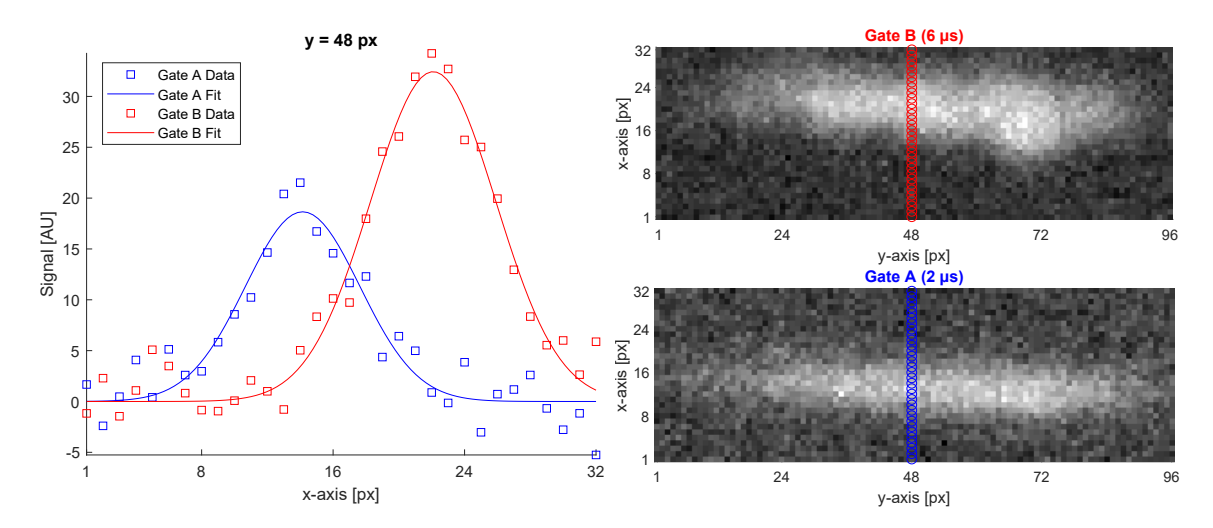


Figure 5.6: (Left) Typical Gaussian fits for gates A (blue) and B (red) in higher-speed jet (nitrogen, $35\,\mathrm{m\,s^{-1}}$ bulk velocity, $25\,\mathrm{cm}$ focusing, $1.0\,\mathrm{mJ}$ energy and no row-wise binning). (Right) Corresponding raw image pair from un-intensified PCO camera ($5\,\mu\mathrm{s}$ inter-frame delay). Fitted data identified by circles. Flow in positive x-direction for both figures.

positive x-direction for both figures. The mean background was subtracted, hence the reason for negative signal intensities, but no row-wise binning was performed. Only the vertical column of pixels in the middle of the frame (identified by circles) was used for displacement determination. Physically, this location corresponds to the centerline axis of the free jet. The thickness of the FLEET signal in gate A (first exposure, blue) is determined by the focusing of the laser beam. Tighter focusing tends to produce thicker (and shorter) FLEET lines. Fluid dynamics, molecular diffusion and longer gate width contribute to the noticeably different structure of the tagged line in gate B (second exposure, red). The mild waviness of the line suggests the inter-frame delay and second gate width are slightly long with respect to the flow timescales. Unfortunately, these settings could not be readily adjusted for the un-intensified PCO camera.

The influence of signal decay on the spatial intensity profile was not accounted for in the present study since its effect on precision was expected to be insignificant. However, for future accuracy studies in which FLEET velocimetry is compared to a reference velocity, it would be important to account for the signal decay when the gate widths are unequal. This is because the signal decay influences the apparent line center unevenly for unequal gates, causing the measured displacement to be shorter than it should be. When the gates are similar or identical in duration, the influence of signal decay on apparent line center is the same for each gate and is effectively canceled out.

Row-wise Digital Binning

It is possible to bin the signal intensity prior to fitting in order to achieve a higher signal-to-noise ratio (SNR). Higher SNR improves the reliability and precision of the line-center determination process (i.e., Gaussian fitting procedure) and thereby improves the precision of the velocity measurement. We explore two types of binning in this chapter. The first is called 'row-wise digital binning' (or simply 'row-wise binning') and consists of summing the signal intensity in adjacent pixels along a horizontal row of an image (where the laser beam is oriented nearly parallel to the rows of pixels on the camera). Figure 5.7 illustrates the concept which is done in post-processing after the image is captured (and after rotation of the image for better horizontal alignment of the tagged lines and rows of pixels). Binning improves the SNR by averaging out the noise (i.e., the random, undesirable variations in signal intensity caused by dark current in the sensor, electronic readout of the sensor, the discrete nature of photon arrival, etc.). Assuming nearby pixels have similar signal intensity, S, and similar root mean square noise, N, and signal adds linearly whereas noise is random and uncorrelated and therefore adds in quadrature, the improvement to SNR by binning n pixels in post-processing is given by:

$$\frac{S+S+\cdots}{\sqrt{N^2+N^2+\cdots}} = \frac{n\times S}{\sqrt{n\times N^2}} = \sqrt{n}\times \frac{S}{N}.$$
 (5.2)

Thus, the improvement is proportional to \sqrt{n} , based on the assumption of similar signal and noise, which approximately holds for pixels near one another. Although row-wise binning improves SNR, it sacrifices spatial resolution since those pixels that are binned are no longer available to provide velocity information for the regions from which they originated. However, the FLEET line has finite thickness (and therefore finite spatial resolution) in the laser's transverse direction which is several pixels wide. We adopted a rule of thumb to bin no more than the thickness of the FLEET line in pixels since that thickness already represents the minimum spatial resolution in the advective direction. Also, it is important to note that row-wise binning should be avoided if turbulence is observed in the delayed images since binning would smooth out the turbulent structures and potentially eliminate the velocity fluctuations that are actually present in the flow.

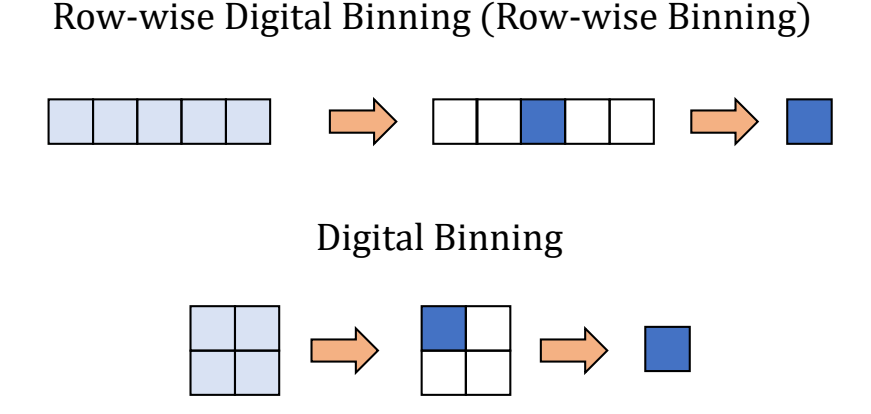


Figure 5.7: Conceptual illustration of two types of binning done in post-processing (i.e., digitally). Observe that aggregating signal intensity costs spatial resolution.

For the SNR calculations, signal is defined as the peak intensity of the Gaussian fit and noise is estimated as the root mean square of the residuals of the Gaussian fit. Therefore, estimated SNR has a direct correlation to the quality of the Gaussian fit.

Digital Binning

Another technique to improve SNR and thereby improve measurement precision is to perform what we call 'digital binning,' identical in concept to symmetric on-sensor hardware binning (e.g., bin four adjacent pixels from a 2×2 grid into one pixel) except that it is performed to the image using software in post-processing. Figure 5.7 illustrates the concept. Digital binning was thought of as a means to improve the SNR of some of the cameras tested that had smaller pixels than others, allowing for a fairer comparison. Given the same quantum efficiency, dark current noise and readout noise, the camera with the largest pixels will have the highest SNR (but worst spatial resolution). In order to effectively increase the pixel size of the other cameras, 2×2 and 3×3 digital binning was performed on images taken by cameras with pixels respectively one-half and one-third the size of the largest pixels. Improvement to SNR occurs in the same manner as with row-wise binning (by averaging out noise) and the tradeoff is the same in that the spatial resolution is sacrificed. Digital binning offers the possibility of enhancing the SNR of cameras with smaller pixels while still maintaining the capability of the camera to revert back to higher spatial resolution, assuming the SNR penalty is acceptable.

Inter-frame Delay

The intensified PCO and Photron cameras were tested with both short and long inter-frame delays (see Table 5.1). The reason for varying the inter-frame delay was to investigate the potential improvement to precision achieved by increasing the time delay. The time delay⁹ is computed as

$$\Delta t = \frac{1}{2} \Delta t_{1\text{st gate}} + \Delta t_{\text{inter-frame}} + \frac{1}{2} \Delta t_{2\text{nd gate}}, \tag{5.3}$$

⁹Sometimes this duration is referred to as the 'time interval' to distinguish it from the time delay after the laser pulse.

where Δt , $\Delta t_{1\text{st gate}}$, $\Delta t_{inter-frame}$ and $\Delta t_{2\text{nd gate}}$ represent the time delay, first gate width, inter-frame delay and second gate width, respectively. According to basic uncertainty analysis [123], the uncertainty in a calculated velocity is

$$\delta v \le \left| \frac{\partial v}{\partial (\Delta x)} \right| \delta (\Delta x) + \left| \frac{\partial v}{\partial (\Delta t)} \right| \delta (\Delta t), \qquad (5.4)$$

where Δx and v are measured displacement and calculated velocity, respectively, and $\delta(\cdot)$ denotes the uncertainty of a quantity. The uncertainty in line-center determination is the primary source of random uncertainty in the measured displacement. There is also systematic uncertainty resulting from errors in magnification (i.e., the conversion from pixels to physical length). An example of temporal uncertainty is the timing jitter between the start of the gates of the image pair which causes random uncertainty in the duration of the inter-frame delay.¹⁰ Since calculated velocity is given by

$$v = \frac{\Delta x}{\Delta t},\tag{5.5}$$

the uncertainty in velocity is given by

$$\delta v \le \frac{\delta(\Delta x)}{\Delta t} + |v| \frac{\delta(\Delta t)}{\Delta t},$$
(5.6)

which shows that increasing the time delay acts to decrease the uncertainty in velocity—it reduces errors associated with both spatial uncertainty and temporal uncertainty. However, it should be noted that for very long time delays, finite fluorescence lifetime and diffusion of the tagged molecules reduces the SNR enough to make locating the line center difficult (i.e., imprecise). This is especially true for images taken without intensification. Thus, there is a maximum time delay that optimizes precision. A further limitation of long delay times is that the spatial

¹⁰Note that since images are acquired well after the laser pulse, the timing jitter between the laser and camera system cancels out when using image pairs.

resolution is proportionally worse as the gas travels a farther distance. Even worse, for long delays, the idea of computing a velocity comes into question since the gas may accelerate or decelerate along this path. Moreover, long time delays would be inappropriate for flows where the turbulence timescale is shorter than the chosen time delay. Accordingly, the optimal time delay depends on the flow regime (which dictates how quickly the FLEET line will break up), the pressure and temperature¹¹ of the flow (which affects the rate of diffusion of the FLEET line as well as the lifetime) and whether the flow is composed of air or nitrogen (since signal lifetimes are dramatically shorter in air than in nitrogen).

5.3 Results and Discussion

5.3.1 Improvement in Precision due to Row-wise Binning and Inter-frame Delay

No Row-wise Binning

Precision was defined as the standard deviation of the set of single-shot velocity measurements for a particular flow rate. FLEET velocimetry was performed in the pure nitrogen higher-speed jet for a range of velocities. Figures 5.8 and 5.9 show precision results for the un-intensified and intensified Photron camera, respectively. The relevant laser and camera parameters are detailed in the figure titles and captions. The first gate was 1 µs after the laser pulse. The standard deviation contains contributions from both the imprecision of the technique (in particular, the line-center determination) and the actual velocity fluctuations of the flow. For the case of no row-wise binning (i.e., binning row-wise by one pixel), the standard deviation is similar for the low speeds and then increases as the flow speed increases. This increase occurs

¹¹See Chapter 3 for the effect of low temperatures and pressures.

because the velocity fluctuations being measured are real fluctuations attributable to turbulence. The similarity in standard deviation at the lower bulk velocities (below $6\,\mathrm{m\,s^{-1}}$) suggests that the precision is limited by the measurement technique as opposed to turbulent fluctuations. Above $11\,\mathrm{m\,s^{-1}}$, the standard deviation increases substantially, suggesting that the precision is now limited by the turbulent fluctuations of the flow.

Effect of Row-wise Binning

The effect of row-wise binning on precision for the un-intensified and intensified Photron camera is shown in Figures 5.8 and 5.9, respectively. Comparing the effect of row-wise binning up to eight pixels in the two figures reveals a more pronounced improvement for the un-intensified case than the intensified case. As binning increases, the SNR of the data increases which causes the Gaussian fit and therefore the line-center determination to be more precise. This improves the precision of the velocity measurement (i.e., standard deviation decreases). However, for the intensified case, the SNR of the data is already relatively high and additional increases do not substantially enhance the precision of the line-center determination.

The improvement in precision is greatest at low velocity and decreases as velocity increases and the flow becomes turbulent. At higher bulk velocities, such as above $11 \,\mathrm{m\,s^{-1}}$, small amounts of row-wise binning do not necessarily improve precision because turbulent fluctuations are present. For both the un-intensified and intensified cases, binning row-wise by a large number of pixels (more than eight) substantially reduces the standard deviation of the velocity measurement because the turbulent structures (and therefore the velocity fluctuations) are smoothed out. Both figures show that above $11 \,\mathrm{m\,s^{-1}}$, the standard deviation associated with binning row-wise by 32 and especially by 96 pixels is substantially lower than for binning row-wise by 8

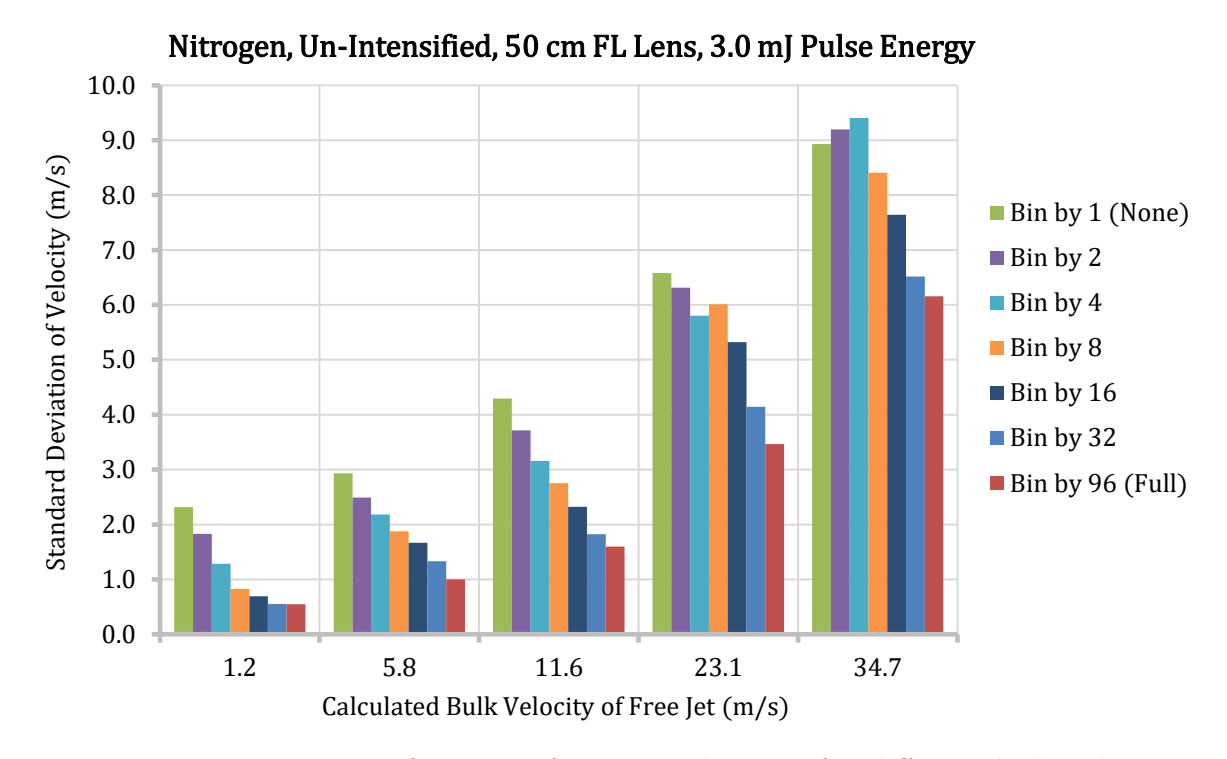


Figure 5.8: Precision as function of row-wise binning for different bulk velocities in higher-speed jet. Inter-frame delay held constant at $6.4 \,\mu s$. Based on over 333 single-shot image pairs taken by un-intensified Photron camera (1.95 μs gates).

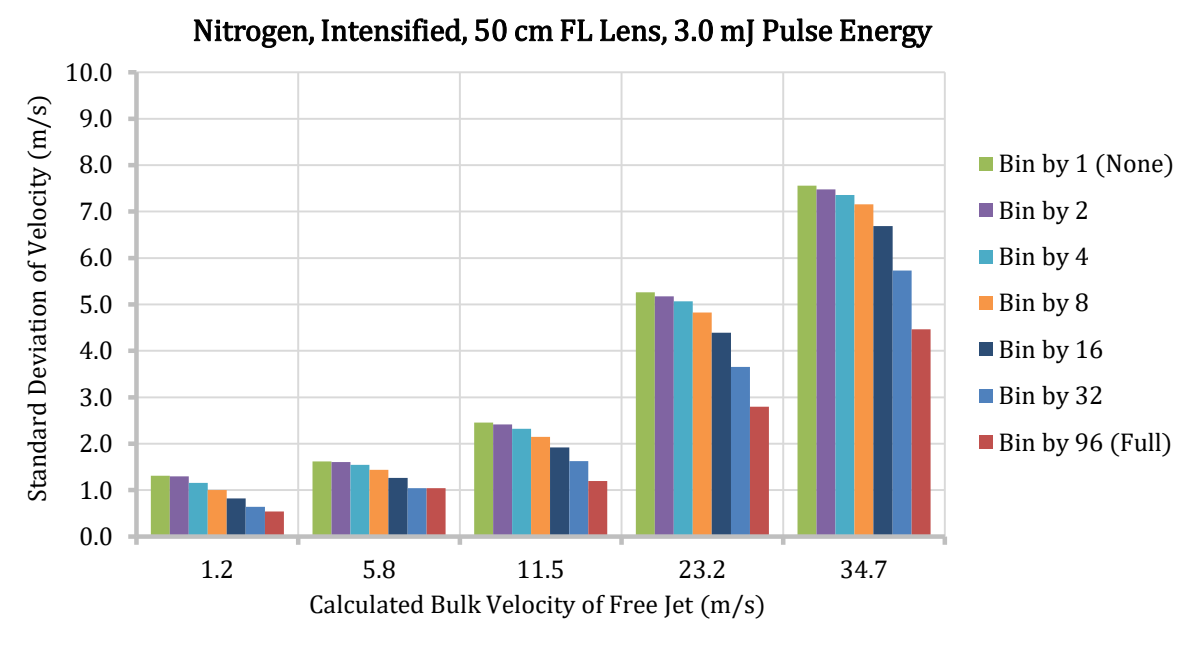


Figure 5.9: Precision as function of row-wise binning for different bulk velocities in higher-speed jet. Inter-frame delay held constant at $6.3\,\mu s$. Based on over 350 single-shot image pairs taken by intensified Photron camera ($2\,\mu s$ gates).

pixels or less. Since binning by a large number of pixels alters the velocity fluctuations being measured, it is not appropriate for highly turbulent flows.

Furthermore, it was found that the SNR improvement scales with $n^{0.4}$ for up to 16 pixels of row-wise binning, which roughly agrees with the theoretical scaling of \sqrt{n} as dictated by Equation 5.2.

Effect of Increased Inter-frame Delay

Figure 5.10 shows how the inter-frame delay affects the precision of FLEET velocimetry measurements taken in the low-speed jet for air and nitrogen. Three different inter-frame delays were used and the amount of row-wise binning was fixed to 8 pixels (about the apparent thickness of the FLEET line). Images were acquired with the intensified Photron camera. As before, precision was defined as the standard deviation of the set of single-shot velocities measured by FLEET velocimetry. Several trends can be identified in the data. First, increasing the inter-frame delay improves the precision. The improvement in precision is slightly less than the $1/\Delta t$ relationship expected from Equation 5.6. The likely reason is that the time-dependent effects of diffusion and signal decay impair line-center determination (making it more imprecise) and therefore curtail the improvement provided by longer time delays. Second, the inherently better signal intensity and lifetime characteristics of FLEET in nitrogen enable more precise line-center determination, especially in the second exposure, and therefore cause FLEET velocimetry in nitrogen to have better precision than in air. Lastly, the precision is worst for the slowest velocities in air and nitrogen which is counterintuitive since this is when the flow fluctuations should be minimal. For these cases, the SNR is substantially reduced, compromising line-center determination. It is speculated that this SNR reduction occurs because the same volume of gas is being repeatedly interrogated with the femtosecond pulse (which operates at 1 kHz and 3.0 mJ), perturbing the gas present there and perhaps leading to the accumulation of new gas species that degrade the FLEET signal. Thus, care must be exercised when probing a stagnated gas (for example in static gas cells, or at stagnation points in fluid flows) with FLEET in order to avoid impacting the precision of the technique. Possible workarounds could include operating the laser system at a lower repetition rate or pulse energy in order to limit the rate at which new species are generated.

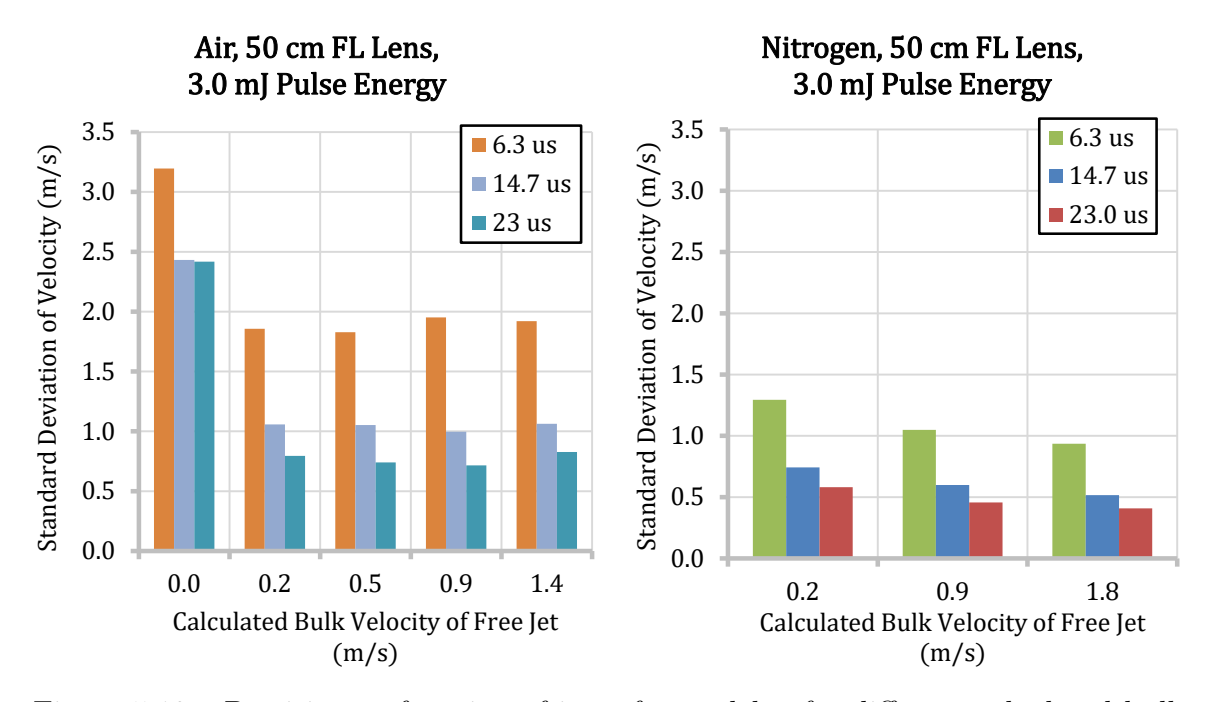


Figure 5.10: Precision as function of inter-frame delay for different calculated bulk velocities in low-speed jet. Row-wise binning is 8 pixels. Based on over 300 single-shot image pairs taken by intensified Photron camera (2 μ s gates) using 70 % gain for air and 60 % gain for nitrogen.

Combined Effect of Row-wise Binning and Increased Inter-frame Delay

Figure 5.11 illustrates the combined effects of row-wise binning and inter-frame delay on the precision of FLEET velocimetry in the low-speed jet. Four inter-frame delays were used with 8 pixels of row-wise binning (corresponding to the approximate thickness of the FLEET line). The first gate was 1 μ s after the laser pulse. The laser beam was focused by a 50 cm FL lens and had a slightly higher pulse energy of 3.2 mJ. Images were acquired with the intensified Photron camera (2 μ s gates) using 70 % gain

for air and 60% gain for nitrogen. With the combined benefits of row-wise binning by 8 pixels and using an inter-frame delay of $64.7\,\mu\text{s}$, values of $0.5\,\text{m}\,\text{s}^{-1}$ for air and $0.2\,\text{m}\,\text{s}^{-1}$ for pure nitrogen were achieved. These values represent the current observed limit for the precision of the technique using a realistic amount of row-wise binning. The figure also shows an asymptotic limit for the precision in both air and nitrogen, likely explained by diffusion and signal decay as discussed in the previous section, though in the case of nitrogen, it is possible that the true velocity fluctuations are $0.2\,\text{m}\,\text{s}^{-1}$. While comparison with another measurement technique would verify the true level of fluctuations within the flow, the data presented herein identify an upper limit on the technique's measurement precision, as implemented in the current setup. Furthermore, the precision in nitrogen is better than in air due to the aforementioned higher signal intensity and longer lifetime of the FLEET signal in nitrogen.

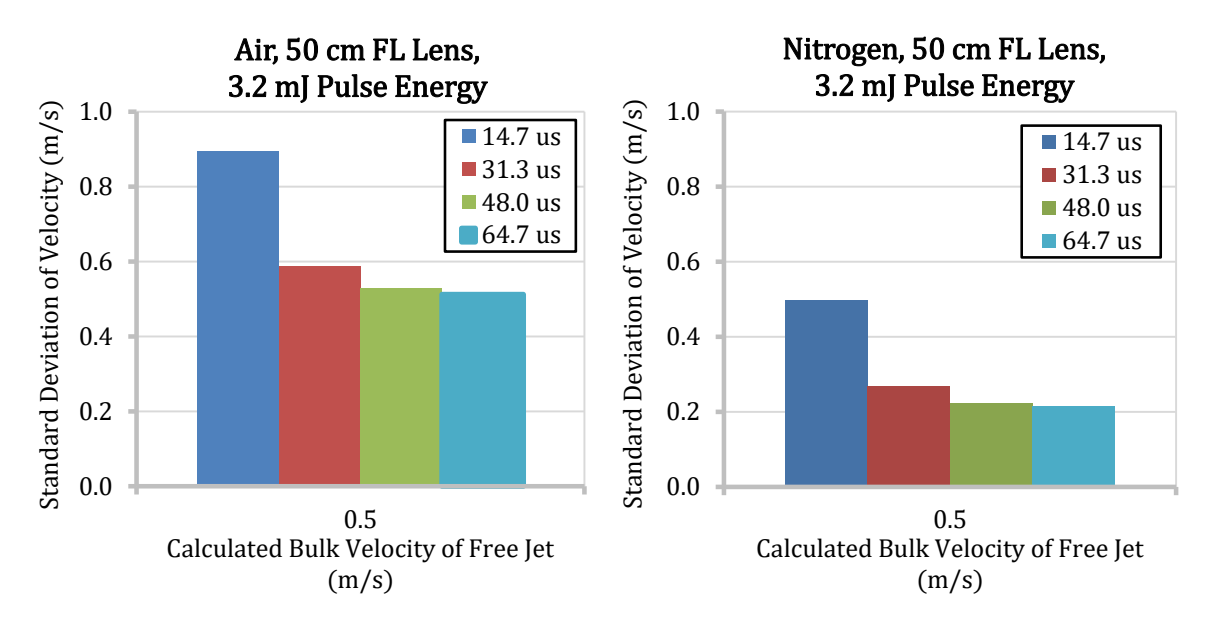


Figure 5.11: Precision as function of long inter-frame delays for $0.5\,\mathrm{m\,s^{-1}}$ low-speed jet combined with 8 pixels of row-wise binning. Based on over 166 single-shot image pairs taken by intensified Photron camera (2 μ s gates) using 70 % gain for air and 60 % gain for nitrogen.

5.3.2 High-Speed CMOS Camera Comparison

Without Digital Binning

Table 5.2 shows selected single-shot raw images (background subtracted and autoscaled to peak intensity) from each of the high-speed CMOS camera systems. Each image was taken $1\,\mu s$ after the laser pulse using a $2\,\mu s$ gate width. FLEET was performed in a $0.9\,\mathrm{m\,s^{-1}}$ pure nitrogen flow from the low-speed jet. A $3.0\,\mathrm{mJ}$ laser pulse was focused using a $50\,\mathrm{cm}$ FL lens. The images visually convey the signal-tonoise ratio and FLEET line thickness expected from each system. The first column contains raw images that have equal pixel dimensions (96 by 32), but different physical length scales since the pixel sizes are different. In the second column, each image has been rescaled such that the physical length scales are equal. The standoff distance between the objective lens and FLEET emission was held constant. The pixels of the Photron camera were roughly twice and three times as large as those on the PCO and LaVision, respectively. Clearly, intensification greatly improves the continuity and SNR of the FLEET line. It should be noted that the Photron employed built-in background subtraction.

The precision and SNR results of the CMOS camera comparison are contained in Figures 5.12–5.15. Data came from the low- and higher-speed jet using air and nitrogen (as indicated on the plots). The first gate occurred 1 μs after the laser pulse. A femtosecond laser beam with a pulse energy of 3.0 mJ and focused by a 50 cm FL lens was used for tagging. When possible, gate widths of 2 μs were selected. Table 5.1 contains a comprehensive listing of the settings for each camera system. All camera systems that used an intensifier had a gain of 70% except for the Photron in nitrogen, which used 60%. Decreasing from 70% to 60% corresponds to a factor of 5.3 reduction in gain. To accentuate the performance differences of the various camera configurations, row-wise binning was not employed.

Table 5.2: Background subtracted raw images from each camera system with intensity scaled to peak value. Images are in native scale and rescaled for equal physical length. Pure nitrogen low-speed jet at $0.9\,\mathrm{m\,s^{-1}}$, $3.0\,\mathrm{mJ}$ energy, $50\,\mathrm{cm}$ FL and $2\,\mu\mathrm{s}$ gate.

Camera System	Native	Rescaled
$\frac{\text{pco.dimax HD}}{\text{No Intensifier}} (11 \mu\text{m})$		
$\frac{\rm pco.dimax~HD~with~Intensifier}{70\%~Gain}$ (11 $\mu m)$		
$\frac{\mathrm{Photron\ FASTCAM\ SA-X2}}{\mathrm{No\ Intensifier}}\ (20\mu\mathrm{m})$	THE WASHINGTON	in the
$\frac{Photron\ FASTCAM\ SA-X2\ with\ Intensifier}{60\%\ Gain}$ (20 $\mu m)$		
LaVision Imager sCMOS with Intensifier $(6.5\mu\mathrm{m})$ 70 % Gain		

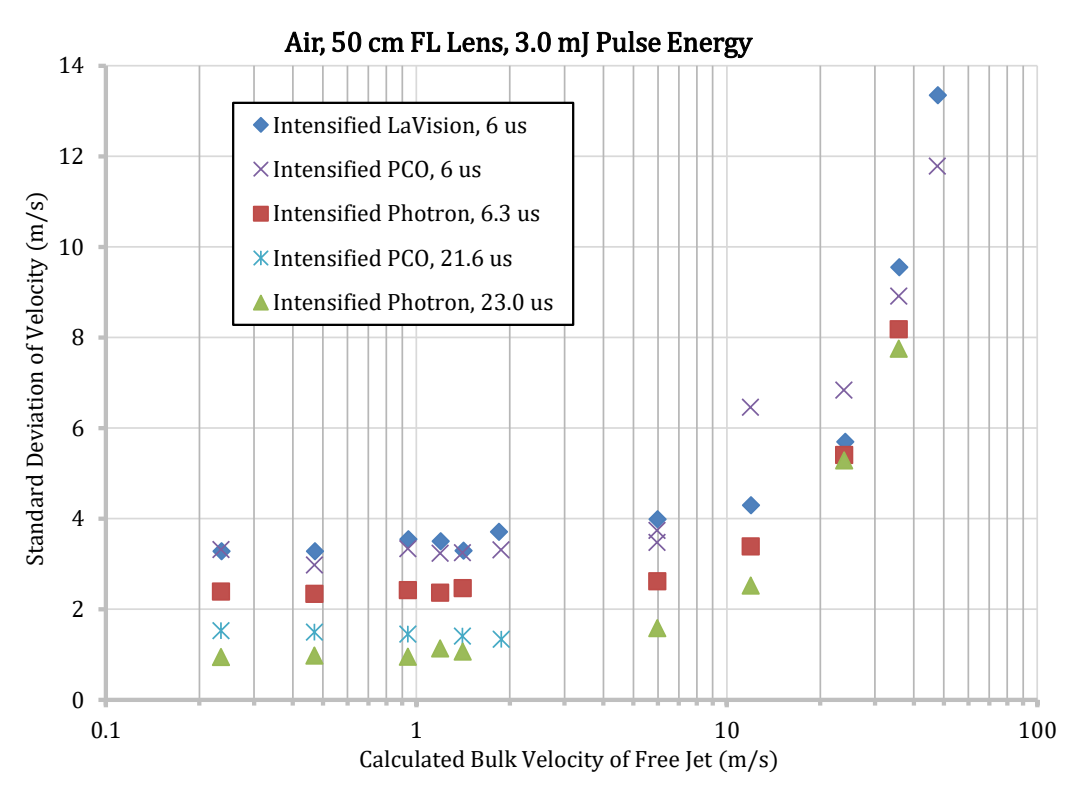


Figure 5.12: Precision as function of bulk velocity for CMOS camera systems (interframe delay noted) in air. No binning. Data from low- and higher-speed jet.

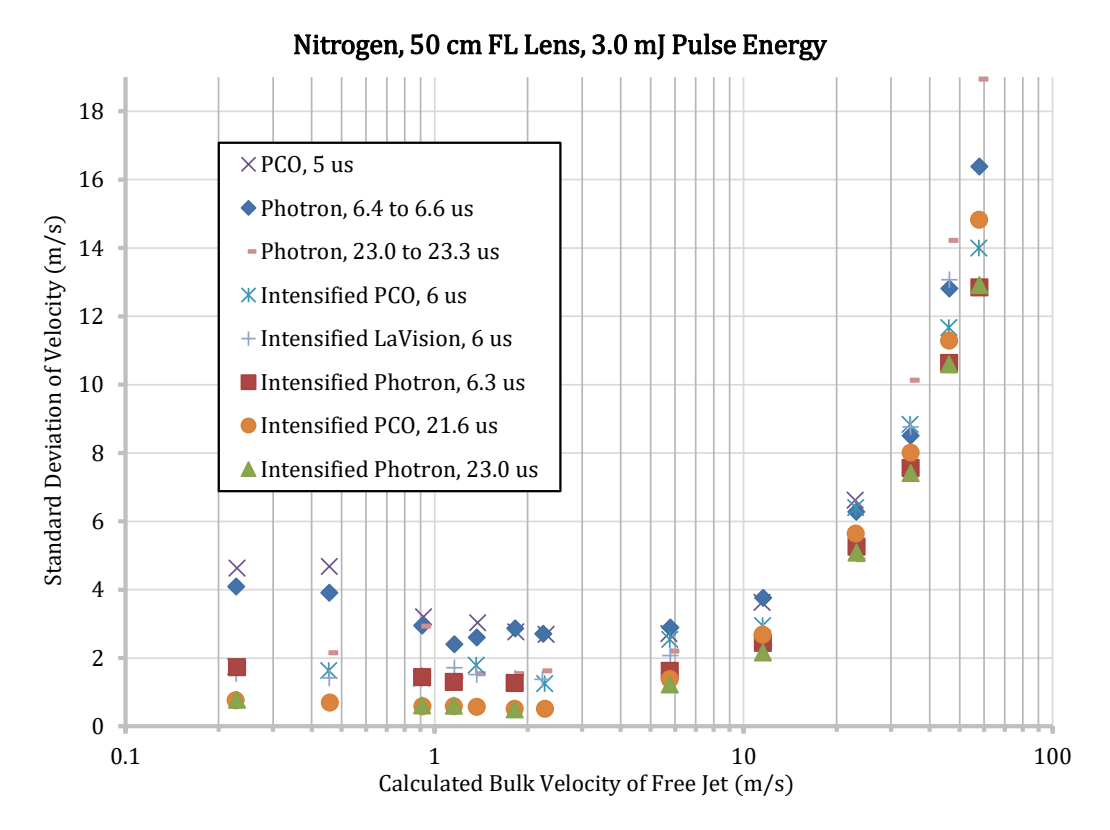


Figure 5.13: Precision as function of bulk velocity for CMOS camera systems (interframe delay noted) in nitrogen. No binning. Data from low- and higher-speed jet.

Figures 5.12 and 5.13 show the precision for the different camera systems as a function of bulk velocity in air and nitrogen, respectively. The standard deviation increases above $5\,\mathrm{m\,s^{-1}}$ because of turbulent fluctuations in the jet, as opposed to a loss of precision of the measurement technique. Increasing the inter-frame delay between the first and second exposures improves precision. The best results obtained with a long inter-frame delay have a standard deviation lower than $1\,\mathrm{m\,s^{-1}}$, even in air. Precision is generally better in the pure nitrogen flow (Figure 5.13) because the FLEET signal is more intense and has a longer lifetime which facilitates more precise line-center determination in the second exposure. The best un-intensified system using a short inter-frame delay for nitrogen was the Photron camera, but only by a slight margin. It demonstrated better precision than the PCO camera probably because its larger pixels had greater ability to capture higher SNR data (discussed in more detail

later). Lengthening the inter-frame delay of the Photron camera generally improved precision for speeds up to 23 m s⁻¹, even approaching the performance of the short delay intensified systems. But for higher speeds, the precision was drastically worsened due to turbulent diffusion of the FLEET line which effectively reduced the intensity of the signal. Without the aid of intensification, it was difficult to identify the line center of the diffuse tagged region in the delayed second image. The best intensified system using a short inter-frame delay for air and nitrogen was the intensified Photron camera. For speeds up to $12 \,\mathrm{m\,s^{-1}}$ in pure nitrogen, the short delay intensified PCO and LaVision cameras had comparable performance to the Photron. The best intensified system using a long inter-frame delay was the intensified Photron camera for air and nitrogen. For speeds up to $6\,\mathrm{m\,s^{-1}}$ in pure nitrogen, the long delayed intensified PCO camera also exhibited similar performance. The spikes at about $0.2\,\mathrm{m\,s^{-1}}$ and $0.5\,\mathrm{m\,s^{-1}}$ for the un-intensified PCO and Photron cameras in nitrogen (see Figure 5.13) are due to a drop in SNR because of the previously discussed reasons of the flow velocity being slow enough to allow for accumulation of new gas species that degrade the FLEET signal. This degradation is more severe for the un-intensified cases since the SNR is already relatively low. Therefore, for cases of very slow flow speed, it is advisable to reduce the laser repetition rate, lower the pulse energy or utilize an intensifier. In summary, intensification of the camera is advised, providing a factor of two to three improvement in measurement precision. Furthermore, longer time delays between exposures provide a corresponding improvement in precision; however, longer time delays also increase the spatial extent of the measurement (i.e., reduce spatial resolution), reduce the time resolution of the measurement, and can lead to degraded signal in turbulent flow. Each of these criteria needs to be evaluated in a specific experiment and an optimal compromise found.

The estimated signal-to-noise ratio of the FLEET emission as captured by the first gate is shown for air and nitrogen in Figures 5.14 and 5.15, respectively. Note that

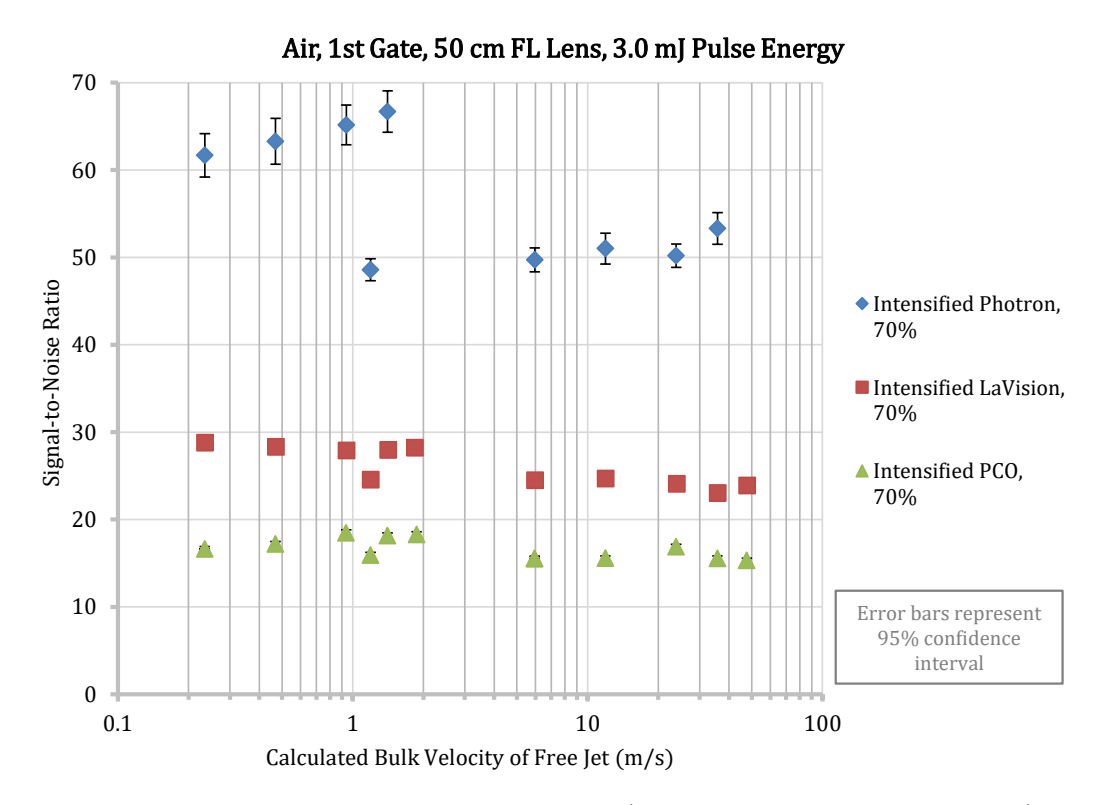


Figure 5.14: SNR for CMOS camera systems (intensifier gain setting noted) in air. No binning. Data from low- and higher-speed jet.

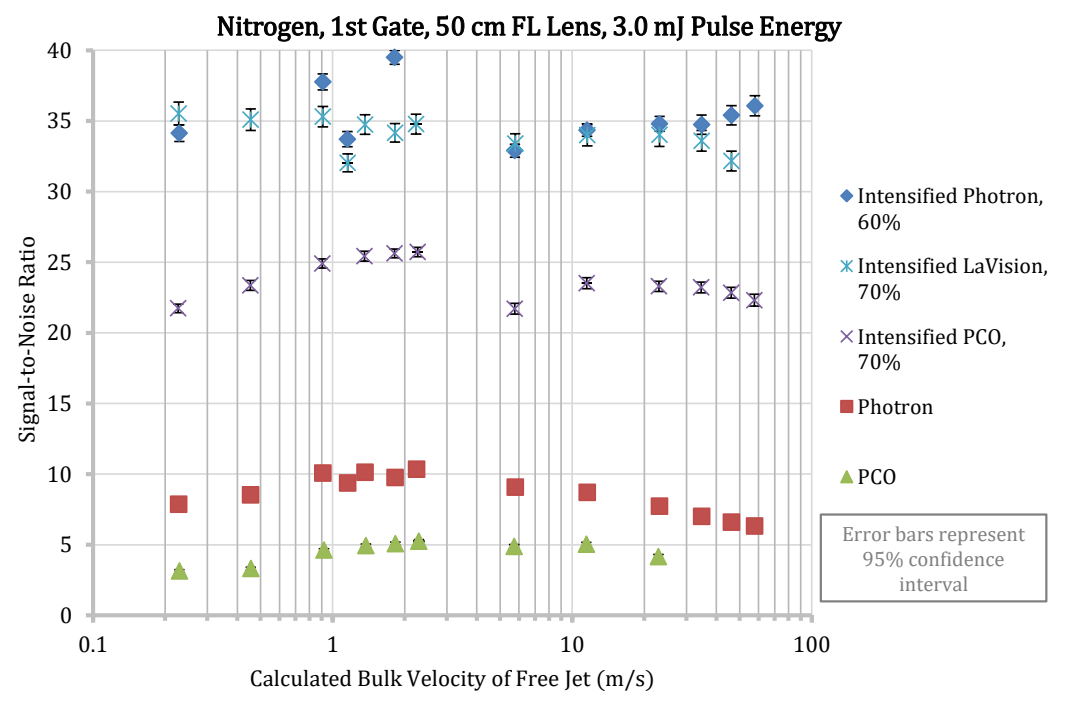


Figure 5.15: SNR for CMOS camera systems (intensifier gain setting noted) in nitrogen. No binning. Data from low- and higher-speed jet.

row-wise binning was not applied which would have enhanced SNR. The plot includes data from both the low- and higher-speed jet. The dip in the data points at $1.2\,\mathrm{m\,s^{-1}}$ is due to the fact that the data points are from the higher-speed jet which sometimes exhibited lower SNR. The difference in SNR for the low- and higher-speed jet is most prominent for the air case (Figure 5.14), especially for the intensified Photron camera. As expected, intensification greatly improves the SNR which Figure 5.15 illustrates. The intensified Photron camera demonstrated the best SNR performance in air and nitrogen. The intensified LaVision showed comparable performance in nitrogen, but employed a higher gain. The un-intensified Photron had higher SNR than the un-intensified PCO in nitrogen. The Photron's overall better SNR performance is probably because its CMOS sensor had larger pixels (with more light gathering capability) while having similar quantum efficiency as the other cameras. Although these larger pixels improve the precision and SNR, they also limit the minimum spatial resolution, which (based on pixel sizes) would be roughly three and two times larger than the LaVision and PCO cameras, respectively. Based on pixel area, which is proportional to the number of photons collected, they are roughly nine and four times larger, respectively. The camera with the second best intensified SNR was the LaVision. Its sCMOS sensor, with its innately lower readout noise (about nine times lower than the PCO according to manufacturer datasheets), likely contributed to it performing better than the intensified PCO camera.

With Digital binning

If lower spatial resolution can be tolerated, symmetric digital binning offers another means of increasing the precision of FLEET velocimetry data acquired with an unintensified camera. The motivation behind performing digital binning was to determine if the superior performance of the Photron system could be emulated by increasing the effective pixel size of the PCO and LaVision cameras. Accordingly,

images from the PCO and LaVision cameras were symmetrically binned 2×2 and 3×3 , respectively, in post-processing before being fit to Gaussian intensity profiles. No additional row-wise binning was done. Figures 5.16–5.19 showcase the results of digital binning and are identical to Figures 5.12–5.15, except that the image data for the PCO and LaVision cameras were symmetrically binned before the line-center determination procedure. The data points for the Photron camera were not modified.

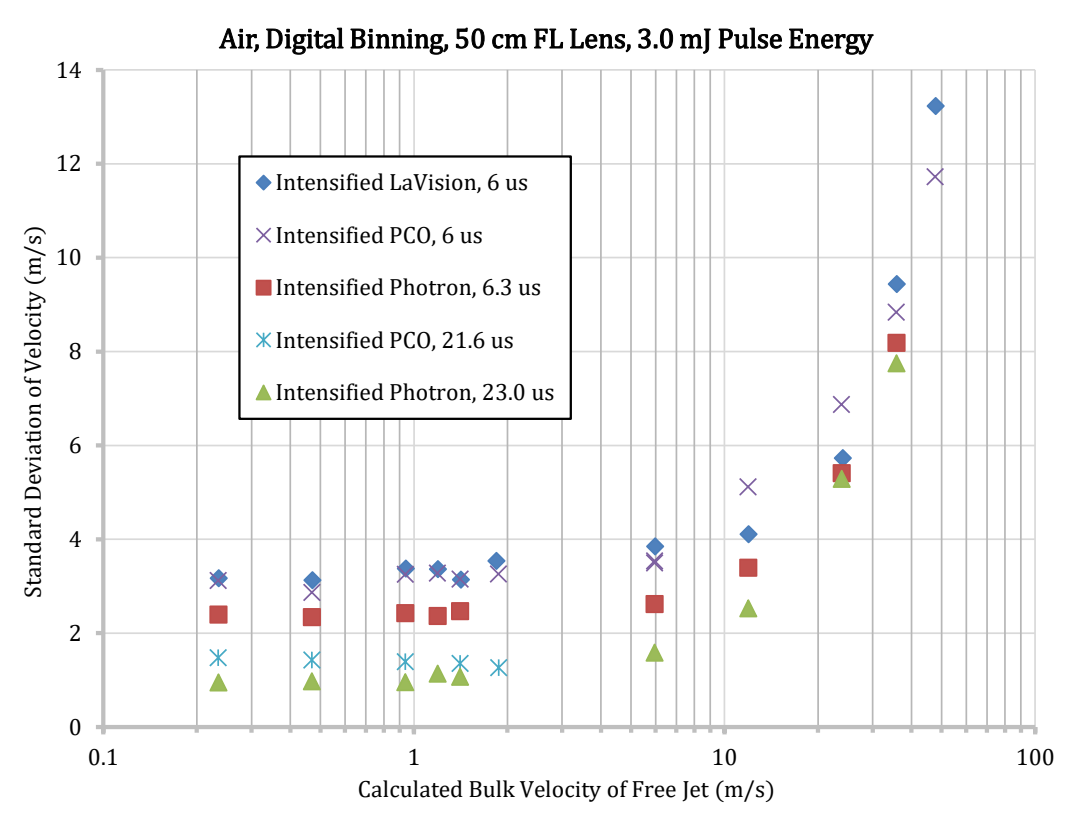


Figure 5.16: Precision as function of calculated bulk velocity for CMOS camera systems (inter-frame delay noted) in air. Digital binning applied before processing $(2 \times 2 \text{ for PCO}, 3 \times 3 \text{ for LaVision})$. Data from low- and higher-speed jet.

For the air free jets, Figure 5.16, the intensified PCO and LaVision systems benefited modestly from digital binning, with typical improvements in precision of around $0.1\,\mathrm{m\,s^{-1}}$. For the nitrogen free jets, Figure 5.17, the intensified PCO and LaVision cameras mostly showed similarly small precision improvements from digital binning. Of all the camera configurations, the one that benefited most from digital binning was the un-intensified PCO camera, with a typical improvement in precision of around

Nitrogen, Digital Binning, 50 cm FL Lens, 3.0 mJ Pulse Energy

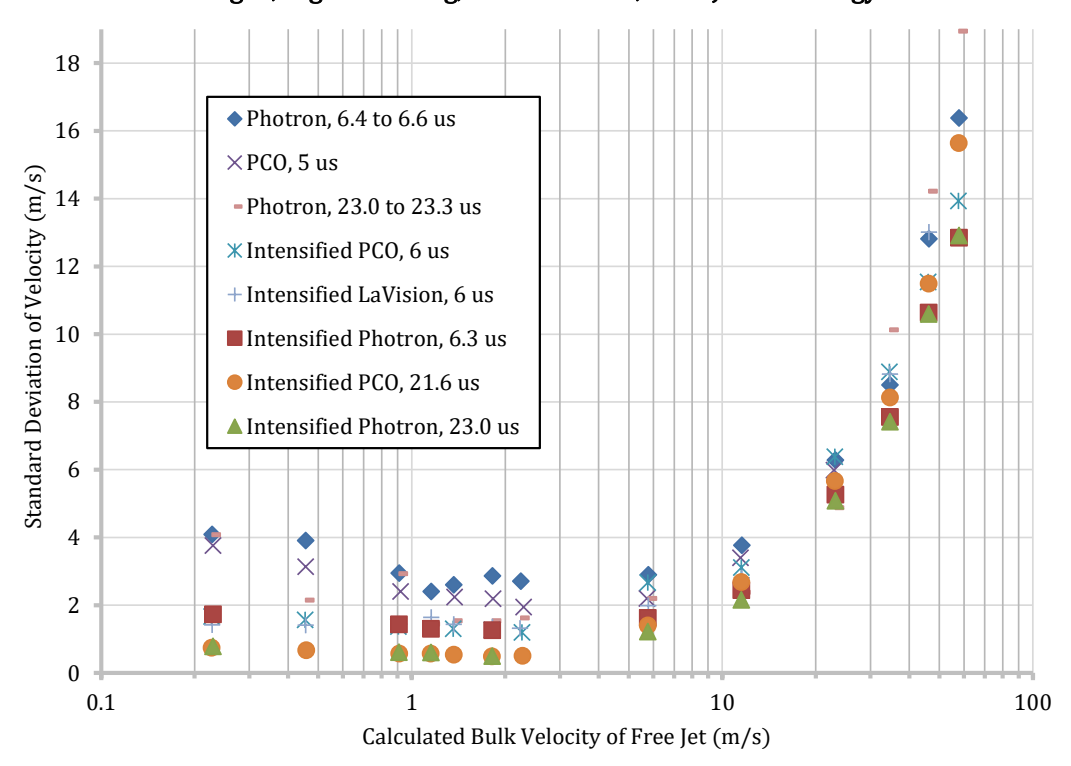


Figure 5.17: Precision as function of calculated bulk velocity for CMOS camera systems (inter-frame delay noted) in nitrogen. Digital binning applied before processing $(2 \times 2 \text{ for PCO}, 3 \times 3 \text{ for LaVision})$. Data from low- and higher-speed jet.

 $0.7\,\mathrm{m\,s^{-1}}$ and one instance (at a velocity of $0.4\,\mathrm{m\,s^{-1}}$) of about $1.6\,\mathrm{m\,s^{-1}}$. For this camera, digital binning allowed its precision to surpass that of the un-intensified Photron.

The change in SNR due to digital binning is shown in Figures 5.18 and 5.19. For the air case (Figure 5.18), which only considered systems with intensification, the intensified LaVision received the greatest SNR enhancement, with improvements as high as 27%. The intensified PCO experienced only marginal improvement. For the nitrogen case (Figure 5.19), the un-intensified PCO experienced the largest relative improvement, with SNR increases as high as 83%. The intensified LaVision experienced some benefit (increases as high as 9%) and the intensified PCO experienced only minimal gains.

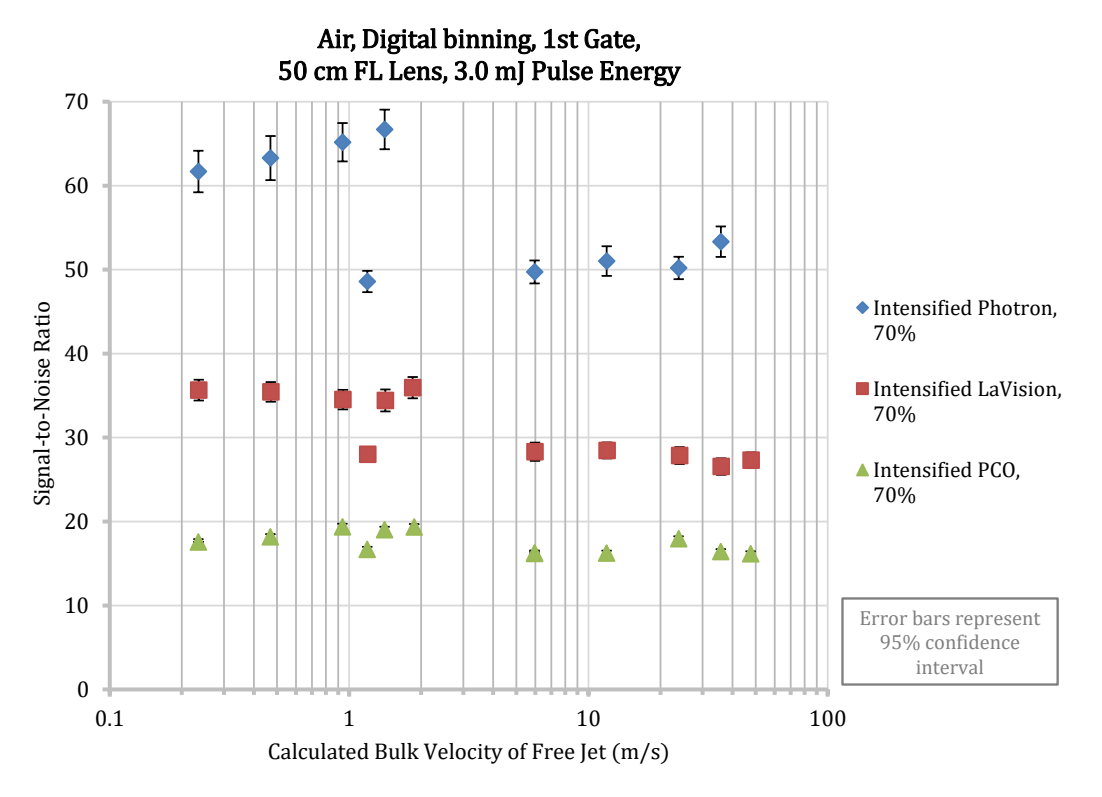


Figure 5.18: SNR for CMOS camera systems (intensifier gain setting noted) in air. Digital binning applied before processing $(2 \times 2 \text{ for PCO}, 3 \times 3 \text{ for LaVision})$. Data from low- and higher-speed jet.

The reason that the intensified cameras experienced less performance boost (with respect to precision) than the un-intensified camera is as follows. The intensified systems already had high signal-to-noise ratios, high enough to ensure reliable line-center determination. In contrast, the initial SNR of the un-intensified camera was relatively low (similar to the level of the readout noise of the camera) and near the threshold at which line-center determination is imprecise. Therefore, when such a system experiences SNR improvement, there is significant gain in precision since finding the line center becomes much easier. Also, it should be noted that the SNR performance enhancements from post-processing digital binning are not equivalent to (and less than) on-sensor hardware binning. The reason for this is that in the case of hardware binning, the photoelectron charge from multiple pixels is noiselessly shifted and added together before readout occurs. Accordingly, the readout noise is

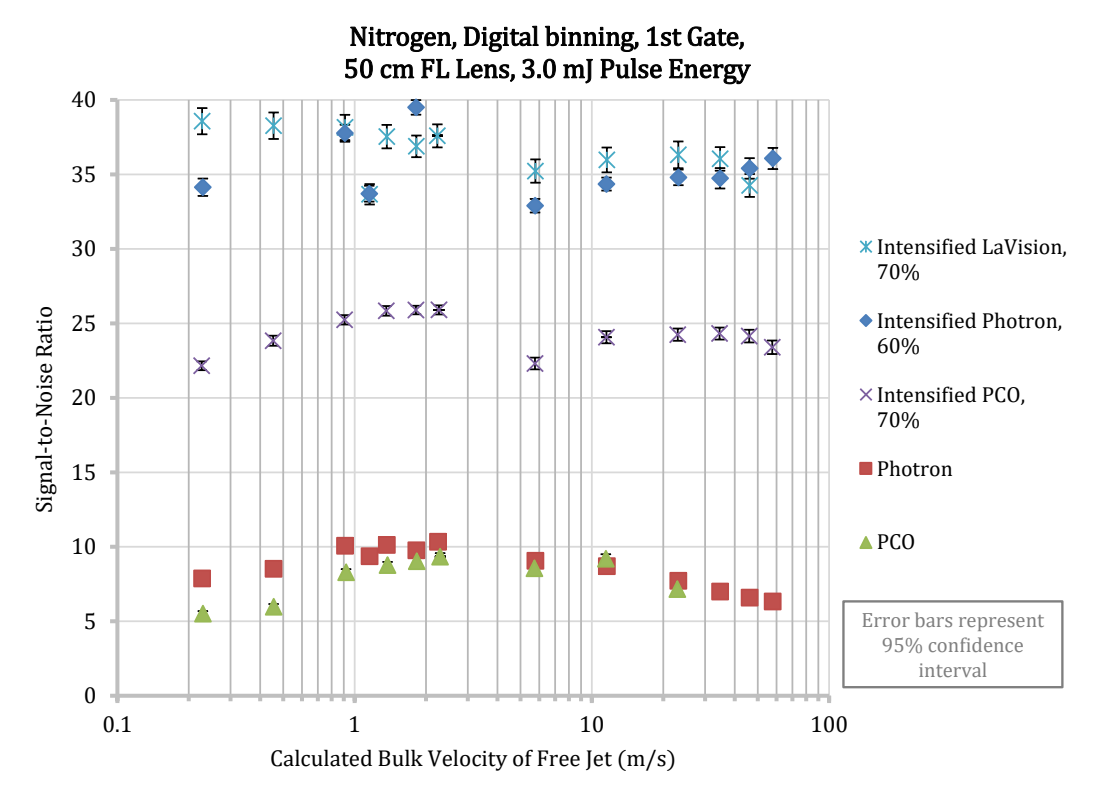


Figure 5.19: SNR for CMOS camera systems (intensifier gain setting noted) in nitrogen. Digital binning applied before processing (2×2 for PCO, 3×3 for LaVision). Data from low- and higher-speed jet.

added only once to the signal summed from four pixels (in the case of 2×2 binning) or from nine pixels (in the case of 3×3 binning). Therefore, the readout noise is effectively reduced by one-quarter or one-ninth, respectively. In the case of post-processing digital binning, every pixel contains readout noise. When the pixels are added together in post-processing, the readout noise is added in quadrature since the noise is uncorrelated and random. So for the case of 2×2 binning, the noise is $\sqrt{4 \times 1^2} = 2$ units and is reduced by one-half. For 3×3 binning, the noise is $\sqrt{9 \times 1^2} = 3$ units and is reduced by one-third. Thus, the readout noise reduction with post-processing digital binning is less than on-sensor hardware binning and the SNR improvement is not as great. The architecture of the CMOS sensors in the tested cameras did not permit on-sensor hardware binning; therefore, the only available binning option was digital binning done in post-processing.

5.4 Summary and Conclusions

The use of high-speed intensified and un-intensified CMOS cameras for performing FLEET velocimetry was demonstrated and the associated precision of the technique was characterized in air and nitrogen flows. All velocimetry measurements were made with two successive exposures (a reference and a delayed) in order to eliminate the uncertainty in initial position of the tagged region that comes from facility vibrations.

The pco.dimax HD camera suffered from two drawbacks, namely, the CMOS sensor exhibited negative ghosting after capturing a relatively high intensity event (while operating in the lower end of its dynamic range) and there was no straightforward means of directly controlling the width of the second gate in double shutter mode. The workaround for the negative ghosting was to take two background images for each data image and then discard the background image that contained the ghosting artifact. Shortening of the second gate width was accomplished by substantially shrinking the region of interest. This workaround is not entirely satisfactory because it decreases the field of view for the exposure and therefore limits the displacements that can be measured.

The measurement precisions obtained using different camera configurations were evaluated. Several methods were investigated for improving the precision of the measurement in post-processing. Row-wise binning of the signal in adjacent pixels increased the signal-to-noise ratio of the FLEET line, which enhanced the precision of the line-center determination and therefore also the precision of the displacement measurement. Row-wise binning was more effective for improving the precision of the un-intensified systems rather than the intensified systems because the intensified systems already possessed high enough SNR to ensure precise line-center determination. Row-wise binning's utility is limited by the fact that it sacrifices spatial resolution for SNR. Additionally, it is most effective when the FLEET line is fairly straight, contiguous and advecting with uniform velocity. Employing longer inter-frame delays

increased precision because velocity measurement uncertainty is inversely proportional to time delay. However, the improvement due to long inter-frame delays is tempered by the time-dependent processes of molecular diffusion and signal decay which worsen precision as time delay increases. Furthermore, long time delays are only acceptable for non-accelerating flows and flows where the turbulence timescale is longer than the time delay. In general, there is a maximum time delay that optimizes precision. This maximum depends on the flow regime and whether the gas is air or nitrogen.

The greatest improvement in precision was obtained with row-wise binning by 8 pixels (about the apparent thickness of the FLEET line) and using a long inter-frame delay ($\geq 48\,\mu s$). Precisions of $0.5\,m\,s^{-1}$ in air and $0.2\,m\,s^{-1}$ in pure nitrogen were achieved at a bulk velocity of $0.5\,m\,s^{-1}$. These values represent the current observed limits for the precision of the method using a realistic amount of binning. Lower velocities could possibly have been measured if the flow were even steadier. These single-shot precisions are better¹² (in absolute terms) than what has been previously reported for FLEET in air: $0.53\,m\,s^{-1}$ (in quiescent air) [115], $5\,m\,s^{-1}$ (at velocities of 0, 40 and $480\,m\,s^{-1}$) [2, 6, 124] and $10\,m\,s^{-1}$ (at a velocity of $100\,m\,s^{-1}$) [125]. Additionally, the precision in nitrogen is better than what has been previously reported: $0.41\,m\,s^{-1}$ (in quiescent nitrogen) [5] and less than about $10\,m\,s^{-1}$ (at a velocity of approximately $1900\,m\,s^{-1}$) [96]. Moreover, the precision in nitrogen is even superior to the low temperature and pressure results presented in Section 3.5.3 of Chapter 3: $5.6-15\,m\,s^{-1}$ (at velocities of $42-480\,m\,s^{-1}$).

In comparison to other unseeded air, single-laser methods, FLEET is more precise: FRS has an estimated precision of roughly $15-30\,\mathrm{m\,s^{-1}}$ (at velocities of about $200-400\,\mathrm{m\,s^{-1}}$) [126], and IRS reports $8-11\,\mathrm{m\,s^{-1}}$ (in quiescent air) [127, 128] and $7\,\mathrm{m\,s^{-1}}$ (time-averaged for $1\,\mathrm{m\,s}$, at a velocity of $10\,\mathrm{m\,s^{-1}}$) [129]. In comparison to

¹²These exceptional absolute precisions were achieved with row-wise binning and relatively long time delays, strategies which may not always be feasible.

unseeded air, multiple-laser methods, FLEET has comparable precision: LITA exhibits $0.5\,\mathrm{m\,s^{-1}}$ (in quiescent air) [130] and $0.8\,\mathrm{m\,s^{-1}}$ (at a velocity of $20\,\mathrm{m\,s^{-1}}$) [131], RELIEF demonstrates $7\,\mathrm{m\,s^{-1}}$ (at a velocity of $270\,\mathrm{m\,s^{-1}}$) [117] and APART shows $2.7\,\mathrm{m\,s^{-1}}$ (at a velocity of $630.8\,\mathrm{m\,s^{-1}}$) [132]. Of course, each velocimetry method has its relative advantages. FRS provides whole images of the velocity field. FRS, IRS and LITA simultaneously measure other parameters like temperature, density, pressure and/or Mach number. FLEET affords ease of implementation (requiring only a single laser and camera) in addition to precise velocity determination. Furthermore, with a modified setup, FLEET offers simultaneous measurements of temperature [3] or mixture fraction [13].

It was also observed that the standard deviation was not minimized at very slow or stagnant flows, which is counterintuitive because this is when velocity fluctuations are the smallest. Precision worsened because SNR was reduced. This SNR reduction likely occurs because the same volume of gas is being repeatedly interrogated by the femtosecond pulse (which operates at 1 kHz and 3.0 mJ), leading to the accumulation of contaminant gas species that act to degrade the FLEET signal, reduce SNR and make line-center determination imprecise. Accordingly, care must be exercised when probing stagnant gases (such as in static gas cells or at stagnation points) with FLEET in order to avoid impacting the precision of the method. To mitigate the impact, the laser system could be operated at a lower repetition rate or a lower pulse energy.

Three different high-speed CMOS cameras in five different configurations were compared for FLEET velocimetry performance. The best precisions observed were better than $1\,\mathrm{m\,s^{-1}}$. Of the camera systems tested, the Photron FASTCAM SA-X2 showed the best precision and highest SNR in both the intensified and un-intensified configuration for flows of air and nitrogen. This camera also possessed the fastest full-frame repetition rate. The likely reason for the Photron's better performance was that its CMOS sensor had larger pixels than the other sensors while having

similar quantum efficiency. This enabled it to have a generally higher SNR than the other systems. However, the tradeoff for the Photron's higher SNR is that it had a lower spatial resolution, about one-third and one-half that of the LaVision and PCO cameras, respectively.

In nitrogen, the un-intensified PCO camera with short inter-frame delay had only slightly worse precision than the un-intensified Photron. For speeds up to $12\,\mathrm{m\,s^{-1}}$ in pure nitrogen, the short delay intensified PCO and LaVision cameras had comparable precision to the Photron. For speeds up to $6\,\mathrm{m\,s^{-1}}$ in pure nitrogen, the long delayed intensified PCO camera also exhibited comparable precision to the intensified Photron.

Lengthening the inter-frame delay generally improved precision, except for the un-intensified case when the flow was highly turbulent (above speeds of $23\,\mathrm{m\,s^{-1}}$). In these instances, turbulent diffusion of the FLEET line drastically lowered the SNR of the second exposure causing line-center determination to be imprecise. For equivalent flow and laser settings, FLEET velocimetry in nitrogen is more precise than in air because of the higher signal intensity and longer lifetime of FLEET emission in nitrogen. Longer lifetime enables the FLEET signal in the second exposure to remain relatively strong.

Digital binning did not significantly improve precision, except for the case of the un-intensified PCO camera. For the PCO, digital binning allowed its precision to surpass that of the un-intensified Photron. Nevertheless, digital binning improvement comes at a cost of spatial resolution. For the intensified measurements in air and nitrogen, the Photron still had better precision, even after the other cameras were digitally binned to (partially) account for the larger pixels. The precision of the intensified PCO and LaVision systems did not significantly change when the pixels were binned. It was noted that digital binning in post-processing does not improve SNR as much as on-chip binning, or equivalently, using a sensor with larger pixels.

In future experiments, it would be desirable to have a simultaneous reference measurement, such as a hot-wire anemometer or a PIV system, for comparison to the FLEET method. This would not only provide a means to gauge the accuracy of FLEET measurements, but would also afford a way to determine the velocity fluctuations within the flow itself, apart from using FLEET. The hot-wire is especially suited to resolve transient fluctuations and could reveal the limit for the best achievable precision.

Lastly, note that this study does not endorse any particular manufacturer of equipment. The names of the manufacturers are included for clarity and the equipment tested was mainly chosen because of its availability. Equipment from other manufacturers may perform equally as well or better.

Chapter 6

Conclusion

Each chapter contains its own specific summary and conclusions; therefore, this chapter provides a few general remarks and some possible future directions for the work.

6.1 Concluding Thoughts

The nature of high-speed flows (transonic, supersonic and hypersonic) demands certain performance from femtosecond laser electronic excitation tagging (FLEET) such as satisfactory signal-to-noise ratio (SNR) at depressed static conditions (i.e., low temperatures, pressures and densities), wide dynamic range for velocity determination, and, of course, measurements with acceptable accuracy and precision. A simplified kinetics model (Chapter 2) explains signal intensity changes as a function of density/pressure and temperature in terms of plasma-chemical reactions. Modeling results indicate an optimization of initial signal intensity at reduced density/pressure (due to overall slowing of reaction rates which delays the climax and slows the decay of excited populations) and a small, but measurable enhancement from reduced temperature (due to enlarged N_4 ⁺ population which contributes to excited species via dissociative recombination). Furthermore, modeling shows a strong coupling (i.e.,

¹I.e., short time delay, $t \ll 1 \,\mu s$.

interdependence) among $N_2(A)$, $N_2(B)$ and $N_2(C)$ because of energy pooling, collisional quenching and fluorescence processes. A purpose-built flow facility capable of unheated subsonic through Mach 4.0 operation provided experimental validation (Chapter 3) of the model. Results obtained in the facility confirm signal intensity's primary dependence on density and secondary dependence on temperature (with optimal value at reduced density and temperature), although particular quantitative aspects differ between the model and experiment. The three highest experimental initial signals (acquired in Mach 3.6–4.0 flow) occur at densities $\rho = 0.016-0.055 \,\mathrm{kg} \,\mathrm{m}^{-3}$, roughly corresponding to altitudes $h \approx 23-31$ km (based on the static densities alone). The experimental signal lifetimes exhibit a moderate inverse correlation² to initial signal, translating into relatively short lifetimes for these data (around $2 \mu s$ for $1/e^2$). Fortunately, high-speed velocimetry often uses short time delays to limit displacement of the tagged molecules. Furthermore, these data, despite their swift signal decay, maintain good normalized accuracies and the best normalized precisions for time intervals³ up to $\Delta t = 4.9\,\mu s$. In contrast, higher densities ($\rho \gtrsim 0.31\,\mathrm{kg\,m^{-3}}$) display much longer lifetimes (the longest at atmospheric conditions: 4 145 μ s for $1/e^2$) and substantially lower initial signals (by a factor of roughly 16–18). Successful application of FLEET to a sweeping jet actuator operating in the compressible regime (Chapter 4)—a challenging problem of practical interest—showcases numerous advantages of the method. FLEET's demonstrated abilities include resolving subsonic through supersonic velocities within the same measurement, non-intrusively mapping the internal flow features inside millimeter-scale passageways, tolerating wildly unsteady wind loading in the external flow field and simultaneously ascertaining the quality of jet mixing (via sensitivity of initial signal to oxygen concentration). These advantages stand in contrast to the comparatively limited capabilities of a more traditional

²Note that lifetimes actually depend on density in an approximately U-shaped trend.

³In particular, the normalized accuracies and precisions improve with increasing time interval for these data.

⁴In a flow with a Mach number of approximately 0.1.

approach: single-probe hot-wire anemometry. For this particular optical setup, the use of relatively low femtosecond laser fluence caused a loss of precision (noticeable in the ostensibly quiescent regions of the external velocity fluctuation profiles). Efforts to characterize the fundamental precision of FLEET velocimetry using fast-framing cameras (Chapter 5) led to the development of a number of practical strategies to improve the overall measurement. Despite being initially applied to lower speed free jets (of roughly 0.2–60 m s⁻¹), many of these strategies are readily applied to higher speed flows: 1) utilizing multi-frame bursts to eliminate imaging artifacts, provide suitable backgrounds and separate data frames for easier processing, 2) fitting Gaussian functions to recorded intensity profiles for robust determination of displacement, and 3) avoiding highly repetitive excitation of stagnant regions which impairs SNR (and thus precision). Additionally, the effort produced several pragmatic observations: 1) precision (i.e., standard deviation of velocity measurements) inversely relates to time interval Δt and/or SNR, 2) digital binning of image data raises SNR, and 3) camera sensors with larger pixels (and similar quantum efficiency) acquire higher SNR data. Note that these latter two effects come at the price of spatial resolution.

6.2 Future Work

6.2.1 Kinetics Model Improvements

One area of immediate interest is incorporating a spatial dimension and the accompanying physics into the kinetics model (from Chapter 2) to increase its experimental agreement and predictive capability beyond several hundred nanoseconds after the laser pulse. Although the model's current timescales have relevance for very fast hypersonic flows, measurements in slower flows (e.g., transonic) typical require time delays of several microseconds for adequate precision. Following the approach of Shneider et al. [73], we would invoke symmetry along the laser propagation axis to

reduce each governing equation in cylindrical coordinates to its radial components. Like the original model, species balance (continuity) equations would track production and consumption rates; however, all variables would now include a radial dependence and the balance equations would have additional terms accounting for transport fluxes related to electrical mobility, mass diffusivity and bulk fluid motion. The vibrational and electronic temperature equations would be cast in cylindrical form with variables depending on the radial coordinate. Furthermore, the Navier-Stokes equations (continuity, momentum and energy) would portray the bulk fluid motion driven by heating and the evolution of gas properties (such as overall density and translational temperature). The Poisson equation (for the electric potential) would describe the electric field generated by the charged species which contributes to their transport. Ultimately, the additional physics would better account for the spatial distribution⁵ of species by transport processes and the low density region that forms in the center of the tagging, both of which act to slow reaction rates, and the work done by gas dynamic expansion, which permits more accurate evaluation of translational temperature.

After these model revisions, it would be prudent to retune the unknown coefficients, preferably with an intelligent optimization algorithm. The presently tuned values likely contain contributions associated with attempting to match the long signal life of the photomultiplier tube results. However, incorporation of the above physics would naturally lengthen the signal lifetimes and eliminate the need for using solely these rate coefficients to match the experimental results at long time delays.

As mentioned in Chapter 2, it would be desirable to validate the model with more than simply measurements of the first and second positive emission (i.e., B- and C-state population). In particular, the photoionization submodel could be validated as a function of initial density/pressure with microwave scattering [89] for electron

⁵Also, the model could now consider the effect of a Gaussian laser intensity profile on the initial photoionization.

number density and laser Thomson scattering for electronic temperature. Such diagnostics would facilitate tracking in time as well. Measurement of the metastable A-state population could be accomplished with laser absorption (or laser-induced fluorescence). It would also be beneficial to enhance the spectral and time resolution of the first and second positive emission measurements. Using a fast photomultiplier and monochromator (to isolate individual rovibrational features) would enable validation and/or refinement of the monolithic assumption for the spectral bands within the time-varying signal. Given the significant and rapid widening of the tagged line with respect to the initial laser beam waist (attributed to hot atom diffusivity and gas dynamic expansion, Appendix B), it might likewise be prudent to compare the modeling results to experiments using similar laser fluence, but larger tagging volume (i.e., higher pulse energy, but looser beam focusing).

6.2.2 Simultaneous Measurements of Density, Mixing and Velocity in Compressible Flow

Experiments have shown that the strength of the FLEET initial signal depends on not only oxygen concentration [13], but also gas density [5] (Section 3.4.1 in Chapter 3). Therefore, without adequate compensation⁶ for the density variation in the external flow field, compressible operation of the sweeping jet actuator (Chapter 4) precludes quantitative measurements of jet mixing by FLEET. Nonetheless, it is desirable to perform simultaneous and instantaneous (i.e., single-shot) quantitative measurements of jet mixing or oxygen mixture fraction in compressible flows. Such measurements would require at least three sequential data frames⁷ per laser pulse: the first frame at t=0 to capture the Rayleigh scattering (from the femtosecond laser) whose intensity is directly proportional to density [12], the second frame at an early time delay (e.g.,

 $^{^6\}mathrm{A}$ baseline image in quiescent air readily calibrates for initial signal's dependence on laser fluence since modern ultrafast lasers provide very stable shot-to-shot pulse energies.

⁷And probably several preceding frames to eliminate imaging artifacts and provide backgrounds.

 $t \approx 0.1 \,\mu\text{s}$) to acquire the FLEET signal related to oxygen mixture fraction via a nonlinear calibration curve [13], and the third frame at an appropriate later delay (e.g., $t > 1 \,\mu s$) to image the displaced tagged line for determination of velocity. Note that Edwards [2] first described the use of FLEET for simultaneous measurement of multiple flow parameters. The reference (initial) line for comparison to the displaced line can come from either the first (Rayleigh scattering) or second (oxygen mixture fraction) frame. Furthermore, depending on the speed of the flow, it may be possible to make the velocity measurement using the displacement between the first two frames (since the second frame may be taken as late as $t \approx 0.2 \,\mu\text{s}$), though precision may suffer based on the results of Chapter 3. To avoid potential contamination by the second positive and other intense emissions from the plasma, a spectrally narrow bandpass filter centered on the laser wavelength and a very short gate width (tens of nanoseconds) will be needed when capturing the Rayleigh scattering signal. Although this three-parameter measurement would ideally employ only one intensified camera system, multiple intensified cameras with synchronized timing and jointly indexed fields of view will likely be needed since each parameter requires a different time delay, gate width, gain setting and filter.

6.2.3 Velocity Measurements in Supersonic Shape Morphing Flow Facility

The supersonic shape morphing flow facility (shown in Figure 6.1) of the Applied Physics Group at Princeton University offers a unique opportunity to leverage the advantages of FLEET velocimetry. This small-scale⁸ supersonic wind tunnel can dynamically vary its nozzle contour and thus its test section Mach number from 2.5 to 3.8 [133–135]. The wind tunnel's indraft nature, along with its polycarbonate and acrylic construction, limit its operation to atmospheric stagnation conditions

⁸The test section exit has a fixed cross section of 50.8 by 48.5 mm.

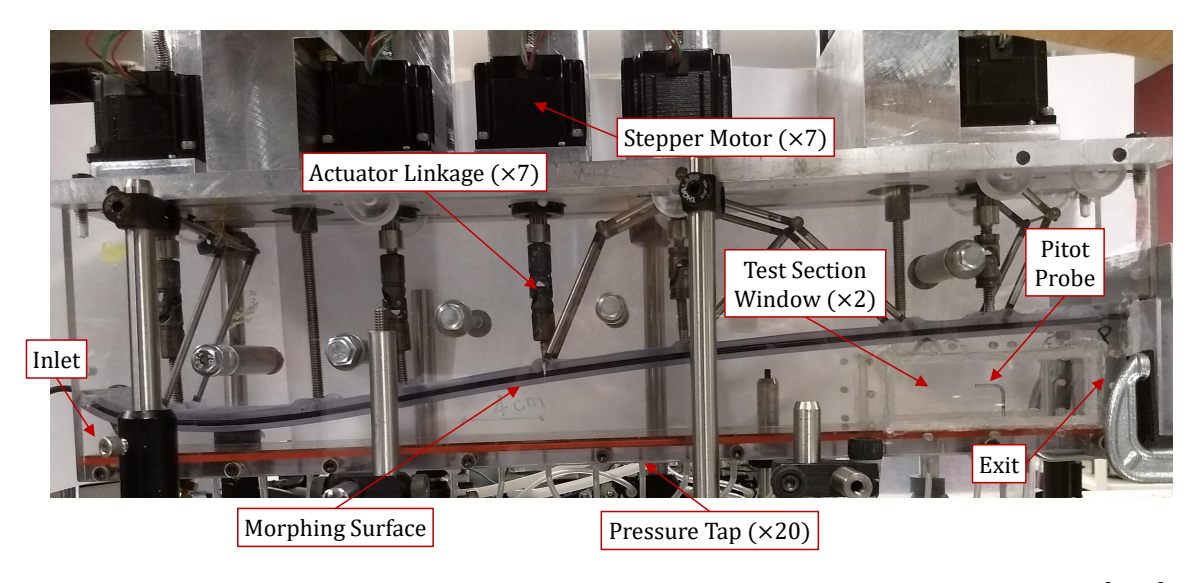


Figure 6.1: Side-view of supersonic shape morphing facility. Adapted from Ref. [133].

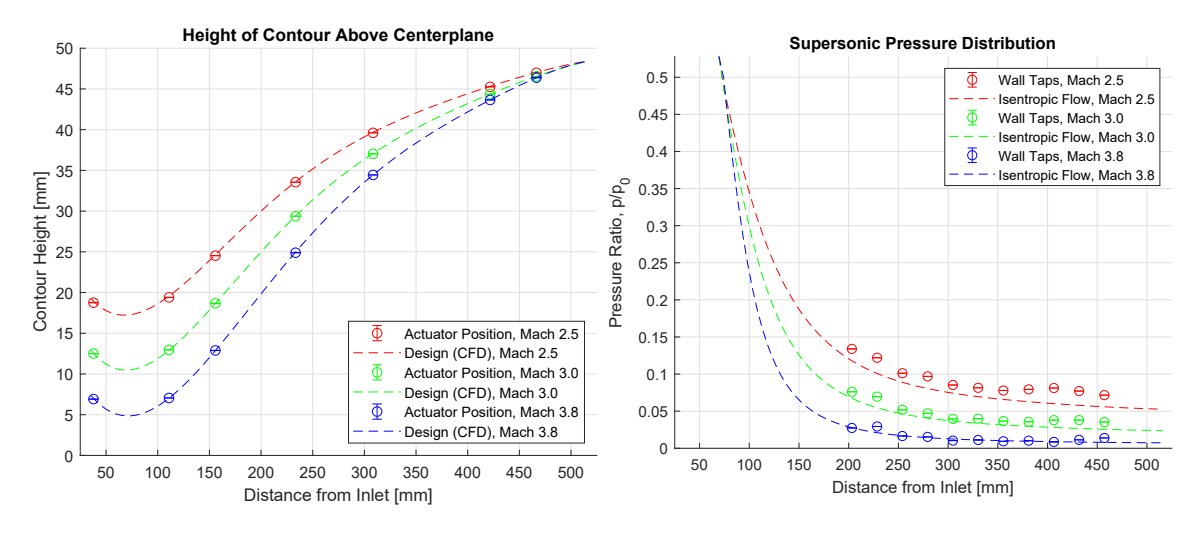


Figure 6.2: Measured (circles) and ideal (dashed lines) contour shape (left) and pressure distribution (right). Flow is left to right. Markers and error bars respectively denote mean and 95% confidence interval. Adapted from Ref. [133].

(101.3 kPa, 300 K). Stepper motor actuators, discretely connected to the deformable upper wall, enable morphing of the expansion contour. Linear potentiometers sense actuator displacement to track the shape of the contour (Figure 6.2, left). The stationary lower wall serves as the centerplane of the two-dimensional nozzle and is instrumented with taps for streamwise static pressure measurement along its length (Figure 6.2, right). Software, written in MATLAB and similar to that which runs the variable temperature and pressure free jet facility described in Chapter 3, provides data acquisition and control functionality. Figure 6.2 also compares the ideal (dashed lines) contour height⁹ and pressure ratio¹⁰ to the experimentally measured (circles) ones, based on 3s worth of data acquired at a rate of 1 kHz. In addition to serving as a variable Mach number wind tunnel, the flow facility enables the investigation of: a) the feasibility of improving flow quality via active optimization of the nozzle contour, and b) the ability to counteract supersonic inlet unstart with shape morphing and other technologies such as plasma actuators.

The test section, which begins around 400 mm on the plots, contains three wall static taps, one centrally located pitot probe, and two schlieren-grade quartz windows¹¹ (for optical measurements). While a simple two-lens schlieren setup affords qualitative visualization of the region, the four pressure measurements presently represent the sole source of quantitative information for the test section. The indraft tunnel's situation in the open laboratory and operation by two-stage air jet ejector system make diagnostic seeding prohibitively difficult. Therefore, to avoid concerns of contamination or damage, unseeded methods such as FLEET are preferred.

FLEET velocimetry would complement existing measurements and immediately contribute greater quantitative awareness of the flow within the test section. In particular, it would support the aforementioned investigative tasks by evaluating

⁹The ideal contour height is based on computational fluid dynamics (CFD) optimization.

¹⁰Ratio of local static pressure, p, to inlet (ambient) stagnation pressure, p_0 .

¹¹Providing a view with dimensions of 95.0 by 30.2 mm.

the uniformity of velocity profiles before and after shape morphing optimization, confirming the presence or absence of strong shockwaves (or other flow features), and measuring the extent of velocity boundary layers. Observe that the tunnel already has non-ideal flow features to explore such as the compression and expansion phenomena indicated by the slight departures from the isentropic curve in Figure 6.2 (right).

We can expect reasonable performance from FLEET in the tunnel using a bore-sight or quasi-boresight configuration (i.e., camera view nearly coaxial with the laser beam [5]). In an indraft tunnel of similar (though fixed) geometry operating at Mach 2.8, Kinefuchi et al. [136] successfully employed FLEET velocimetry (using a frequency-doubled, i.e., 400 nm, femtosecond laser and boresight configuration) to probe the boundary layer impinged by an oblique shockwave. Additionally, results from Chapter 3 illustrate satisfactory performance at the densities and temperatures associated with roughly Mach 3.0–3.8 operation of the shape morphing tunnel, although achieving identical results would require running the tunnel with pure nitrogen (e.g., by affixing a nitrogen filled balloon to the inlet).

6.3 Author's Contribution to Presented Work

The author performed the dissertation research under the guidance and direction of Richard Miles (doctoral adviser) and Paul Danehy (NASA fellowship mentor), supported by numerous technical staff (listed in the Acknowledgments), using facilities at Princeton University and NASA Langley Research Center. The kinetics model was developed under the guidance of Mikhail Shneider. Except as otherwise noted, the author acquired, processed and analyzed the experimental¹³ and computational data.

 $^{^{12}}$ As part of an overall effort to characterize the ability of nanosecond-pulsed plasma actuators to control the shockwave/boundary-layer interaction.

¹³Chapter 3 contains the most detailed description of the algorithms (primarily written in MAT-LAB) used to process and analyze the image data.

Appendix A

Accuracy and Precision

Figure A.1 illustrates the difference between accuracy (i.e., error) and precision (i.e., repeatability or variance). High accuracy implies the velocity measurement conveys the correct value. High precision suggests a minimal spread in measured velocity, translating into fewer required measurements for a steady, laminar flow or detection of smaller velocity fluctuations in an unsteady or turbulent flow.

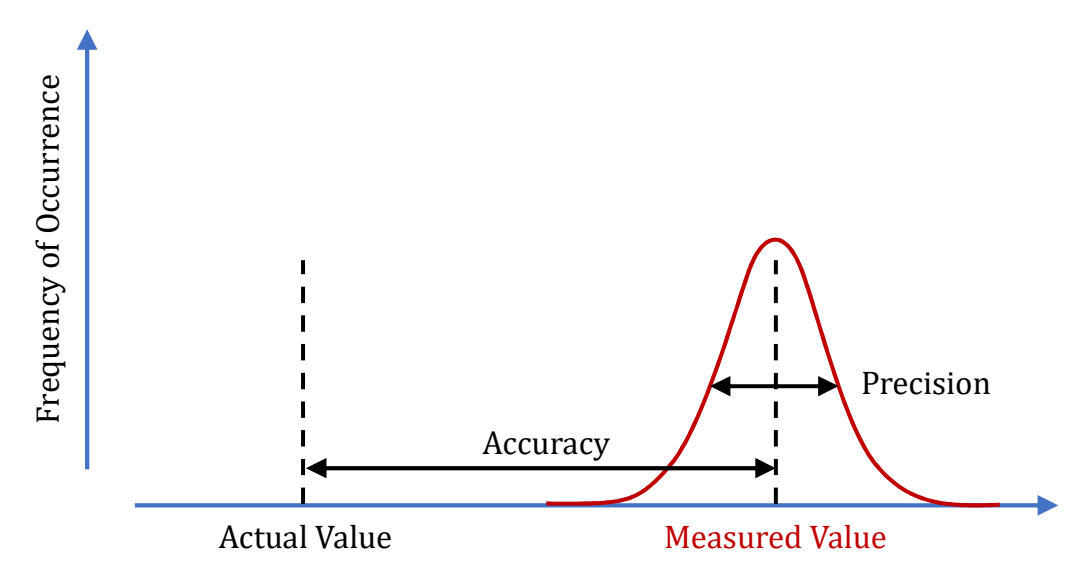


Figure A.1: Qualitative depiction of accuracy and precision for measurement of some value or quantity.

Appendix B

Influence of Mass Diffusivity on Low Temperature and Pressure Signal Results

This appendix extends the Gaussian signal intensity results of Chapter 3 to incorporate the rapid mass diffusion of hot (i.e., kinetically energetic) atoms generated by electron-ion dissociative recombination and electron impact dissociation (respectively R12 and R40 in the kinetics model of Chapter 2).

B.1 Width (Thickness) of Tagged Region

The $1/e^2$ radial width (i.e., tagged line thickness) of the signal intensity profile is given by $2\sigma'_0$, where σ'_0 corresponds to the standard deviation of the Gaussian fit.¹ Figure B.1 plots this width for the center of the tagged region as a function of density, temperature and time delay. The markers and error bars denote the mean and standard deviation, respectively, based on the same data as that of Figure 3.8 in Chapter 3.

¹See Equation (5.1) in Chapter 5 for the functional form of the Gaussian.

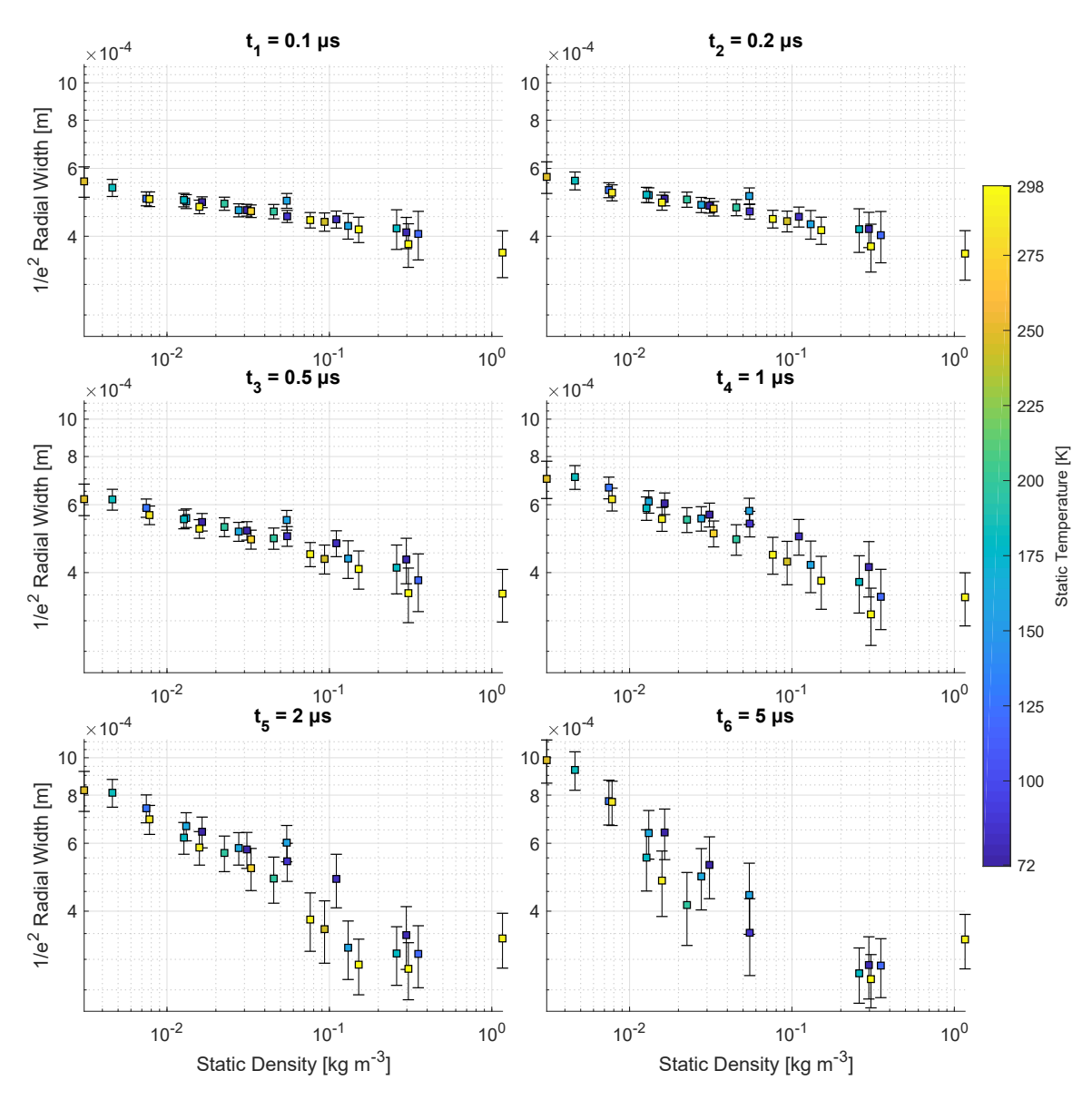


Figure B.1: Radial width (i.e., transverse thickness) of central tagged region as a function of density, temperature and time delay. Markers and error bars denote mean and standard deviation, respectively.

Observe that these widths are tens of times larger than the laser beam's nominal $1/e^2$ waist radius ($w_0 \approx 18 \times 10^{-6}$ m, see Section 3.2.3 for details) used to produce the signal in the experiment. This substantial difference in size presents itself even at early time delays² ($t_1 = 0.1 \,\mu s$) and is likely caused by the rapid diffusion of hot atoms (which possess significant kinetic energy from R12 and R40, among others). Furthermore, Figure B.1 generally shows the expected³ trend of decreasing width (i.e., decreasing diffusivity) with increasing gas density. Although width increases in time as expected³ at lower densities, it decreases in time at higher densities. Section 3.4.3 discusses the increase in dissociation fraction (i.e., relative atomic population) with decreasing gas density which may partly explain the increased diffusivity at low densities. Also, width fails to increase with gas temperature as expected³ probably because the atoms which drive the rapid diffusion process are far hotter than the prevalent gas temperature of the molecules (i.e., mean energies of $\bar{\epsilon}_N \approx 0.5$ –1.75 eV versus $\bar{\epsilon}_{N_2} \approx 0.009$ –0.039 eV for $T \approx 72$ –298 K).

B.2 Integrated Signal Intensity

Integrating across the spatial intensity profile can compensate for diffusion of the signal along the transverse axis, y (with units of px). For the Gaussian signal intensity profile, S(y),

$$\int S(y)dy = \sqrt{2\pi}\sigma_0' S_0, \tag{B.1}$$

where S_0 corresponds to the peak signal of the Gaussian fit (in units of AU). Figure B.2 shows this integrated signal (for the center of the tagged region) as a function of density, temperature and time delay. Markers and error bars denote mean and standard deviation, respectively. This figure serves as the integrated counterpart to

²The relatively long gate ($\Delta t_{\rm gate} = 0.5\,\mu s$) also contributed to the presence of diffusion effects at $t_1 = 0.1\,\mu s$.

³According to basic kinetic theory, mass diffusivity, D, relates to gas temperature, T, and gas density, ρ , via $D \propto \sqrt{T}/\rho$. Furthermore, diffusion length scale, l_D , relates to time, t, via $l_D \propto \sqrt{Dt}$.

Figure 3.8 in Chapter 3 which plots peak Gaussian signal and relies upon the same data.

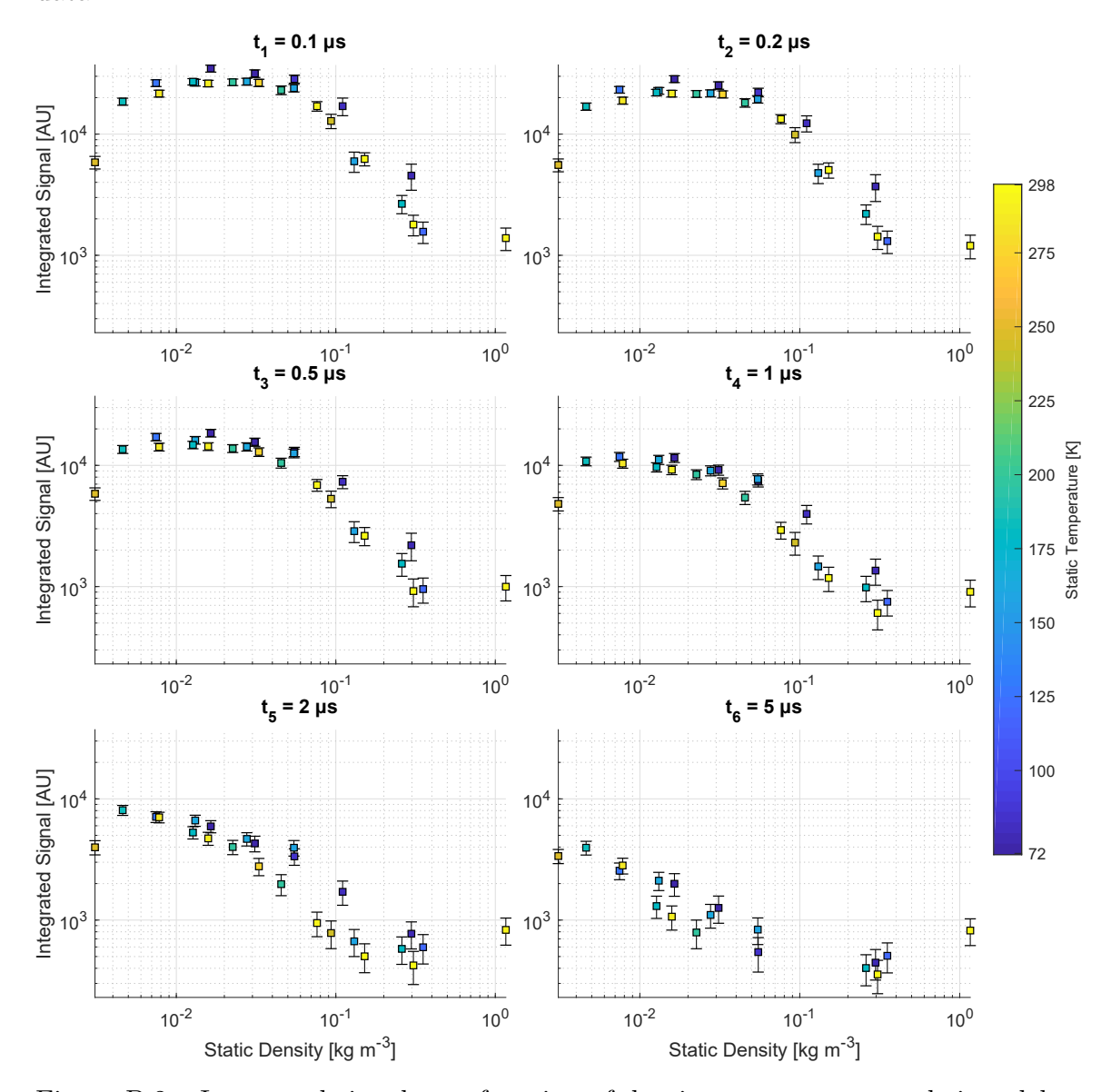


Figure B.2: Integrated signal as a function of density, temperature and time delay. Markers and error bars denote mean and standard deviation, respectively.

Other than the expected difference in absolute signal strengths, the integrated and peak signals (Figures B.2 and 3.8, respectively) exhibit remarkably similar trends with density, temperature and time up to about $2\,\mu s$. For $t \geq 2\,\mu s$, at lower densities (roughly $\rho \lesssim 0.1\,\mathrm{kg\,m^{-3}}$), the integrated signal decays more slowly than the peak signal and thereby maintains a stronger dependence on density. Despite this quanti-

tative difference, the two plots remain qualitatively very similar. Therefore, the peak Gaussian signal can be regarded as generally representative of the signal intensity in the center of the tagged region for these experimental conditions.

B.3 Initial Integrated Signal Compared to Model

Considering just the initial delay ($t_1 = 0.1 \,\mu s$) from Figure B.2 and then plotting these data against the initial signal of the simulation produces Figure B.3, the integrated counterpart to Figure 3.9 in Chapter 3.

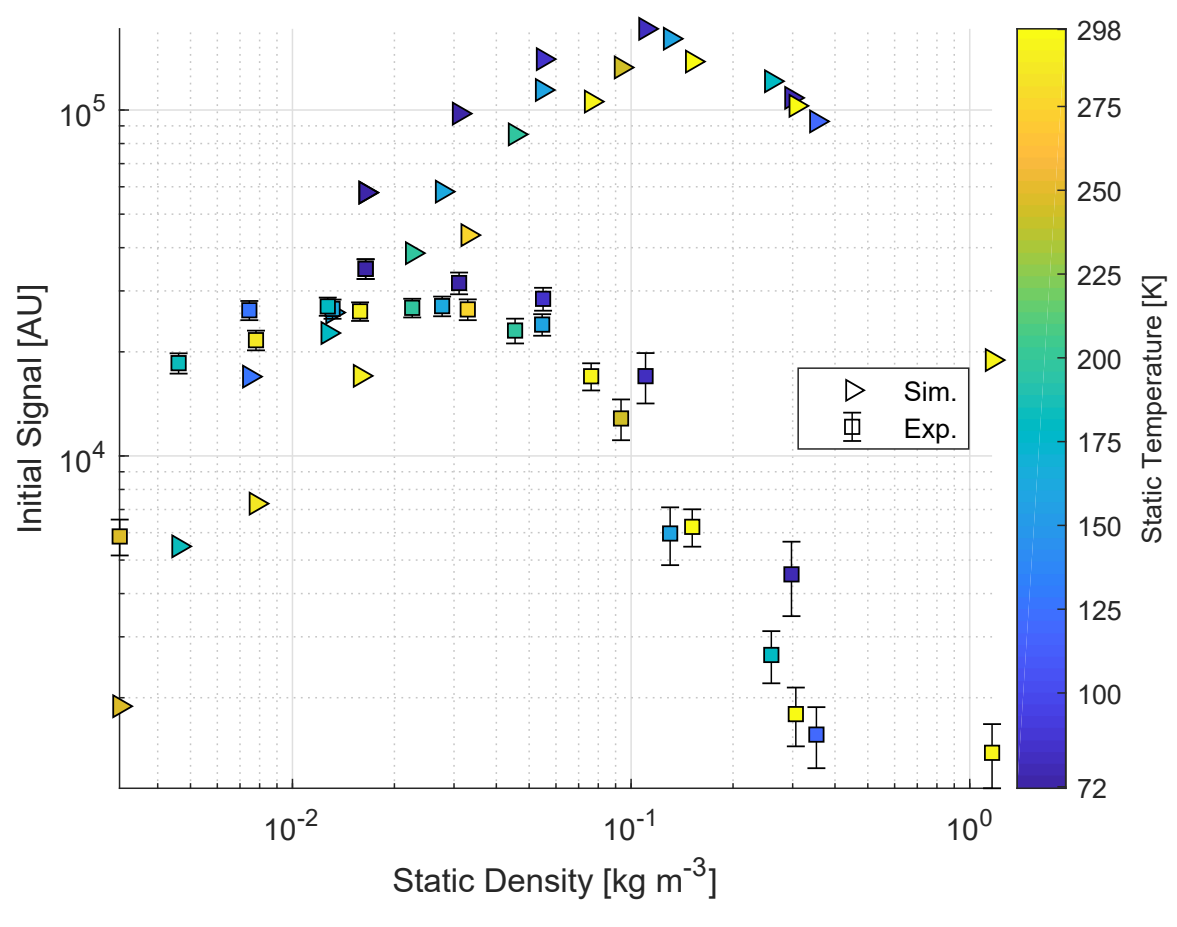


Figure B.3: Simulation (triangles) compared to experiment (boxes) for initial signal as a function of density and temperature. Simulation accounts for total signal of tagged region whereas experiment considers integrated signal along central profile. Error bars correspond to one standard deviation.

The primary difference between Figures B.3 and 3.9 is the higher absolute signal strength for the integrated experimental data (expected from the integration operation) which yields better agreement to the absolute magnitude of the simulation data. Secondary differences include stronger signal relative to the atmospheric value (greater by a few tens of percent) and slightly faster signal roll-off with increasing density. Both of these differences arise from the modest decrease in tagged line width as density increases and suppresses diffusion (see Figure B.1, $t_1 = 0.1 \,\mu\text{s}$).

Appendix C

Sweeping Jet Actuator FLEET Measurement Details

C.1 Single-Shot Velocity Measurements

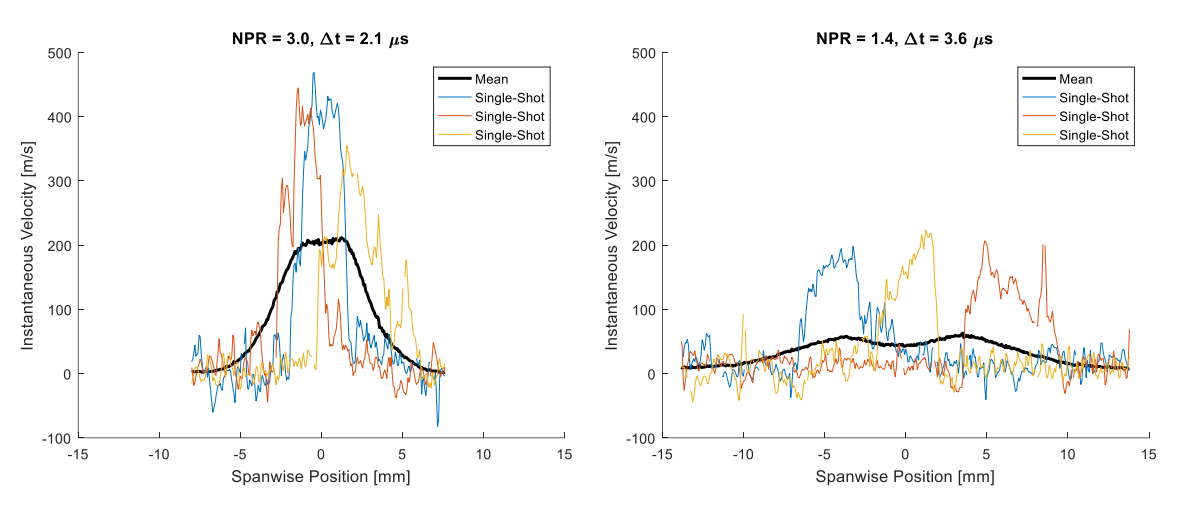


Figure C.1: FLEET single-shot and mean velocity profiles for two NPRs (in air) at 2.5 mm downstream.

Figure C.1 shows a sampling of the FLEET single-shot (i.e., instantaneous) velocity profiles in the external flow field for nozzle pressure ratios (NPRs) of 1.4 and 3.0 at 2.5 mm downstream of the exit. Two different time delays, denoted by Δt ,

¹I.e., time intervals used to calculate velocities.

are necessary for adequate displacement of the tagged line. Compared to the mean profiles, the single shots are nosier and have finite negative velocities. Both of these aspects are artifacts of the line-fitting imprecision associated with low signal-to-noise ratio (SNR), discussed in the next section.

C.2 Analysis of Velocity Precision

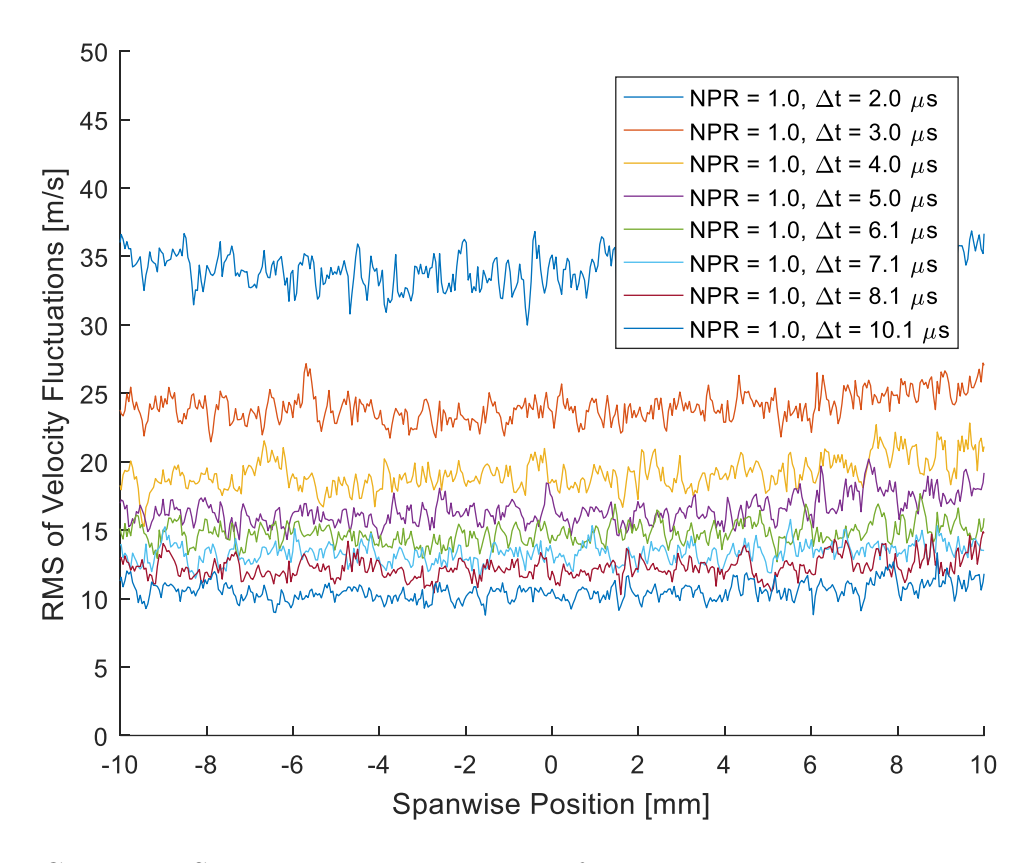


Figure C.2: Post-SWJ testing measurement of FLEET precision in quiescent air for 1 m focal length and 2.0 mJ pulse energy.

At the conclusion of the sweeping jet tests, the precision of the FLEET setup was characterized by measuring the velocity of quiescent air using the same laser and camera settings as the sweeping jet tests. Figure C.2 shows these results in terms of the root mean square (RMS) of the mean-subtracted velocity fluctuations

(i.e., standard deviation of velocity). As expected,² the precision improved with time delay.

Table C.1: Precision comparison of FLEET in air using intensified cameras (CMOS, 20 µm pixels).

SWJ Testing, Est. RMS in Jet ^a	Time Delay ^a
$[{ m m}{ m s}^{-1}]$	$[\mu s]$
25	2.1
20	3.6
10	10.6
Post-SWJ Testing, RMS in Quiescent Air ^a	Time Delay ^a
$[\mathrm{m}\mathrm{s}^{-1}]$	$[\mu s]$
34	2.0
24	3.0
19	4.0
10	10.1
Ref. [11], Approx. RMS in Quiescent Air ^b	Time Delay ^b
$[\mathrm{m}\mathrm{s}^{-1}]$	$[\mu s]$
3.2	8.3
2.4	16.7

^a 1.0 m FL, 2.0 mJ energy, 1.0 µs gate

Table C.1 compares these post-test precisions to the estimated precisions of the sweeping jet measurements (based on the RMS value in the quiescent regions) and the precisions reported by Reference [11] for a similar camera/intensifier setup, but at higher laser fluence. Measurement precision is proportional to SNR which itself is proportional to the laser fluence for these focal lengths (FLs). Accordingly, the precision improves three- to fourfold when laser fluence is raised sevenfold. This suggests the lower precision of FLEET as compared to hot-wire anemometry is not a fundamental limitation of the technique, but rather of the experimental setup and could be remedied with tighter focusing or use of a higher power laser. Therefore, an

^b 0.5 m FL, 3.0 mJ energy, 2.0 µs gate

²See Equation (5.6) in Chapter 5.

alternative approach might have been to focus more tightly (with a shorter line) and pan the field of view, although this may have led to new experimental uncertainties (such as those associated with stitching fields of view together). Note there were additional sources of imprecision such as facility vibration or beam pointing since the reference and delayed images were not recorded sequentially.

C.3 Data Point Density of Internal Velocity Measurements

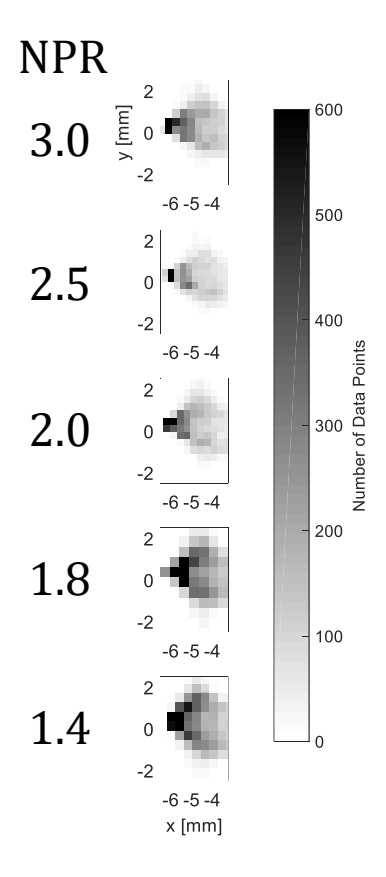


Figure C.3: Number of data points within each grid position used for producing mean and RMS values.

Figure C.3 shows the distribution of data points (velocities and corresponding positions) on the uniform grid. Note the grid size varies slightly among the different

plots. The greatest density of data points is near the origin of the FLEET spot at $(-6.2 \,\mathrm{mm}, 0.2 \,\mathrm{mm})$ and decreases with progressing distance downstream.

Appendix D

Characterization of Low-speed Jet

The low-speed jet was characterized in order to verify that the facility was actually capable of providing a clean flow without significant fluctuations. Figure D.1 shows schlieren images of the inverted low-speed jet for a range of bulk Reynolds numbers (based on nozzle exit diameter). The flow is from top to bottom. The bulk Reynolds number was varied by adjusting the flow rate of gaseous nitrogen into the cooler and chilling the flow by boiling off liquid nitrogen inside the cooler. For a given velocity, cooling the gas changes its density and viscosity and thus its Reynolds number. As seen in the images, breakup and mixing of the jet does not begin until roughly 2 cm below the nozzle exit. This 2 cm region was where all FLEET velocity measurements were taken when using this facility.

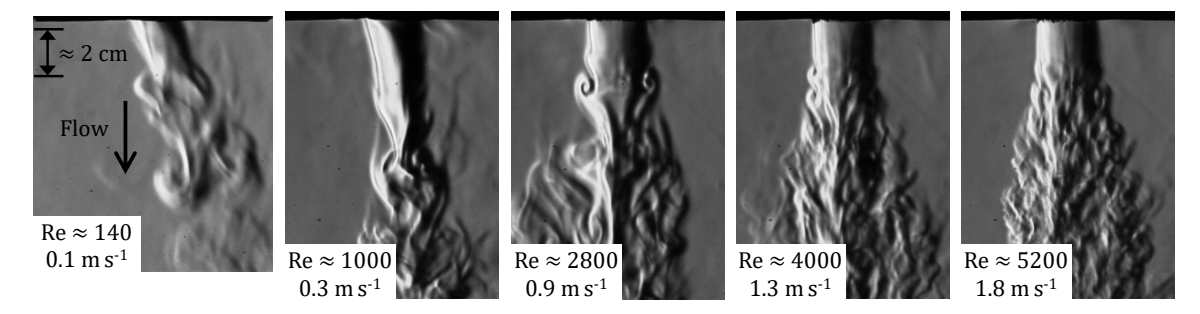


Figure D.1: Schlieren images of inverted low-speed jet. Nozzle exit at top of frame. Flow is top to bottom. All velocity measurements occurred within 2 cm of nozzle exit.

Bibliography

- [1] J. B. Michael, M. R. Edwards, A. Dogariu, and R. B. Miles, "Femtosecond laser electronic excitation tagging for quantitative velocity imaging in air," *Appl. Opt.*, vol. 50, no. 26, pp. 5158–5162, Sep. 2011. DOI: 10.1364/A0.50.005158.
- [2] M. R. Edwards, "Femtosecond laser electronic excitation tagging," B.S.E. Thesis, Princeton University, Department of Mechanical & Aerospace Engineering, May 2012.
- [3] M. R. Edwards, A. Dogariu, and R. B. Miles, "Simultaneous temperature and velocity measurements in air with femtosecond laser tagging," AIAA J., vol. 53, no. 8, pp. 2280–2288, Aug. 2015. DOI: 10.2514/1.J053685.
- [4] M. R. Edwards, C. M. Limbach, R. B. Miles, and A. A. Tropina, "Limitations on high-spatial resolution measurements of turbulence using femtosecond laser tagging," in *53rd AIAA Aerospace Sciences Meeting*, AIAA, Jan. 2015. DOI: 10.2514/6.2015-1219.
- [5] R. A. Burns, C. J. Peters, and P. M. Danehy, "Unseeded velocimetry in nitrogen for high-pressure, cryogenic wind tunnels: Part I. Femtosecond-laser tagging," *Meas. Sci. Technol.*, vol. 29, no. 11, p. 115 302, 2018. DOI: 10.1088/1361-6501/aade1b.
- [6] N. D. Calvert, A. Dogariu, and R. B. Miles, "FLEET boundary layer velocity profile measurements," in 44th AIAA Plasmadynamics and Lasers Conference, AIAA, Jun. 2013. DOI: 10.2514/6.2013-2762.
- [7] N. J. DeLuca, R. B. Miles, N. Jiang, W. D. Kulatilaka, A. K. Patnaik, and J. R. Gord, "FLEET velocimetry for combustion and flow diagnostics," *Appl. Opt.*, vol. 56, no. 31, pp. 8632–8638, Nov. 2017. DOI: 10.1364/A0.56.008632.
- [8] R. B. Miles, M. R. Edwards, J. B. Michael, N. D. Calvert, and A. Dogariu, "Femtosecond laser electronic excitation tagging (FLEET) for imaging flow structure in unseeded hot or cold air or nitrogen," in 51st AIAA Aerospace Sciences Meeting Including the New Horizons Forum and Aerospace Exposition, AIAA, Jan. 2013. DOI: 10.2514/6.2013-340.
- [9] C. J. Peters, R. B. Miles, R. A. Burns, B. F. Bathel, G. S. Jones, and P. M. Danehy, "Femtosecond laser tagging characterization of a sweeping jet actuator operating in the compressible regime," in 32nd AIAA Aerodynamic Measurement Technology and Ground Testing Conference, AIAA, Jun. 2016. DOI: 10.2514/6.2016-3248.

- [10] A. Lofthus and P. H. Krupenie, "The spectrum of molecular nitrogen," *J. Phys. Chem. Ref. Data*, vol. 6, no. 1, pp. 113–307, 1977. DOI: 10.1063/1.555546.
- [11] C. J. Peters, P. M. Danehy, B. F. Bathel, N. Jiang, N. D. Calvert, and R. B. Miles, "Precision of FLEET velocimetry using high-speed CMOS camera systems," in 31st AIAA Aerodynamic Measurement Technology and Ground Testing Conference, AIAA, Jun. 2015. DOI: 10.2514/6.2015-2565.
- [12] R. A. Burns, P. M. Danehy, and C. J. Peters, "Multiparameter flowfield measurements in high-pressure, cryogenic environments using femtosecond lasers," in 32nd AIAA Aerodynamic Measurement Technology and Ground Testing Conference, AIAA, Jun. 2016. DOI: 10.2514/6.2016-3246.
- [13] B. R. Halls, N. Jiang, J. R. Gord, P. M. Danehy, and S. Roy, "Mixture-fraction measurements with femtosecond-laser electronic-excitation tagging," *Appl. Opt.*, vol. 56, no. 11, E94–E98, Apr. 2017. DOI: 10.1364/A0.56.000E94.
- [14] N. J. DeLuca, "Femtosecond laser electronic excitation tagging (FLEET) for a hypersonic optical air data system," M.S.E. Thesis, Princeton University, Department of Mechanical & Aerospace Engineering, Jun. 2014.
- [15] N. D. Calvert, "Femtosecond laser electronic excitation tagging for aerodynamic and thermodynamic measurements," Ph.D. Dissertation, Princeton University, Department of Mechanical & Aerospace Engineering, Sep. 2016.
- [16] Y. Zhang, "The development and characterization of femtosecond laser velocimetry methods," Ph.D. Dissertation, Princeton University, Department of Mechanical & Aerospace Engineering, Jun. 2018.
- [17] C. M. Limbach, "Characterization of nanosecond, femtosecond and dual pulse laser energy deposition in air for flow control and diagnostic applications," Ph.D. Dissertation, Princeton University, Department of Mechanical & Aerospace Engineering, Nov. 2015.
- [18] M. Capitelli, C. M. Ferreira, B. F. Gordiets, and A. I. Osipov, *Plasma Kinetics in Atmospheric Gases*, 1st ed., ser. Springer Series on Atomic, Optical, and Plasma Physics. Springer-Verlag Berlin Heidelberg, 2000, ISBN: 978-3-642-08683-0. DOI: 10.1007/978-3-662-04158-1.
- [19] F. R. Gilmore, R. R. Laher, and P. J. Espy, "Franck-Condon factors, r-centroids, electronic transition moments, and Einstein coefficients for many nitrogen and oxygen band systems," *J. Phys. Chem. Ref. Data*, vol. 21, no. 5, pp. 1005–1107, 1992. DOI: 10.1063/1.555910.
- [20] C. J. Peters, M. N. Shneider, and R. B. Miles, "Kinetics model of femtosecond laser ionization in nitrogen and comparison to experiment," *J. Appl. Phys.*, vol. 125, no. 24, p. 243 301, 2019. DOI: 10.1063/1.5098306.
- [21] M. N. Shneider, A. Baltuška, and A. M. Zheltikov, "Population inversion of molecular nitrogen in an Ar: N₂ mixture by selective resonance-enhanced multiphoton ionization," *J. Appl. Phys.*, vol. 110, no. 8, p. 083112, 2011. DOI: 10.1063/1.3646478.

- [22] Y. Zhang, N. Calvert, M. N. Shneider, and R. B. Miles, "Enhancement of FLEET in argon gas mixtures," in 32nd AIAA Aerodynamic Measurement Technology and Ground Testing Conference, AIAA, Jun. 2016. DOI: 10.2514/6.2016-3249.
- [23] V. Guerra, P. A. Sá, and J. Loureiro, "Kinetic modeling of low-pressure nitrogen discharges and post-discharges," *Eur. Phys. J. Appl. Phys.*, vol. 28, no. 2, pp. 125–152, Nov. 2004. DOI: 10.1051/epjap:2004188.
- [24] J. Henriques, E. Tatarova, and C. M. Ferreira, "Microwave N₂-Ar plasma torch. I. Modeling," J. Appl. Phys., vol. 109, no. 2, p. 023 301, 2011, Rate coefficient for N₂(A) + N₂ \longrightarrow 2 N₂ taken from Clark et al. (1980) seems to have been multiplied by 1×10^2 . Also, the reaction $2 \, \mathrm{N} + \mathrm{N}_2 \longrightarrow \mathrm{N}_2(\mathrm{a}^1 \Pi_\mathrm{g}) + \mathrm{N}_2$ should actually be a two-body radiative recombination process, i.e., $2 \, \mathrm{N} \longrightarrow \mathrm{N}_2(\mathrm{a}^1 \Pi_\mathrm{g}) + h \nu$, according to the original source Becker et al. (1972). DOI: 10.1063/1.3532055.
- [25] N. A. Popov, "Associative ionization reactions involving excited atoms in nitrogen plasma," *Plasma Phys. Rep.*, vol. 35, no. 5, pp. 436–449, May 2009. DOI: 10.1134/S1063780X09050092.
- [26] I. A. Kossyi, A. Y. Kostinsky, A. A. Matveyev, and V. P. Silakov, "Kinetic scheme of the non-equilibrium discharge in nitrogen-oxygen mixtures," *Plasma Sources Sci. Technol.*, vol. 1, no. 3, pp. 207–220, 1992. DOI: 10.1088/0963-0252/1/3/011.
- [27] M. A. A. Clyne and D. H. Stedman, "Rate of recombination of nitrogen atoms," J. Phys. Chem., vol. 71, no. 9, pp. 3071–3073, Aug. 1967. DOI: 10.1021/j100868a056.
- [28] I. M. Campbell and B. A. Thrush, "The recombination of nitrogen atoms and the nitrogen afterglow," *Proc. R. Soc. Lond. A*, vol. 296, no. 1445, pp. 201–221, Jan. 1967. DOI: 10.1098/rspa.1967.0014.
- [29] K. H. Becker, E. H. Fink, W. Groth, W. Jud, and D. Kley, "N₂ formation in the Lewis-Rayleigh afterglow," *Faraday Discuss. Chem. Soc.*, vol. 53, no. 0, pp. 35–51, 1972. DOI: 10.1039/DC9725300035.
- [30] T. Yamashita, "Rate of recombination of nitrogen atoms," J. Chem. Phys., vol. 70, no. 9, pp. 4248–4253, May 1979. DOI: 10.1063/1.437998.
- [31] G. N. Hays and H. J. Oskam, "Reaction rate constant for $2 N_2(A^3 \Sigma_u^+) \longrightarrow N_2(C^3 \Pi_u) + N_2(X^1 \Sigma_g^+, v' > 0)$," *J. Chem. Phys.*, vol. 59, no. 11, pp. 6088–6091, 1973. DOI: 10.1063/1.1679974.
- [32] —, "Population of $N_2(B^3\Pi_g)$ by $N_2(A^3\Sigma_u^+)$ during the nitrogen afterglow," J. Chem. Phys., vol. 59, no. 3, pp. 1507–1516, 1973. DOI: 10.1063/1.1680208.
- [33] L. G. Piper, "State-to-state $N_2(A^3\Sigma_u^+)$ energy-pooling reactions. II. The formation and quenching of $n_2(b^3\Pi_g, v'=1-12)$," *J. Chem. Phys.*, vol. 88, no. 11, pp. 6911–6921, 1988. DOI: 10.1063/1.454388.

- [34] K. S. Klopovsky, A. V. Mukhovatova, A. M. Popov, N. A. Popov, O. B. Popovicheva, and T. V. Rakhimova, "Kinetics of metastable states in high-pressure nitrogen plasma pumped by high-current electron beam," J. Phys. D Appl. Phys., vol. 27, no. 7, pp. 1399–1405, 1994. DOI: 10.1088/0022-3727/27/7/010.
- [35] N. A. Popov, "Fast gas heating in a nitrogen-oxygen discharge plasma: I. Kinetic mechanism," J. Phys. D Appl. Phys., vol. 44, no. 28, p. 285 201, Jun. 2011. DOI: 10.1088/0022-3727/44/28/285201.
- [36] B. F. Gordiets, C. M. Ferreira, V. L. Guerra, J. M. A. H. Loureiro, J. Nahorny, D. Pagnon, M. Touzeau, and M. Vialle, "Kinetic model of a low-pressure N_2 - O_2 flowing glow discharge," *IEEE Trans. Plasma Sci.*, vol. 23, no. 4, pp. 750–768, Aug. 1995, Rate coefficient for $N_2(A) + N_2 \longrightarrow 2 N_2$ taken from Clark et al. (1980) seems to have been multiplied by 1×10^2 . DOI: 10.1109/27.467998.
- [37] Y. Ikezoe, S. Matsuoka, and H. Nakamura, "Recombination of N_4^+ and N_3^+ with electrons in atmospheric pressure nitrogen," *Chem. Phys. Lett.*, vol. 177, no. 4-5, pp. 366–370, Mar. 1991. DOI: 10.1016/0009-2614(91)85067-7.
- [38] K. E. Keister, C. J. Wagner, J. L. Putney, J. D. Hewitt, and J. G. Eden, "Determination of Ar₂⁺ and N₄⁺ recombination coefficients by subpicosecond multiphoton ionization at 248 nm and microwave interferometry," *Phys. Rev. A*, vol. 89, no. 1, p. 013 401, Jan. 2014. DOI: 10.1103/PhysRevA.89.013401.
- [39] Y. S. Cao and R. Johnsen, "Recombination of N_4^+ ions with electrons," *J. Chem. Phys.*, vol. 95, no. 10, pp. 7356–7359, Nov. 1991. DOI: 10.1063/1.461361.
- [40] N. A. Popov, "Investigation of the mechanism for rapid heating of nitrogen and air in gas discharges," *Plasma Phys. Rep.*, vol. 27, no. 10, pp. 886–896, Oct. 2001. DOI: 10.1134/1.1409722.
- [41] M. H. Bortner and T. Baurer, Eds., *Defense Nuclear Agency Reaction Rate Handbook*, 2nd ed. Department of Defense Nuclear Information & Analysis Center (DASIAC), Nov. 1972.
- [42] K. Takaki, J.-S. Chang, and K. G. Kostov, "Atmospheric pressure of nitrogen plasmas in a ferro-electric packed bed barrier discharge reactor. Part I. Modeling," *IEEE Trans. Dielectr. Electr. Insul.*, vol. 11, no. 3, pp. 481–490, Jun. 2004. DOI: 10.1109/TDEI.2004.1306726.
- [43] M. Moravej, X. Yang, M. Barankin, J. Penelon, S. E. Babayan, and R. F. Hicks, "Properties of an atmospheric pressure radio-frequency argon and nitrogen plasma," *Plasma Sources Sci. Technol.*, vol. 15, no. 2, pp. 204–210, 2006, Rate coefficient for $e^- + N_2 \longrightarrow 2 e^- + N_2^+$ taken from Takaki et al. (2004) used wrong unit conversion and should be multiplied by 1.16×10^4 . Rate coefficient for $e^- + N_2 \longrightarrow e^- + 2 N$ was slightly modified from Park (1988). DOI: 10. 1088/0963-0252/15/2/005.

- [44] Y. Akishev, M. Grushin, V. Karalnik, A. Petryakov, and N. Trushkin, "On basic processes sustaining constricted glow discharge in longitudinal N₂ flow at atmospheric pressure," *J. Phys. D Appl. Phys.*, vol. 43, no. 21, p. 215 202, May 2010. DOI: 10.1088/0022-3727/43/21/215202.
- [45] L. S. Polak, P. A. Sergeev, and D. I. Slovetsky, in *Plasmachemical Reactions and Processes*, L. S. Polak, Ed., Moscow: Nauka, 1977, pp. 87–107.
- [46] D. I. Slovetsky, Mechanisms of Chemical Reactions in Non-Equilibrium Plasmas. Moscow: Nauka, 1980.
- [47] J. T. Herron, "Evaluated chemical kinetics data for reactions of $N(^2D)$, $N(^2P)$, and $N_2(A^3\Sigma_u^+)$ in the gas phase," *J. Phys. Chem. Ref. Data*, vol. 28, no. 5, pp. 1453–1483, 1999. DOI: 10.1063/1.556043.
- [48] W. G. Clark and D. W. Setser, "Energy transfer reactions of $N_2(A^3\Sigma_u^+)$. 5. Quenching by hydrogen halides, methyl halides, and other molecules," *J. Phys. Chem.*, vol. 84, no. 18, pp. 2225–2233, 1980. DOI: 10.1021/j100455a003.
- [49] D. Levron and A. V. Phelps, "Quenching of $N_2(A^3\Sigma_u^+, v=0,1)$ by N_2 , Ar, and H_2 ," *J. Chem. Phys.*, vol. 69, no. 5, pp. 2260–2262, Sep. 1978. DOI: 10.1063/1.436788.
- [50] D. M. Hunten and M. B. McElroy, "Quenching of metastable states of atomic and molecular oxygen and nitrogen," Rev. Geophys., vol. 4, no. 3, pp. 303–328, DOI: 10.1029/RG004i003p00303.
- [51] J. F. Noxon, "Active nitrogen at high pressure," J. Chem. Phys., vol. 36, no. 4, pp. 926–940, Feb. 1962, Hunten et al. (1966) and Bortner et al. (1972) must infer the rate coefficient for $N_2(A) + N_2 \longrightarrow 2 N_2$ from this article since it does not explicitly state the value. DOI: 10.1063/1.1732691.
- [52] R. A. Young and G. A. Saint John, "Experiments on $N_2(A^3\Sigma_u^+)$. I. Reaction with N," *J. Chem. Phys.*, vol. 48, no. 2, pp. 895–897, 1968. DOI: 10.1063/1. 1668731.
- [53] B. A. Thrush, "Kinetic behavior of $N_2(A^3\Sigma_u^+)$ in active nitrogen," *J. Chem. Phys.*, vol. 47, no. 9, p. 3691, 1967. DOI: 10.1063/1.1712458.
- [54] K. L. Wray, "Excitation studies on the $N_2(1+)$ and $N_2^+(1-)$ systems in shockheated N-N₂ mixtures," *J. Chem. Phys.*, vol. 44, no. 2, pp. 623–632, 1966. DOI: 10.1063/1.1726735.
- [55] L. G. Piper, "Energy transfer studies on $N_2(X^1\Sigma_g^+, v)$ and $N_2(B^3\Pi_g)$," *J. Chem. Phys.*, vol. 97, no. 1, pp. 270–275, 1992. DOI: 10.1063/1.463625.
- [56] R. F. Heidner III, D. G. Sutton, and S. N. Suchard, "Kinetic study of $N_2(B^3\Pi_g, v)$ quenching by laser-induced fluorescence," *Chem. Phys. Lett.*, vol. 37, no. 2, pp. 243–248, 1976. DOI: 10.1016/0009-2614(76)80207-2.
- [57] J. W. Dreyer and D. Perner, "The deactivation of $n_2(b^3\Pi_g, v = 0-2)$ and $N_2(a'^1\Sigma_u^-, v = 0)$ by nitrogen," *Chem. Phys. Lett.*, vol. 16, no. 1, pp. 169–173, 1972. DOI: 10.1016/0009-2614(72)80483-4.

- [58] M. S. Bak, W. Kim, and M. A. Cappelli, "On the quenching of excited electronic states of molecular nitrogen in nanosecond pulsed discharges in atmospheric pressure air," *Appl. Phys. Lett.*, vol. 98, no. 1, p. 011502, 2011. DOI: 10.1063/1.3535986.
- [59] L. Pereira, A. Morozov, M. M. Fraga, T. Heindl, R. Krücken, J. Wieser, and A. Ulrich, "Temperature dependence of the quenching of $N_2(C^3\Pi_u)$ by $N_2(X)$ and $O_2(X)$," *Eur. Phys. J. D*, vol. 56, no. 3, pp. 325–334, 2010. DOI: 10.1140/epjd/e2009-00313-4.
- [60] K. Hiraoka and G. Nakajima, "A determination of the stabilities of $N_2^+(N_2)_n$ and $O_2^+(N_2)_n$ with n=1–11 from measurements of the gas-phase ion equilibria," *J. Chem. Phys.*, vol. 88, no. 12, pp. 7709–7714, 1988, Provides equilibrium constant as function of temperature for $N_4^+ + N_2 \rightleftharpoons N_2^+ + 2 N_2$. DOI: 10.1063/1.454285.
- [61] H. Böhringer and F. Arnold, "Temperature dependence of three-body association reactions from 45 to 400 K. The reactions $N_2^+ + 2 N_2 \longrightarrow N_4^+ + N_2$ and $O_2^+ + 2 O_2 \longrightarrow O_4^+ + O_2$," J. Chem. Phys., vol. 77, no. 11, pp. 5534–5541, 1982, Provides reverse rate coefficient as function of temperature for $N_4^+ + N_2 \Longrightarrow N_2^+ + 2 N_2$. DOI: 10.1063/1.443758.
- [62] F. Kaufman, "The production of atoms and simple radicals in glow discharges," in Chemical Reactions in Electrical Discharges, ser. Advances in Chemistry,
 B. D. Blaustein, Ed., vol. 80, Assumes rate coefficient for N₄⁺ + N → N₃⁺ + N₂ equals that of O₄⁺ + O → O₃⁺ + O₂ since molecular velocities are similar.,
 American Chemical Society, 1969, ch. 3, pp. 29–47. DOI: 10.1021/ba-1969-0080.ch003.
- [63] S. Dheandhanoo and R. Johnsen, "Laboratory measurements of the association rate coefficients of NO⁺, O₂⁺, N⁺, and N₂⁺ ions with N₂ and CO₂ at temperatures between 100 K and 400 K," *Planet. Space Sci.*, vol. 31, no. 8, pp. 933–938, 1983. DOI: 10.1016/0032-0633(83)90148-4.
- [64] A. Bultel, B. G. Chéron, and P. Vervisch, "Measurement of the ground state and metastable atomic nitrogen number density in a low-pressure plasma jet," Plasma Sources Sci. Technol., vol. 4, no. 4, pp. 597–605, 1995, Rate coefficient for $e^- + N_2 \longrightarrow e^- + 2 N$ was slightly modified from Park (1988). DOI: 10. 1088/0963-0252/4/4/011.
- [65] C. Park, "Assessment of a two-temperature kinetic model for dissociating and weakly ionizing nitrogen," *J. Thermophys. Heat Tr.*, vol. 2, no. 1, pp. 8–16, 1988. DOI: 10.2514/3.55.
- [66] Y. Itikawa, "Cross sections for electron collisions with nitrogen molecules," J. Phys. Chem. Ref. Data, vol. 35, no. 1, pp. 31–53, 2006. DOI: 10.1063/1.1937426.

- [67] G. J. M. Hagelaar and L. C. Pitchford, "Solving the Boltzmann equation to obtain electron transport coefficients and rate coefficients for fluid models," *Plasma Sources Sci. Technol.*, vol. 14, no. 4, pp. 722–733, 2005. DOI: 10. 1088/0963-0252/14/4/011.
- [68] A. V. Phelps and L. C. Pitchford, "Anisotropic scattering of electrons by N₂ and its effect on electron transport," *Phys. Rev. A*, vol. 31, no. 5, pp. 2932–2949, May 1985. DOI: 10.1103/PhysRevA.31.2932.
- [69] LXCat, SIGLO database, www.lxcat.net/SIGLO, retrieved on June 4, 2013.
- [70] A. R. Blythe, T. L. Cottrell, and A. W. Read, "Transition probability in molecular encounters: Part 4. Temperature dependence of relaxation time in methyl chloride and nitrogen," Trans. Faraday Soc., vol. 57, no. 0, pp. 935–942, 1961, Using the "modified" theory which better agrees with the experimental data. Recall that the rate coefficient, $k_{\rm VT}$, relates to the relaxation time, γ , via $k_{\rm VT}n_{\rm N_2}=1/\gamma$. DOI: 10.1039/TF9615700935.
- [71] T. L. Cottrell and A. W. Read, "Temperature dependence of relaxation time in nitrogen," *J. Chem. Phys.*, vol. 37, no. 11, pp. 2733–2734, 1962, Provides experimental confirmation of the theory of Blythe et al. (1961) for vibrational-translation relaxation in N_2 for roughly 500 K to 5500 K. DOI: 10.1063/1.1733096.
- [72] D. A. McQuarrie, *Statistical Mechanics*, 1st ed. Mill Valley, California: University Science Books, 2000, ISBN: 978-1-891389-15-3.
- [73] M. N. Shneider, A. M. Zheltikov, and R. B. Miles, "Tailoring the air plasma with a double laser pulse," *Phys. Plasmas*, vol. 18, no. 6, p. 063509, 2011. DOI: 10.1063/1.3601764.
- [74] C. M. Limbach and R. B. Miles, "Rayleigh scattering measurements of heating and gas perturbations accompanying femtosecond laser tagging," AIAA J., vol. 55, no. 1, pp. 112–120, Jan. 2017, Article describes a higher temperature rise and N₂ dissociation fraction in the FLEET tagged region than reported elsewhere (or calculated by the kinetics model). DOI: 10.2514/1.J054772.
- [75] M. R. New-Tolley, M. N. Shneider, and R. B. Miles, "Evolution of the hot channel generated by femtosecond laser tagging in quiescent air," in 2018 Aerodynamic Measurement Technology and Ground Testing Conference, Paper uses the elevated temperature rise of Limbach et al. (2017) as input for the simulation to converge with the results of blast wave theory., AIAA, Jun. 2018. DOI: 10.2514/6.2018-2990.
- [76] M. J. DeWitt and R. J. Levis, "Calculating the Keldysh adiabaticity parameter for atomic, diatomic, and polyatomic molecules," *J. Chem. Phys.*, vol. 108, no. 18, pp. 7739–7742, 1998. DOI: 10.1063/1.476208.

- [77] A. Talebpour, J. Yang, and S. L. Chin, "Semi-empirical model for the rate of tunnel ionization of N₂ and O₂ molecule in an intense Ti:sapphire laser pulse," *Opt. Commun.*, vol. 163, no. 1-3, pp. 29–32, 1999, Due to a typographical error, the plotted ionization rate of nitrogen should be reduced by a factor of 10 according to Kasparian et al. (2000). DOI: 10.1016/S0030-4018(99)00113-3.
- [78] J. Kasparian, R. Sauerbrey, and S. L. Chin, "The critical laser intensity of self-guided light filaments in air," *Appl. Phys. B*, vol. 71, no. 6, pp. 877–879, 2000. DOI: 10.1007/s003400000463.
- [79] A. Couairon and A. Mysyrowicz, "Femtosecond filamentation in transparent media," *Phys. Rep.*, vol. 441, no. 2-4, pp. 47–189, 2007. DOI: 10.1016/j.physrep.2006.12.005.
- [80] J.-F. Daigle, A. Jaron-Becker, S. Hosseini, T.-J. Wang, Y. Kamali, G. Roy, A. Becker, and S. L. Chin, "Intensity clamping measurement of laser filaments in air at 400 and 800 nm," *Phys. Rev. A*, vol. 82, no. 2, p. 023405, 2010. DOI: 10.1103/PhysRevA.82.023405.
- [81] J. Bernhardt, W. Liu, S. L. Chin, and R. Sauerbrey, "Pressure independence of intensity clamping during filamentation: Theory and experiment," *Appl. Phys. B*, vol. 91, no. 1, pp. 45–48, 2008. DOI: 10.1007/s00340-008-2956-z.
- [82] Á. Börzsönyi, Z. Heiner, A. P. Kovács, M. P. Kalashnikov, and K. Osvay, "Measurement of pressure dependent nonlinear refractive index of inert gases," *Opt. Express*, vol. 18, no. 25, pp. 25847–25854, 2010. DOI: 10.1364/0E.18.025847.
- [83] S. Zahedpour, J. K. Wahlstrand, and H. M. Milchberg, "Measurement of the nonlinear refractive index of air constituents at mid-infrared wavelengths," *Opt. Lett.*, vol. 40, no. 24, pp. 5794–5797, 2015. DOI: 10.1364/OL.40.005794.
- [84] J. K. Wahlstrand, Y.-H. Cheng, and H. M. Milchberg, "Absolute measurement of the transient optical nonlinearity in N₂, O₂, N₂O, and Ar," *Phys. Rev. A*, vol. 85, no. 4, p. 043 820, 2012, Although measurements were performed at 550–635 nm, they also apply to 800 nm to within 3 %. DOI: 10.1103/PhysRevA. 85.043820.
- [85] D. H. Stedman and D. W. Setser, "Energy pooling by triplet nitrogen $(A^3\Sigma_u^+)$ molecules," *J. Chem. Phys.*, vol. 50, no. 5, pp. 2256–2258, 1969. DOI: 10.1063/1.1671359.
- [86] L. G. Piper, "State-to-state $N_2(A^3\Sigma_u^+)$ energy-pooling reactions. I. The formation of $N_2(C^3\Pi_u)$ and the Herman infrared system," *J. Chem. Phys.*, vol. 88, no. 1, pp. 231–239, 1988. DOI: 10.1063/1.454649.
- [87] F. Valk, M. Aints, P. Paris, T. Plank, J. Maksimov, and A. Tamm, "Measurement of collisional quenching rate of nitrogen states $N_2(C^3\Pi_u, v=0)$ and $N_2^+(B^2\Sigma_g^+, v=0)$," *J. Phys. D Appl. Phys.*, vol. 43, no. 38, p. 385 202, 2010. DOI: 10.1088/0022-3727/43/38/385202.

- [88] J. B. Michael, M. R. Edwards, A. Dogariu, and R. B. Miles, "Velocimetry by femtosecond laser electronic excitation tagging (FLEET) of air and nitrogen," in 50th AIAA Aerospace Sciences Meeting Including the New Horizons Forum and Aerospace Exposition, AIAA, Jan. 2012. DOI: 10.2514/6.2012-1053.
- [89] M. N. Shneider and R. B. Miles, "Microwave diagnostics of small plasma objects," *J. Appl. Phys.*, vol. 98, no. 3, p. 033 301, 2005. DOI: 10.1063/1.1996835.
- [90] C. J. Peters, R. A. Burns, R. B. Miles, and P. M. Danehy, "Effect of low temperatures and pressures on signal, lifetime, accuracy and precision of femtosecond laser tagging velocimetry," 2019, in preparation.
- [91] C. E. Dedic, A. D. Cutler, and P. M. Danehy., "Characterization of supersonic flows using hybrid fs/ps CARS," in *AIAA Scitech 2019 Forum*, AIAA, Jan. 2019. DOI: 10.2514/6.2019-1085.
- [92] R. L. Gaffney Jr., B. K. Stewart, and S. F. Harvin, "The design of a High-Q, Mach-5 nozzle for the NASA Langley 8-Foot HTT," in 25th AIAA Aerodynamic Measurement Technology and Ground Testing Conference, Jun. 2006. DOI: 10.2514/6.2006-2954.
- [93] R. L. Gaffney Jr., "Design of Mach-4 and Mach-6 nozzles for the NASA LaRC 8-Ft High Temperature Tunnel," in 45th AIAA/ASME/SAE/ASEE Joint Propulsion Conference & Exhibit, Aug. 2009. DOI: 10.2514/6.2009-5368.
- [94] J. D. Anderson Jr., Modern Compressible Flow with Historical Perspective, 2nd ed. Boston: McGraw-Hill, 1990, ISBN: 978-0-07-001673-6.
- [95] C. Leys, C. Ley, O. Klein, P. Bernard, and L. Licata, "Detecting outliers: Do not use standard deviation around the mean, use absolute deviation around the median," *J. Exp. Soc. Psychol.*, vol. 49, no. 4, pp. 764–766, Jul. 2013. DOI: 10.1016/j.jesp.2013.03.013.
- [96] L. E. Dogariu, A. Dogariu, R. B. Miles, M. S. Smith, and E. C. Marineau, "Non-intrusive hypersonic freestream and turbulent boundary-layer velocity measurements in AEDC Tunnel 9 using FLEET," in 2018 AIAA Aerospace Sciences Meeting, In this paper, the authors found that pseudo-Voigt profiles fit the initial time delay data much better than pure Gaussian functions., AIAA, Jan. 2018. DOI: 10.2514/6.2018-1769.
- [97] S. Raghu, "Fluidic oscillators for flow control," *Exp. Fluids*, vol. 54, no. 2, p. 1455, Jan. 2013. DOI: 10.1007/s00348-012-1455-5.
- [98] B. C. Bobusch, R. Woszidlo, J. M. Bergada, C. N. Nayeri, and C. O. Paschereit, "Experimental study of the internal flow structures inside a fluidic oscillator," *Exp. Fluids*, vol. 54, no. 6, p. 1559, Jun. 2013. DOI: 10.1007/s00348-013-1559-6.

- [99] S. A. Gokoglu, M. A. Kuczmarski, D. E. Culley, and S. Raghu, "Numerical studies of a supersonic fluidic diverter actuator for flow control," in 5th Flow Control Conference, AIAA, Jun. 2010. DOI: 10.2514/6.2010-4415.
- [100] D. Hirsch, E. C. Graff, and M. Gharib, "Compressible flows in fluidic oscillators," in 66th Annual Meeting of the APS Division of Fluid Dynamics, Schlieren video of internal and external flows of sweeping jet actuator., APS, Nov. 2013.
- [101] S. Gärtlein, R. Woszidlo, F. Ostermann, C. N. Nayeri, and C. O. Paschereit, "The time-resolved internal and external flow field properties of a fluidic oscillator," in 52nd Aerospace Sciences Meeting, AIAA, Jan. 2014. DOI: 10.2514/6.2014-1143.
- [102] O. Krüger, B. C. Bobusch, R. Woszidlo, and C. O. Paschereit, "Numerical modeling and validation of the flow in a fluidic oscillator," in 21st AIAA Computational Fluid Dynamics Conference, AIAA, Jun. 2013. DOI: 10.2514/6.2013-3087.
- [103] M. Koklu and L. P. Melton, "Sweeping jet actuator in a quiescent environment," in 43rd Fluid Dynamics Conference, AIAA, Jun. 2013. DOI: 10.2514/6.2013-2477.
- [104] G. Raman and S. Raghu, "Cavity resonance suppression using miniature fluidic oscillators," AIAA J., vol. 42, no. 12, pp. 2608–2611, Dec. 2004. DOI: 10.2514/ 1.521.
- [105] V. N. Vatsa, M. Koklu, I. L. Wygnanski, and E. Fares, "Numerical simulation of fluidic actuators for flow control applications," in 6th AIAA Flow Control Conference, AIAA, Jun. 2012. DOI: 10.2514/6.2012-3239.
- [106] B. C. Bobusch, R. Woszidlo, O. Krüger, and C. O. Paschereit, "Numerical investigations on geometric parameters affecting the oscillation properties of a fluidic oscillator," in 21st AIAA Computational Fluid Dynamics Conference, AIAA, Jun. 2013. DOI: 10.2514/6.2013-2709.
- [107] R. Seele, E. Graff, J. Lin, and I. Wygnanski, "Performance enhancement of a vertical tail model with sweeping jet actuators," in 51st AIAA Aerospace Sciences Meeting Including the New Horizons Forum and Aerospace Exposition, AIAA, Jan. 2013. DOI: 10.2514/6.2013-411.
- [108] K. Northon, Ed., NASA, Boeing finish tests of 757 vertical tail with advanced technology, NASA Press Release 13-340, Nov. 2013.
- [109] W. E. Milholen II, G. S. Jones, D. T. Chan, S. L. Goodliff, S. G. Anders, L. P. Melton, M. B. Carter, B. G. Allan, and F. J. Capone, "Enhancements to the FAST-MAC circulation control model and recent high-Reynolds number testing in the National Transonic Facility," in 31st AIAA Applied Aerodynamics Conference, AIAA, Jun. 2013. DOI: 10.2514/6.2013-2794.

- [110] G. S. Jones, W. E. Milholen II, J. S. Fell, S. R. Webb, and C. M. Cagle, "Using computational fluid dynamics and experiments to design sweeping jets for high Reynolds number cruise configurations," in 8th AIAA Flow Control Conference, AIAA, Jun. 2016. DOI: 10.2514/6.2016-3311.
- [111] L. S. G. Kovásznay, "The hot-wire anemometer in supersonic flow," *J. Aeronaut. Sci.*, vol. 17, no. 9, pp. 565–572, 1950. DOI: 10.2514/8.1725.
- [112] C. E. Willert, D. M. Mitchell, and J. Soria, "An assessment of high-power light-emitting diodes for high frame rate schlieren imaging," *Exp. Fluids*, vol. 53, no. 2, pp. 413–421, Aug. 2012. DOI: 10.1007/s00348-012-1297-1.
- [113] S. B. Pope, *Turbulent Flows*, 1st ed. Cambridge: Cambridge University Press, 2000, ISBN: 978-0-521-59886-6.
- [114] Y. Andreopoulos, J. H. Agui, and G. Briassulis, "Shock wave—turbulence interactions," *Annu. Rev. Fluid Mech.*, vol. 32, no. 1, pp. 309–345, Jan. 2000. DOI: 10.1146/annurev.fluid.32.1.309.
- [115] R. A. Burns, P. M. Danehy, B. R. Halls, and N. Jiang, "Application of FLEET velocimetry in the NASA Langley 0.3-Meter Transonic Cryogenic Tunnel," in 31st AIAA Aerodynamic Measurement Technology and Ground Testing Conference, AIAA, Jun. 2015. DOI: 10.2514/6.2015-2566.
- [116] R. Miles, C. Cohen, J. Connors, P. Howard, S. Huang, E. Markovitz, and G. Russell, "Velocity measurements by vibrational tagging and fluorescent probing of oxygen," *Opt. Lett.*, vol. 12, no. 11, pp. 861–863, Nov. 1987. DOI: 10.1364/0L.12.000861.
- [117] R. B. Miles, J. J. Connors, E. C. Markovitz, P. J. Howard, and G. J. Roth, "Instantaneous profiles and turbulence statistics of supersonic free shear layers by Raman excitation plus laser-induced electronic fluorescence (RELIEF) velocity tagging of oxygen," *Exp. Fluids*, vol. 8, no. 1-2, pp. 17–24, Oct. 1989. DOI: 10.1007/BF00203060.
- [118] N. Dam, R. J. H. Klein-Douwel, N. M. Sijtsema, and J. J. ter Meulen, "Nitric oxide flow tagging in unseeded air," *Opt. Lett.*, vol. 26, no. 1, pp. 36–38, Jan. 2001. DOI: 10.1364/OL.26.000036.
- [119] R. W. Pitz, T. M. Brown, S. P. Nandula, P. A. Skaggs, P. A. DeBarber, M. S. Brown, and J. Segall, "Unseeded velocity measurement by ozone tagging velocimetry," *Opt. Lett.*, vol. 21, no. 10, pp. 755–757, May 1996. DOI: 10.1364/ 0L.21.000755.
- [120] J. N. Forkey, W. R. Lempert, and R. B. Miles, "Accuracy limits for planar measurements of flow field velocity, temperature and pressure using filtered Rayleigh scattering," *Exp. Fluids*, vol. 24, no. 2, pp. 151–162, Feb. 1998. DOI: 10.1007/s003480050162.

- [121] R. G. Seasholtz, F. J. Zupanc, and S. J. Schneider, "Spectrally resolved Rayleigh scattering diagnostic for hydrogen-oxygen rocket plume studies," *J. Propul. Power*, vol. 8, no. 5, pp. 935–942, Sep. 1992–Oct. 1992. DOI: 10.2514/3.23575.
- [122] E. B. Cummings, "Laser-induced thermal acoustics: Simple accurate gas measurements," *Opt. Lett.*, vol. 19, no. 17, pp. 1361–1363, Sep. 1994. DOI: 10. 1364/OL.19.001361.
- [123] J. R. Taylor, An Introduction to Error Analysis: The Study of Uncertainties in Physical Measurements, 2nd ed. Sausalito, California: University Science Books, 1997, ISBN: 978-0-935702-75-0.
- [124] N. D. Calvert, A. Dogariu, and R. B. Miles, "2-D velocity and vorticity measurements with FLEET," in 30th AIAA Aerodynamic Measurement Technology and Ground Testing Conference, AIAA, Jun. 2014. DOI: 10.2514/6.2014–2229.
- [125] P. M. Danehy, B. F. Bathel, N. D. Calvert, A. Dogariu, and R. B. Miles, "Three-component velocity and acceleration measurement using FLEET," in 30th AIAA Aerodynamic Measurement Technology and Ground Testing Conference, AIAA, Jun. 2014. DOI: 10.2514/6.2014-2228.
- [126] G. S. Elliott, M. Samimy, and S. A. Arnette, "A molecular filter based velocimetry technique for high speed flows," *Exp. Fluids*, vol. 18, no. 1-2, pp. 107–118, Dec. 1994. DOI: 10.1007/BF00209367.
- [127] D. Bivolaru, A. D. Cutler, and P. M. Danehy, "Spatially- and temporally-resolved multi-parameter interferometric Rayleigh scattering," in 49th AIAA Aerospace Sciences Meeting Including the New Horizons Forum and Aerospace Exposition, AIAA, Jan. 2011. DOI: 10.2514/6.2011-1293.
- [128] D. Bivolaru, P. M. Danehy, R. L. Gaffney Jr., and A. D. Cutler, "Direct-view multi-point two-component interferometric Rayleigh scattering velocimeter," in 46th AIAA Aerospace Sciences Meeting and Exhibit, AIAA, Jan. 2008. DOI: 10.2514/6.2008-236.
- [129] A. F. Mielke, K. A. Elam, and C.-J. Sung, "Rayleigh scattering diagnostic for measurement of temperature, velocity, and density fluctuation spectra," in 44th AIAA Aerospace Sciences Meeting and Exhibit, AIAA, Jan. 2006. DOI: 10.2514/6.2006-837.
- [130] R. C. Hart, R. J. Balla, G. C. Herring, and L. N. Jenkins, "Seedless laser velocimetry using heterodyne laser-induced thermal acoustics," in 19th International Congress on Instrumentation in Aerospace Simulation Facilities, ICIASF, Aug. 2001. DOI: 10.1109/ICIASF.2001.960265.
- [131] R. C. Hart, R. J. Balla, and G. C. Herring, "Simultaneous velocimetry and thermometry of air by use of nonresonant heterodyned laser-induced thermal acoustics," *Appl. Opt.*, vol. 40, no. 6, pp. 965–968, Feb. 2001. DOI: 10.1364/A0.40.000965.

- [132] W. P. N. van der Laan, R. A. L. Tolboom, N. J. Dam, and J. J. ter Meulen, "Molecular tagging velocimetry in the wake of an object in supersonic flow," *Exp. Fluids*, vol. 34, no. 4, pp. 531–533, Apr. 2003. DOI: 10.1007/s00348-003-0593-1.
- [133] C. J. Peters, R. B. Miles, and P. M. Danehy, Flow quality analysis of structures for hypersonic ground testing applications, NSTRF Final Report: NASA Grant Number NNX13AL63H, Aug. 2017.
- [134] K. H. Timpano, "Design and test of a morphing supersonic nozzle," M.S.E. Thesis, Princeton University, Department of Mechanical & Aerospace Engineering, Sep. 2007.
- [135] C. A. Steeves, K. H. Timpano, P. T. Maxwell, L. Martinelli, and R. B. Miles, "Design and manufacture of a morphing structure for a shape-adaptive super-sonic wind tunnel nozzle," *J. Appl. Mech.*, vol. 76, no. 3, p. 031012, May 2009. DOI: 10.1115/1.3005572.
- [136] K. Kinefuchi, A. Y. Starikovskiy, and R. B. Miles, "Control of shock-wave/boundary-layer interaction using nanosecond-pulsed plasma actuators," *J. Propul. Power.*, vol. 34, no. 4, pp. 909–919, Jul. 2018–Aug. 2018. DOI: 10.2514/1.B36530.